

# Numerical studies of higher-dimensional localized black holes and holographic Weyl semimetals

## Dissertation

zur Erlangung des akademischen Grades  
*doctor rerum naturalium* (Dr. rer. nat.)



**FRIEDRICH-SCHILLER-  
UNIVERSITÄT  
JENA**

vorgelegt dem Rat der Physikalisch-Astronomischen  
Fakultät der Friedrich-Schiller-Universität Jena

von M. Sc. Sebastian Möckel  
geboren am 14.03.1989 in Schlema

**Gutachter:**

1. Jun.-Prof. Dr. Martin Ammon  
Friedrich-Schiller-Universität Jena  
Theoretisch-Physikalisches-Institut
2. Prof. Dr. Johanna Erdmenger  
Julius-Maximilians-Universität Würzburg  
Theoretische Physik III
3. Prof. Dr. Oscar Campos Dias  
University of Southampton  
STAG research centre and Mathematical Science

**Datum der Disputation: 23.10.2018**

---

# Zusammenfassung

---

In unserem alltäglichen Leben können wir drei räumliche sowie eine zeitliche Dimension wahrnehmen. Jedoch könnte die Betrachtung zusätzlicher Dimensionen einen Ansatz zur Lösung verschiedener Probleme der modernen Physik bieten, unter anderem für das Hierarchieproblem und die Vereinigung der elementaren Wechselwirkungen. Zudem gibt uns die Stringtheorie, welche generisch zur Annahme zusätzlicher Dimensionen führt, Hinweise auf die Äquivalenz zwischen bestimmten stark gekoppelten Quantenfeldtheorien und Gravitationstheorien in höheren Dimensionen. Speziell die AdS/CFT Korrespondenz induzierte die Untersuchung zahlreicher höherdimensionale Gravitationstheorien mit verschiedenem Materieinhalt.

Der erste Teil dieser Arbeit ist der numerischen Konstruktion von lokalisierten Schwarzen Löchern in fünf, sechs und zehn dimensional Kaluza-Klein-Theorien gewidmet. Der Fokus liegt hierbei auf der Untersuchung statischer, asymptotisch flacher Lösungen der Einsteingleichungen im Vakuum mit einer periodisch kompaktifizierten Dimension. Speziell der kritische Bereich, innerhalb dessen die Pole der lokalisierten Schwarzen Löcher nahe dem Verschmelzen sind, steht im Zentrum unserer Aufmerksamkeit. Die dafür erforderlichen Genauigkeiten werden durch Verwendung eines besonders angepassten pseudospektralen Mehrgebietsverfahrens erreicht, wodurch das entsprechende Phasendiagramm weit über den bisher bekannten Bereich ausgedehnt werden kann. Als Ergebnis erhalten wir eine spiralförmige Struktur im Phasenraum der fünf- und sechsdimensionalen Konfigurationen, welche sich nahtlos an die kürzlich für Schwarze Strings mit ungleichmäßiger Horizontgeometrie gefundenen Resultate fügen. Im Gegensatz dazu zeigt der Phasenraum der zehndimensionalen Konfiguration keine spiralförmigen Kurven der thermodynamischen Größen. Die im Rahmen dieser Arbeit numerisch berechneten Werte der kritischen Exponenten zeigen eine besonders gute Übereinstimmung mit den theoretischen Vorhersagen.

Die Untersuchung stark gekoppelter Weyl-Halbmatalle unter Verwendung der AdS/CFT Korrespondenz steht im Fokus des zweiten Teils dieser Arbeit. Konkret analysieren wir unter Zuhilfenahme numerischer, pseudo-spektraler Techniken die Auswirkungen von Inhomogenitäten in einem holographischen Weyl-Halbmatalle, insbesondere werden Grenzflächeneffekte sowie die Folgen von zeitlich konstanter Unordnung studiert. Als Resultat der Untersuchung von Grenzflächen zwischen verschiedenen Phasen eines Weyl-Halbmatalles erhalten wir lokalisierte Grenzflächenstromdichten bei Anwesenheit eines äußeren chemischen Potentials. Der diesbezügliche integrierte Grenzflächenstrom hängt nur von der Topologie der sich berührenden Phasen ab und ist in diesem Sinne universell. Als Konsequenz stellen unsere Resultate einen wichtigen Beitrag für das Verständnis anomaler Transporteigenschaften in inhomogenen Magnetfeldern dar.

Als weiteren Aspekt wird die Auswirkung von zeitunabhängiger Unordnung auf den Quantenphasenübergang (QPT) im holographischen Weyl-Halbmatalle untersucht. Hier lässt sich eine Ausschmierung des scharfen QPTs beobachten, welche mit der Ausbildung sogenannter seltener Regionen mit lokal nicht verschwindendem Ordnungsparameter einhergeht. Außerdem untersuchen wir den Einfluss der Korrelationslänge der implementierten Unordnung und vergleichen unsere Resultate mit theoretischen Vorhersagen der Festkörperphysik.





---

# Abstract

---

In our everyday lives, we experience three spatial dimensions and a fourth dimension of time. Nevertheless, several intricate problems of modern physics may be mastered with the introduction of additional dimensions, including the hierarchy problem and the unification of the fundamental forces. Furthermore, dualities between certain strongly coupled quantum field theories and particular gravitational theories in higher dimensions were conjectured based on string theory, which generically comes with the premise of extra dimensions. Specifically, the AdS/CFT correspondence or rather gauge/gravity duality motivated the study of a wide variety of higher dimensional gravitational theories with additional matter.

The first part of this thesis covers the numerical construction of localized black holes in five, six and ten dimensional Kaluza-Klein theories. We focus on static, asymptotically flat vacuum solutions of Einstein's field equations with one periodic compact dimension. Our study concentrates on the critical regime, where the poles of the localized black holes are about to merge. We utilize a well adapted multi-domain pseudo-spectral scheme for obtaining high accuracy results and investigate the phase diagram of the localized solutions far beyond previous results. A spiral phase space structure is found for the five and six dimensional setups which matches to the results that were recently obtained for non-uniform black strings. On the contrary, the phase space structure of the ten dimensional configuration exhibits no spiraling behavior of the thermodynamical quantities. These critical exponents were extracted from the numerical data of the aforementioned configurations and show an excellent agreement with the theoretical predictions.

In the second part of this thesis, the AdS/CFT correspondence is employed for studying strongly coupled Weyl semimetals. More concretely, we numerically investigate the effects of inhomogeneities within a holographic Weyl semimetal by using a pseudo-spectral scheme, including interfaces of Weyl semimetals and the impact of time independent disorder. When studying interfaces between different Weyl semimetal phases, we observe the appearance of an electric current, that is restricted to the interface in the presence of an electric chemical potential. The related integrated current is universal in the sense that it only depends on the topology of the phases. These results may shed some light on anomalous transport for inhomogeneous magnetic fields.

As another point, we study the effects of time independent one-dimensional disorder on the holographic Weyl semimetal quantum phase transition (QPT), with a particular focus on the quantum critical region. We observe the smearing of the sharp QPT linked to the appearance of rare regions where the order parameter is locally non-zero. We discuss the role of the disorder correlation and we compare our results to expectations from condensed matter theory at weak coupling. We also analyze the interplay of finite temperature and disorder.



---

# Contents

---

<b>1</b>	<b>Introduction</b>	<b>3</b>
<b>2</b>	<b>Theoretical foundations</b>	<b>9</b>
2.1	General relativity basics . . . . .	9
2.1.1	Gravity as geometry . . . . .	9
2.1.2	Einstein's field equations . . . . .	11
2.2	Important spacetimes . . . . .	13
2.2.1	The anti-de Sitter spacetime . . . . .	13
2.2.2	Black hole spacetimes . . . . .	15
2.3	The AdS/CFT correspondence . . . . .	20
2.3.1	A concrete example for the AdS/CFT correspondence . . . . .	20
2.3.2	Relating fields in AdS to composite operators of the CFT . . . . .	22
<b>3</b>	<b>Numerical methods</b>	<b>27</b>
3.1	Theory of spectral methods . . . . .	27
3.1.1	The Fourier expansion . . . . .	28
3.1.2	The Chebyshev expansion . . . . .	29
3.2	Spectral methods for boundary value problems . . . . .	30
3.2.1	Multiple domains . . . . .	32
<b>4</b>	<b>Localized Kaluza-Klein black holes</b>	<b>33</b>
4.1	Static Kaluza-Klein black holes . . . . .	34
4.1.1	Physical quantities . . . . .	34
4.1.2	Black strings and localized black holes . . . . .	35
4.1.3	The Gregory-Laflamme instability . . . . .	38
4.1.4	The thermodynamic stability of static Kaluza-Klein black holes . . . . .	39
4.1.5	Critical behavior and the double-cone metric . . . . .	40
4.2	Numerical construction . . . . .	42
4.2.1	Metric and boundary conditions . . . . .	43
4.2.2	Gauging and reference metric . . . . .	45
4.2.3	Domain decomposition . . . . .	46
4.2.4	Parameters and observables . . . . .	49
4.3	Results . . . . .	52
4.3.1	Thermodynamics . . . . .	52
4.3.2	Geometry . . . . .	55
4.3.3	Critical behavior . . . . .	56
4.4	Summary . . . . .	60

---

<b>5</b>	<b>Weyl semimetals</b>	<b>61</b>
5.1	Theory of Weyl semimetals . . . . .	61
5.1.1	Weyl nodes and transport properties . . . . .	62
5.1.2	The chiral anomaly . . . . .	64
5.1.3	An effective quantum field model of Weyl semimetals . . . . .	67
5.2	Holographic model of Weyl semimetals . . . . .	71
5.2.1	The holographic action . . . . .	71
5.2.2	Equations of motion . . . . .	72
5.3	Surface states in holographic Weyl semimetals . . . . .	73
5.3.1	Effective quantum field model . . . . .	73
5.3.2	Holographic model . . . . .	75
5.3.3	Numerical construction . . . . .	77
5.3.4	Results . . . . .	79
5.4	Finite temperature and disorder effects in holographic Weyl semimetals . . . . .	83
5.4.1	Physical background . . . . .	83
5.4.2	Holographic model . . . . .	85
5.4.3	Numerical construction . . . . .	87
5.4.4	Results . . . . .	90
5.5	Summary . . . . .	95
<b>6</b>	<b>Conclusions and outlook</b>	<b>97</b>
<b>A</b>	<b>Supplementary material</b>	<b>101</b>
A.1	Theoretical basics . . . . .	101
A.2	Localized black holes . . . . .	104
A.3	Holographic Weyl semimetals . . . . .	113
A.4	Details of the numerical implementation . . . . .	125
	<b>Bibliography</b>	<b>132</b>
	<b>References</b>	<b>133</b>
	<b>Abbreviations and notation</b>	<b>147</b>
	<b>Acknowledgements</b>	<b>149</b>
	<b>Ehrenwörtliche Erklärung</b>	<b>151</b>

---

# Introduction

---

The beginning of the 20th century was marked by two major revolutions in science, which consequently changed our perception of nature and are both linked to Albert Einstein. The first revolution is related to Einstein's utilization of Planck's quantum hypothesis when explaining the photoelectric effect in 1905 [63], which was one of the pioneering works for establishing quantum theory. Quantum theory aims for describing nature at microscopic scales, whereas gravity determines structures at large scales. As a tremendous breakthrough, Einstein revealed the geometric origin of the gravitational interaction when presenting his final theory of general relativity (GR) in 1915 [64]. Accordingly, the gravitational attraction of matter is a direct consequence of spacetime curvature, which is in turn induced by the energy content of the matter.

The success of general relativity was, despite its mathematical complexity, a result of its geometric clarity and its capability to explain the perihelion precession of Mercury [65], that had remained mysterious for a long time. Furthermore, GR made predictions about the observation of physical effects, that had not been recognized so far, such as the deflection of light by the Sun [62] and the gravitational redshift of light [170]. In particular, the recent measurement of gravitational waves from a binary neutron star merger by LIGO [1], accompanied with a direct optical validation of the event, highlights the verification of one of the last missing tests for general relativity.

Due to the successes of field theoretic formulations in the electromagnetic realm and similarities between gravitational and electromagnetic interactions, physicists started early to combine Maxwell's formulation of electromagnetism with Einstein's theory of general relativity. Already shortly after Einstein published his work, Nordström tried to derive both theories from a unified description by adding a fourth spatial dimension to the GR framework [160]. This idea was further developed by Kaluza, who noticed that a five-dimensional formulation of GR can be reduced to Einstein's description of gravity in four dimension coupled to electromagnetic fields [124]. The basis of Kaluza's ansatz was the interpretation of the additional degrees of freedom as components of a four-dimensional vector potential augmented by an additional scalar field, while all fields were constrained to be independent of the new fifth dimension. This cylinder condition led to a significant simplification of the regarding field equations, but a physical motivation for it remained unclear. Subsequently, Klein replaced the cylinder condition by assuming a compactified nature of the fifth dimension in 1926 [130, 129]. Klein's ansatz came with the advantage of a nice physical interpretation of the extra dimension related to quantum theory: As a consequence of its compact topology, the field momentum  $p_5$  should be quantized in the periodic dimension according to de Broglie's condition  $p_5 = hk/L$ , where  $h$  is the Planck constant,  $L$  is the extension of the compact dimension and  $k$  is an integer. Klein's modification provided a simple explanation, why the predicted additional dimension has not been spotted yet: A very small value of  $L$  would make excitations of the higher non-trivial modes  $k > 0$  inaccessible to experimental observation.

The ideas of Kaluza and Klein (KK) were further extended and analyzed by several researchers in the following years<sup>1</sup>. However, the presence of an additional scalar field in KK

---

<sup>1</sup>Reference [20] provides a nice review on these developments.

theory without any physical interpretation was considered as a major inconvenience. Meanwhile the quantization of fields was put on profound grounds by the successive development of quantum field theory. The vast number of new particles detected in the different high energy accelerators together with the discovery of the weak and strong interactions let rise the need for a unified explanation of these phenomena. The efforts for a unification of the fundamental electromagnetic, weak and strong interactions culminated in the so-called Standard Model (SM) of particle physics. Being based on quantum field theory, the SM includes a wide range of physics, such as spontaneous symmetry breaking and anomalies. Consequently, the SM was able to explain many of the observed phenomena, while providing important experimental predictions, that led amongst others to the discovery of the W and Z bosons, the gluon, top and charm quarks and recently the Higgs boson, cf. [8, 214] for comprehensive reviews on these topics. Despite its successes, the SM fails to incorporate the gravitational interaction as described by general relativity and a unified theory of all fundamental interactions is not available today. The formulation of such a unification poses one of the most important challenges to contemporary theoretical physics.

A possible framework for such a unified theory is provided by string theory, which is based on the replacement of the point-like particle model by one-dimensional strings. The first studies of string theory as a possible candidate to model the strong nuclear force date back to the late 1960s. Only after being abandoned in favor of quantum chromodynamics, it was realized that string theory could serve as a possible candidate for a quantum theory of gravity. A detailed review of string theory is certainly out of the scope of this thesis<sup>2</sup>, but the most important ideas can be summarized as follows: Strings propagate through space, interact with each other and are subject to different vibrational states corresponding to the analogs of the elementary particles of particle physics. In particular, one of these vibrational states can be interpreted in terms of the graviton, which is the predicted quantum particle that mediates the gravitational force. A consistent quantization of the strings necessitates the introduction of additional dimensions, where the concrete number depends on the different particle classes (bosons, fermions) to be incorporated. Correspondingly, superstring theory, in which bosonic and fermionic strings are connected by so-called supersymmetric transformations, requires six additional spatial dimensions resulting in a total number of ten spacetime dimensions. The idea of extra dimensions brings us back to Kaluza's and Klein's formulation of five-dimensional gravity. A much richer set of possible compactifications are considered within string theory due to the higher number of excess dimensions, but the missing evidence for additional dimensions can again be justified with Klein's argument about their tiny extension. As desired, we recover classical GR in ten dimensions coupled to additional fields in the low energy limit of superstring theory. Accordingly, we can consider KK theory as one of the possible classical limits of superstring theory, if the additional dimensions are compactified in a suitable way.

An important relationship between string theory and quantum field theory was established in 1997, when the so-called anti-de Sitter/conformal field theory (AdS/CFT) correspondence was discovered [153, 213, 90, 3]. In a nutshell, this correspondence implies the equivalence of certain string theories in anti-de Sitter (AdS) spacetimes<sup>3</sup> to specific conformal quantum field theories (CFTs). Consequently, the AdS/CFT correspondence is also commonly denoted as gauge/gravity correspondence or holographic duality. The original formulation of the correspondence [153] related a CFT in four dimensions to the geometry of an AdS space in five

<sup>2</sup>We refer the reader to [218] for an instructive textbook on string theory.

<sup>3</sup>The anti-de Sitter space is a maximally symmetric vacuum solution to Einstein's equations with constant negative curvature.

---

dimensions. More generally, the correspondence relates strongly coupled quantum field theories to the classical dynamics of gravity with an additional dimension. This puts us in the beneficial position to study the physics of strongly coupled quantum systems by performing calculations within higher dimensional theories of gravity. Specifically, the AdS/CFT driven analysis of collective phenomena in strongly correlated condensed matter systems has attracted recent attention, after a number of exotic states of matter were discovered in experiments, including high temperature superconductors and Weyl semimetals. In the context of condensed matter physics, s-wave [98] and p-wave [91, 14, 16, 15, 13] superfluids were investigated, as well as Non-Fermi liquids [147, 15], topological insulators [109, 125, 17] and Quantum Hall transitions [50]. Recently, the spontaneous and/or explicit breaking of translational symmetry were investigated within holographic massive gravity theories [6, 7] giving rise to transverse phonons whose speed is dictated by elasticity theory. In this thesis we concentrate on modeling the quantum phase transition within a strongly coupled Weyl semimetal, which is hard to address by standard methods, which usually rely on weak coupling assumptions, that are not applicable in this case. However, the gauge/gravity correspondence and its implications are still not fully understood yet and are subject to current research.

Besides the numerous discoveries and new developments in physics, a large variety of new methods for tackling the related mathematical problems were established in the 20th century. Most of all, the development of modern computers stimulated research by facilitating the solution of problems that had been out of reach before. A problem class of particular importance is provided by differential equations due to their omnipresence in the different physical disciplines. Accordingly, various numerical methods for the efficient and accurate approximation of solutions to differential equations were designed, implemented and applied to many different problems. Among the distinct approximation schemes, we would like to mention spectral methods, which rely on a truncated expansion of the target function in terms of an appropriate set of basis functions. Under certain conditions, these methods can show extraordinary convergence properties, which are desirable when a high accuracy of the approximation is required. Consequently, these methods play a major role for the construction of numerical solutions of partial differential equations within this thesis.

## Subjects of this work

As previously discussed, by studying problems related to gravity in higher dimensions we can make predictions about possible impacts of a unification of forces at higher energy scales. On the other hand, we may relate our findings directly to results within certain quantum field theories depending on the number of dimensions and the asymptotic structure of the underlying spacetime.

This work is divided into two major parts. In the first half, we consider the numerical construction of static higher dimensional localized black holes (LBHs) in KK theory. The second part addresses the study of Weyl semimetals by utilizing the aforementioned gauge/gravity duality.

### Localized black holes

Black holes assume a special role among the various objects and effects that are predicted by GR as a consequence of their event horizon, which prevents all classical matter from escaping their vicinity. First considered as a mathematical curiosity, they were later recognized as generic

predictions of general relativity. While the number of possible stationary vacuum black hole configurations in four dimensions is constrained due to uniqueness theorems (i.e. the Schwarzschild and Kerr solutions), higher dimensions provide a much richer set of different time-independent black holes without additional matter fields. This fact, together with the aforementioned importance of higher dimensions within string theory, explains that the study of higher-dimensional black hole systems was receiving a growing attention over the last decades [107].

Localized black holes are a special class of static vacuum spacetimes with one compact periodic dimension considered in KK theory and were first discussed in [156]. The study of LBHs was initially motivated when examining the stability of so-called black strings. A black string is a black hole whose event horizon wraps the compact dimension completely. Gregory and Laflamme showed, that the perturbation of a black string with a uniform horizon geometry can lead to an instability, if the string mass surpasses a certain threshold at given extension of the compact dimension [84, 85]. The subsequent search for an endpoint of this instability led to the discovery of new static black hole configurations, such as non-uniform black string (NBS) with broken translational invariance along the compact dimension [89] and localized black holes. LBHs can be thought of as forming a never ending necklace of black hole “pearls” along the compact dimension. Soon after the discovery of the NBS solution, a parametric transition between the NBS and LBH branch was conjectured [93, 132]. Moreover, the so-called double cone metric as a candidate for the critical transit solution was studied by Kol [132, 133, 24], including a scaling analysis of physical quantities in the critical region.

In this work we present a sophisticated approach for numerically constructing LBH solutions, which is based on spectral methods. We remark, that this approach was used in [121, 122, 123] to analyze the merger of the LBH and NBS branch in five and six dimensions with an unprecedented level of accuracy. We further analyze the critical scaling of the physical quantities in the critical region and compare the results with Kols predictions about the double-cone metric. Moreover we show, that the method works in principle for arbitrary dimensions by constructing LBHs not only in five and six, but also in ten spacetime dimensions, where the critical behavior differs qualitatively.

We remark, that the NBS to LBH phase transition is first order and consequently comes with a significant release of energy. As a result, test signatures for extra dimensions in accelerator or astronomic observations can benefit from a high-precision study of the physical quantities in the critical regime [131].

As a peculiarity, the LBH solution in ten dimensions can be related to thermal states of a two dimensional supersymmetric Yang-Mills theory (SYM), which is compactified to a circle [113, 59]. We provide an analysis of the corresponding thermodynamic quantities in the appendix.

## Holographic Weyl semimetals

Black holes also play a major role in the second half of this thesis, which covers the construction of holographic Weyl semimetals (WSMs). Within this context, black holes in asymptotically anti-de Sitter (aAdS) space provide the proper boundary asymptotics for studying field configurations on the gravity side that can be related to strongly coupled quantum field theories at finite temperature via the aforementioned AdS/CFT correspondence. The corresponding quantum field theory can be thought of as living on the special conformal boundary structure of the aAdS space, which explains the notion “holographic duality”. As mentioned previously, the AdS/CFT correspondence allows us to investigate strongly coupled solid state systems by performing calculations within higher dimensional theories of classical gravity coupled to ad-



ditional fields. Thus non-perturbative results for quantum theories can be obtained by solving differential equations.

WSMs provide a particularly interesting strongly coupled condensed matter system for a study based on AdS/CFT, because they are connected to several exotic physical effects, such as a quantum phase transition, the chiral anomaly and topological surface states. Furthermore, they are subject to current experimental research [215, 112], such that theoretical predictions can be confronted with experimental results. Accordingly, a first holographic model of WSMs was introduced by Landsteiner [140]. It was shown, that this model can reproduce the characteristics of the quantum phase transition (QPT) and a corresponding modification of the available weak-coupling results was obtained [142].

Within this thesis we aim for extending the model of Landsteiner, that was used to study homogeneous configurations, to more complicated setups. The implementation of more realistic field configurations gives us the opportunity to check, whether the holographic model can, besides the QPT, also reproduce the special surface states of WSMs. Furthermore, we study the influence of disorder on the QPT in WSMs, which marks the first investigation of disorder effects in WSMs based on AdS/CFT so far. Especially the disorder analysis depends on a good performance to accuracy ratio of the underlying numerical approximation, which is again based on spectral methods.

## Outline

The thesis is structured as follows. In chapter 2 we start with a review of the most important theoretical basics, including the formulation of general relativity and Einstein's equations, the relevant non-trivial spacetimes and fundamental properties of black holes. We conclude chapter 2 with a brief overview of the AdS/CFT correspondence and provide important duality relations that are used within the investigation of holographic WSMs. The numerical techniques, i.e. spectral methods, that are used for both, the LBH and the WSM projects, are considered in chapter 3. Chapter 4 is dedicated to a detailed description of the numerical construction of localized LBHs, starting with a review of the most important properties of LBHs and related physical quantities. Chapter 4 concludes with a presentation of the LBH results in five, six and ten dimensions. After a short review of the physical characteristics and effects in WSMs, we present the numerical construction of holographic WSMs in chapter 5, concluding with a summary of the obtained results. The final chapter 6 provides a conclusion focusing on the physical relevance of our results. Additionally, some remarks on potentially interesting future developments are given.

We provide supplementary material, such as theoretical derivations and accuracy estimates in appendix A. Furthermore, additional details about the numerical implementation are given in appendix A.4.

We remark that the construction of LBHs in five and six dimensions, which is covered in chapter 4 of this thesis, was published in reference [123]. Consequently, the results of this cooperation, including the numerical construction and critical phase space analysis of LBHs and NBSs in five and six dimensions, were presented before in detail within the recently published PhD thesis of Michael Kalisch [120].

The investigation of surface states as well as finite temperature and disorder effects in holographic WSMs (contained in chapter 5) were published in [18, 11]. In particular, the numerical construction of surface states in holographic WSMs was covered in detail in the (unpublished) Master thesis of Markus Heinrich, which was supported by the author.



---

# Theoretical foundations

---

This chapter contains an overview of the theoretical foundations of this thesis. We start with discussing the basics of general relativity in section 2.1, including a short review of Einstein's field equations in subsection 2.1.2. We continue with an overview of the most important spacetimes to be used in this thesis in section 2.2. Finally, we outline the essential elements of the AdS/CFT correspondence, that will be important in the scope of this work, in section 2.3.

## 2.1 General relativity basics

### 2.1.1 Gravity as geometry

General relativity (GR) provides a description of the interaction between matter (or more general energy, including all types of fields) and space together with time. Accordingly, within GR, gravity is interpreted as a geometrical property of a 4-dimensional curved spacetime manifold. This approach can be easily extended to the description of spacetimes with arbitrary dimension  $D$ . The key ingredient of this model is the rank 2 metric tensor  $g_{\mu\nu}$ , which defines how the invariant spacetime interval  $ds^2$  between two spacetime events is measured

$$ds^2 = g_{\mu\nu} dx^\mu dx^\nu, \quad (2.1)$$

where  $dx^\mu$  denotes an infinitesimal displacement in the metric space. Here, Greek indices are running from 0 to  $D - 1$  where  $D$  denotes the dimension of the manifold and repeated indices imply summation. Note the invariance of equation (2.1) under general coordinate transformations  $x \mapsto x'$ .

As a next step, a covariant derivative  $\nabla$  is introduced since the ordinary partial derivative related to a given coordinate basis is not covariant under general coordinate transformations. Its component-wise action on a general tensor  $T$  within a given coordinate system reads as follows

$$\begin{aligned} (\nabla_\mu T)^{\alpha_1 \dots \alpha_r}_{\beta_1 \dots \beta_s} &= \frac{\partial}{\partial x^\mu} T^{\alpha_1 \dots \alpha_r}_{\beta_1 \dots \beta_s} \\ &+ \Gamma_{\nu\mu}^{\alpha_1} T^{\nu\alpha_2 \dots \alpha_r}_{\beta_1 \dots \beta_s} + \dots + \Gamma_{\nu\mu}^{\alpha_r} T^{\alpha_1 \dots \alpha_{r-1}\nu}_{\beta_1 \dots \beta_s} \\ &- \Gamma_{\beta_1\mu}^\nu T^{\alpha_1 \dots \alpha_r}_{\nu\beta_2 \dots \beta_s} - \dots - \Gamma_{\beta_s\mu}^\nu T^{\alpha_1 \dots \alpha_r}_{\beta_1 \dots \beta_{s-1}\nu}, \end{aligned} \quad (2.2)$$

where  $\Gamma_{\nu\mu}^\sigma$  is the Christoffel symbol

$$\Gamma_{\mu\nu}^\sigma = \frac{g^{\sigma\lambda}}{2} (\partial_\mu g_{\lambda\nu} + \partial_\nu g_{\lambda\mu} - \partial_\lambda g_{\mu\nu}). \quad (2.3)$$

The curvature of a given spacetime is encoded in the Riemann tensor

$$R^\rho_{\mu\sigma\nu} = \partial_\sigma \Gamma_{\mu\nu}^\rho - \partial_\nu \Gamma_{\mu\sigma}^\rho + \Gamma_{\mu\nu}^\lambda \Gamma_{\lambda\sigma}^\rho - \Gamma_{\mu\sigma}^\lambda \Gamma_{\lambda\nu}^\rho \quad (2.4)$$

Note that its components are determined by nonlinear combinations of first and second partial derivatives of the metric tensor. Its trace  $R_{\mu\nu} = R^{\rho}_{\mu\rho\nu}$  is called the Ricci tensor. By taking the trace  $R = R^{\mu}_{\mu}$  of the Ricci tensor, one obtains the Ricci scalar. These geometrical objects play a major role when relating the spacetime curvature to the energy content of a manifold.

### Non-coordinate Basis

Coordinate compactifications lead usually to singular entries of coordinate basis tensors which are cumbersome for numerical evaluation. The usage of non-coordinate basis tensors can help here and can be considered as a generalization of the usual conformal approach, which allows only for dealing with one singular factor that can be removed from all metric tensor entries. The starting point is the introduction of the frame coefficients  $e_{\mu}^i$  and the inverse coefficients  $e^{\mu}_i$  according to

$$e^{\mu}_i e_{\nu}^i = \delta_{\nu}^{\mu}, \quad e_{\mu}^i e^{\mu}_j = \delta_j^i, \quad (2.5)$$

where the Latin indices  $\{i, j, k, \dots\}$  run from 0 to  $D - 1$  and repeated indices imply summation. As a result we obtain a new frame basis metric

$$\eta_{ij} = g_{\mu\nu} e^{\mu}_i e^{\nu}_j, \quad (2.6)$$

where we do not put any constraints on  $\eta_{ij}$ . The inverse transformation reads

$$g_{\mu\nu} = e_{\mu}^i e_{\nu}^j \eta_{ij}. \quad (2.7)$$

Note that equation (2.6) can be considered as a spacetime dependent similarity transformation of  $g_{\mu\nu}$ . A tensor  $T$  can now be transformed to the non-coordinate frame and back

$$T^i = e_{\mu}^i T^{\mu}, \quad T^{\mu} = e^{\mu}_i T^i, \quad (2.8)$$

$$T_i = e^{\mu}_i T_{\mu}, \quad T_{\mu} = e_{\mu}^i T_i, \quad (2.9)$$

where the generalization to multi-index tensors or even mixed basis tensors follows straightforwardly. Covariant derivatives are now augmented by the spin connection  $\omega$  if expressed in the new tensor basis

$$\begin{aligned} (\nabla_{\mu} T)^{i_1 \dots i_r}_{j_1 \dots j_s} &= \frac{\partial}{\partial x^{\mu}} T^{i_1 \dots i_r}_{j_1 \dots j_s} \\ &+ \omega_{\mu}^{i_1 k} T^{ki_2 \dots i_r}_{j_1 \dots j_s} + \dots + \omega_{\mu}^{i_r k} T^{i_1 \dots i_{r-1} k}_{j_1 \dots j_s} \\ &- \omega_{\mu}^k_{j_1} T^{i_1 \dots i_r}_{kj_2 \dots j_s} - \dots - \omega_{\mu}^k_{j_s} T^{i_1 \dots i_r}_{j_1 \dots j_{s-1} k}. \end{aligned} \quad (2.10)$$

The relation of  $\omega$  to the Christoffel connection is obtained by expressing  $\nabla T$  in the coordinate basis and comparing the coefficients, yielding

$$\Gamma_{\mu\lambda}^{\nu} = e^{\nu}_i \partial_{\mu} e_{\lambda}^i + e^{\nu}_i e_{\lambda}^j \omega_{\mu}^i_j, \quad (2.11)$$

or equivalently

$$\omega_{\mu}^i_j = e_{\nu}^i e^{\lambda}_j \Gamma_{\mu\lambda}^{\nu} - e^{\lambda}_j \partial_{\mu} e_{\lambda}^i. \quad (2.12)$$

The Riemann tensor and related quantities expressed in the non-coordinate frame can be found in appendix A.1.1.

### 2.1.2 Einstein's field equations

The relation between the geometry and the energy content of a spacetime manifold is given by Einstein's field equations

$$R_{\mu\nu} - \frac{1}{2}Rg_{\mu\nu} + \Lambda g_{\mu\nu} = 8\pi G_D T_{\mu\nu}, \quad (2.13)$$

where  $T_{\mu\nu}$  is the energy-momentum tensor of the spacetime matter content,  $\Lambda$  is the cosmological constant and  $G_D$  is the gravitational constant in  $D$  spacetime dimensions. Together with the equations of the matter fields, the tensor equation (2.13) comprises a set of nonlinear second order partial differential equations (PDEs) for the spacetime metric  $g_{\mu\nu}$ .

The shape of the field equations (2.13) is neither suitable for the numerical solution of boundary value problems nor for the evolution of initial data. How to recast the equations into an applicable form will be covered within the next subsection.

### Reformulations of Einstein's field equations and the DeTurck method

The full set of Einstein's equations (2.13) is usually overdetermined and exhibits another important flaw with respect to its principal part (the part with second derivatives of  $g_{\mu\nu}$ ). For the stable solution of a boundary value problem it is required that the underlying system is well-posed.<sup>1</sup> (Uniform) Strong ellipticity<sup>2</sup> of the regarding differential operator and a certain regularity of the boundary data are sufficient conditions for well-posedness.<sup>3</sup> A similar notion holds for the evolution of initial data, where the principal symbol must be strongly hyperbolic as a requirement for a stable time evolution [28]. In the following, we will constrain the discussion to the elliptic case, since we deal only with boundary value problems in the scope of this thesis.

One can show that the principal part of the field equations (2.13) is not strongly elliptic and additional procedures have to be carried out to implement this feature. There are many approaches known for obtaining the desired system. For example one ansatz relies on recombining the equations into a strongly elliptic subset plus supplementary constraint equations while another is to introduce additional terms into equation (2.13), which render the system well-posed. We will give a short description of a concrete realization of the latter procedure, since it will be used within this thesis.

For understanding this method, which is also denoted as DeTurck method [212], we need to consider Einstein's equations (2.13) in their trace-reversed form

$$R_{\mu\nu} - \Lambda g_{\mu\nu} = 8\pi G_D \left( T_{\mu\nu} - \frac{1}{2}Tg_{\mu\nu} \right), \quad (2.14)$$

where  $T$  denotes the trace of the energy-momentum tensor. From (2.14) we can infer, that the principal part of the PDE system is completely contained in  $R_{\mu\nu}$ . Separating the second metric

<sup>1</sup>Consider section 3.2 for a proper definition of well-posedness in the context of elliptic boundary value problems.

<sup>2</sup>We refer the reader to [70] for a definition of (uniform) strong ellipticity.

<sup>3</sup>However, solutions can be constructed for not-strongly elliptic operators, cf. reference [180] for the Dirichlet problem and reference [122] for an example in numerics. Nevertheless, strongly elliptic operators usually lead to better convergence properties when solving the underlying problem with numerical methods.

derivatives within the Ricci tensor  $R_{\mu\nu}$  into a definite principal part and additional contributions gives the following decomposition

$$R_{\mu\nu} = -\frac{1}{2}g^{\alpha\beta}\partial_\alpha\partial_\beta g_{\mu\nu} + \nabla_{(\mu}\Gamma_{\nu)} + g^{\alpha\beta}g^{\delta\epsilon}(\partial_\delta g_{\alpha\mu}\partial_\epsilon g_{\beta\nu} - \Gamma_{\mu\alpha\delta}\Gamma_{\nu\beta\epsilon}), \quad (2.15)$$

where  $\Gamma_{\alpha\mu\nu} = g_{\alpha\beta}\Gamma_{\mu\nu}^\beta$  and  $\Gamma_\alpha = g^{\mu\nu}\Gamma_{\alpha\mu\nu}$ . The first term in (2.15) is the desired strongly elliptic principal part, while the second term includes additional second metric derivatives, which cause the problems discussed above. The remaining terms contain no second order derivatives of the metric and are not important for the discussion. Within the DeTurck approach the term  $\nabla_{(\mu}\Gamma_{\nu)}$  is canceled by adding a suitable tensor  $\nabla_{(\mu}\zeta_{\nu)}$  to  $R_{\mu\nu}$  with  $\zeta_\nu$  being constructed as

$$\zeta_\nu = \hat{\Gamma}_\nu - \Gamma_\nu, \quad (2.16)$$

where  $\hat{\Gamma}_\nu$  is a pre-defined gauge function<sup>4</sup>. Note that the difference in (2.16) will give a tensor, if  $\hat{\Gamma}_\nu$  shares the transformation properties of a Christoffel symbol on the manifold of consideration. Accordingly, we aim for solving the following system which is also denoted as Einstein-DeTurck equation

$$R_{\mu\nu} + \nabla_{(\mu}\zeta_{\nu)} - \Lambda g_{\mu\nu} = 8\pi G_D \left( T_{\mu\nu} - \frac{1}{2}Tg_{\mu\nu} \right), \quad (2.17)$$

together with the gauge-fixing condition  $\zeta_\nu = 0$ . Fortunately, the vanishing of  $\zeta_\nu$  does not need to be enforced by solving  $\zeta_\nu = 0$  explicitly, since one can show that  $\zeta_\nu$  satisfies an inhomogeneous Laplace equation [212]

$$\nabla^2\zeta_\nu + R_\nu{}^\mu\zeta_\mu = 0.$$

As a result, it is sufficient to require the vanishing of  $\zeta_\nu$  at the boundaries of the domain of consideration. A smart ansatz for satisfying this requirement is to derive  $\hat{\Gamma}_\nu$  from another pre-defined metric  $\hat{g}_{\mu\nu}$ , which has the same boundary asymptotics as  $g_{\mu\nu}$ ,

$$\hat{\Gamma}_\mu = g^{\alpha\beta}g_{\mu\nu}\hat{\Gamma}_{\alpha\beta}^\nu,$$

where  $\hat{\Gamma}_{\alpha\beta}^\nu$  is the Christoffel symbol related to  $\hat{g}_{\mu\nu}$ .

It is important to note that the method can fail due to the existence of so-called Ricci solitons which could obstruct the vanishing of  $\zeta_\nu$  within the domain of consideration. However, according to reference [72] the existence of Ricci solitons is ruled out in the static case. Nevertheless, we always need to check the norm of  $\zeta_\nu$  when computing numerical solutions of the Einstein-DeTurck equations (2.17).

---

<sup>4</sup>In more general approaches  $\hat{\Gamma}_\nu$  can contain new unknown fields and supplementary equations are used for determining the solution.

## 2.2 Important spacetimes

After having discussed the field equations, it remains to provide a brief overview of the most important solution classes to be considered in this thesis.

### 2.2.1 The anti-de Sitter spacetime

A manifold of constant sectional curvature in Lorentzian geometry is locally isometric to either de Sitter, Minkowski or anti-de Sitter space, depending on the sign of the curvature<sup>5</sup>. This can be seen in comparison to Riemannian geometry where the same holds for the sphere, the Euclidean space and the hyperbolic space.

The anti-de Sitter (AdS) space is maximally symmetric with a constant negative sectional curvature and the Ricci tensor  $R_{\mu\nu}$  and the scalar curvature  $R$  are related as follows

$$R_{\mu\nu} = \frac{R}{d+1}g_{\mu\nu}, \quad (2.18)$$

where  $d$  denotes the number of spacelike coordinates, such that there is a total dimension of  $D = d + 1$ . Relation (2.18) can be rewritten into

$$R_{\mu\nu} - \frac{1}{2}Rg_{\mu\nu} + \frac{d-1}{2(d+1)}Rg_{\mu\nu} = 0, \quad (2.19)$$

which shows that the anti-de Sitter space is a solution of Einstein's field equations (2.13) in vacuum with cosmological constant

$$\Lambda = \frac{d-1}{2(d+1)}R. \quad (2.20)$$

The anti-de Sitter space can be constructed by considering a hyperboloidal hypersurface embedded in  $\mathbb{R}^{d,2}$ :

$$\|X\|^2 = -(X^0)^2 + \sum_{i=1}^d (X^i)^2 - (X^{d+1})^2 = -l_{AdS}^2, \quad (2.21)$$

where  $l_{AdS}$  is the radius of the AdS space. Note that this submanifold is not simply connected since the loop in the  $X^0 - X^{d+1}$ -plane is not contractible, so the universal cover needs to be considered.

The hypersurface (2.21) can now be covered by different coordinate charts as a preliminary for explicit calculations. The definition as a hyperboloid suggests the utilization of hyper-polar coordinates covering the entire manifold

$$\begin{aligned} X^0 &= l_{AdS} \cosh \varrho \cos \tau, \\ X^i &= l_{AdS} \Omega_i \sinh \varrho \quad (i = 1, \dots, d), \\ X^{d+1} &= l_{AdS} \cosh \varrho \sin \tau, \end{aligned} \quad (2.22)$$

with the coordinate ranges  $\varrho \in \mathbb{R}_{\geq 0}$ ,  $\tau \in [0, 2\pi)$  and the  $\Omega_i$  parametrize the  $(D - 2)$ -dimensional unit sphere, i.e.  $\Omega_1 = \sin \theta \sin \phi_1 \cdots \sin \phi_{D-3}$ ,  $\Omega_2 = \sin \theta \sin \phi_1 \cdots \cos \phi_{D-3}$ ,

<sup>5</sup>In mathematically correct words the universal cover of the manifold is isometric to one of these spaces.

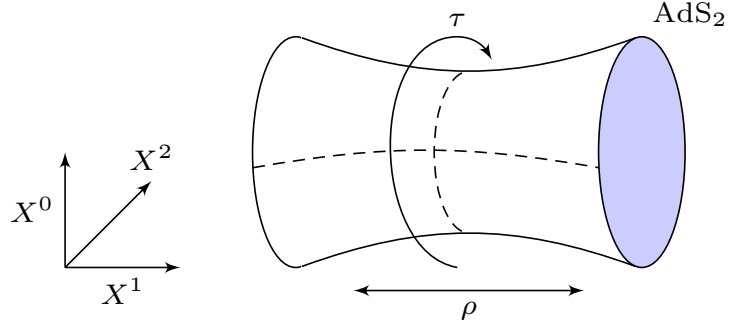


**Figure 2.1:** Schematic picture of  $AdS_2$  embedded in  $\mathbb{R}^{1,2}$ .

$\Omega_3 = \sin \theta \sin \phi_1 \cdots \cos \phi_{D-2}$  etc. This leads to the induced metric

$$ds^2 = l_{AdS}^2 \left( -\cosh^2 \varrho d\tau^2 + d\varrho^2 + \sinh^2 \varrho d\Omega_{D-2}^2 \right), \quad (2.23)$$

where  $d\Omega_{D-2}^2$  is the line element of the  $(D-2)$ -dimensional unit sphere. This cover can now be enhanced to be universal by extending the periodic time-like coordinate  $\tau$  to  $\mathbb{R}$  which corresponds to unwrapping the hyperboloid along  $\tau = \text{const.}$  (see figure 2.1).

A more common form of the metric (2.23) is obtained by introducing the coordinates  $t = l_{AdS} \tau$  and  $r = l_{AdS} \sinh \varrho$ :

$$ds^2 = - \left( 1 + \frac{r^2}{l_{AdS}^2} \right) dt^2 + \frac{1}{1 + \frac{r^2}{l_{AdS}^2}} dr^2 + r^2 d\Omega_{D-2}^2. \quad (2.24)$$

A simple calculation yields the scalar curvature related to the metric (2.23) to be

$$R = - \frac{d(d+1)}{l_{AdS}^2}, \quad (2.25)$$

i.e. the considered submanifold has the desired constant negative curvature. The cosmological constant is determined by employing relation (2.20)

$$\Lambda = - \frac{d(d-1)}{2l_{AdS}^2}. \quad (2.26)$$

Another convenient chart are so-called Poincaré coordinates, which are introduced by setting

$$\begin{aligned} X^0 &= \frac{l_{AdS}^2}{2r} \left( 1 + \frac{r^2}{l_{AdS}^4} (\bar{x}^2 - t^2 + l_{AdS}^2) \right), \\ X^i &= \frac{rx^i}{l_{AdS}} \quad (i = 1, \dots, d), \\ X^d &= \frac{l_{AdS}^2}{2r} \left( 1 + \frac{r^2}{l_{AdS}^4} (\bar{x}^2 - t^2 - l_{AdS}^2) \right), \\ X^{d+1} &= \frac{rt}{l_{AdS}}, \end{aligned}$$



for  $r \in \mathbb{R}_{>0}$  and  $x^\mu = (t, \vec{x}) \in \mathbb{R}^{d-1,1}$ . In Poincaré coordinates the metric reads

$$ds^2 = \frac{l_{AdS}^2}{r^2} dr^2 + \frac{r^2}{l_{AdS}^2} (-dt^2 + d\vec{x}^2). \quad (2.27)$$

Note that the Poincaré chart covers only half of the AdS space, where a Killing horizon at  $r = 0$  separates the given patch from the other half.

The knowledge of the conformal structure of the AdS space is of crucial importance for the AdS/CFT correspondence. Note that (2.27) is conformally equivalent to

$$d\bar{s}^2 = \frac{l_{AdS}^4}{r^4} dr^2 + (-dt^2 + d\vec{x}^2), \quad (2.28)$$

which resembles the  $d$ -dimensional Minkowski metric for  $r \rightarrow \infty$ .

Another coordinate system is obtained by setting  $\rho = l_{AdS}^2/r$  in (2.27) leading to the line element

$$ds^2 = \frac{l_{AdS}^2}{\rho^2} (d\rho^2 - dt^2 + d\vec{x}^2), \quad (2.29)$$

which is sometimes better suited for specific numerical purposes since the conformal horizon is now located at  $\rho = 0$  and the Killing horizon is mapped to infinity.

Black holes in anti-de Sitter space will play an important role for the construction of holographic Weyl semimetals in chapter 5. More details about black holes are provided in the next subsection.

### 2.2.2 Black hole spacetimes

Black holes are particularly interesting solutions to Einstein's field equations (2.13). The characteristic property of a classic black hole is the existence of an event horizon, a surface which can be identified with the boundary of the black hole. The event horizon can not be crossed by any type of information located in the inside of the black hole, including all physical matter, while being permeable for all matter on the outside. There are additional notions of horizons besides the event horizon for black holes, such as the apparent and the Killing horizon. However, all these notions coincide in the realm of this work, since we are only considering static solutions to Einstein's equations. Static solutions are time-independent and do not change under time reversal, which constrains the mixed temporal-spatial components of the metric tensor to vanish  $g_{tj} = 0$ . It is important to note the difference to stationary solutions describing rotating configurations, which are also time-independent but not invariant under time reversal.

We start by providing some basic aspects of black holes followed by a compact summary of their thermodynamic properties. Subsequently, we give a brief introduction to the class of Kaluza-Klein black holes, which will be important for chapter 4 and conclude with a short review of black holes in anti-de Sitter space.

## Basic aspects

The prototype of a black hole vacuum solution is the asymptotically flat Schwarzschild solution in  $D = 4$ , which was discovered by Schwarzschild in 1915 [182]<sup>6</sup> soon after Einstein's equations were published [64]. The corresponding line element reads

$$ds_{Schw}^2 = -f_4(r) dt^2 + \frac{dr^2}{f_4(r)} + r^2 d\Omega_2^2, \quad (2.30)$$

where  $r \in [0, \infty)$  and  $f_4$  is given by

$$f_4(r) = 1 - \frac{r_{\mathcal{H}}}{r}, \quad (2.31)$$

and  $d\Omega_2^2$  is the line element of the unit 2-sphere  $d\Omega_2^2 = d\theta^2 + \sin^2\theta d\phi^2$  with polar angle  $\theta \in [0, \pi)$  and azimuth  $\phi \in [0, 2\pi)$ . We approach the flat  $D = 4$  Minkowski spacetime for large values of the radius  $r \rightarrow \infty$  as desired. Moreover the line element becomes singular for two specific values of  $r$ , namely  $r = 0$  and  $r = r_{\mathcal{H}}$ . By considering scalar curvature invariants it can be shown that  $r = 0$  is the location of a true spacetime singularity, while  $r = r_{\mathcal{H}}$  is only a coordinate singularity and can be removed by changing to suitable coordinates, cf. reference [206] for a review of this topic. In addition  $r_{\mathcal{H}}$  is related to the mass  $M$  of the source of the Schwarzschild spacetime according to  $r_{\mathcal{H}} = 2G_4M$ .

In principle the Schwarzschild spacetime can be used for describing the asymptotic region outside of a spherically symmetric static astrophysical object. In practice, generic observable objects feature additional properties such as angular momentum  $J$  and charge  $Q$ , hence generalizations of the Schwarzschild solution are necessary. Such a generalization for charged black holes was discovered independently by Reissner in 1916 [173] and Nordström in 1918 [161]. Furthermore, the solution for stationary rotating black holes was found by Kerr in 1963 [126]. It is worth to mention that the axially symmetric Kerr solution exhibits a much more complicated mathematical description related to its interesting horizon structure, which is one of the reasons for its late discovery. Combining the Reissner-Nordström and the Kerr solution to charged stationary rotating black holes led to the Kerr-Newman solution class in 1965 [158].

Nevertheless, the Schwarzschild solution provides an instructive example for understanding basic black hole features. For ordinary astrophysical objects the radius  $r_{\mathcal{H}}$  is smaller than the outer radius defined by the object-surface and therefore the singularities of the line element (2.30) are of no concern, since the Schwarzschild metric cannot be used to describe the interior of the corresponding object. We are speaking of a black hole as an astrophysical object if  $r_{\mathcal{H}}$  exceeds the objects extensions, then the horizon of the Schwarzschild black hole is located at  $r_{\mathcal{H}}$ .

We provide a short review of the laws of black hole thermodynamics in the next subsection, before turning to more general black hole types.

---

<sup>6</sup>Actually, Schwarzschild published his result one year later. Meanwhile, Johannes Droste found the same solution independently in 1916, using a more direct derivation [61].

## Thermodynamics

Bardeen, Carter and Hawking published the first version of the four laws of black hole mechanics in 1973 [26]. Generally speaking, these laws are physical properties that black holes are believed to satisfy. Importantly, they resemble the four laws of thermodynamics and read as follows:

0. The surface gravity<sup>7</sup>  $\kappa$  is constant over the horizon for a stationary black hole.
1. Perturbations of the mass  $M$  of a stationary black hole are related to a change of its horizon area  $A_{\mathcal{H}}$ , angular momentum  $J$  and electric charge  $Q$  according to

$$dM = \frac{\kappa}{8\pi G_4} dA_{\mathcal{H}} + \Omega dJ + \Phi dQ, \quad (2.32)$$

where  $\Omega$  is the angular velocity and  $\Phi$  is the electrostatic potential of the black hole.

2. The horizon area is a non-decreasing function of time:

$$\frac{dA_{\mathcal{H}}}{dt} \geq 0. \quad (2.33)$$

3. It is not possible to reduce the surface gravity  $\kappa$  of a black hole to zero by a finite sequence of operations.

Due to the the aforementioned similarity to the four laws of thermodynamics, we can interpret the zeroth law as a statement about the thermodynamic equilibrium and therefore identify  $\kappa$  to be related to the temperature of a black hole. The first law can be thought of as the thermodynamic statement about the conservation of the internal energy. Accordingly, the mass  $M$  corresponds to the total internal energy  $U$ . By recalling the role of  $\kappa$  as a temperature, we associate the surface area  $A_{\mathcal{H}}$  with the entropy  $S$  of the black hole as conjectured by Bekenstein in 1973.

In 1974 Hawking showed that black holes emit thermal Hawking radiation [103] when taking quantum effects into account, corresponding to a finite temperature of

$$T_{\mathcal{H}} = \frac{\kappa}{2\pi}. \quad (2.34)$$

Thus, after fixing the suggested proportionality between  $\kappa$  and the temperature, we are able to obtain a concrete expression for the entropy of a black hole by comparing the first law (2.32) for  $dJ = dQ = 0$  with the first law of thermodynamics  $dU = TdS$ :

$$dM = \frac{T_{\mathcal{H}}}{4G_4} dA_{\mathcal{H}} \equiv T_{\mathcal{H}} dS_{BH} \Rightarrow S_{BH} = \frac{A_{\mathcal{H}}}{4G_4}. \quad (2.35)$$

This is the so-called Bekenstein-Hawking entropy formula, that was first established in 1974 [103].

We note that the second law has to be adapted due to Hawking's discovery of black hole radiation, which implies a shrinking of the black hole's mass and horizon area over time. By generalizing the second law to the sum of black-hole and outside entropy  $dS_{tot} = dS_{matter} + dS_{BH} \geq 0$ , we obtain an entropy formula, that implies no violation of the second law of thermodynamics.

The third law is the black hole analog of Nernst's theorem, i.e. no thermodynamical system can be cooled down to zero temperature within a finite time.

---

<sup>7</sup>The surface gravity of a black hole is defined by the relation  $\kappa k^{\mu} = k^{\nu} \nabla_{\nu} k^{\mu}$ , where  $k^{\mu}$  is defined as the Killing vector associated with the black hole Killing horizon. For our purposes, we can consider  $\kappa$  as a general relativistic version of the gravitational acceleration at the horizon, which is undefined in terms of Newtonian physics.

Following the thermodynamical interpretation presented so far, we obtain another interesting property of the Schwarzschild black hole (2.30) with Hawking temperature  $T = 1 / (8\pi G_4 M)$ . In particular, we note that it has a negative specific heat  $\partial M / \partial T$ , i.e. its temperature increases when its mass decreases. We conclude, that small Schwarzschild black holes emit more radiation in a given time as larger ones. However, this is not a generic feature of all possible black holes and we will provide an example of black holes with positive specific heat  $\partial M / \partial T$  in chapter 4.

In addition, Hawking and Page were able to extend the laws of black hole thermodynamics by assigning entropy and temperature to cosmological event horizons. This together with the former results on black holes suggested the surprising conjecture that the maximal entropy in any three-dimensional region scales with its surface area, instead of its volume, which was expected from classical thermodynamics and information theory arguments. These findings were combined with string theoretic arguments to the so-called holographic principle, which states that the description of a volume of space can be thought of as being encoded on a lower-dimensional boundary of the regarding region. Despite this connection is still not fully understood today, it manifests itself specifically in the AdS/CFT correspondence, which will be discussed in section 2.3. Regarding the content of the following subsections, we underline that the laws of black hole thermodynamics consistently adapt to higher dimensions.

### More general black holes

One intent of this thesis is not the description of black holes as astrophysical objects, but the numerical construction of black hole spacetimes, which can be related to quantum field theories by means of string theory arguments and the AdS/CFT correspondence (see section 2.3). Therefore we need to consider black holes in general dimensions  $D \geq 4$ . The corresponding generalization of the asymptotically flat Schwarzschild spacetime was found in 1963 by Tangherlini [191]

$$ds_{ST}^2 = -f_D(r) dt^2 + \frac{dr^2}{f_D(r)} + r^2 d\Omega_{D-2}^2, \quad (2.36)$$

where  $f_D$  reads

$$f_D(r) = 1 - \left(\frac{r_H}{r}\right)^{D-3}. \quad (2.37)$$

The mass of the Schwarzschild-Tangherlini (ST) black hole reads

$$M_{ST} = \frac{(D-2) \Omega_{D-2} r_H^{D-3}}{16\pi G_D}. \quad (2.38)$$

In the following we will outline some basic aspects of other black hole types that play a major role in the scope of this thesis.

### Kaluza-Klein black holes

Another class of more general black holes emerges from considering Kaluza-Klein compactified geometries, which can also be considered in a general number of dimensions. For such constructions some of the additional dimensions are compactified, where in principle an endless variety of compactifications is possible. The idea goes back to the early attempt of Kaluza, who considered Einstein's field equations in five-dimensions by adding one additional spatial dimension. He was able to show that the resulting five dimensional field equations can be separated into

a set of Einstein's equations for a four dimensional subspace and Maxwell's equations on this space. Unfortunately he had to impose some additional constraints on the underlying fields, leading to rather unphysical field configurations. Nevertheless, his approach was one of the early attempts to unify gravity and electromagnetism and thus can be seen as a predecessor to string theory, which also funds on the idea of compactified extra-dimensions. A simple example for a Kaluza-Klein black hole is obtained by adding one additional periodic dimension to a Schwarzschild-Tangherlini spacetime, resulting in the following line element

$$ds_{UBS}^2 = -f_D(r) dt^2 + \frac{dr^2}{f_D(r)} + r^2 d\Omega_{D-2}^2 + dz^2, \quad (2.39)$$

where  $z \in [-L/2, L/2]$ . The resulting spacetime can be considered as a Schwarzschild black hole extended along the new dimension, giving it the shape of a uniform black string with radius  $L$  (see figure 2.2).

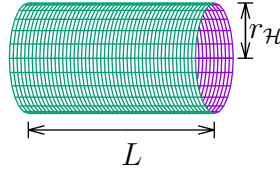


**Figure 2.2:** Illustration of the spatial embedding of a uniform black string horizon. The compact coordinate  $z$  of length  $L$  is aligned with the horizontal direction. The coaxial circles illustrate the  $z = \text{const.}$  slices of the horizon, which are actually (hyper-)spheres with radius  $r_{\mathcal{H}}$ . The end points of the string correspond to the same points in spacetime as a result of the periodic nature of the compact dimension.

### AdS black holes

As we will see in section 2.3, black holes in asymptotically anti-de Sitter spacetimes play a major role when examining strongly coupled quantum field theories at finite temperatures through the AdS/CFT correspondence. A particularly interesting vacuum solution class is given by the so-called  $AdS_{d+1}$  Schwarzschild or black brane (BB) solution, where its name originates from the spatial  $\mathbb{R}^{d-1}$  topology of the event horizon. In Poincaré coordinates (see subsection 2.2.1) the solution reads

$$ds_{BB}^2 = \frac{l_{AdS}^2}{\rho^2} \left( -f_{BB,d}(\rho) dt^2 + \frac{d\rho^2}{f_{BB,d}(\rho)} + d\vec{x}^2 \right), \quad (2.40)$$

where  $f_{BB,d}$  is given by

$$f_{BB,d}(\rho) = 1 - \left( \frac{\rho}{\rho_{\mathcal{H}}} \right)^d, \quad (2.41)$$

$\rho_{\mathcal{H}}$  denotes the location of the event horizon and  $l_{AdS}$  is the AdS radius, cf. section 2.2.1. The line element (2.40) resembles the  $AdS_{d+1}$  space for  $\rho \rightarrow 0$ , because  $\lim_{\rho \rightarrow 0} f_{BB,d}(\rho) = 1$  as desired.

After having discussed the most important spacetime configurations for this thesis, we provide a short review on the AdS/CFT correspondence in the next section.

## 2.3 The AdS/CFT correspondence

The AdS/CFT correspondence, or more generally gauge/gravity duality, states that certain quantum field theories in  $d$ -dimensional Minkowski spacetime are dynamically equivalent to certain gravitational theories in asymptotically  $d + 1$ -dimensional AdS spacetimes. Since quantum field theories are related to higher-dimensional gravity theories, it is also referred to as holographic duality. In fact, the following picture emerges: The conformal boundary of  $AdS_{d+1}$  is conformally equivalent to flat Minkowski space  $\mathbb{R}^{d-1,1}$ . Consequently, the quantum field theory is said to be living on the conformal boundary of  $AdS_{d+1}$  and the AdS/CFT correspondence is considered as a realization of the so-called holographic principle.

Originally, concrete examples for the AdS/CFT correspondence were conjectured by Juan Maldacena in 1997 [153] and subsequently extended by Witten, Gubser, Klebanov, Polyakov and many more [213, 90, 3]. Although it still remains a conjecture, the AdS/CFT correspondence has been very fruitful for many developments in theoretical physics within the last two decades. In particular, we obtained new insights into the physics of black holes. For example, before the advent of AdS/CFT, it was quite a mystery why the four laws of black hole mechanics resemble the four laws of thermodynamics.

Moreover, the AdS/CFT correspondence allows for insights into strongly coupled quantum field theories in the large- $N$  limit. In particular, profound questions may be answered, which are inaccessible within more conventional approaches such as lattice gauge theory. For example, using AdS/CFT, we may determine the phase diagram, transport coefficients and even the non-equilibrium dynamics within the strongly coupled quantum field theory.

This section is structured as follows: We first discuss a concrete example for the AdS/CFT correspondence in subsection 2.3.1. Subsequently we introduce the dictionary of the AdS/CFT correspondence, i.e. how to relate gravitational fields and quantum fields, in subsection 2.3.2. Finally, the computation of expectation values and correlation functions is presented.

### 2.3.1 A concrete example for the AdS/CFT correspondence

First, let us give one concrete example for the AdS/CFT correspondence, involving  $\mathcal{N} = 4$  Super Yang-Mills (SYM) theory and type IIB superstring theory on  $AdS_5 \times S^5$ .

The strongest form of the duality conjectures the equivalence of an  $\mathcal{N} = 4$  SYM theory with gauge group  $SU(N)$  and Yang-Mills coupling  $g_{YM}$  in  $3 + 1$ -dimensions to a type IIB superstring theory with string length  $l_s = \sqrt{\alpha'}$  and coupling constant  $g_s$  on  $AdS_5 \times S^5$  with radius of curvature  $l_{AdS}$ .

Here, the word equivalence means that the Hilbert spaces of both theories are isomorphic and the dynamics of both theories agree. The latter can be expressed in terms of the equality of the partition functions  $Z_{CFT} = Z_{AdS}$ . Moreover, the parameters of both sides are related as follows:

$$g_{YM}^2 = 2\pi g_s, \quad 2g_{YM}^2 N = \frac{l_{AdS}^4}{\alpha'^2}. \quad (2.42)$$

The strongest form of the duality is not utilizable for practical purposes since both sides cannot be solved. For example, we do not have a working definition of non-perturbative string theory on  $AdS_5 \times S^5$ . Hence, we may take limits to simplify the string theory side. Taking the large- $N$  limit  $N \rightarrow \infty$  while keeping  $\lambda = N g_{YM}^2$  fixed and successively taking  $\lambda \rightarrow \infty$ , the superstring theory reduces to classical supergravity, while the aforementioned SYM theory is still non-trivial in the limit of a large number of degrees of freedom  $N$  and large 't Hooft coupling  $\lambda = N g_{YM}^2$ .

Since the first work of Maldacena, who conjectured the correspondence for large  $N$ , the conjecture was thoroughly studied but not proven rigorously by today. Nevertheless it was extended for providing duality between conformal field theories in  $d$  spacetime dimensions and asymptotically  $AdS_{d+1}$  spaces. Furthermore the duality between less supersymmetric and non-conformal field theories was conjectured. A comprehensive book about the AdS/CFT correspondence, including its recent extensions and applications, is given by reference [12].

In this thesis we will only use the weak form of the correspondence as a mere black box in the sense that we assume the correctness of the conjecture and use it to derive physical results for specific strongly coupled quantum systems by utilizing numerical calculations on the asymptotically anti-de Sitter gravity side.

### Composite operators in $\mathcal{N} = 4$ SYM

In this section we discuss examples of local operators  $\mathcal{O}(x)$  which are gauge-invariant under the  $SU(N)$  gauge transformation. The elementary fields of  $\mathcal{N} = 4$  SYM, i.e. gauge fields, fermions and scalar fields transform in the adjoint representation of the gauge group, and hence only composite fields are gauge-invariant. For example, the energy-momentum tensor  $T_{ab}$  of  $\mathcal{N} = 4$  SYM is a gauge-invariant, local operator. Other examples are the scalar operator  $\mathcal{O} = \text{tr}(F_{ab}F^{ab})$  and the (conserved) currents  $J_a$  related to the so-called R-symmetry<sup>8</sup>.

In the following we denote local composite and gauge-invariant operators by  $\mathcal{O}^I$ . Since  $\mathcal{N} = 4$  SYM theory is a conformal field theory, i.e. invariant under conformal transformations<sup>9</sup>, the corresponding field operators  $\mathcal{O}^I$  transform in irreducible representations of the conformal algebra. In particular, the operators  $\mathcal{O}^I$  are characterized by their spin  $s^I$  and their conformal dimension  $\Delta^I$ . The latter one can be obtained from the commutator action of the dilatation operator  $D$  on a conformal operator  $\mathcal{O}$ :

$$[D, \mathcal{O}(0)] = -i\Delta\mathcal{O}(0). \quad (2.43)$$

For a finite dilatation  $x \mapsto \lambda x$  the operator transforms as  $\mathcal{O} \mapsto \lambda^{-\Delta}\mathcal{O}$ .

The reader is invited to read more about the interesting features of CFTs<sup>10</sup>.

### Fields on the dual gravity side

In the weak form of the AdS/CFT correspondence, the dual gravity side is given by type IIB supergravity in asymptotically  $AdS_5 \times S^5$ . First, a Kaluza-Klein reduction to the sphere  $S^5$  is performed, giving rise to infinitely many fields defined on the (asymptotically)  $AdS_5$  spacetime. Besides the metric  $g_{\mu\nu}$  we denote the matter fields by  $\{\phi_I\}$ , where  $I$  labels (the infinitely many) different fields. Note that the notation does not imply that there are only scalar fields. In particular, the Kaluza-Klein reduction to  $S^5$  leads also to gauge fields, as well as fermionic fields. Moreover, we denote the Kaluza-Klein reduced supergravity action by  $S_{SG}$ .

<sup>8</sup> $\mathcal{N} = 4$  SYM has four supercharges  $Q^i$  which are rotated into each other by the  $SU(4)$  R-symmetry.

<sup>9</sup>Consider appendix A.1.2 for a short review on conformal symmetries.

<sup>10</sup>Cf. reference [32] for an instructive book on CFTs with applications to string theory.

### 2.3.2 Relating fields in AdS to composite operators of the CFT

Within this section we portray the dictionary relating the field content on the gravity side to composite (gauge-invariant) operators in the dual quantum field theory. For simplicity, we work in the weak form of the AdS/CFT correspondence, relating strongly coupled large- $N$  field theories in  $d$  dimensions to supergravity theories in asymptotically  $AdS_{d+1} \times \mathcal{M}$  spacetimes, where  $\mathcal{M}$  is a compact manifold, e.g.  $\mathcal{M} = S^5$  in the concrete example presented previously.

#### The dictionary

As before we perform a Kaluza-Klein reduction on the compact manifold  $\mathcal{M}$ , accordingly the supergravity metric  $g_{\mu\nu}$  and all other fields, e.g. gauge fields  $A_\mu$  and scalar fields  $\phi$  depend only on the coordinates of AdS spacetime.

The AdS/CFT dictionary can now be obtained by matching the conformal dimension and the spin of the fields and operators on both sides. As shown in [12], we arrive at the schematic dictionary provided in table 2.1.

A more detailed dictionary for the concrete AdS/CFT correspondence, that was provided in subsection 2.3.1, can be found in table 7 of reference [53].

**Table 2.1:** Schema of the AdS/CFT dictionary, taken from reference [12].  $T_{ab}$  is the energy-momentum tensor,  $J_a$  is a conserved current and  $\mathcal{O}$  a scalar operator on the quantum field side. The Greek indices  $\{\mu, \nu, \dots\}$  in the bulk space run from 0 to  $d$ , where the  $d$ -th component is the additional dimension of the asymptotically anti-de Sitter space. The Latin indices  $\{a, b, \dots\}$  of the boundary CFT quantities run from 0 to  $d - 1$ .

conformal field theory	$\longleftrightarrow$	gravity theory
$T_{ab}$	$\longleftrightarrow$	$g_{\mu\nu}$
$J_a$	$\longleftrightarrow$	$A_\mu$
$\mathcal{O}$	$\longleftrightarrow$	$\phi$

#### Equality of generating functional and partition function

Having established the dictionary, we focus on the dynamics of both sides, in particular how to compute one-point functions of composite operators of the conformal field theory by solving the equations of motion of supergravity. A starting point for relating observables on the CFT side to the regarding objects on the gravity side is to use the aforementioned equality of the partition functions  $Z_{CFT} = Z_{AdS}$ .

On the conformal field theory side, the generating functional,  $Z_{CFT}$ , is defined by

$$Z_{CFT}[\{j_I\}] = \left\langle \exp \left( \int d^d x j_I(x) \mathcal{O}^I(x) \right) \right\rangle, \quad (2.44)$$

where  $j_I$  are the sources for the operators  $\mathcal{O}^I$ . We can compute correlation functions of the form  $\langle \mathcal{O}^{I_1}(x_1) \cdots \mathcal{O}^{I_2}(x_2) \rangle$ , by taking functional derivatives of (2.44) with respect to  $j_I$ , and subsequently setting the sources to zero.



It is more subtle to define and compute the partition function  $Z_{AdS}$ . Since we are only interested in the weak form of the correspondence within this thesis, we can compute  $Z_{AdS}$  through a saddle point approximation by the Euclidean supergravity on-shell action  $S_{SG}$  on  $AdS_{d+1}$ . Within this approximation,  $S_{SG}$  is evaluated at classical solutions of the equations of motion for the metric together with additional fields  $\{\phi_I\}$  coupled to the gravity background.

As a result we can express the AdS/CFT correspondence on the level of the generating functional of the CFT and the AdS partition function:

$$Z_{CFT}[\{j_I\}] = \exp\left(-S_{SG}[g_{\mu\nu}, \{\phi_I\}]|_{\phi_I \rightarrow j_I}\right), \quad (2.45)$$

where we require  $g_{\mu\nu}$  to be asymptotically  $AdS_{d+1}$ .

Note that the on-shell action  $S_{SG}$  is generically divergent. Hence, we have to renormalize the theory by a procedure that is denoted as holographic renormalization. As a common strategy, we first regularize the divergent action  $S_{SG}$  by introducing a cut-off distance  $\rho = \epsilon > 0$ <sup>11</sup>, yielding the regularized action  $S_{SG,reg}$ . Subsequently a counter term  $S_{SG,ct}$  is introduced to cancel the divergent contributions for  $\epsilon \rightarrow 0$  and the remaining part gives the desired renormalized result:

$$S_{SG,ren} = \lim_{\epsilon \rightarrow 0} (S_{SG,reg}(\epsilon) + S_{SG,ct}(\epsilon)). \quad (2.46)$$

It is important to note that the methods outlined above also apply to finite temperature quantum field theories. A finite temperature QFT is usually obtained by Wick rotating the functional integral into its Euclidean version and constraining it to (anti-)periodic field configurations with period  $\beta = 1/T$ . Applying the same procedure to the quantum gravity path integral and performing the saddle point approximation (2.45) corresponds now to looking for extrema of the Euclidean gravity action with compactified time coordinate. These are (amongst others) black hole solutions with Hawking temperature  $T_{\mathcal{H}} = 1/\beta = T$ . On the classical gravity perspective this implies to require appropriate boundary conditions for the metric tensor at the event horizon  $\rho = \rho_{\mathcal{H}}$ . In particular, we have to impose regularity of the fields there.

After presenting the abstract formalism, it remains to provide some concrete manifestations of how to map boundary asymptotics of the gravity-side fields  $g_{\mu\nu}$  and  $\{\phi_I\}$  to the sources and (vacuum) expectation values of the corresponding quantum field operators.

For doing so we introduce Gaussian normal coordinates by foliating the asymptotically  $AdS_{d+1}$  spacetime in terms of  $d$  dimensional hypersurfaces labeled by the spatial coordinate  $\rho$  where the conformal boundary is located at  $\rho = 0$ . Accordingly the line element can be brought to the form

$$ds^2 = \frac{l_{AdS}^2}{\rho^2} \left( d\rho^2 + \tilde{g}_{ij}(\rho, x) dx^i dx^j \right), \quad (2.47)$$

where we have pulled out  $l_{AdS}^2$  by convention. Asymptotically  $AdS_{d+1}$  spaces permit the Fefferman-Graham (FG) expansion [71]

$$\tilde{g}_{ij}(\rho, x) = \tilde{g}_{ij}^{(0)}(x) + \cdots + \tilde{g}_{ij}^{(1)}(x) \rho^d + h_{ij}^{(1)} \rho^d \log \rho + \cdots \quad (2.48)$$

<sup>11</sup>The classical supergravity action is computed by integrating the on-shell Lagrange density over all coordinates, which causes divergences as can be seen when looking at the metric tensor  $g_{\mu\nu}$  close to the conformal boundary at  $\rho = 0$ .

Note that this expansion can only be constructed asymptotically around  $\rho = 0$  and up to a certain order for a generic spacetime. One can show, that  $\tilde{g}_{ij}^{(1)}(x)$  is directly related to the 1-point function of the energy-momentum tensor of the dual quantum field theory, cf. reference [12].

For modeling a quantum theory with a single scalar operator  $\mathcal{O}$  of conformal dimension  $\Delta$  which couples to a source  $j$  by an action term

$$S \mapsto S + \int d^d x j(x) \mathcal{O}(x) \quad (2.49)$$

one must introduce a minimally coupled scalar field  $\phi$  with appropriate mass<sup>12</sup>  $m^2 = \Delta(\Delta - d) / l_{AdS}^2$  on the gravity side and solve the regarding scalar field equation

$$\frac{1}{\sqrt{-g}} \partial_\mu (\sqrt{-g} g^{\mu\nu} \partial_\nu \phi) - m^2 \phi = 0 \quad (2.50)$$

together with Einstein's field equations (2.13). The scalar field  $\phi$  can also be expanded in the FG coordinates

$$\phi(\rho, x) = \phi^{(0)}(x) \rho^{d-\Delta} + \dots + \phi^{(1)}(x) \rho^\Delta + \phi^{(1)}(x) \rho^\Delta \log \rho + \dots \quad (2.51)$$

The expansion coefficients  $\phi^{(0)}$  and  $\phi^{(1)}$  are related to the source and to the (sourced) vacuum expectation value (VEV) of  $\mathcal{O}$  according to (cf. [12])

$$j(x) = \phi^{(0)}(x) \quad (2.52)$$

$$\langle \mathcal{O}(x) \rangle = l_{AdS}^{d-1} (2\Delta - d) \phi^{(1)}(x) . \quad (2.53)$$

To model a CFT having a conserved Noether current  $J_a$ , i.e. being invariant under the action of a group  $G$ , we introduce a  $G$  gauge field  $A_\mu$  on  $AdS_{d+1}$ . Consequently one needs to solve the corresponding coupled system of Einstein's equations together with the gauge field equations. The boundary expansion of  $A_\mu$  in FG coordinates reads

$$A_\mu(\rho, x) = A_\mu^{(0)}(x) + \dots + A_\mu^{(1)}(x) \rho^{d-2} + a_\mu^{(1)}(x) \rho^{d-2} \log \rho + \dots , \quad (2.54)$$

where color/group indices have been suppressed for simplicity. As in the scalar case, the source of the dual current operator  $J_a$  can be identified with  $A_a^{(0)}$  and the  $A_a^{(1)}$  coefficient is proportional to the VEV (cf. [12])

$$\langle J_a(x) \rangle \propto A_a^{(1)}(x) . \quad (2.55)$$

Note that (2.55) incorporates only the Latin indices of  $A_\mu^{(1)}$ , corresponding to the boundary coordinates of the FG expansion. Moreover it is straightforward to obtain the gravity dual of the quantum finite particle density  $\rho$  and chemical potential  $\mu$  associated with  $J_a$ . The chemical potential at finite temperature is associated with the difference of the temporal gauge field component at the conformal horizon at  $A_t(0)$  and its value at the black hole horizon  $A_t(\rho_H)$

$$\mu = A_t|_{\rho=0} - A_t|_{\rho=\rho_H} .$$

<sup>12</sup>The mass square of a scalar field in  $AdS_{d+1}$  is constrained by the so-called Breitenlohner-Freedman bound:  $m^2 \geq -d^2 / (4l_{AdS}^2)$  (see reference [12]).

---

The density  $\rho$  is proportional to the  $A_t^{(1)}$  coefficient of the expansion (2.54)

$$\rho \propto A_t^{(1)}(x),$$

which is in agreement with the covariant expression (2.55).



---

# Numerical methods

---

In this chapter we provide a short overview of the numerical techniques that were applied in the scope of this thesis. Additional details are provided in appendix A.4.

We start with a brief review of spectral methods in section 3.1, including the Fourier and the Chebyshev approach. In section 3.2 we explain the utilization of spectral methods for solving differential equations and comment on the basics of domain decomposition.

## 3.1 Theory of spectral methods

Spectral methods are a special subcategory within the broad framework of weighted residual methods (MWR) for partial differential equations.<sup>1</sup> A generic MWR method relies on a set of expansion functions and weight functions. The expansion functions (or basis functions) are used for approximating the solution in terms of a truncated series expansion. The weight functions control how the expansion is supposed to satisfy the related differential equation by minimizing the residual.

Spectral methods rely on infinitely differentiable global expansion functions, which distinguishes them from finite-element and finite-difference methods. Typical basis functions are trigonometric polynomials or eigenfunctions of singular Sturm-Liouville problems for which particularly good convergence estimates can be shown. In comparison, finite-element methods rely on the division of the domain of consideration into small elements and a basis function is specified for each element.

The three most common spectral methods can be differentiated according to the choice of test functions into Galerkin, tau and collocation schemes. For the Galerkin approach the set of basis and weight functions coincides, which are accordingly infinitely smooth functions that individually satisfy the boundary conditions. As a result the residual is minimized by requiring the orthogonal projection of the differential equation on the basis functions to vanish. Spectral tau methods resemble the Galerkin approach in the way the residual is minimized, but use a supplementary set of equations to enforce the boundary conditions, which need therefore not to be integrated into the basis. The collocation method (also called pseudospectral method, cf. reference [163]) can be considered as the simplest of the MWR. The corresponding weight functions are Dirac delta distributions centered at special collocation points, whose choice is crucial for the accuracy of the solution. As a result the convergence of the method can be significantly enhanced by employing maps to rearrange the collocation points (consider reference [34] for a collection of useful maps). The collocation method is distinguished from the other approaches due to its simple applicability to variable-coefficient and non-linear problems, which is the main reason for employing it in the scope of this thesis. Comprehensive reviews about spectral methods are provided for instance by the following references: [34, 106, 40, 39].

In the following we outline some of the basic properties of the Fourier and Chebyshev expansions which play a major role in the scope of this thesis and show how the method is applied for

---

<sup>1</sup>A review on MWR methods is provided by reference [74].

solving differential equations.

### 3.1.1 The Fourier expansion

The Fourier method became especially popular with the development of the fast Fourier transformation (FFT, [47]) by improving its numerical expense to  $\mathcal{O}(N_{total} \log N_{total})$ , where  $N_{total}$  is the total number of unknowns. The basis functions are the complex or the real valued trigonometric polynomials making the method attractive for representing periodic functions on  $[0, 2\pi)$ . Of course, functions exhibiting periodicity on different intervals can be mapped to  $[0, 2\pi)$  by applying appropriate transformations. Here we restrict ourselves to the uneven real valued basis case (cf. reference [106]). As a result we have the following approximation of a target function  $\psi$  in terms of the discrete Fourier coefficients  $\{\alpha_k^\psi, \beta_k^\psi\}$

$$\psi_N(x) = \frac{\alpha_0^\psi}{2} + \sum_{k=1}^N \left( \alpha_k^\psi \cos(kx) + \beta_k^\psi \sin(kx) \right), \quad (3.1)$$

and the collocation grid is given by the equidistant Fourier nodes on  $[0, 2\pi)$

$$x_j = \frac{2\pi j}{2N+1}, \quad j \in 0, \dots, 2N. \quad (3.2)$$

We can infer the following nice relation between the coefficients  $\{\alpha_k^{\psi'}, \beta_k^{\psi'}\}_{k=1}^N$  of the derived target function and the original coefficients  $\{\alpha_k^\psi, \beta_k^\psi\}_{k=0}^N$  from the expansion formula (3.1)

$$\alpha_k^{\psi'} = k\beta_k^\psi, \quad \beta_k^{\psi'} = -k\alpha_k^\psi, \quad k = 1, \dots, N. \quad (3.3)$$

Furthermore, the integral of a periodic function over the interval  $[0, 2\pi)$  is given by its first Fourier coefficient. Accordingly, the first coefficient of the truncated Fourier series provides a good approximation of the regarding integral and exhibits the same convergence features as the spectral expansion (in terms of global convergence measures).

For  $N \rightarrow \infty$  the approximation (3.1) converges towards the periodic target function  $\psi$ , if certain criteria apply. According to [34] the convergence can be classified into the following categories:

- **Supergeometric convergence:**  
The coefficients  $\{\alpha_k^\psi, \beta_k^\psi\}$  decay faster than any exponential  $\exp(-\gamma k)$  with  $\gamma > 0$ . This ideal convergence rate can only be found for entire functions, i.e. functions whose analytic continuation into the complex plane has only singularities at infinity.
- **Geometric convergence:**  
The convergence can be characterized by the following leading behavior  $\{\alpha_k^\psi, \beta_k^\psi\} \sim \exp(-\gamma k)$  with  $\gamma > 0$ . This case occurs for functions that are not entire but analytic on the interpolation interval  $[0, 2\pi)$ .
- **Subgeometric convergence:**  
The spectral coefficients decay with a rate that is slower than any exponential  $\exp(-\gamma k)$  with  $\gamma > 0$ , but faster than any inverse power of  $k^{-\delta}$  with  $\delta > 0$ . Subgeometric convergence concerns functions that are smooth, but not analytic on the interpolation interval.

- Algebraic convergence:

The coefficients fall-off like  $\{\alpha_k^\psi, \beta_k^\psi\} \sim k^{-\delta}$  with  $\delta > 0$  which marks the worst convergence scenario. This can be observed when the underlying function has only a finite number of existing derivatives in the interpolation interval.

Some nice examples demonstrating the different convergence categories can be found in the appendix of [120]. We remark, that the first three convergence categories point to the excellent convergence properties of spectral methods, that cannot be obtained by local methods such as finite-difference and finite-element schemes. Whereas the convergence of a spectral method reduces to that of the aforementioned local methods in the case of algebraic convergence. Often a bad convergence can be lifted into one of the higher categories by applying a suitable mapping.

### 3.1.2 The Chebyshev expansion

The Chebyshev method, which is also applicable to non-periodic functions on  $[-1, 1]$ , uses the Chebyshev polynomials of the first kind as basis functions:

$$T_k(x) = \cos(k \arccos(x)), \quad x \in [-1, 1], \quad (3.4)$$

resulting in the expansion

$$\psi_N(x) = \frac{c_0}{2} + \sum_{k=1}^N c_k^\psi T_k(x). \quad (3.5)$$

Again the extension to functions not normalized to  $[-1, 1]$  can be achieved by applying an appropriate map. The method owns its popularity mainly due to the fact, that it can be considered as a cosine expansion resulting in the applicability of the FFT algorithm for the computation of the coefficients.

The most important collocation grids for the Chebyshev method are the following:

- Chebyshev-Lobatto points:

$$x_j = \cos\left(\frac{\pi j}{N}\right), \quad j = 0, \dots, N, \text{ including both end points,}$$

- Chebyshev-Gauss points:

$$x_j = \cos\left(\frac{\pi(j+\frac{1}{2})}{N+1}\right), \quad j = 0, \dots, N, \text{ excluding both end points,}$$

- Left sided Chebyshev-Radau points:

$$x_j = -\cos\left(\frac{2\pi j}{2N+1}\right), \quad j = 0, \dots, N, \text{ including only the left end point,}$$

- Right sided Chebyshev-Radau points:

$$x_j = \cos\left(\frac{2\pi j}{2N+1}\right), \quad j = 0, \dots, N, \text{ including only the right end point.}$$

In addition, the following recursive relation between the coefficients  $\{c_k^{\psi'}\}_{k=0}^N$  of the derived target function and the original coefficients  $\{c_k^\psi\}_{k=0}^N$  can be established (cf. reference [106])

$$c_{N+1}^{\psi'} = c_N^{\psi'} = 0, \quad c_k^{\psi'} = 2kc_k^\psi + c_{k+1}^{\psi'}. \quad (3.6)$$

The integral of a Chebyshev expanded function over the interval  $[-1, 1]$

$$I = \int_{-1}^1 \psi_N(x) dx = \int_{-1}^1 \left( \frac{c_0}{2} + \sum_{k=1}^N c_k^\psi T_k(x) \right) dx, \quad (3.7)$$

is given by a simple summation

$$I = c_0 - 2 \sum_{k=1}^{\lfloor N/2 \rfloor} \frac{c_{2k}}{4k^2 - 1}, \quad (3.8)$$

where  $\lfloor \cdot \rfloor$  denotes the floor function. We remark that this integral has the same convergence properties as the Chebyshev expansion (in terms of global convergence measures).

The convergence scenarios for  $N \rightarrow \infty$  fall into the same categories as for the Fourier method.

### Basis functions in higher dimensions

For higher dimensions products of lower dimensional basis functions are employed. The choice of the basis for each direction is guided by the properties of the underlying system. For example, the area of a circle in two dimensions can be covered by combining Chebyshev polynomials in the radial direction with a Fourier series in the angular direction.

## 3.2 Spectral methods for boundary value problems

A set of elliptic differential equations together with a set of boundary conditions (BCs) is called a boundary value problem (BVP). Many branches of science are devoted to the solution of different types of BVPs originating from mathematical models of different processes.

The notion of well-posedness is elementary for extracting data of practical use from a given BVP. Well-posedness can be summarized as follows (cf. reference [164]):

1. There is a solution of the given BVP.
2. The solution is unique.
3. The solution depends continuously on the input (including the BCs).

For simplicity we consider the application of the collocation method to a single second order ordinary differential equation (ODE), which can then be straightforwardly extended to more general cases by adding additional indices. Given an ODE for the unknown function  $u(x)$  on the interval  $x \in [a, b]$  of the form

$$F(x; u, u', u'') = 0, \quad (3.9)$$

together with the boundary conditions

$$F_a(u(a), u'(a)) = 0 \quad \text{and} \quad F_b(u(b), u'(b)) = 0, \quad (3.10)$$

we start by approximating  $u(x)$  with a truncated spectral expansion

$$u(x) \approx \hat{u}_N(x) = \sum_{k=0}^N c_k \Phi_k(x), \quad (3.11)$$



with coefficients  $\{c_k\}_{k=0}^N$  and basis functions  $\{\Phi_k\}_{k=0}^N$ . Subsequently, we introduce a suitable collocation grid  $\{x_k\}_{k=0}^N$  for discretizing  $u(x)$  on this grid, yielding a vector of unknown collocation values

$$\vec{X} = (u_0, u_1, \dots, u_N)^T, \quad (3.12)$$

where  $u_k = u(x_k)$ . Under the assumption that we can also approximate the derivative of  $u$  by a spectral expansion, we obtain

$$u'(x) \approx \hat{u}'_N(x) = \sum_{k=0}^N c'_k \Phi_k(x). \quad (3.13)$$

Since the basis functions are differentiable, we can also approximate their derivatives in terms of a truncated basis

$$\Phi'_k(x) \approx \sum_{i=0}^N d_{ki}^1 \Phi_i(x), \quad (3.14)$$

where the last relation becomes exact if  $\Phi'_k$  has no overlap with  $\Phi_i$  for  $i > N$ , which is guaranteed for all common expansions. If we now approximate the derivative  $u'(x)$  by the derivative of the approximation  $\hat{u}'_N(x)$  we can obtain a relation for the coefficients of the derivative

$$\begin{aligned} u'(x) \approx \hat{u}'_N(x) &= \sum_{k=0}^N c_k \Phi'_k(x), \\ &= \sum_{i,k=0}^N c_k d_{ki}^1 \Phi_i(x). \end{aligned} \quad (3.15)$$

By comparing the coefficients of (3.13) and (3.15) a linear relation can be established for the coefficients of the derivative

$$c'_k = \sum_{i=0}^N c_i d_{ik}^1, \quad (3.16)$$

which reduces to relation (3.3) for the Fourier expansion and relation (3.6) for the Chebyshev expansion.

Accordingly, we define two more vectors  $\vec{X}'$  and  $\vec{X}''$  containing the spectral approximations of the derivatives of  $u(x)$  at the collocation points. Consequently, we collocate the ODE by evaluating (3.9) in the interior and (3.10) at the boundaries of the grid, giving the residual vector

$$\vec{F} = (F_0, F_1, \dots, F_N)^T, \quad (3.17)$$

where

$$F_k = \begin{cases} F_a(u_0, u'_0), & \text{for } k = 0, \\ F(x_k; u_k, u'_k, u''_k), & \text{for } 0 < k < N, \\ F_b(u_N, u'_N), & \text{for } k = N. \end{cases} \quad (3.18)$$

In order to compute the unknown collocation values we must solve

$$\vec{F}(\vec{X}, \vec{X}', \vec{X}'') = 0, \quad (3.19)$$

which is essentially equivalent to approximating the original equation (3.9) together with its boundary conditions (3.10) as a truncated series. By recalling that  $\vec{X}'$  and  $\vec{X}''$  are in a linear relationship to the spectral coefficients  $c_k$  of  $\vec{X}$  and therefore to  $\vec{X}$  we can write equivalently

$$\vec{F}(\vec{X}) = 0, \quad (3.20)$$

which can be solved by standard methods. A Newton-Raphson solver was utilized for solving the nonlinear problems of the later chapters. Solutions to the corresponding linear problem were obtained with a matrix-free iterative Krylov subspace method<sup>2</sup>. Further details about the implementation can be found in appendix A.4.

### 3.2.1 Multiple domains

Splitting the computational domain  $\Omega$  into several subdomains becomes necessary, if we need to adapt to the complicated geometry of a specific problem, which might be difficult or even impossible with a single domain ansatz. Furthermore, multiple domains allow us to increase the resolution and apply distinct convergence improving maps in certain regions of  $\Omega$ . This can improve the accuracy of our computation a lot, while keeping the necessary computational resources low. Using multiple domains is the basis of parallelizing computations and thus makes large scale problems feasible. We are only covering non-overlapping decompositions here, since only these are used within this thesis.

The computational domain  $\Omega$  is covered by  $N_\Omega$  non-overlapping subdomains

$$\Omega = \bigcup_{i=1}^{N_\Omega} \Omega_i, \quad (3.21)$$

each with an individual set of basis functions and expansion coefficients:

$$u_{N_i}^i(x) = \sum_{k=0}^{N_i} c_k^i \Phi_k^i(x), \quad x \in \Omega_i, \quad i = 1, \dots, N_\Omega. \quad (3.22)$$

Accordingly, we need additional conditions to couple the functions  $u_{N_i}^i(x)$  for yielding one sufficiently smooth solution of the boundary value problem. For touching subdomains  $\Omega_i$  and  $\Omega_j$  of a second order PDE it is sufficient to impose continuity of the functions and of their normal derivatives at the boundaries (cf. reference [154])

$$u_{N_i}^i(x) = u_{N_j}^j(x), \quad \frac{\partial u_{N_i}^i}{\partial n_i}(x) = \frac{\partial u_{N_j}^j}{\partial n_j}(x), \quad x \in \partial\Omega_i \cap \partial\Omega_j. \quad (3.23)$$

Once again, we refer the reader to the appendix for more details about the implementation of these conditions.

<sup>2</sup>Consider reference [155] for an instructive review on Krylov subspace methods.

---

# Localized Kaluza-Klein black holes

---

Throughout the last decades, the topic of black holes in higher dimensions  $D > 4$  attracted a lot of attention. Special focus was devoted to the study of  $D$ -dimensional black objects in spacetimes with one periodic dimension. In this context there are various solutions to Einstein's vacuum equations with different horizon topologies, such as localized black holes and black strings.

By appending a compact, periodic dimension to the solution of a  $(D - 1)$ -dimensional Schwarzschild black hole, we obtain uniform black strings (UBSs) in  $D$  dimensions. As shown by Gregory and Laflamme [84, 85], a uniform black string with a fixed size of the compact dimension  $L$  is stable for large masses  $M > M_{GL}$  and unstable for small masses  $M < M_{GL}$ , where the critical mass  $M_{GL}$  defines the so-called Gregory-Laflamme point.

Subsequently, a new branch of static solutions emanating from the Gregory-Laflamme point was discovered. These non-uniform black strings (NBSs) were first constructed in  $D = 5$  by considering small perturbations around the Gregory-Laflamme point [89]. This procedure was later adapted to higher dimensions [211, 185]. We note, that non-perturbative results could only be obtained numerically, cf. [211, 128, 186, 104, 73, 121, 122, 59] for a series of papers covering the dimensions from  $D = 5$  up to  $D = 15$ .

Localized black holes (LBHs) define another static vacuum solution class with a compact direction in higher dimensions, which was first discussed in [156]. First results on LBHs were obtained in the perturbative regime of small black holes, where the LBH solution can be approximated by a  $D$ -dimensional Schwarzschild solution, cf. the references [93, 82, 83]. Again, numerical approaches were required for constructing solutions beyond perturbation theory. Numerical results are available for  $D = 5, 6$  [210, 187, 137, 138, 104] and were recently obtained for  $D = 10$  [59].

The merger of the NBS and LBH branch was early conjectured by Kol [132], when numerical data for both branches was still rare. According to Kol, the singular transit solution is described by the so-called double-cone metric, which provides a local model of the merging LBHs or rather pinching-off NBSs solutions. We remark, that none of the previously mentioned numerical results contradicts Kol's conjecture, though all implementations break down before reaching the critical transition. Numerical evidence in favor of the double-cone conjecture was provided in the references [136, 186] for  $D = 6$ , where the NBS branch was shown to approach the double-cone metric in the vicinity of the critical point.

Numerical data of NBS solutions in  $D = 5, 6$  far beyond previous results were recently provided by [122], including an investigation of the regime close to the critical transition. In addition, further evidence of a convergence of the horizon configuration towards the double-cone geometry was provided by the authors. Furthermore, an oscillation of the associated thermodynamic quantities was observed, which was characterized to resemble a distorted logarithmic spiral. Accordingly, the numerical data suggests the existence of an infinite number of oscillations before the NBS horizon pinches off.

This chapter of the underlying thesis concentrates on the construction of LBHs in  $D = 5$ ,  $D = 6$  and  $D = 10$  dimensions. Special attention is devoted to the critical regime, where

the poles of the horizons are about to merge along the compact dimension. For  $D = 5$  and  $D = 6$ , evidence is provided for a similar log-spiraling behavior of the related thermodynamic quantities as was acquired before for the NBS branch [122]. On the contrary, we are able to show that the critical regime in  $D = 10$  is approached in a qualitatively different manner, i.e. without oscillations. We are able to show that the obtained critical exponents for  $D = 5, 6$  and  $D = 10$  are in excellent agreement with the values that were predicted by Kol [132, 133]. Furthermore, the relation of the  $D = 10$  localized black hole solution to thermal states of a supersymmetric Yang-Mills theory (SYM) on the circle  $S^1$  is discussed in appendix A.2.4.

This chapter is structured as follows: We give a short review of static Kaluza-Klein black holes in section 4.1. Subsequently, we discuss the numerical implementation of localized black holes in great detail in section 4.2. The regarding results are provided in section 4.3, followed by summary in section 4.4.

The contents of this chapter rely partially on the results that were presented in references [123, 120].

## 4.1 Static Kaluza-Klein black holes

In this section we provide a short overview on static asymptotically flat black holes in KK theory. We start by defining the most important parameters and physical quantities in subsection 4.1.1. Subsequently, we give a short summary of the important class of black strings in subsection 4.1.2 before turning to the class of localized black holes, which are the main focus of this chapter. We conclude this section with a brief review of the Gregory-Laflamme instability in subsection 4.1.3 followed by a discussion of the corresponding phase diagram in subsection 4.1.4.

### 4.1.1 Physical quantities

Before presenting the physical quantities that are used for the description of the KK black holes, we need to recall the background metric that any spacetime in KK theory with only one compact dimension shall approach at infinity. The background for asymptotically flat KK black holes in  $D$  dimensions with one periodic spatial direction  $z \in [-L/2, L/2]$  is a direct product of the Minkowski spacetime  $\mathbb{R}^{1,D-2}$  and the circle  $S^1$

$$ds_{\text{BG}}^2 = -dt^2 + dr^2 + r^2 d\Omega_{D-3}^2 + dz^2. \quad (4.1)$$

As in chapter 2, we use (hyper-)spherical coordinates for the  $D - 2$  spatially extended dimensions with radial coordinate  $r \in [0, \infty]$ . Keeping this in mind we can proceed with the definition of two asymptotically measured charges and further thermodynamic quantities that are important for the formulation of the first law of black hole thermodynamics in KK theory.

### Asymptotic charges

A black hole introduces the following leading order corrections to the background metric (4.1) at infinity  $r \rightarrow \infty$  [95, 135]

$$g_{tt} \simeq -1 + \frac{c_t}{r^{D-4}}, \quad g_{zz} \simeq 1 + \frac{c_z}{r^{D-4}}, \quad (4.2)$$

where the coefficients  $c_t$  and  $c_z$  are directly related to the total mass  $M$  and tension  $\mathcal{T}$  of the black hole space time

$$M = \frac{L \Omega_{D-3}}{16\pi G_D} [(D-3)c_t - c_z], \quad (4.3)$$

$$\mathcal{T} = \frac{\Omega_{D-3}}{16\pi G_D} [c_t - (D-3)c_z]. \quad (4.4)$$

The so-called relative tension is obtained by the following combination:

$$n = \frac{L\mathcal{T}}{M} = \frac{c_t - (D-3)c_z}{(D-3)c_t - c_z}. \quad (4.5)$$

As shown in references [95, 184, 193]  $n$  is bounded from two sides:

$$0 \leq n \leq D-3.$$

### Thermodynamics

The equations (2.34) and (2.35) relating surface gravity  $\kappa$  and area  $A_{\mathcal{H}}$  to temperature  $T$  and entropy are also valid for KK black holes. Whereas the presence of the new asymptotic charge  $n$  leads to a modification of the first law of black hole thermodynamics

$$\delta M = T\delta S + \mathcal{T}\delta L = T\delta S + \frac{nM}{L}\delta L. \quad (4.6)$$

When comparing (4.6) with the fundamental thermodynamic equation  $\delta U = T\delta S - P\delta V$  and recalling that the black hole mass  $M$  is identified with the internal energy  $U$ , we can confirm the interpretation of  $\mathcal{T}$  as a force acting to compress the length of the compact dimension.

Integrating relation (4.6) yields the so-called Smarr relation in the presence of tension [135, 95]:

$$(D-2)TS = (D-3-n)M. \quad (4.7)$$

We now proceed with the discussion of black strings and localized black holes based on the given thermodynamic terminology.

#### 4.1.2 Black strings and localized black holes

##### Uniform black strings

The line element (2.39) for the asymptotically flat uniform black string (UBS) was presented in subsection 2.2.2 as the simplest example of a KK black hole. Since this spacetime is a direct product of a  $(D-1)$ -dimensional ST black hole and a circle  $S^1$ , we can easily provide the expressions for the related black hole mass and entropy

$$M_{UBS} = \frac{(D-3)\Omega_{D-3}r_{\mathcal{H}}^{D-4}}{16\pi G_D} = \frac{(D-3)\Omega_{D-3}r_{\mathcal{H}}^{D-4}L}{16\pi G_{D-1}}, \quad (4.8)$$

$$S_{UBS} = \frac{A_{\mathcal{H},UBS}}{4G_D} = \frac{\Omega_{D-3}r_{\mathcal{H}}^{D-3}L}{4G_{D-1}L} = \frac{\Omega_{D-3}r_{\mathcal{H}}^{D-3}}{4G_{D-1}}, \quad (4.9)$$

where we used the relation  $G_D = G_{D-1}L$  between the gravitational constants in the unconstrained  $(D-1)$ -dimensional subspace and the KK compactified space. Furthermore, the relative tension and temperature of the UBS solution read

$$n_{UBS} = \frac{1}{D-3}, \quad (4.10)$$

$$T_{UBS} = \frac{D-4}{4\pi r_{\mathcal{H}}}. \quad (4.11)$$

We can build one dimensionless parameter  $K := L/r_{\mathcal{H}}$  from the two characteristic length scales  $r_{\mathcal{H}}$  and  $L$  of a UBS, which is the only parameter that allows us to differentiate between different solutions due to the scale invariance of GR.

When analyzing the stability of the UBS solution branch in dependence of  $K$ , we need to consider perturbations of the symmetric event horizon configuration which leads us to the branch of non-uniform black strings (NBS).

### Non-uniform black strings

The class of NBS was discovered when searching for a stable configuration of the dynamic evolution of a perturbed UBS and can be characterized by a modulated concentric string radius along the compact coordinate  $z$  (see figure 4.2). The properties of NBSs beyond the perturbative scope can only be accessed by highly accurate numerical methods. The interesting critical regime comes with the highest requirements in terms of accuracy due to the extremely thin waist region. Accordingly, only a small number of configurations have been studied with detail in the critical region.

Nevertheless, the available numerical data (references [211, 138, 128, 186, 104, 73, 59, 185, 122]) excludes the NBS branch as stable end configuration for the perturbed UBS for  $D \leq 11$  due to its lower entropy than the related UBS branch. For configurations with  $D > 11$  the picture changes and the entire NBS branch has a higher entropy than the corresponding UBS branch for  $D \geq 14$ .

### Localized black holes

Since the NBS branch cannot serve as a stable endpoint for the perturbed UBS evolution, another class of static KK black holes with different horizon topology needs to be considered. For localized black holes (LBH) the horizon does not wrap the entire compact dimension. Instead LBH solutions have a hyper-spherical horizon structure homeomorphic to  $S^{D-2}$  in  $D$  dimensions. Thus, the extension  $l_{BH}$  of the black hole has to be smaller than the size of the compact dimension  $L$  and we recover the  $D$ -dimensional ST black hole with horizon radius  $l_{BH}$  for  $L \rightarrow \infty$ . Small LBHs with  $L \gg l_{BH}$  are well approximated by the ST metric 2.36 in the vicinity of the event horizon, while deviations from the ST solution occur at the periodic boundaries. Correspondingly, the horizon shape of an LBH is stretched along the compact dimension due to the presence of its mirror images (figure 4.1). Again, only high precision numerical methods are suited for constructing LBH solutions beyond the perturbative regime. Previous results [59, 104, 137, 138, 187, 210] suggest that the mass of a LBH is bounded as a direct consequence of its limited extension in the compact direction. The construction of the LBH solutions in  $D = 5, 6$  and  $10$  with unprecedented accuracy is the main focus of this chapter.

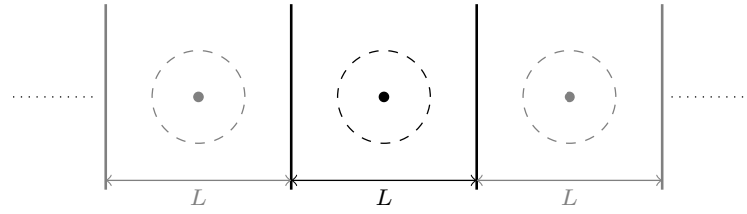


**Figure 4.1:** Illustration of a small localized black hole in a spacetime with one compact periodic dimension. The black dot corresponds to the black hole with horizon topology  $S^{D-2}$ . The region in vicinity of the black hole that is well approximated by the  $D$  dimensional ST metric (2.36) is indicated by the dashed circle. The ST solution fails to describe the spacetime as the boundary of the compact dimension is approached.

It remains to address the question of stability by comparing the entropy  $S$  of UBS and LBH solutions having the same mass  $M$ . According to the given analysis we can estimate the entropy of a small LBH by using the results of a ST black hole. Combining the Bekenstein-Hawking entropy formula (2.35) with the mass formula of the ST black hole (2.38) yields

$$S_{LBH} \sim M^{\frac{D-2}{D-3}}, \quad (4.12)$$

whereas the UBS entropy behaves asymptotically as (cf. (4.8) and (4.9))

$$S_{UBS} \sim M^{\frac{D-3}{D-4}}. \quad (4.13)$$

Comparing (4.12) and (4.13) leads to the conclusion that the entropy of a LBH exceeds the entropy of a UBS for sufficiently small  $M$ . As a result, we expect the UBS solution to be unstable at least for small masses.

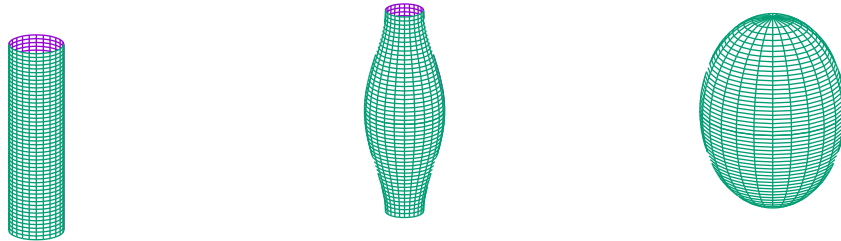


**Figure 4.2:** Comparison of the spatial embeddings of the UBS, NBS and LBH (left to right) horizon structure in  $D = 5$ . The vertical direction corresponds to the compact coordinate  $z$ . The  $z = \text{const.}$  slices of the horizon are (hyper-)spheres, here illustrated as circles.

### 4.1.3 The Gregory-Laflamme instability

Motivated by the entropy driven stability analysis presented so far, Gregory and Laflamme studied linear perturbations of the UBS in the early 1990s [84, 85]. The corresponding results can be summarized as follows: For small  $K = L/r_{\mathcal{H}}$  the energetic costs of the horizon deformations are too high and they decay exponentially. Moreover, there exists a threshold value  $K_{GL}$  where the UBS is marginally stable and becomes unstable for  $K > K_{GL}$ .

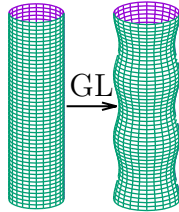


**Figure 4.3:** Schematic horizon deformation of an unstable UBS perturbed by a GL mode. The shape of the horizon changes since the perturbations that trigger the GL instability are non-uniform along the  $z$ -direction.

This Gregory-Laflamme (GL) instability causes the growth of small perturbations into large deformations accompanied by the redistribution of mass (figure 4.3) until a new stable configuration is reached.

It should be pointed out that the occurrence of GL type instabilities is not constrained to UBSs, but appears for a variety of higher dimensional black objects<sup>1</sup>. Furthermore, the GL instability can be classified within a broader class of similar instabilities, such as the Jeans instability [115, 94], leading to the formation of compact objects rather than widely spread structures.

Investigating the end state of the GL instability requires high precision time evolution of a perturbed unstable UBS, which is out of the scope of this thesis, but we give a brief summary of the current scientific progress. The problem was considered by different research groups mostly for  $D = 5$ , where the perturbed UBS was shown to collapse to a self-similar cascade of decreasing hyper-spherical black objects interconnected by shrinking black string segments [45, 144, 145]. This cascade continues until the string segments reach zero size and the horizon pinches off, leading to the formation of a naked singularity in finite asymptotic time (as extrapolated from the numerical data). This naked singularity is interpreted to signal the limited validity of classical physics and quantum effects are expected to circumvent its appearance. Furthermore, this configuration is inherently unstable against small perturbations in the compactified dimension, causing the merger of these black objects into a single LBH. Investigating the time evolution for large  $D$  showed that these configurations eventually relaxate to a NBS solution [69]. This is in accordance with the thermodynamic analysis, which shows a higher entropy for the NBS than for the UBS having the same mass for  $D \geq 12$ . Nevertheless, numerical results for  $D > 5$  are still rare and determining the corresponding end states of the GL instability is subject of ongoing research.

<sup>1</sup>Actually, Gregory and Laflamme considered black branes in the original work about the GL instability.



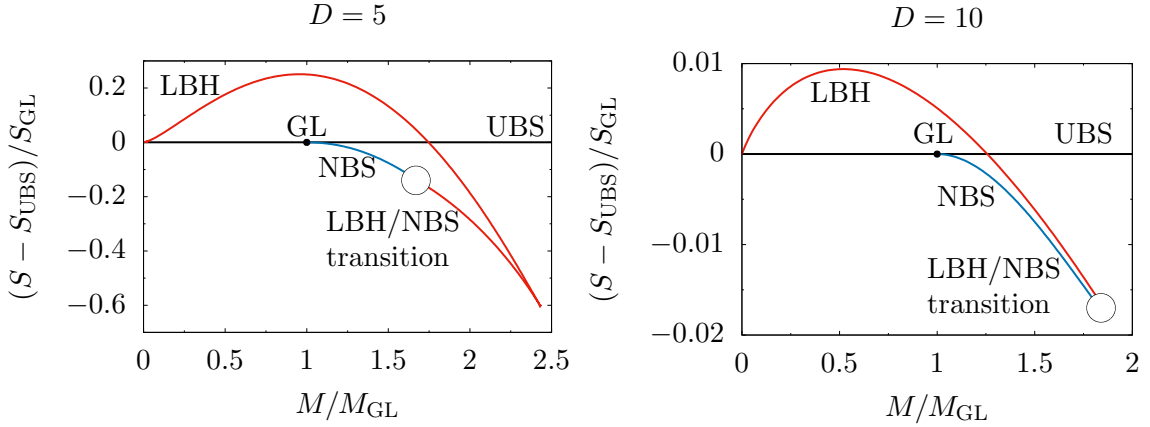


**Figure 4.4:** **Left:** Microcanonical phase diagram of KK black holes in  $D = 5$ . Mass  $M$  and entropy  $S$  are shifted by the corresponding values of a UBS and normalized by the UBS value at the GL point. LBHs have highest entropy and are thermodynamically preferred for small masses (red line). When the LBH branch crosses the UBS branch (black line), the UBSs become thermodynamically preferred. Note that the intersection point of the LBH and UBS branches corresponds to a first order phase transition. The NBS branch (blue line) starts from the GL instability point with a lower entropy than the UBS branch. At the maximum of entropy and mass the LBH branch exhibits a turning point and approaches the NBS branch. The merger of both branches in  $D = 5, 6$  was extensively studied in [123]. **Right:** The situation in  $D = 10$  differs qualitatively, since the LBH branch and the NBS branch are expected to asymptote to each other when approaching the finite maximum mass configuration of the LBH. The NBS data for  $D = 10$  was extrapolated from [59].

#### 4.1.4 The thermodynamic stability of static Kaluza-Klein black holes

In the following we give a summary of the phase diagrams for static KK black holes related to the LBH solutions in  $D = 5$ ,  $D = 6$  and  $D = 10$ , whose numerical construction is presented in section 4.2.

The phase diagram for  $D = 6$  is qualitatively similar to the picture for  $D = 5$ , so it suffices to discuss the latter one, which is depicted in figure 4.4 for the microcanonical ensemble, i.e. for a given mass the configuration with the highest entropy is physically preferred. We note that the UBS branch has the higher entropy for large values of the mass parameter, whereas the LBH branch predominates for small and moderate masses. Consequently, we have a first order phase transition where both branches intersect.

Starting with a UBS above the phase transition point, we have a globally stable configuration. Reducing its mass the stability of our UBS is reduced from global to local, when traversing the intersection point with the LBH branch, whose entropy is now higher. The local stability is lost when the GL point is passed and already small perturbations will grow as described above.

On the other hand, a LBH with small mass parameter is globally stable until its mass parameter is increased to the point where the entropy of the UBS branch dominates. The configuration remains locally stable when the mass is further increased until a maximum mass for the LBH is reached. Raising the mass beyond this point must lead to another configuration, whose stable end state is given by a UBS of the regarding mass. When looking at figure 4.4, we see that the LBH branch does not end at the maximum mass configuration, but continues with solutions having a lower mass and entropy. Finally, the LBH branch approaches the NBS branch which emanates from the UBS branch at the GL point.

The turning point of the LBH branch in  $D = 5, 6$  is the main qualitative difference to the phase diagram in  $D = 10$ . Here the LBH branch is not expected to turn around when reaching the maximum mass configuration. Instead the NBS and LBH branches are expected to approach each other at a finite maximum mass configuration (cf. right panel of figure 4.4). As we will see in the next subsection, the behavior for  $D < 10$  is qualitatively the same as for  $D = 5, 6$ , while a significant change of the critical behavior is observed for  $D \geq 10$ .

The details of the merger of these branches, were subject of a controversial scientific debate for  $D = 5, 6$ , since the available numerical results were not conclusive [128, 73] in the critical region. This issue was finally resolved with the results presented in [122, 123]. A critical scaling analysis of the LBH/NBS transition was first carried out by Kol [132], who analyzed linear perturbations around the so-called double-cone metric, which he claimed to be a local model of the proper limit at which both configurations meet. A brief summary of the double-cone metric and the related scaling analysis is provided in the next subsection.

#### 4.1.5 Critical behavior and the double-cone metric

Kol's analysis together with the merger hypothesis was confirmed for  $D = 5$  and  $D = 6$  in [122, 123] by a direct numerical construction of the NBS and LBH sides. The construction of the LBH side for  $D = 5, D = 6$  and  $D = 10$  and the regarding evaluation of the predicted scaling coefficients is covered in section 4.2 of this work.

Kol predicted the limiting spacetime of the LBH/NBS transition to be described by the Ricci-flat double cone metric [132]

$$ds_{DC}^2 = d\rho^2 + \frac{\rho^2}{D-2} [d\Omega_2^2 + (D-4) d\Omega_{D-3}^2], \quad (4.14)$$

which describes two separate cones with coinciding tips and a curvature singularity at the intersection point  $\rho = 0$ . A heuristic motivation of this ansatz can be obtained from figure 4.5, which shows that the corresponding horizon shape of the double cone "interpolates" between the corresponding horizons of the LBH and NBS branches. Accordingly, the  $D$  dependent prefactors in (4.14) prescribe the angle at which the poles of the LBH merge (or the horizon of the NBS pinches off) close to the transition point. A more detailed derivation of the double cone ansatz is rather complicated and can be found in reference [134].

Linear perturbations of the double cone metric were analyzed in [132, 24], where the form of the perturbations was chosen as follows

$$ds_{pDC}^2 = d\rho^2 + \frac{\rho^2}{D-2} \left[ e^{\epsilon(\rho)} d\Omega_2^2 + (D-4) e^{-2\epsilon(\rho)/(D-3)} d\Omega_{D-3}^2 \right]. \quad (4.15)$$

The linear contributions in  $\epsilon$  can be reduced to the following fundamental solution

$$\epsilon(\rho) = \rho^{s_{\pm}}, \quad (4.16)$$

with the complex exponents

$$s_{\pm} = \frac{D-2}{2} \left( -1 \pm i \sqrt{\frac{8}{D-2} - 1} \right). \quad (4.17)$$

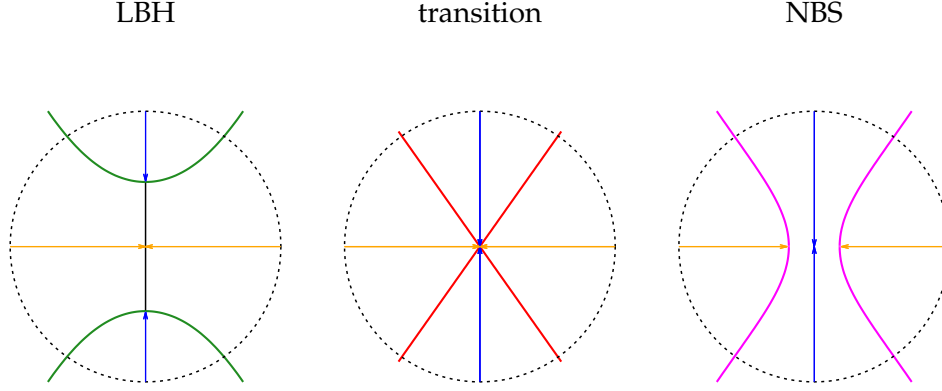


**Figure 4.5:** Sketch of the horizon shape of a LBH close to the merger, the double-cone and a NBS in vicinity of the critical point.

While the imaginary part of (4.17) leads to oscillations in  $\epsilon(\rho)$  for  $D < 10$ , we see that  $s_{\pm}$  become both purely real for  $D \geq 10$ . A physical interpretation of the exponents  $s_{\pm}$  can be taken from reference [133]: If  $\epsilon$  is related to the distance of physical observable  $p$  from its value at the critical point  $p_c$  according to  $\epsilon \simeq \Delta p := p - p_c$ , we expect  $\Delta p$  to show the following leading behavior on length scales of the double cone

$$\Delta p \simeq \tilde{a}\rho^{-s_+} + \tilde{b}\rho^{-s_-}, \quad (4.18)$$

with some constants  $\tilde{a}$  and  $\tilde{b}$ . For  $D < 10$  we can simplify the last expression to

$$\Delta p_{<10} \simeq a\rho^b \cos(c \log \rho + d), \quad (4.19)$$

where  $b = -\text{Re}(s_+)$ ,  $c = \text{Im}(s_+)$  and  $c, d \in \mathbb{R}$ . For  $D = 10$  the expression (4.18) degenerates and we have to consider an additional logarithmic solution branch, giving the leading behavior according to

$$\Delta p_{10} \simeq \rho^{-4} (a + b \log \rho), \quad (4.20)$$

where  $a, b \in \mathbb{R}$ .

From the given analysis we conclude that physical observables close to the transient LBH/NBS region are expected to follow a scaling law. The theoretical prediction for this scaling law can be tested by fitting numerical data to the given expressions (4.19) (for  $D < 10$ ) or (4.20) (for  $D = 10$ ), after some appropriate length scale  $\rho_0$  for the parametrization of the LBH and NBS branches close to the critical point has been identified. Previous studies of the critical behavior in  $D = 6$  can be found in [136, 186]. The numerical construction of the critical LBH region for  $D = 5$ ,  $D = 6$  and  $D = 10$  is covered within this thesis, based on the references [122, 123].

## 4.2 Numerical construction

We start with the description of the coordinate system, that we employed for the construction of the LBH solutions. The LBH is centered in the origin of the  $r - z$  plane. Here,  $r \in [0, \infty]$  is the radial coordinate associated with the  $S^{D-2}$  hyper-spherical horizon topology.  $z$  denotes the coordinate along the compact dimension with asymptotic length  $L$  as it was described in the previous sections. The setup is reflection-symmetric with respect to  $z = 0$  and we can constrain the domain of integration to  $z \in [0, L/2]$ , while using appropriate boundary conditions at  $z = 0$ . Since we want to construct static solutions, we can always choose a suitable coordinate system, where the LBH attains a hyper-spherical shape in the  $(r, z)$ -coordinates, making the problem effectively two-dimensional. As a result we can describe the horizon by a circle-equation  $r^2 + z^2 = \varrho_0^2$ , where  $\varrho_0$  denotes the coordinate radius of the horizon. The corresponding domain of integration is shown in figure 4.6, its boundary structure can be divided into:

- The horizon  $\mathcal{H} = \{(r, z) : r \geq 0, z \geq 0, r^2 + z^2 = \varrho_0^2\}$ ,
- The exposed axis of symmetry  $\mathcal{A} = \{(r, z) : r = 0, \varrho_0 \leq z \leq L/2\}$ ,
- The lower mirror boundary  $\mathcal{M}_0 = \{(r, z) : r \geq \varrho_0, z = 0\}$ ,
- The upper mirror boundary  $\mathcal{M}_1 = \{(r, z) : r \geq 0, z = L/2\}$ ,
- The asymptotic boundary  $\mathcal{I} = \{(r, z) : r \rightarrow \infty, 0 \leq z \leq L/2\}$ .

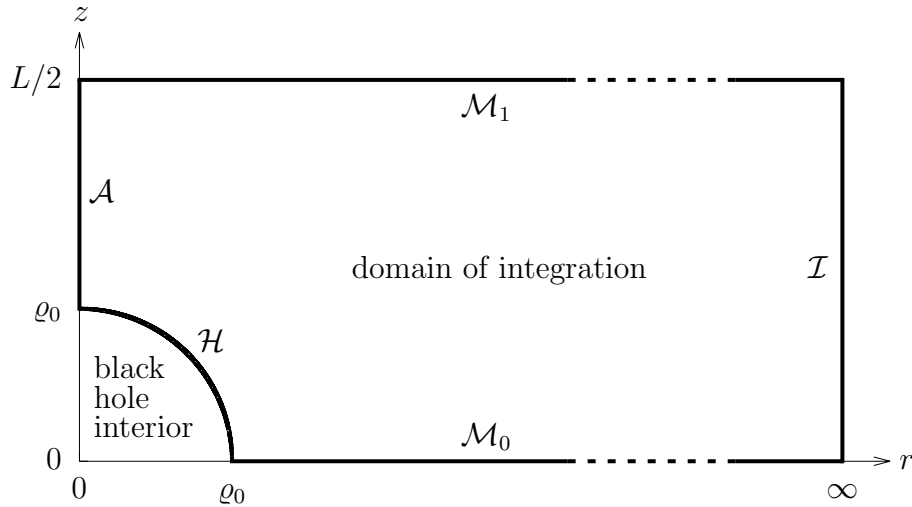


**Figure 4.6:** Sketch of the domain of integration with the following boundaries: horizon  $\mathcal{H}$ , exposed axis of spherical symmetry  $\mathcal{A}$ , lower mirror boundary  $\mathcal{M}_0$ , upper mirror boundary  $\mathcal{M}_1$ , and asymptotic boundary  $\mathcal{I}$ .

Subsequently, the numerical procedure for constructing LBH solutions to Einstein's field equations on the above domain of integration is covered in detail with a special focus on the critical regime, where the poles of neighboring LBHs approach each other. We start with introducing the metric tensors and the regarding boundary conditions in subsection 4.2.1, followed by the description of the gauge procedure and the related reference metric tensors in subsection 4.2.2. More information on the underlying domain decomposition and the numerical strategy are given in subsection 4.2.3, before completing this section with a summary of the parameters and physical quantities in subsection 4.2.4.

### 4.2.1 Metric and boundary conditions

Instead of introducing a single coordinate system that fits to all five boundaries at once (cf. eg. reference [137]), we decided to use two different coordinate charts in the different asymptotical regions of the setup. This approach, which has been employed previously by different authors ([104, 187]), comes with the advantage of being not spoiled by any coordinate singularity while keeping the complexity of the coordinate transformations comparatively low. The following two paragraphs contain a detailed discussion of the regarding coordinate charts, where the first is adapted to the asymptotic behavior at large  $r \rightarrow \infty$ , while the other is specifically designed to cover the near horizon region.

#### Asymptotic chart

We use the following general ansatz for the metric tensor at large  $r$

$$ds_{LBH_a}^2 = -T_a dt^2 + A_a dz^2 + B_a dr^2 + 2F_a dz dr + r^2 S_a d\Omega_{D-3}^2, \quad (4.21)$$

which complies with the required symmetries. Note that the functions  $T_a$ ,  $A_a$ ,  $B_a$ ,  $F_a$  and  $S_a$  depend on the coordinates  $(r, z)$ . The following boundary conditions are imposed on the four external boundaries of the asymptotic region:

- The asymptotic boundary  $\mathcal{I}$  ( $r \rightarrow \infty$ ):  
The background metric (4.1) has to be approached in the limit  $r \rightarrow \infty$ , i.e.

$$0 = T_a - 1 = A_a - 1 = B_a - 1 = S_a - 1 = F_a. \quad (4.22)$$

- The exposed axis  $\mathcal{A}$  ( $r = 0$ ):  
This is the location of the hyper-sphere axis, i.e. the metric degenerates. We obtain the following regularity conditions

$$0 = A_a - S_a = \frac{\partial T_a}{\partial r} = \frac{\partial A_a}{\partial r} = \frac{\partial B_a}{\partial r} = \frac{\partial S_a}{\partial r} = F_a. \quad (4.23)$$

- The mirror boundaries  $\mathcal{M}_0$  ( $z = 0$ ) and  $\mathcal{M}_1$  ( $z = L/2$ ):  
As a result of the mirror symmetry we obtain

$$0 = \frac{\partial T_a}{\partial z} = \frac{\partial A_a}{\partial z} = \frac{\partial B_a}{\partial z} = \frac{\partial S_a}{\partial z} = F_a. \quad (4.24)$$

The next paragraph covers the near horizon chart which is based on polar coordinates that are adapted to the spherical symmetry of the horizon.

### Near horizon chart

The polar coordinates  $(\varrho, \varphi)$ , which adapt naturally to the spherical horizon shape, are related to the  $(r, z)$  coordinates as follows

$$r = \varrho \sin \varphi, \quad z = \varrho \cos \varphi, \quad (4.25)$$

with the horizon located at  $\varrho = \varrho_0$ . The corresponding metric ansatz reads

$$ds_{LBH_h}^2 = -T_h dt^2 + A_h d\varrho^2 + \varrho^2 B_h d\varphi^2 + 2\varrho F_h d\varrho d\varphi + \varrho^2 \sin^2 \varphi S_h d\Omega_{D-3}^2, \quad (4.26)$$

where the functions  $T_h$ ,  $A_h$ ,  $B_h$ ,  $F_h$  and  $S_h$  depend on the coordinates  $(\varrho, \varphi)$ . Apart from the trivial identification  $T_h = T_a$  and  $S_h = S_a$ , we need to apply the coordinate transformation (4.25) to the line element (4.21) for obtaining the relations between the metric functions in the different coordinate charts, yielding

$$A_h = \sin^2 \varphi A_a + \cos^2 \varphi B_a + 2 \sin \varphi \cos \varphi F_a, \quad (4.27)$$

$$B_h = \cos^2 \varphi A_a + \sin^2 \varphi B_a - 2 \sin \varphi \cos \varphi F_a, \quad (4.28)$$

$$F_h = \sin \varphi \cos \varphi (A_a - B_a) + (\cos^2 \varphi - \sin^2 \varphi) F_a. \quad (4.29)$$

In addition we introduce a redefined version of  $T_h$  that includes the blackness factor

$$T_h = \kappa^2 (\varrho - \varrho_0)^2 \tilde{T}_h, \quad (4.30)$$

where  $\tilde{T}_h$  is regular at the horizon. The boundary conditions on  $\mathcal{H}$ ,  $\mathcal{A}$ ,  $\mathcal{M}_0$  and  $\mathcal{M}_1$  are summarized subsequently:

- The horizon boundary  $\mathcal{H}$  ( $\varrho = \varrho_0$ ):

The following conditions are derived from regularity requirements at the horizon

$$0 = \tilde{T}_h - A_h = \frac{\partial \tilde{T}_h}{\partial \varrho} = \frac{\partial A_h}{\partial \varrho} = \frac{\partial}{\partial \varrho} (\varrho^2 B_h) = \frac{\partial}{\partial \varrho} (\varrho^2 S_h) = F_h. \quad (4.31)$$

- The exposed axis  $\mathcal{A}$  ( $\varphi = 0$ ):

As above, we obtain the regularity conditions

$$0 = B_h - S_h = \frac{\partial \tilde{T}_h}{\partial \varphi} = \frac{\partial A_h}{\partial \varphi} = \frac{\partial B_h}{\partial \varphi} = \frac{\partial S_h}{\partial \varphi} = F_h. \quad (4.32)$$

- The lower mirror boundary  $\mathcal{M}_0$  ( $\varphi = \pi/2$ ):

The symmetry conditions yield

$$0 = \frac{\partial T_h}{\partial \varphi} = \frac{\partial A_h}{\partial \varphi} = \frac{\partial B_h}{\partial \varphi} = \frac{\partial S_h}{\partial \varphi} = F_h. \quad (4.33)$$

- The upper mirror boundary  $\mathcal{M}_1$  ( $\varrho \cos \varphi = L/2$ ):

The symmetry conditions for the upper mirror boundary can be obtained by transforming the regarding conditions from the old coordinate frame (4.24) to the new one. This leads to rather lengthy expressions, thus we refrain from presenting them here.

We notice that the number of conditions at  $\mathcal{A}$  and  $\mathcal{H}$  exceeds the number of unknown fields by one. According to reference [58], one of the conditions can be dropped and will be satisfied automatically up to the precision of our numerical algorithm once the computation has been carried out. Accordingly, the condition  $\partial\tilde{T}_h/\partial\varrho = 0$  at  $\mathcal{H}$  and  $\partial S_h/\partial\varphi = 0$  at  $\mathcal{A}$  were omitted.

#### 4.2.2 Gauging and reference metric

The DeTurck method, which was outlined in section 2.1.2, was used for rendering the field equations strongly elliptic. The required reference metric must comply with the different boundary asymptotics in the different coordinate charts that were discussed in the last section. Therefore we use different reference line elements in the different asymptotic regions and connect them via a suitable interpolation technique.

We divide the domain of integration in two regions separated at some distance  $\varrho_1$  with  $\varrho_0 < \varrho_1 < L/2$  (see figure 4.7). For  $\varrho > \varrho_1$  we can use the the background metric (4.1) as a reference, since it satisfies all the external boundary conditions within this region. In the remaining near-horizon region  $\varrho_0 < \varrho < \varrho_1$  we need to construct a reference that complies with the horizon boundary condition at  $\mathcal{H}$  as well as the conditions at the exposed axis  $\mathcal{A}$  and the lower mirror boundary  $\mathcal{M}_0$ . In addition this reference needs to attach to the background metric at  $\varrho = \varrho_1$  with a certain level of smoothness. For constructing the reference in  $\varrho_0 < \varrho < \varrho_1$  we start with the following ansatz

$$d\tilde{s}_{LBH_{ref}}^2 = -\bar{H}(\varrho) dt^2 + d\varrho^2 + \bar{G}(\varrho) d\Omega_{D-2}^2, \quad (4.34)$$

where  $d\Omega_{D-2}^2 = d\varphi^2 + \sin^2\varphi d\Omega_{D-3}^2$ . We note that the functions  $\bar{H}(\varrho)$  and  $\bar{G}(\varrho)$  depend only on  $\varrho$ , as a result (4.34) satisfies the boundary conditions on  $\mathcal{A}$  and  $\mathcal{M}_0$ . For matching the background metric (4.1) at  $\varrho = \varrho_1$ , we consider its form in polar coordinates

$$ds_{BG}^2 = -dt^2 + d\varrho^2 + \varrho^2 (d\varphi^2 + \sin^2\varphi d\Omega_{D-3}^2). \quad (4.35)$$

Accordingly, the functions for  $\bar{H}(\varrho)$  and  $\bar{G}(\varrho)$  can be constrained to the following shapes

$$\bar{H}(\varrho) = \begin{cases} \bar{H}_{hor}(\varrho) & \text{if } \varrho < \varrho_1, \\ 1 & \text{if } \varrho \geq \varrho_1, \end{cases} \quad \text{and} \quad \bar{G}(\varrho) = \begin{cases} \bar{G}_{hor}(\varrho) & \text{if } \varrho < \varrho_1, \\ \varrho^2 & \text{if } \varrho \geq \varrho_1. \end{cases} \quad (4.36)$$

The approximability of the LBH solution by the ST black hole in the vicinity of its horizon, that was mentioned in the previous section, gives us the near horizon asymptotics of  $\bar{H}_{hor}(\varrho)$  and  $\bar{G}_{hor}(\varrho)$

$$\bar{H}_{hor}(\varrho) = \kappa^2 (\varrho - \varrho_0)^2 + \mathcal{O}[(\varrho - \varrho_0)^4], \quad (4.37)$$

$$\bar{G}_{hor}(\varrho) = \frac{(D-3)^2}{4\kappa^2} + \frac{D-3}{2} (\varrho - \varrho_0)^2 + \mathcal{O}[(\varrho - \varrho_0)^3]. \quad (4.38)$$

To obtain a  $C^k$  continuous reference line element at  $\varrho = \varrho_1$ , we require that

$$\bar{H}_{hor}(\varrho) = 1 + \mathcal{O}[(\varrho - \varrho_1)^{k+1}], \quad (4.39)$$

$$\bar{G}_{hor}(\varrho) = \varrho^2 + \mathcal{O}[(\varrho - \varrho_1)^{k+1}]. \quad (4.40)$$

From the PDE point of view it suffices to require  $\bar{H}_{hor}(\varrho)$  and  $\bar{G}_{hor}(\varrho)$  to be  $C^2$  in each single domain of integration and at least  $C^1$  at the external and internal boundaries. This corresponds to creating a  $C^1$  global cover of the underlying manifold, which is not a problem as long as the regularity at the boundaries is high enough to guarantee the existence of the physical quantities, that we are going to extract. In practice we used at least  $k = 2$  regularity at the matching contour  $\varrho = \varrho_1$ , so that all curvature measures are globally well defined. Furthermore, we compared the results obtained at  $k = 2$  with a  $k = \infty$  ansatz and saw agreement in terms of the extracted physical quantities at the level of machine precision.

The  $k = 2$  ansatz, is obtained by simple polynomial interpolation

$$\bar{H}_{hor}(\varrho) = \kappa^2 (\varrho - \varrho_0)^2 + \bar{h}_1 (\varrho - \varrho_0)^4 + \bar{h}_2 (\varrho - \varrho_0)^6 + \bar{h}_3 (\varrho - \varrho_0)^8, \quad (4.41)$$

$$\bar{G}_{hor}(\varrho) = \frac{(D-3)^2}{4\kappa^2} + \frac{D-3}{2} (\varrho - \varrho_0)^2 + \bar{g}_1 (\varrho - \varrho_0)^4 + \bar{g}_2 (\varrho - \varrho_0)^6 + \bar{g}_3 (\varrho - \varrho_0)^8, \quad (4.42)$$

where the coefficients  $\bar{h}_1, \bar{h}_2, \bar{h}_3, \bar{g}_1, \bar{g}_2$  and  $\bar{g}_3$  are determined by the aforementioned matching conditions. In contrast, the  $k = \infty$  version is obtained by an exponential ansatz

$$\bar{H}_{hor}(\varrho) = 1 - E(\varrho), \quad (4.43)$$

$$\bar{G}_{hor}(\varrho) = \varrho^2 - E(\varrho) \left[ \varrho^2 - \frac{(D-3)^2}{4\kappa^2} - (\varrho - \varrho_0)^2 \left( \frac{D^2}{4} - D + \frac{3}{4} - \kappa^2 \varrho_0^2 \right) \right], \quad (4.44)$$

where  $E(\varrho)$  is given by

$$E(\varrho) = \exp \left[ -\kappa^2 \frac{(\varrho - \varrho_0)^2}{1 - (\varrho - \varrho_0)^2 / (\varrho_1 - \varrho_0)^2} \right]. \quad (4.45)$$

There are important differences between the two approaches in terms of numerical implementation and convergence. First, we note that the function  $E(\varrho)$  has an essential singularity at  $\varrho = \varrho_1$ , which needs to be cured in the numerical implementation. Furthermore, the non-analytic form of  $E(\varrho)$  leads to a lower convergence rate than the polynomial ansatz. The polynomial ansatz is analytic on the closure of each patch of our non-overlapping domain decomposition, which is depicted in figure 4.7.

### 4.2.3 Domain decomposition

A sketch of the domain configuration is depicted in figure 4.7. As stated in the previous section, the domain of integration is divided into an asymptotic region with  $r \geq L/2$  and a near horizon region, where  $r \leq L/2$ . Moreover, the aforementioned structure of the reference metric implies another decomposition of the near horizon region. An additional decomposition is introduced at  $\varphi = \pi/4$  for avoiding domains with more than four boundaries leading to simpler coordinate transformations to the standard cube  $[-1, 1]^2$ , where the two-dimensional Chebyshev expansion is defined. The final domain configuration includes 12 subdomains, which are not all covered in the schematic sketch of figure 4.7. More details on the specific decompositions in the asymptotic and the near horizon region are given in the next paragraphs.



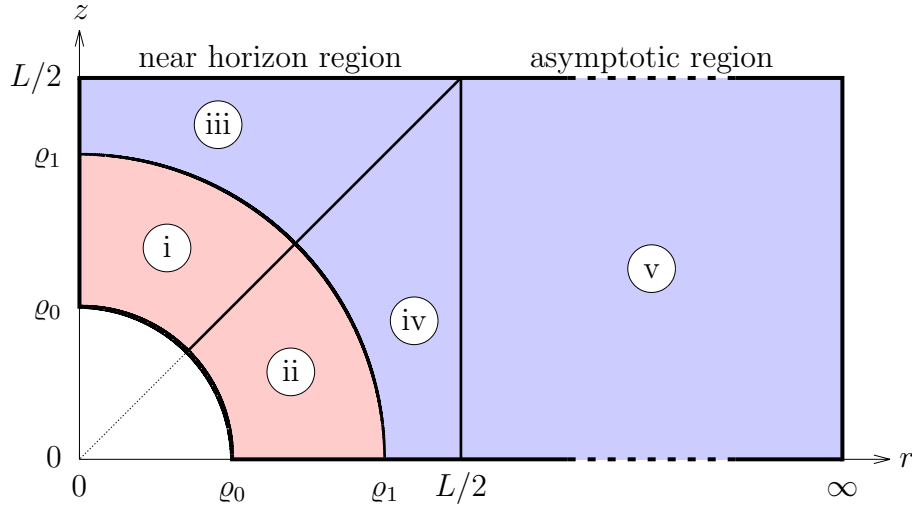


**Figure 4.7:** Schematic decomposition of the LBH domain of integration obtained from [120]. The region  $r \geq L/2$  is denoted as the asymptotic region and  $r \leq L/2$  as the near horizon region. The near horizon region is divided into four subdomains at the contours  $r = z$  (or  $\varphi = \pi/4$ ) and  $r^2 + z^2 = \varrho^2 = \varrho_1^2$ . The background metric (4.35) is used as reference for the DeTurck method in the region  $\varrho \geq \varrho_1$  (blue shaded region corresponding to subdomains (iii), (iv) and (v)). For  $\varrho \leq \varrho_1$  (red shaded region corresponding to subdomains (i) and (ii)) the reference metric approximates an ST solution at the horizon  $\varrho = \varrho_0$  and matches the background metric at  $\varrho = \varrho_1$ .

### Asymptotic region

A simple algebraic coordinate compactification is applied to cover the asymptotic region which extends to  $r \rightarrow \infty$

$$r(s) = \frac{L}{1-s}, \quad (4.46)$$

where  $s \in [-1, 1]$  such that infinity is mapped to  $s = 1$  and  $r = L/2$  corresponds to  $s = -1$ . Analyzing the asymptotic behavior of the solution, we discover exponentially decaying  $z$ -dependent modes and algebraically decaying  $z$ -independent modes. Thus, we expect a rather slow decay of the spectral coefficients related to the  $s$ -direction, while the coefficients of the  $z$ -expansion are expected to decay much faster. We divide the asymptotic region into three linearly connected subdomains for improving the numerical accuracy in the asymptotic region (figure 4.8). Reducing the width of the subdomain which is connected to  $s = 1$  blocks the spreading of the bad convergence rate, which is caused by the non-analytic  $z$ -independent modes, to the other subdomains. Furthermore, adapting the resolutions in the three subdomains makes the computation more effective in terms of computational costs, while a higher accuracy can be obtained.

As covered in subsection 4.1.1, computing the mass and relative tension relies on determining the  $(D-4)$ th Taylor coefficients of the metric functions  $T_a$  and  $B_a$ . In  $D = 5$  and  $D = 6$  we use direct numerical differentiation for obtaining these coefficients, since the accuracy loss is comparatively low. In contrast, for  $D = 10$  we redefine  $T_a = 1 + \frac{(1-s)^5}{32} \tilde{T}_a$  and  $B_a = 1 + \frac{(1-s)^5}{32} \tilde{B}_a$  and use a single numerical differentiation to obtain  $c_t$  and  $c_z$  from  $\tilde{T}_a$  and  $\tilde{B}_a^2$ .

<sup>2</sup>Moreover, we remark, that for  $D = 10$  all metric variables  $T_a, A_a, B_a, F_a$  and  $S_a$  were redefined by pulling out the same factor  $\frac{(1-s)^5}{32}$ .

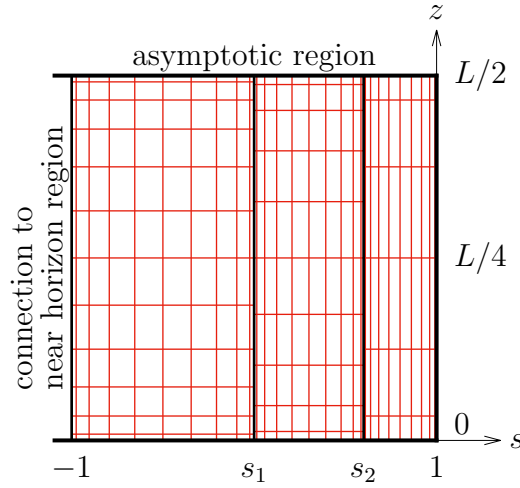


**Figure 4.8:** Domain setup in the asymptotic region with the corresponding coordinate lines. The coordinate  $s$  compactifies infinity to the value  $s = 1$ . The three subdomains are separated at  $s = s_1$  and  $s = s_2$ . At  $s = -1$  this region is connected to the near horizon region corresponding to  $r = L/2$ .

### Near horizon region

As mentioned in the previous section, polar coordinates are used to cover the domains (i) and (ii) (figure 4.9). In the domains (iii) and (iv) we need to adapt the parametrization for aligning the patch boundaries to the rectangular shape:

$$r = \tilde{q}(v, \varphi) \sin \varphi, \quad z = \tilde{q}(v, \varphi) \cos \varphi, \quad (4.47)$$

where

$$\tilde{\rho}(v, \varphi) = q_1 \frac{L/2 - v}{L/2 - q_1} + L/2 \frac{v - q_1}{L/2 - q_1} \begin{cases} (\cos \varphi)^{-1} & \text{for domain (iii),} \\ (\sin \varphi)^{-1} & \text{for domain (iv),} \end{cases} \quad (4.48)$$

with  $v \in [q_1, L/2]$ . For  $v = q_1$  we are at  $\varphi = q_1$ , moreover the value  $v = L/2$  corresponds to the locus  $z = L/2$  in domain (iii) and to  $r = L/2$  in domain (iv).

To satisfy the increased accuracy requirements in the critical regime of nearly touching poles, we split the near horizon domains further close to the exposed axis  $\mathcal{A}$  at an angle  $\varphi_i$  and close to the horizon at the radial distance  $q_i$  (see figure 4.9). On top of that, the high gradients in the vicinity of  $\mathcal{A}$  make additional adjustments necessary. First, we must redefine the functions  $B_h$  and  $S_h$  in the region  $0 < \varphi < \varphi_i$  according to

$$\tilde{B}_h := \frac{1}{B_h}, \quad \text{and} \quad \tilde{S}_h := \frac{1}{S_h}, \quad (4.49)$$

which helps in dealing with the exceedingly high values that those functions approach close to  $\mathcal{A}$ . In addition, an analytic mesh refinement is applied, i.e. a reparametrization of  $\varphi$  on  $[0, \varphi_i]$

$$\varphi(\bar{\varphi}) = \varphi_i \frac{\sinh(\lambda \bar{\varphi})}{\sinh \lambda}, \quad (4.50)$$

where  $\bar{\varphi} \in [0, \varphi_i]$ .

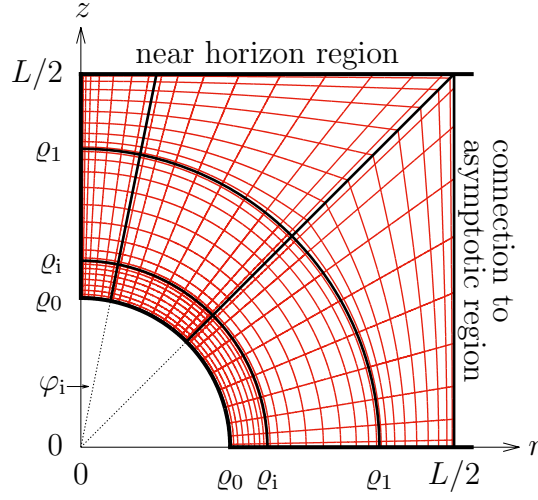


**Figure 4.9:** Domain setup in the near horizon region with the corresponding coordinate lines. The region is further subdivided into nine subdomains with inner boundaries at  $\varrho = \varrho_1$ ,  $\varrho = \varrho_i$ ,  $\varphi = \pi/4$  and  $\varphi = \varphi_i$ . We use polar the coordinates (4.25) for  $\varrho \leq \varrho_1$ . In the other subdomains the radial coordinate is modified according to (4.48). An analytic mesh refinement (4.50) with respect to  $\varphi$  is employed for  $\varphi \leq \varphi_i$ . At  $r = L/2$  this region is connected to the asymptotic region.

Adapting the parameter  $\lambda$  can improve the decay rates of the spectral coefficients significantly. A good review on this mesh refinement technique is provided in the appendix of [120].

#### 4.2.4 Parameters and observables

The set of parameters that enter the numerical scheme can be categorized into those which have a physical meaning ( $L$  and  $\kappa$ ) and non-physical parameters ( $\varrho_0$ ,  $\varrho_1$ ,  $\varrho_i$ ,  $\varphi_i$ ,  $s_1$ ,  $s_2$  and  $\lambda$ ) that are used for gauge-fixing and control of the numerical grid. The specific values that were used to produce the results, which are presented in section 4.3, can be found in appendix A.2.1.

Apart from the parameters that we control explicitly, there are the physical quantities which were presented in subsection 4.1.1. The following paragraphs cover the extraction of the interesting physical quantities from the functions, that are approximated by the numerical scheme.

#### Thermodynamic quantities

The asymptotic coefficients  $c_t$  and  $c_z$  (cf. 4.2) are obtained from  $T_a$  and  $B_a$  as follows

$$c_t = (-1)^{D-3} \frac{L^{D-4}}{(D-4)!} \frac{\partial^{D-4} T_a}{\partial s^{D-4}}, \quad (4.51)$$

$$c_z = (-1)^{D-4} \frac{L^{D-4}}{(D-4)!} \frac{\partial^{D-4} B_a}{\partial s^{D-4}}. \quad (4.52)$$

The mass and relative tension is then obtained from  $c_t$  and  $c_z$  according to the formulas (4.3) and (4.4) that were provided in subsection 4.1.1.

The temperature is directly related to the surface gravity  $\kappa$

$$T/T_{GL} = \frac{2L}{(D-4)K_{GL}}\kappa, \quad (4.53)$$

where  $T_{GL}$  and  $K_{GL}$  denote the temperature and  $K$ -value of a UBS at the GL point. The entropy is obtained from a surface area integral according to

$$S/S_{GL} = 2\frac{\varrho_0^{D-2}}{L^{D-2}}K_{GL}^{D-3} \int_0^{2\pi} \sqrt{B_h S_h^{D-3}} \Big|_{\varrho=\varrho_0} (\sin \varphi)^{D-3} d\varphi, \quad (4.54)$$

where  $S_{GL}$  is the entropy of a UBS at the GL point.

### Geometric quantities

The following quantities are used for classifying the different LBH solutions by simple geometric measures.

The maximal horizon areal radius at the equator is given by

$$R_{max} = \varrho_0 \sqrt{S_h(\varrho_0, \pi/2)}. \quad (4.55)$$

The proper length of the horizon from the north to the south pole reads

$$L_{\mathcal{H}} = 2\varrho_0 \int_0^{2\pi} \sqrt{B_h} \Big|_{\varrho=\varrho_0} d\varphi. \quad (4.56)$$

The proper length of the exposed axis of symmetry  $\mathcal{A}$ , i.e. the pole to pole distance of neighboring LBHs is computed as

$$L_{\mathcal{A}} = 2 \int_{\varrho_0}^{L/2} \sqrt{A_h} \Big|_{\varphi=0} d\varrho. \quad (4.57)$$

For illustration the  $(D-2)$  dimensional horizon surface is embedded into  $(D-1)$ -dimensional flat space

$$ds^2 = dR^2 + dZ^2 + R^2 d\Omega_{D-3}^2. \quad (4.58)$$

Comparing (4.58) with the line element (4.26) yields

$$R(\varphi) = \varrho_0 \sin \varphi \sqrt{S_h(\varrho_0, \varphi)}, \quad (4.59)$$

$$Z(\varphi) = \int_{\varphi}^{2\pi} \sqrt{\varrho_0^2 B_h(\varrho_0, \tilde{\varphi}) - (dR(\tilde{\varphi})/d\tilde{\varphi})^2} d\tilde{\varphi}, \quad (4.60)$$

where we set an arbitrary integration constant in the second expression to zero.

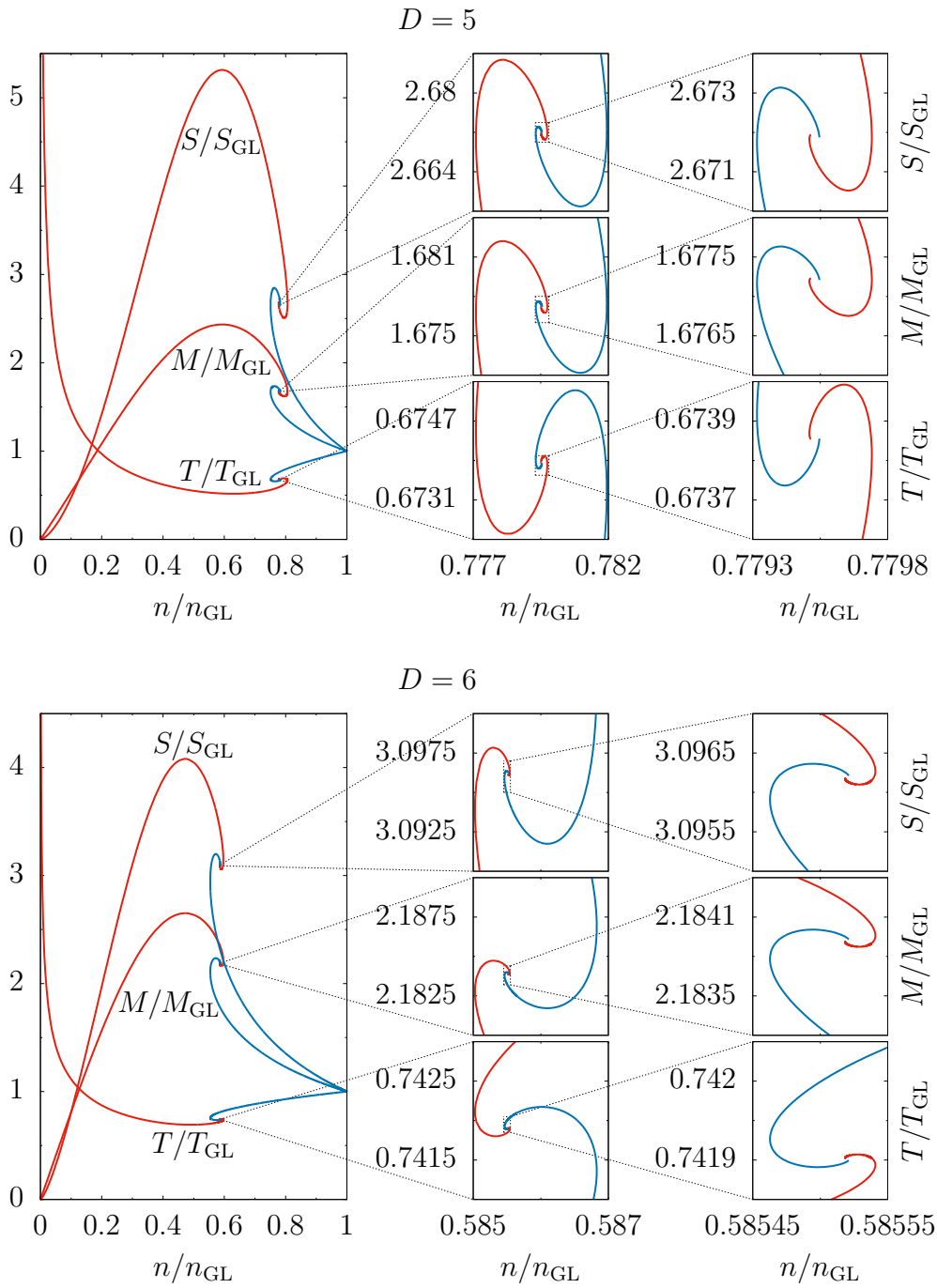


**Figure 4.10:** Entropy  $S$ , mass  $M$  and temperature  $T$  as functions of the relative tension  $n$ . All quantities are normalized with respect to the corresponding values of a UBS at the GL point. The critical region is magnified in two stages in the center and right columns. The upper diagrams corresponds to  $D = 5$  and the lower ones to  $D = 6$ .

### 4.3 Results

The previously described sophisticated numerical scheme enables us to extend the branch of LBH solutions in  $D = 5$ ,  $D = 6$  and  $D = 10$  far beyond previous results. In particular, we probed deeply into the critical regime, where a transition to the NBS branch is supposed to happen. As a result we were able to clarify open issues about the end point of the GL instability in  $D = 5, 6$  by showing in detail how the LBH and NBS branches approach each other. Furthermore, the currently most far-reaching results on the critical behavior of a LBH in  $D = 10$  were obtained and show excellent agreement with the theoretical predictions.

The qualitative behavior of the thermodynamic quantities including the regarding phase space diagrams is provided in subsection 4.3.1 followed by a detailed geometric analysis in subsection 4.3.2. The results related to the critical regime are analyzed in subsection 4.3.3, where we discuss the validity of the predicted critical scaling (4.19) and (4.20) of the physical quantities. The accuracy of the presented solutions is analyzed in appendix A.2.5.

The LBH results in  $D = 5, 6$  are compared to the NBS results of reference [122]. For  $D = 10$  we refer the reader to [59], which provides data for the NBS branch in  $D = 10$ . In addition, in appendix A.2.4, we comment on the relation of the  $D = 10$  localized black hole solution to localized thermal states of a supersymmetric Yang-Mills theory on the circle  $S^1$ , based on the analysis given in [59].

#### 4.3.1 Thermodynamics

In figure 4.10 we show the normalized entropy, mass and temperature as a function of the normalized relative tension  $n/n_{GL}$  for the LBH and the NBS branch in  $D = 5, 6$ , where normalization is done by dividing through the corresponding values of a UBS at the GL point. Each LBH branch starts at small size of the horizon compared to  $L$  where  $n/n_{GL}$  is close to zero and continues with increasing black hole sizes. When following the branch, we come to a maximum value for mass and entropy which is in agreement with previous results. Accordingly, mass and entropy decrease towards the NBS branch values when the tension is further increased.

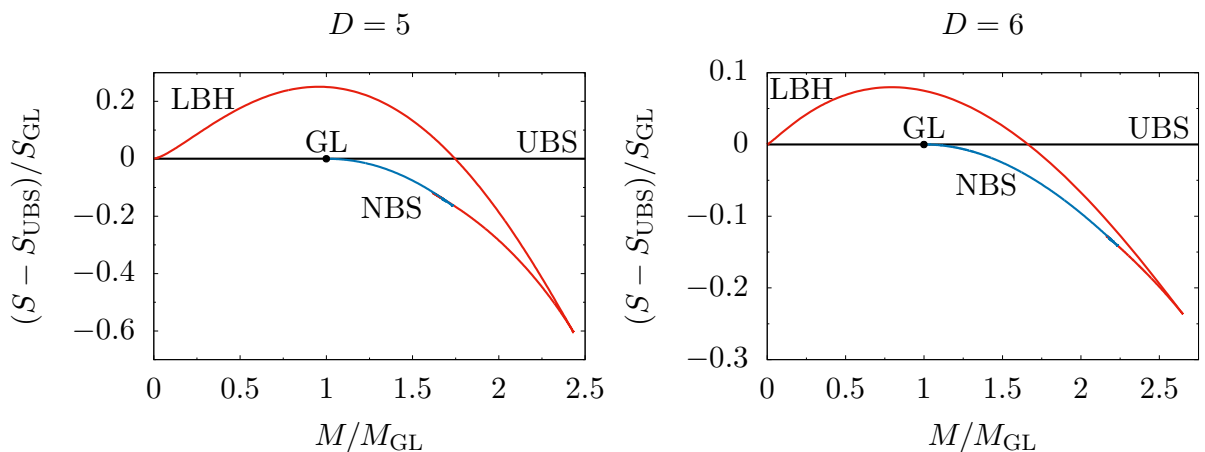


**Figure 4.11:** Phase diagrams of the microcanonical ensemble for  $D = 5$  (left) and  $D = 6$  (right). The values of entropy  $S$  and mass  $M$  are shifted by the corresponding values of a UBS (black line) and normalized by the UBS value at the GL point. The critical region is located where the LBH (red line) and NBS (blue line) branches approach each other.

As a result we can close the gap between the LBH and the NBS branch, as depicted in figure 4.10. Traversing the LBH branch, we notice at least four turning points of the displayed thermodynamic quantities, leading to an inspiraling behavior. The same behavior was previously obtained for the NBS branch in reference [122]. The LBH and NBS branches are coming closer with each spiral revolution, which is a strong indication of their expected merger in the phase diagram. The shrinking rate of this spiral was predicted in reference [133]. These findings will be confirmed in subsection 4.3.3.

Finally, the phase diagram for the microcanonical ensemble in  $D = 5, 6$  is provided in figure 4.11. The solutions with higher entropy  $S$  are thermodynamically preferred over the solutions of lower entropy at the same mass  $M$ . As already discussed in section 4.1.3, we note that the LBH branch is thermodynamically preferred for small masses while the UBS branch supersedes for large masses.

The l.h.s. of figure 4.12 shows the normalized entropy, mass and temperature as a function of the normalized relative tension  $n/n_{GL}$  for the LBH branch in  $D = 10$ . As noted before, the relative tension  $n/n_{GL}$  increases with growing black hole size and a maximum for the mass and entropy is attained, when following the branch into the critical transit region<sup>3</sup>. In contrast to  $D = 5$  and  $D = 6$ , we have no inspiraling behavior when approaching the critical region, which is in agreement with the theoretical predictions of having purely real critical exponents [133].

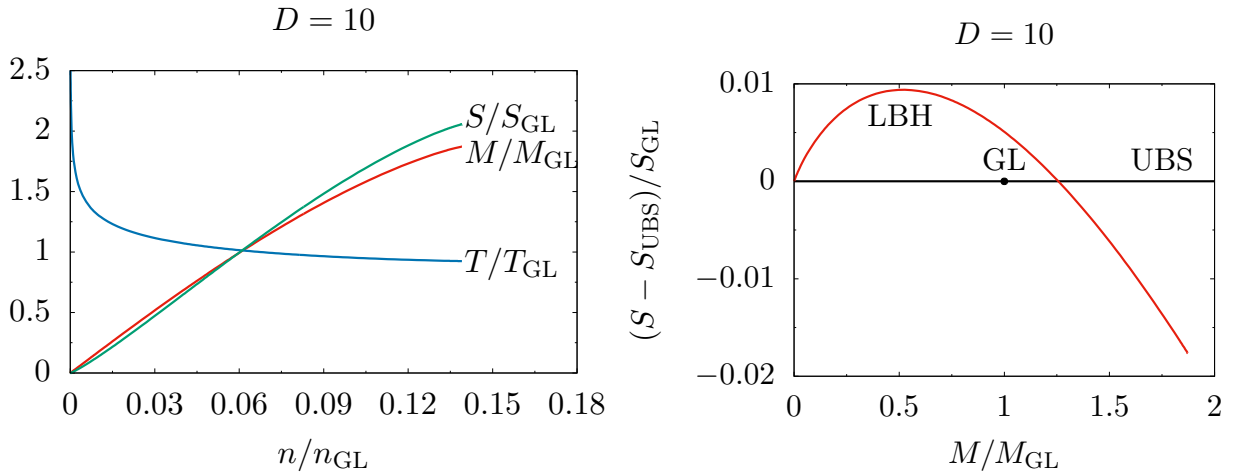


**Figure 4.12:** **Left:** Entropy  $S$  (green), mass  $M$  (red) and temperature  $T$  (blue) as functions of the relative tension  $n$  for the LBH in  $D = 10$ . All quantities are normalized with respect to their corresponding values of a UBS at the GL point. **Right:** Phase diagram of LBHs in the microcanonical ensemble in  $D = 10$ . We plot the difference of the entropy to the corresponding values of the UBS, which is thus represented as the black zero line in these diagrams with the black circle indicating the solution, where the Gregory-Laflamme instability arises. Furthermore, we normalize again with respect to the values of a UBS at the GL point.

The phase diagram for the microcanonical ensemble in  $D = 10$  can be found in the right panel of figure 4.12. As in the lower dimension, the entropy of the LBH is higher than the entropy of a UBS solution with the same mass. Accordingly, LBHs are thermodynamically preferred until a certain threshold value of the mass is reached. Note that reference [59] did already show this picture qualitatively and, moreover, included the non-uniform black string results into the diagram. In ten dimensions the non-uniform black string branch is at no point thermodynamically

<sup>3</sup>The end-point of the data corresponds to  $L_A/L \approx 0.007$ , i.e. the poles of neighboring LBHs are extremely close to the merger.

avored. This changes in higher dimensions, see references [185, 73, 68]. However, we were able to extend the localized black hole solutions much closer to the end point of this branch, where a transition to non-uniform black strings is expected.

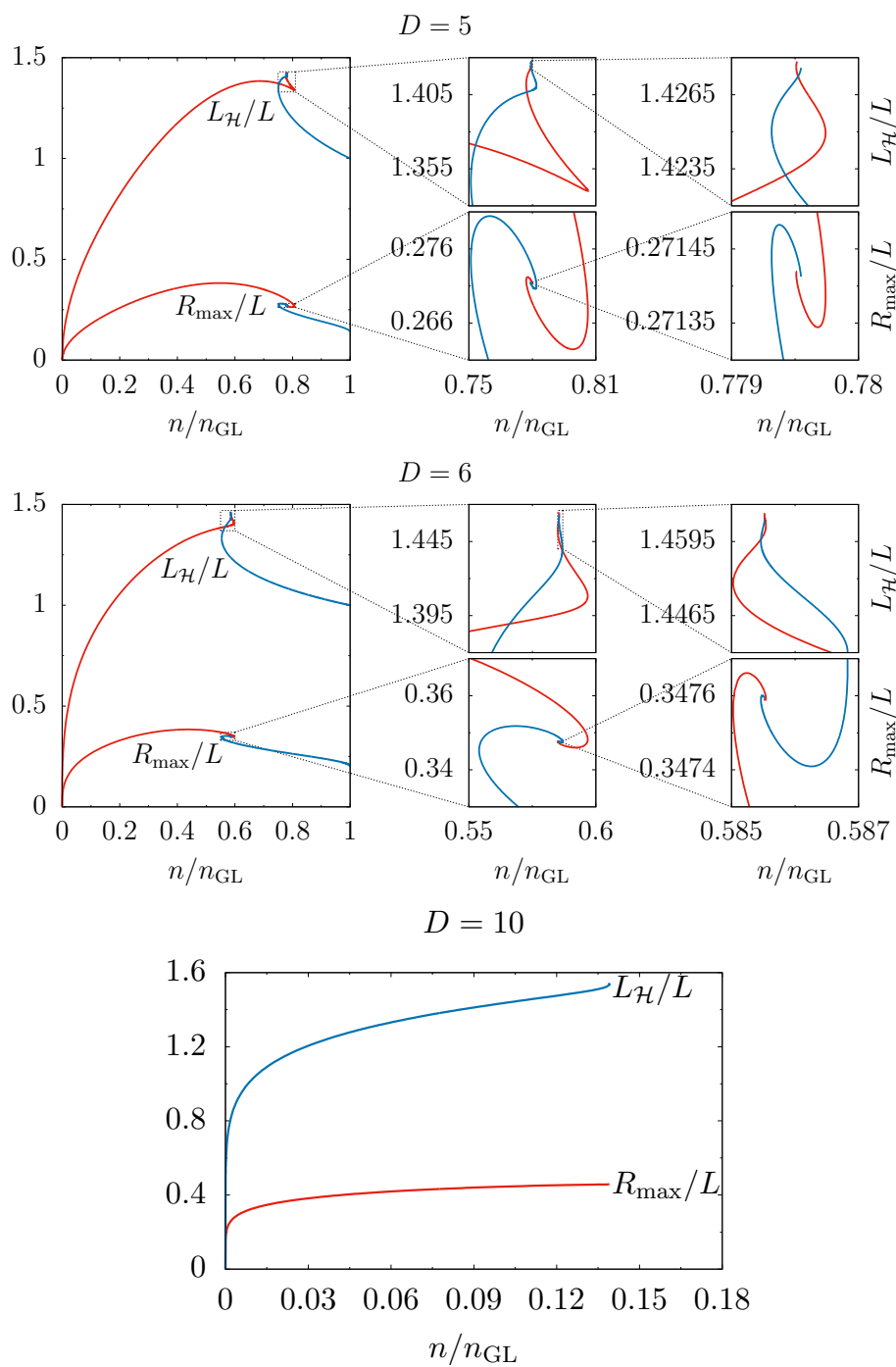


**Figure 4.13:** Proper horizon length  $L_{\mathcal{H}}$  and maximal horizon areal radius  $R_{\max}$  as functions of the relative tension  $n$ . The two upper diagrams correspond to  $D = 5, 6$  and the lower one to  $D = 10$ . For  $D = 5, 6$ , the critical region is magnified in two stages in the center and right columns.



### 4.3.2 Geometry

This section covers a comparison of the geometrical aspects of LBH and NBS solutions close to the transition. Furthermore additional evidence in favor of the double-cone metric is provided.

The maximal horizon areal radius  $R_{max}$  (4.55) and the proper horizon length  $L_{\mathcal{H}}$  (4.56) are plotted versus the normalized relative tension  $n/n_{GL}$  in the two upper diagrams of figure 4.13 for  $D = 5$  and  $D = 6$ . We find the same spiraling behavior for  $R_{max}$  as for the thermodynamic quantities, whereas  $L_{\mathcal{H}}$  approaches a global maximum when moving towards the transition point.

The corresponding geometric quantities for the LBH branch in  $D = 10$  are depicted in the lowest diagram of figure 4.13. Again, the quantities are monotonically growing without additional turning points.

The spatial embeddings of different LBH and NBS horizons are compared in figure 4.14 for  $D = 5$  and  $D = 6$ . The spatial embeddings for the LBH side are computed by employing the relations (4.59) and (4.60). Similar equations can be obtained for the NBS branch (cf. reference [122]). The LBH horizon becomes more and more stretched when approaching the transition point until the poles of neighboring black holes almost touch. A bulge as well a waist region develops in the NBS region when coming closer to the critical point. This waist shrinks subsequently until it is about to pinch off. For  $D = 10$  we cannot compare with the regarding NBS solutions, but a collection of different horizon embeddings can be found in appendix A.2.2.

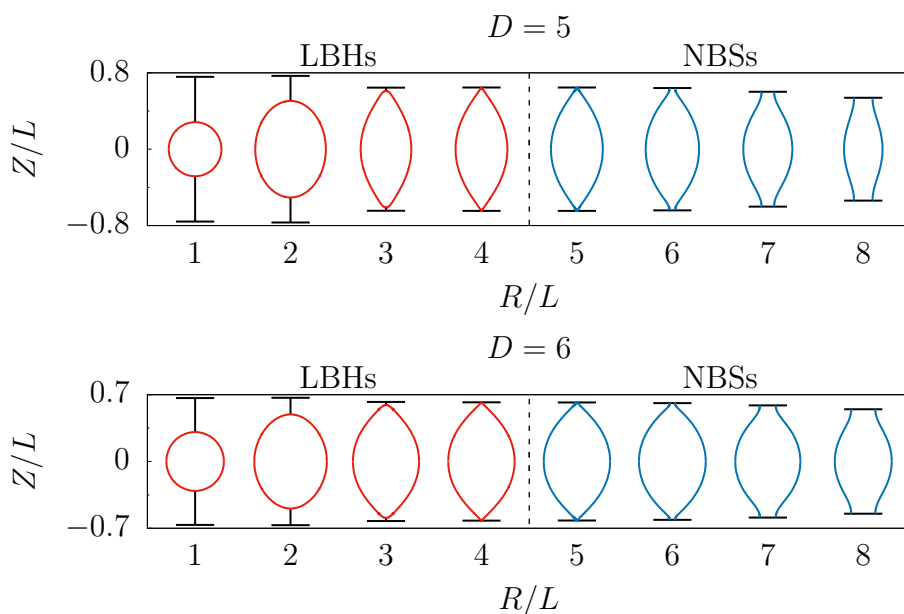


**Figure 4.14:** Spatial embeddings of the horizons of different LBH and NBS solutions for  $D = 5$  and  $D = 6$ .

The upper half of figure 4.15 shows a magnified plot of the periodic boundary together with several LBH and NBS horizon embeddings of configurations close to the transition for  $D = 5, 6$ . The lower half of figure 4.15 shows the corresponding situation for LBH configurations in  $D = 10$ . Furthermore, the horizon embedding corresponding to the double-cone metric (cf. subsection 4.1.5) was added and appears as straight lines with  $D$ -dependent opening angle. We clearly see that the horizon shapes of the LBH (and NBS for  $D = 5, 6$ ) solutions converge to the double-cone horizon, which is a strong qualitative evidence for Kol's conjecture.

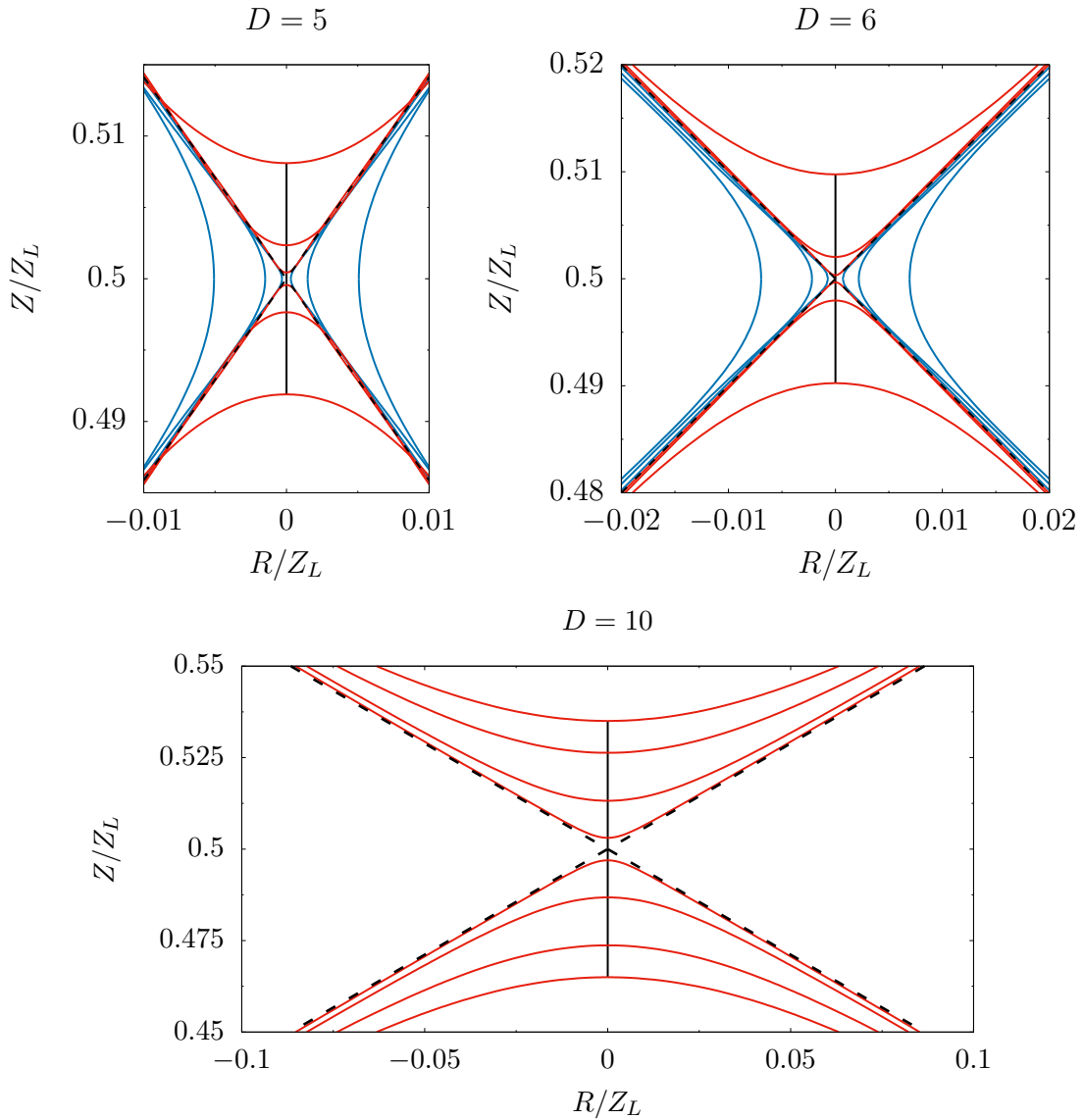


**Figure 4.15:** Magnification of the critical region where the poles of LBHs (red lines) are about to merge and the NBSs (blue lines) are about to pinch-off for  $D = 5$  and  $D = 6$  (upper half), and for  $D = 10$  (lower half, only LBHs). The dashed lines correspond to the double-cone geometry (4.14). The LBH horizons approach the double-cone shape from above/below while the NBS horizons approach it from left/right. The embedding coordinates  $R$  and  $Z$  are normalized by  $Z_L$ , which denotes the length of the compact dimension measured in the coordinate  $Z$ . For the LBH branch, the exposed axis of symmetry is indicated which connects the poles.

### 4.3.3 Critical behavior

It remains to present the results concerning the predicted scaling of physical observables in the critical region (cf. subsection 4.1.5). Since the behavior differs qualitatively between  $D < 10$  and  $D \geq 10$  we have separated the discussion of  $D = 5$  and  $D = 6$  from the corresponding discussion of the  $D = 10$  results. Before investigating the critical scaling of the LBH/NBS, we need to determine appropriate length scales for parameterizing the LBH and NBS branches close to the transition. Such a measure is provided by the proper pole distance  $L_A$  in the LBH case. The minimal horizon areal radius  $R_{min}$  was used in reference [122] for characterizing NBSs close

to the merger. Accordingly, we can define the following dimensionless quantities

$$Q_{LBH} = L_A/L, \quad Q_{NBS} = R_{min}/R_{GL}, \quad (4.61)$$

that are used for the desired parametrization. In (4.61),  $R_{GL}$  denotes the horizon areal radius of a UBS at the GL point. We note, that the parameters  $Q_{LBH}$  and  $Q_{NBS}$  are close to one at the starting point of the regarding branch and tend to zero in the limit of the critical transition.

$D = 5, 6$ : In subsection 4.1.5 we provided the scaling relation of an arbitrary physical quantity  $f$  for  $D < 10$ , which can be written in terms of the above  $Q$ -parametrization

$$f(Q) = f_c + aQ^b \cos(c \log Q + d), \quad (4.62)$$

where  $f_c$  is the value of  $f$  at the critical point ( $Q = 0$ ). The important scaling exponents are identical to  $b$  and  $c$ , which are denoted as real critical exponent and log-periodicity in the following. According to subsection 4.1.5, the predicted values for  $b$  and  $c$  read:

- for  $D = 5$ :  $b_{pred,5} = 3/2$  and  $c_{pred,5} = \sqrt{15}/2 \approx 1.9365$ ,
- for  $D = 6$ :  $b_{pred,6} = c_{pred,6} = 2$ .

The remaining parameters  $a$  and  $d$  differ for each physical quantity and do not have an explicit physical meaning. In the following we analyze the critical scaling for the mass, relative tension, temperature and entropy. A scaling analysis of the proper horizon length is more complicated, since its behavior includes an additional a-priori unknown gauge dependent leading order term. Nevertheless, we have been able to show, that the proper horizon length  $L_{\mathcal{H}}$  exhibits the same oscillatory behavior for  $D = 5$  and  $D = 6$ , whereas we were not able to separate the gauge dependent contribution from the scaling behavior in  $D = 10$ . The analysis of  $L_{\mathcal{H}}$  for  $D = 5$  and  $D = 6$  is provided in appendix A.2.3. Again, the data for the NBS branch was taken from reference [122].

For obtaining the critical exponents  $a$  and  $d$ , the data is fitted with the ansatz (4.62), where we use Mathematica's FindFit routine and treat  $f_c$ ,  $a$ ,  $b$ ,  $c$ ,  $d$  as free parameters. Since all thermodynamic quantities provide a similar picture in the critical region, we provide only the data points and the corresponding fit for the normalized mass  $M/M_{GL}$  in figure 4.16. The exponentially suppressed oscillation can be better observed in the logarithmic scaled plot as shown in the right column of figure 4.16. Only data points of the last cycle were taken for the fit, since larger deviations appear for increasing  $Q$  due to higher order effects. Correspondingly, we see a very good agreement of the data points and the fit for small  $Q$ .

The fit parameters for the mass  $M$ , the relative tension  $n$ , the temperature  $T$  and the entropy  $S$  are all summarized in table 4.1 for the LBH branch. The corresponding fit results for the NBS branch can be found in table A.2 in appendix A.2.3. We see excellent agreement of the fitted values for the real exponent and the log-periodicity  $b$  and  $c$  with the predicted values with deviations of less than 0.5%<sup>4</sup>. In addition, we recognize that all physical quantities yield the same critical exponents for both configurations as expected. Moreover, the critical values  $f_c$  of both branches coincide up to seven significant digits, which corresponds to the best estimation of their actual values so far.

<sup>4</sup>The standard error resulting from the fit of the tabulated values is of the order of the last printed digit.

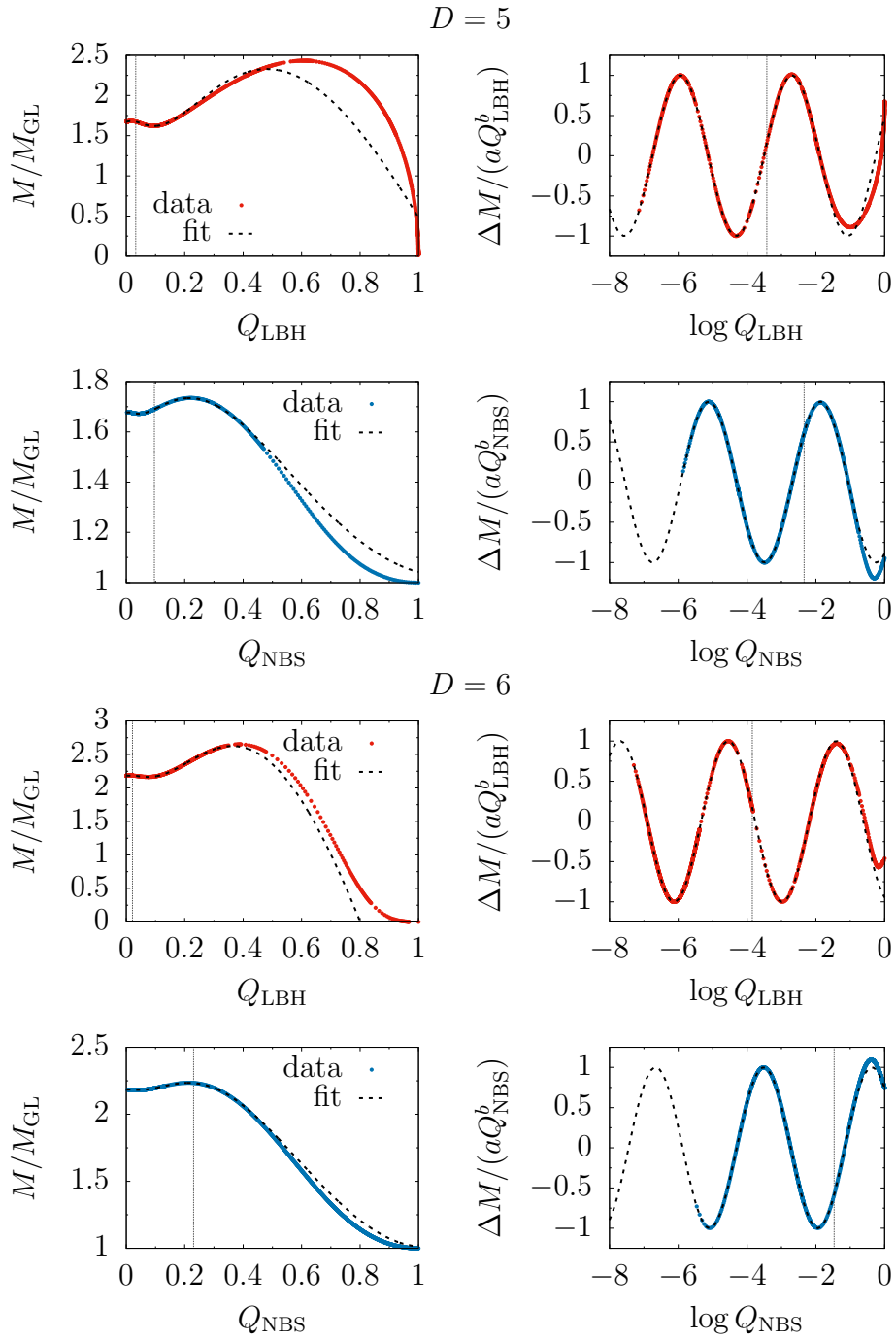


**Figure 4.16:** Data points (red dots for LBHs and blue dots for NBSs) and fit (dashed lines) of the normalized mass  $M/M_{GL}$  as a function of  $Q_{LBH}$  or  $Q_{NBS}$  for  $D = 5$  and  $D = 6$ . The explicit functional dependence is shown in the left column. A rescaled version is shown in the right column to resolve the tiny oscillations of the functions, where  $\Delta M = M/M_{GL} - f_c$  is plotted with a logarithmic rescaling of the abscissa. For each plot, all data points to the left of the dotted vertical line served as input data for the fit.

**Table 4.1:** Parameter values of the fit 4.62 for the thermodynamic quantities of the LBH in  $D = 5$  and  $D = 6$ .

	$f$	$f_c$	$a$	$b$	$c$	$d$
$D = 5$	$M/M_{GL}$	1.6771933	2.4700	1.4997	1.9362	2.0766
	$n/n_{GL}$	0.7795283	0.5762	1.4986	1.9359	4.2842
	$T/T_{GL}$	0.6738645	0.7869	1.4990	1.9367	5.3444
	$S/S_{GL}$	2.6718298	7.3502	1.5001	1.9359	2.0752
$D = 6$	$M/M_{GL}$	2.1839096	4.75319	1.99999	1.99993	5.95517
	$n/n_{GL}$	0.5855194	0.93638	1.99991	1.99994	1.70328
	$T/T_{GL}$	0.7419027	0.65522	1.99991	1.99996	2.92683
	$S/S_{GL}$	3.0961719	9.61169	2.00001	1.99992	5.95511

As an additional result, we are able to answer the question about the existence of LBHs with positive specific heat, raised in reference [104]. In figure 4.10, we recognize that the turning point of the mass does not coincide with the first minimum of the temperature as a function of the relative tension, yielding positive values for  $\partial M/\partial T$  in between. In addition, our data indicates the occurrence of infinitely many regions with positive specific heat due to the inspiraling behavior. This can be seen by recognizing the significant phase shift  $d$  (module  $\pi$ ) between the mass and temperature values in table 4.1 and A.2.

$D = 10$  : The critical behavior in  $D = 10$  differs qualitatively from  $D < 10$ , since there is only a single real valued critical exponent and no oscillation occurs. Accordingly, the data is fitted for the scaling relation (4.20) (cf. subsection 4.1.5)

$$f(Q_{LBH}) = f_c + Q_{LBH}^c (a + b \log Q_{LBH}), \quad (4.63)$$

where  $f_c$  is the value of  $f$  at the critical point ( $Q = 0$ ). For this case, we have only a single scaling exponent  $c$ , which has according to subsection 4.1.5, the predicted value  $c_{pred,10} = 4$ . As before, the remaining parameters  $a$  and  $b$  do not have an explicit physical meaning.

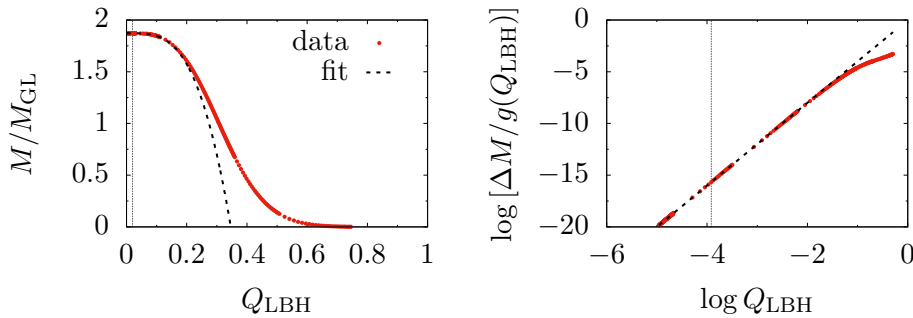


**Figure 4.17:** The left plot shows the rescaled mass  $M/M_{GL}$  as a function of the normalized proper distance between the poles  $Q_{LBH} = L_A/L$ . To illustrate the remarkable agreement of data points and fit, we plot the mass difference  $\Delta M = M/M_{GL} - f_c$  divided by  $g(Q_{LBH}) = a + b \log Q_{LBH}$  versus  $Q_{LBH}$  in a double logarithmic diagram (right). The fit parameters were determined by using all data points to the left of the dotted vertical line (all points with  $Q_{LBH} \lesssim 0.02$ ), which is still a number of 200 data points.

The critical exponent  $c$  is once more obtained by using Mathematica's FindFit routine to fit the data for the mass, relative tension, temperature and entropy. A scaling plot of the normalized mass  $M/M_{GL}$  is available in figure 4.17. As for  $D = 5$  and  $D = 6$ , we obtain a very good agreement of the data points and the fit for small  $Q_{LBH} = L_A/L$ .

Table 4.2 provides the fit parameters for the mass  $M$ , the relative tension  $n$ , the temperature  $T$  and the entropy  $S$ . This time, we obtain an even better agreement with the predicted results, because we have only one critical exponent, i.e. a lower number of fit coefficients. Consequently, this data represents the best estimation of the critical exponent of the LBH branch in  $D = 10$  obtained so far.

**Table 4.2:** Parameter values of the fit 4.63 for the thermodynamic quantities of the LBH in  $D = 10$ .

	$f$	$f_c$	$a$	$b$	$c$
$D = 10$	$M/M_{GL}$	1.87198367	19.50	-104.40	4.0009
	$n/n_{GL}$	0.13911664	-54.76	-43.216	3.9999
	$T/T_{GL}$	0.92615434	-0.4028	8.3508	4.0006
	$S/S_{GL}$	2.05628384	24.47	-131.48	4.0009

The values in tables 4.1-4.2 allow us to perform some consistency checks. As an example, we checked whether the critical values  $f_c$  of the thermodynamic quantities satisfy Smarr's relation, yielding an error bound for  $f_c$  of the order  $10^{-7}$ . There is another consistency check available for the  $D = 5$  and  $D = 6$  data: The first law of black hole thermodynamics, requires the extreme points of mass and entropy to coincide, i.e. the phase shift  $d$  between entropy and mass should be the same. This was verified with deviations of less than 1% (see table 4.1). Additional measures for estimating the accuracy of the obtained data are discussed in appendix A.2.5.

## 4.4 Summary

The main focus of this chapter was the numerical construction of localized black hole solutions in five-, six- and ten-dimensional asymptotically flat Kaluza-Klein gravity with one compact periodic spatial dimension. We utilized pseudo-spectral methods for the solution of the regarding nonlinear partial differential equations, cf. chapter 3. Consequently, a detailed investigation of the LBH solutions close to the critical merger was performed, relying on high-precision numerics and well-prepared coordinate systems combined with domain decomposition.

The thermodynamic quantities associated with the LBHs in five and six dimensions display a spiraling behavior near the transit solution, which matches the observed behavior of the related highly deformed non-uniform black string solutions [122]. The critical exponents, that were obtained by fitting the physical observables of the LBH branch close to the critical region, are in remarkable agreement with the predicted values [132]. This is strong evidence in favor of the double-cone conjecture [132] and was obtained before for the NBS branch [122]. Overall, our data suggests an infinite inspiraling behavior of the LBH and NBS branches in the vicinity of the merger. In addition, the phase shifts associated with the spiraling behavior lead to the formation of an infinite number of tiny phase space regions with positive specific heat.

For ten dimensions we were able to verify the predicted qualitative change of the scaling relations of the physical quantities. Once more, our data shows a very good agreement to the predicted log-polynomial scaling relation predicted by [132]. Accordingly, our results provide strong evidence for the correctness of the the double-cone conjecture also for ten dimensions.

---

# Weyl semimetals

---

The classification of materials according to their electrical conductivity leads traditionally to the categories of insulators, semiconductors and metals. The electrical properties of a condensed matter system are directly related to its possible particle-like excitations. As a result, the collective phenomena in a solid state system can lead to different statistics of the excitations including fermionic, bosonic and even anyonic quasi-particles. Furthermore, condensed matter systems provide the possibility for the realization of exotic quasi-particles, which have not been discovered as elementary particles in nature so far, for example Weyl fermions.

Weyl fermions are massless fermions with a well-defined chirality<sup>1</sup> that were originally considered by Hermann Weyl in 1929 [208] as one of three possible solution classes of the Dirac equation. Due to their properties, Weyl fermions were first confused with neutrinos - a conjecture that had to be rejected with the discovery of the neutrino mass. Despite Weyl fermions have not been observed as fundamental particles in nature, they were recently realized as quasi-particles in a condensed matter system, which was correspondingly denoted as Weyl semimetal (WSM) [112, 127, 148, 215].

The first theoretical studies of condensed matter systems with a close relation to WSMs were carried out by C. Herring in 1937 [105], who studied the effect of band degeneracies in the context of electronic band theory. Subsequently, the chiral anomaly, which plays a major role in the understanding of the special phenomena associated with WSMs, was discussed by Adler, Bell and Jackiw in 1969 [2, 29]. The connection between band touchings in three-dimensional crystals and chiral fermions was further investigated by Nielsen and Ninomiya in 1983 [159], whereas the topological nature of WSMs was discovered in the last years [37, 38, 51, 108, 207, 216, 219].

The goal of this chapter is to investigate the surface states and study the influence of temperature and disorder effects in holographic WSMs, based on [18] and [11]. We start with a brief review of the theory of WSMs in section 5.1. The holographic model of WSMs is introduced in section 5.2. Subsequently, surface states in holographic WSMs are studied in section 5.3. The effects of temperature and weak time-independent disorder in holographic WSMs are considered in section 5.4. We conclude this chapter with a summary of the acquired results in section 5.5.

The contents of this chapter rely on the results published in references [18, 11] and on the unpublished Master thesis of Markus Heinrich.

## 5.1 Theory of Weyl semimetals

WSMs are characterized by special points in the Brillouin zone, where the valence and conduction bands touch at the Fermi energy, which are called Weyl nodes. The corresponding low energy excitations that are localized at the Weyl nodes, behave as massless chiral particles, i.e. Weyl fermions. The Weyl nodes appear only in pairs, such that the number of left-handed and right-handed Weyl fermions are equal, as required by the Nielsen-Ninomiya theorem [159]. The

---

<sup>1</sup>For a massless particle the notion of chirality and helicity agrees, where the latter denotes the projection of the spin along the linear momentum.

existence of these nodes requires either inversion or time reversal symmetry to be broken. In the latter case, Weyl nodes of opposite chirality are separated spatially in the Brillouin zone. A thorough topological analysis of the momentum space shows that Weyl nodes are monopoles of the so-called Berry flux<sup>2</sup> with charge  $\pm 1$  reflecting their chirality. Being topological objects, Weyl nodes are stable under moderate perturbations, such as interactions with external fields. As in topological insulators, WSMs show additional states localized at boundaries between phases of different topology, e.g. surface states. The corresponding surface states of WSMs form so-called Fermi arcs [207], which connect the projections of the Weyl nodes onto the surface Brillouin zone.

The transport properties of WSMs exhibit exotic features such as an anomalous Hall effect, the chiral magnetic effect and a negative magnetoresistance. An effective quantum field theoretic description relates these effects to the so-called chiral anomaly, which originates from the breaking of a classical symmetry in the process of quantization [2, 29]. Moreover, it was predicted that lattice deformations couple to the fermionic low-energy excitations with different signs, giving rise to effective axial gauge fields [49, 48]. Such lattice deformations naturally arise at the surfaces of a WSM, inducing localized axial magnetic fields in their vicinity. Moreover, it was shown that the Fermi arcs can be understood from this perspective as zeroth Landau levels generated by these fields [44].

We emphasize that a description in terms of band theory and correlation functions can not be applied in the strong coupling regime. Nevertheless, band theory can help us to obtain an effective picture of the involved processes for building our strong coupling ansatz.

### 5.1.1 Weyl nodes and transport properties

As mentioned above, in a (three-dimensional) WSM two non-degenerate bands touch exactly at the Fermi energy  $\epsilon_F$ , which marks the location of the Weyl node points in the Brillouin zone. We restrict the discussion here to band touchings in three spatial dimensions, because the complex Dirac spinor representation is only reducible into two complex Weyl spinors for an even total number of dimensions  $D = d + 1$  (i.e. odd number of spatial dimension). Accordingly, we can only have Weyl fermionic excitations in  $d = 1$  or  $d = 3$ , where the one-dimensional case is rather trivial compared to  $d = 3$ .

The non-degeneracy of the two bands, which is necessary for the stability of the configuration, requires the breaking of either time-reversal or inversion symmetry due to Kramers theorem (see for instance [181]). The aforementioned Nielsen-Ninomiya theorem then leads to the chirality pairing of the nodes in the Brillouin zone. Figure 5.1 provides a schematic view of a pair of Weyl nodes at Fermi energy in the energy band structure.

WSMs can be categorized into two classes according to the shapes of their Fermi surfaces, i.e. the section of the Fermi energy level  $\epsilon_F$  with the energy bands. WSMs with point like Fermi surfaces are assigned to type-I, while extended Fermi surfaces are a property of type-II WSMs. The latter exhibit different effects, such as direction dependent conductivity. We restrict ourselves to type-I WSMs in three spatial dimensions in the scope of this thesis.

---

<sup>2</sup>The Berry flux or Berry connection denotes a  $U(1)$  gauge field arising from a geometric description of the momentum space topology. A good review on this topic is provided by [157].



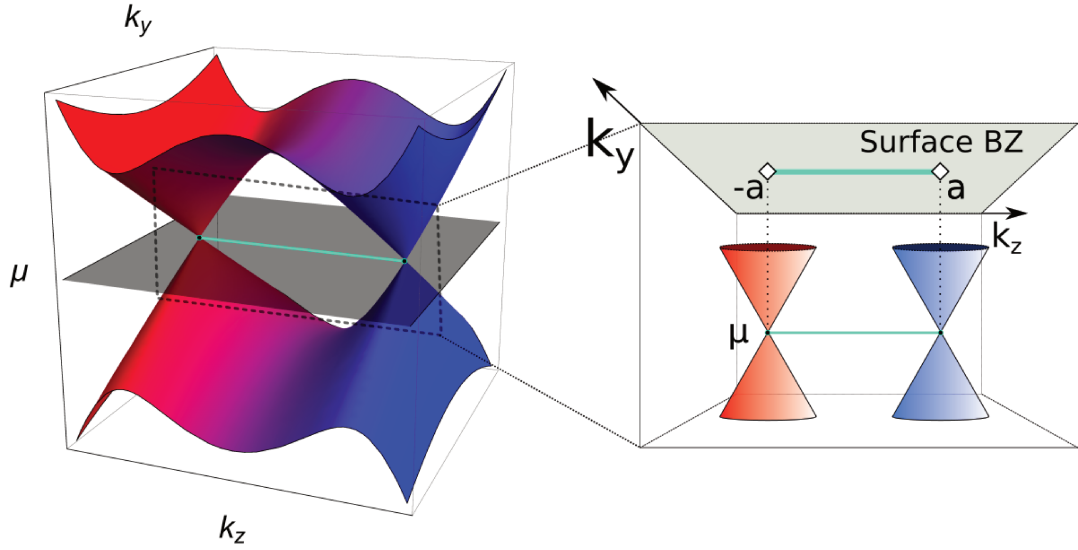


**Figure 5.1:** **Left:** Schematic diagram of the type-I WSM energy band structure at the Fermi level  $\mu$  including a pair of Weyl nodes with opposite chiralities, separated by a distance of  $2a$  in the  $z$ -direction of the Brillouin zone (BZ). **Right:** The magnified plot reveals the conic-structure of the energy bands at the Weyl nodes. Furthermore, we show the projection of the Weyl nodes to the surface BZ, resulting in surface states that are connected by Fermi arcs (thick cyan line).

Expanding the restriction of the Bloch-Hamiltonian  $H(\vec{k})$  to the two-dimensional subspace spanned by valence and conduction states around a single Weyl node at  $\vec{k} = \vec{k}_0$  yields to first order

$$H_{Weyl}(\vec{k}) = E(\vec{k}_0)\sigma_0 + \sum_{i=1}^3 \vec{v}_i \cdot (\vec{k}_0 - \vec{k})\sigma_i + \mathcal{O}\left[(\vec{k}_0 - \vec{k})^2\right], \quad (5.1)$$

here  $\sigma_i$  are the Pauli matrices and  $\sigma_0$  is the identity. The zeroth order term in the Weyl Hamiltonian (5.1) is identified with the Fermi energy  $E(\vec{k}_0) = \epsilon_F$  and we note that the two energy bands have locally the form of a double cone centered at  $\vec{k}_0$ , where the vectors  $\vec{v}_i$  determine the slope of the cone (figure 5.1). As expected, low-energy excitations around the Weyl node at  $\vec{k} = \vec{k}_0$  behave as Weyl fermions with chirality  $\chi = \text{sgn det}(v_{ij}) \in \{\pm 1\}$  as a result of the local form of (5.1). We further note that small perturbations of the Weyl Hamiltonian are not able to alter its overall shape, since they can also be expanded in terms of Pauli matrices and  $\sigma_0$ , which span the space of  $2 \times 2$  matrices. As a result Weyl nodes are comparatively stable under perturbations and can only be destroyed by annihilation with a node of opposite chirality, breaking the translational invariance, or by breaking charge conservation.

It is known from topological band theory, that gapless edge states emerge at the interface between two topologically distinct insulators, since a change of topology is accompanied by closing the band gap.<sup>3</sup> Considering interfaces of WSMs corresponds to considering two-dimensional slices in the three-dimensional Brillouin zone, where slices that do not contain a Weyl node correspond to an two-dimensional insulator. Surprisingly, also WSMs exhibit surface states, the

<sup>3</sup>To be more explicit, the Chern number of an insulator can only be changed by closing the band gap.

so-called Fermi arcs. In contrast to ordinary topological insulators, the surface states of WSMs form no closed curves in the corresponding surface Brillouin zone, but appear as segments connecting to projections of the Weyl nodes.

In the remainder of this subsection we give a short phenomenological overview about two important transport effects in WSMs: the anomalous Hall effect and the negative magnetoresistance. First we recall that every two-dimensional slice in the Brillouin zone that does not contain a Weyl node corresponds to a topological insulator. We consider a pair of Weyl nodes with different chirality that are spatially separated in momentum space by a three-vector  $\vec{a}$ , then every two-dimensional insulator between the nodes shows an anomalous Hall effect in the presence of an external electric field  $\vec{E}$  with the current  $\vec{j}$  proportional to

$$\vec{j} \propto \vec{a} \times \vec{E}. \quad (5.2)$$

We note that this effect only occurs between nodes of different chirality that are spatially separated.

Moreover, in the presence of external magnetic and electric fields,  $\vec{B}$  and  $\vec{E}$ , the spectrum around each Weyl node disperses depending on its chirality in the direction of the  $\vec{B}$  field. For parallel  $\vec{B}$  and  $\vec{E}$  fields, the effect leads to a current proportional to

$$\vec{j} \propto \vec{E} \cdot \vec{B}, \quad (5.3)$$

which is proportional to  $\vec{B}$  and therefore denoted as negative magneto resistance. This effect can be explained as the result of an equalizing current due to a chiral charge imbalance induced by  $\vec{B}$  and  $\vec{E}$  between Weyl nodes of different chirality [159].

The next subsections are devoted to the introduction of an effective quantum field theoretic model as a tool for understanding the transport properties of WSMs on a quantitative level.

### 5.1.2 The chiral anomaly

In the last subsection we saw that the low-energy excitations around Weyl nodes have the properties of localized Weyl fermions, which implies that the fundamental dynamics of WSMs can be described in terms of a low-energy field theory. Before providing a quantum field theoretic model for WSMs, we first give a short review of the chiral anomaly in quantum field theory, since the latter plays a major role for the transport characteristics of WSMs.

#### The chiral anomaly in the presence of external vector fields

A quantum anomaly originates from the breaking of a classical symmetry in the process of quantization. We start by considering the Dirac Lagrangian describing a fermion with mass  $M$  in  $3 + 1$  dimensions, which is coupled to an external  $U(1)$  gauge field  $\mathcal{V}_\mu$

$$\mathcal{L}_D = \bar{\psi} (i\not{\partial} - \not{\mathcal{V}} + M) \psi, \quad (5.4)$$

where  $\psi$  is a 4-component Dirac spinor and the Feynman slash notation was employed, i.e.  $\not{\mathcal{V}} = \gamma^\mu \mathcal{V}_\mu$  with the  $4 \times 4$  gamma matrices  $\{\gamma^\mu\}_{\mu=0,\dots,3}$  and  $\bar{\psi} = \psi^\dagger \gamma^0$  with the adjoint spinor  $\psi^\dagger$ .

As a matter of fact,  $\mathcal{L}_D$  is invariant under a chiral  $U(1)$  transformation, acting on the spinors as follows

$$\psi \mapsto e^{i\theta(x)\gamma^5} \psi, \quad (5.5)$$

where  $\gamma^5 = i\gamma^0\gamma^1\gamma^2\gamma^3$  is the chirality operator and  $\theta(x)$  is a real function of the coordinates  $x$ . Every symmetry of the classical Lagrangian is associated with a classical conserved Noether current. Accordingly, we find for the classical chiral symmetry the chiral current  $j_5^\mu = \bar{\psi}\gamma^\mu\gamma^5\psi$ , which satisfies

$$*d * j_5 = 2iM\bar{\psi}\gamma^5\psi, \quad (5.6)$$

where  $*$  is the Hodge operator and  $d$  denotes the exterior derivative. The conservation law (5.6) fails to be valid after quantization, as pointed out by Adler, Bell and Jackiw in 1969 [2, 29], which marks the first discovery of a quantum anomaly.

A deeper understanding of quantum anomalies can be obtained by considering the Euclidean path integral of the action functional  $S[\psi]$

$$Z = \int D\psi D\bar{\psi} e^{-S[\psi]}. \quad (5.7)$$

Correspondingly, a quantum anomaly corresponds to the missing invariance of the path integral measure under the symmetry transformation, while the action remains symmetric. We need to include an additional Jacobian  $\mathcal{J}[\theta]$  resulting from the gauge transformation (5.6) into the path integral, yielding

$$\int D\psi D\bar{\psi} e^{-S[\psi]} \mapsto \int D\psi D\bar{\psi} \mathcal{J}[\theta] e^{-S[\psi]}, \quad (5.8)$$

where all gauge invariant regularization schemes lead to the following form of the Jacobian (cf. references [30, 78])

$$\mathcal{J}[\theta] = \exp \left[ \int \theta(x) \frac{i}{4\pi^2} \mathcal{G} \wedge \mathcal{G} \right]. \quad (5.9)$$

In (5.9),  $\mathcal{G} = d\mathcal{V}$  denotes the field strength of the external electromagnetic field. As a result, the Ward identity for the chiral current is adapted as follows

$$d * j_5 = \frac{1}{4\pi^2} \mathcal{G} \wedge \mathcal{G} - * (2iM\bar{\psi}\gamma^5\psi), \quad (5.10)$$

where the manifestly covariant term  $\mathcal{G} \wedge \mathcal{G}$  is called the chiral anomaly.

### The chiral anomaly in the presence of an external axial field

After having covered the basics of the chiral anomaly in the preceding subsection, we extend the discussion to the chiral anomaly in the presence of an external axial field, which is important in the context of WSMs. For describing massless Weyl fermions, the following Lagrangian is considered

$$\mathcal{L}_W = \bar{\psi} (i\not{\partial} - \not{\mathcal{A}} - \mathcal{A}\gamma^5) \psi, \quad (5.11)$$

where  $\mathcal{V}$  is an external  $U(1)$  gauge field and the role of the axial  $U(1)$  gauge field  $\mathcal{A}$  is clarified in the next subsection. As a result, we note that  $\mathcal{L}_W$  exhibits a  $U(1)_V \times U(1)_A$  gauge symmetry related to the two gauge fields. Accordingly, we transform (5.11) to the Weyl representation by projecting on the eigenspaces of  $\gamma^5$  to make the description in terms of chiral Weyl fermions manifest. The regarding projectors read

$$P_{\pm} = \frac{1}{2} (\text{id} \pm \gamma^5). \quad (5.12)$$

By defining the following Weyl spinors and chiral gauge fields

$$\psi_{\pm} = P_{\pm} \psi \quad \text{with} \quad \gamma^5 \psi_{\pm} = \pm \psi_{\pm}, \quad (5.13)$$

$$A^{\pm} = \mathcal{V} \pm \mathcal{A}, \quad (5.14)$$

we can decompose the Lagrangian  $\mathcal{L}_W$  into a left-handed and a right-handed part

$$\mathcal{L}_W = \bar{\psi}_+ (i\not{\partial} - \not{A}^+) \psi_+ + \bar{\psi}_- (i\not{\partial} - \not{A}^-) \psi_-, \quad (5.15)$$

with an explicit  $U(1)_+ \times U(1)_-$  chiral gauge symmetry.

Consequently, each of the chiral fields  $A^{\pm}$  gives rise to a chiral anomaly (cf. [30]) and we can employ our results from the previous paragraph, namely equation (5.10), yielding for the divergence of the axial current  $j_A = \bar{\psi} \gamma^{\mu} \gamma^5 \psi$

$$\begin{aligned} d * j_A &= \frac{1}{8\pi^2} (F^+ \wedge F^+ + F^- \wedge F^-), \\ &= \frac{1}{4\pi^2} (\mathcal{F} \wedge \mathcal{F} + \mathcal{G} \wedge \mathcal{G}), \end{aligned} \quad (5.16)$$

where  $F^{\pm} = dA^{\pm}$  are the chiral field strengths and  $\mathcal{F} = d\mathcal{A}$  together with  $\mathcal{G} = d\mathcal{V}$  are the field strengths of the original fields. In addition, also the vector current  $j_V = \bar{\psi} \gamma^{\mu} \psi$  becomes anomalous

$$\begin{aligned} d * j_V &= \frac{1}{8\pi^2} (F^+ \wedge F^+ - F^- \wedge F^-), \\ &= \frac{1}{2\pi^2} \mathcal{F} \wedge \mathcal{G}. \end{aligned} \quad (5.17)$$

The anomaly of the vector current in the presence of the axial field is denoted as axial or chiral gauge anomaly.

The previous result (5.17) leads to a violation of charge conservation, when the vector gauge field  $\mathcal{V}$  is identified with the usual electromagnetic gauge field and the corresponding current  $j_V$  with the electromagnetic current. This problem, which is caused by the underlying regularization scheme, can be cured by adding the following finite, topological counter term to the effective action (cf. reference [27])

$$S_B = -\frac{1}{4\pi^2} \int \mathcal{V} \wedge \mathcal{A} \wedge \mathcal{F}. \quad (5.18)$$

Including (5.18) leads to the modified Ward identities

$$d * j_V = 0, \quad (5.19)$$

$$d * j_A = \frac{1}{4\pi^2} (3\mathcal{F} \wedge \mathcal{F} + \mathcal{G} \wedge \mathcal{G}). \quad (5.20)$$

A low energy quantum field theoretic model of WSMs based on the discussion of the chiral anomaly is considered in the following subsection.

### 5.1.3 An effective quantum field model of Weyl semimetals

We present the effective quantum theoretical model of the low-energy excitations of a WSM in two stages. First, we consider a minimal model, that introduces a splitting of left- and right-handed spinors in momentum space by a constant three-dimensional vector  $2\vec{a}$ , defined by the following Lagrangian

$$\mathcal{L}_{WSM,1} = \bar{\psi} (i\not{\partial} - \not{\mathcal{A}} - \not{a}\gamma^5) \psi, \quad (5.21)$$

where  $\mathbf{a} = (a^0, \vec{a})$  is a constant 4-vector. Figure 5.2 shows the separation of the anti-chiral spinors in the spectrum, where a non-zero  $a^0$  component of the 4-vector  $\mathbf{a}$  introduces an additional shift in the energy direction. The component  $a^0$  is set to zero within our WSM model.

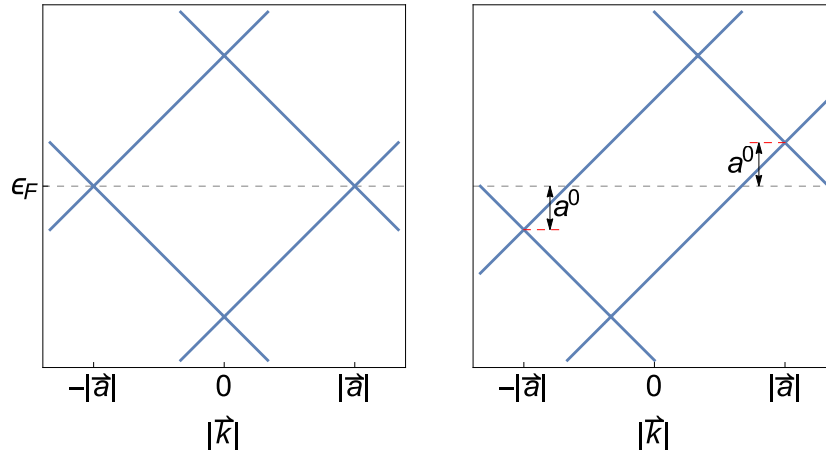


**Figure 5.2:** Spectrum of the WSM Hamiltonian obtained from Lagrangian (5.21) in the direction of  $\vec{a}$  for  $a^0 = 0$  (left) and  $a^0 > 0$  (right).

Consequently, we can give an interpretation of the axial  $U(1)$  gauge field  $\mathcal{A}$ , which was introduced in subsection 5.1.2. A non-constant  $\mathcal{A}$  can be interpreted as spatial variations of the Weyl node distance. Strain in solid crystals is one possible source of such axial gauge fields, which was confirmed for graphene [92] and recently studied for WSMs [48, 169].

The study of linear transport properties in WSMs relies on investigating the linear response of the vector current  $j_V$  due to external fields. The microscopic computation of the regarding conductivities involves the evaluation of retarded 2-point functions of the underlying current operators. The details of this analysis are out of the scope of this thesis, but a good review on this topic can be found in reference [12]. When assuming the more general case of a non-constant axial gauge field  $\mathcal{A}$ , it turns out that the axial anomaly gives rise to new transport properties - this is what we call anomalous transport. When considering external electric and magnetic fields,

$\vec{E}$  and  $\vec{B}$ , we find the following expectation value of the current density (cf. reference [143])

$$\langle j_V \rangle = \frac{1}{2\pi^2} \left( \vec{\mathcal{A}} \times \vec{E} + \mu_5 \vec{B} + \mu \vec{B}_5 \right), \quad (5.22)$$

where  $\vec{\mathcal{A}}$  are the spatial components of the 4-vector  $\mathcal{A}$ ,  $\mu$  and  $\mu_5$  are the chemical potentials associated with the symmetry charges of  $U(1)_V$  and  $U(1)_A$ . The first term in (5.22) is perpendicular to  $\vec{E}$  and therefore denoted as anomalous Hall effect (AHE). The next contribution, which is proportional to  $\mu_5$ , is the chiral magnetic effect (CME). It gives a current contribution parallel to the applied magnetic field and only occurs in the presence of a chiral charge imbalance. As mentioned in subsection 5.1.1, parallel  $\vec{E}$  and  $\vec{B}$  fields induce such an imbalance, where the CME contribution becomes proportional to  $\vec{E} \cdot \vec{B}$ . Thus, the CME can be thought of as the origin of the negative magnetoresistance in WSMs. The last term  $\mu \vec{B}_5$  is the so-called chiral pseudo-magnetic effect (CPME, [195]). The CPME does not require a chiral charge imbalance and hence should be observable in equilibrium.

The simple model (5.21) can reproduce the basic properties of a WSM, namely gapless metallic phases. The next step is to consider a slightly more complicated model, that is also able to describe the aforementioned two-dimensional insulating phases between the Weyl nodes. The corresponding model is obtained by adding an additional mass term  $\bar{\psi} M \psi$  to the Lagrangian (5.21), giving

$$\mathcal{L}_{WSM,2} = \bar{\psi} (i\cancel{\partial} - \cancel{\mathcal{N}} - \cancel{\alpha}\gamma^5 + M) \psi. \quad (5.23)$$

References [87, 88] show that the Lagrangian (5.23) emerges from a low-energy ansatz of lattice Hamiltonians for WSMs, which confirms the approach. As we saw already in the previous subsection 5.1.2, a mass term breaks the axial  $U(1)_A$  gauge symmetry explicitly by introducing an additional contribution  $M\bar{\psi}\gamma^5\psi$  on the right hand side of the Ward identity. The modification of the Lagrangian leads to the emergence of two different phases depending on the ratio  $\vec{a}^2/M^2$ , which are depicted in figure 5.3.

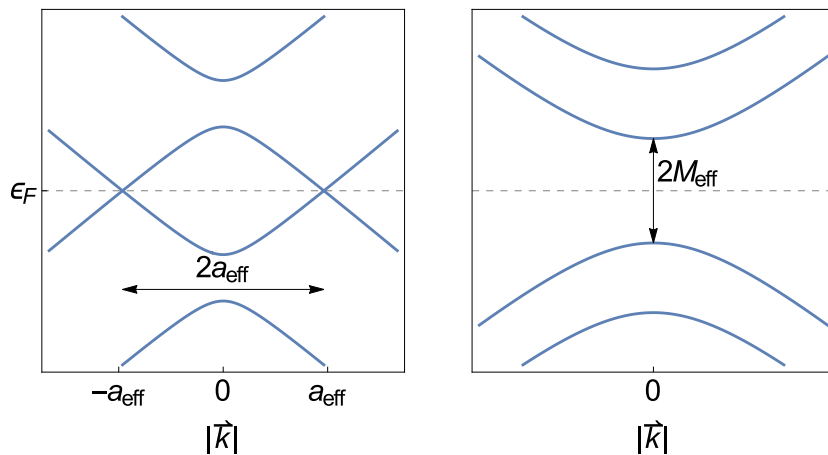


**Figure 5.3:** Spectrum of the WSM Hamiltonian obtained from Lagrangian (5.23) in the direction of  $\vec{a}$ . For  $\vec{a}^2 > M^2$  (left) two Weyl nodes in a distance of  $2a_{\text{eff}} = 2\sqrt{a^2 - M^2}$  appear while for  $\vec{a}^2 < M^2$  (right) the spectrum is gapped with band gap  $2M_{\text{eff}} = 2\sqrt{M^2 - a^2}$ .

**Phase I:** A system with ungapped spectrum is obtained for  $\vec{a}^2 > M^2$  where the Weyl nodes are separated by the distance  $2\sqrt{\vec{a}^2 - M^2}$  in momentum space (for  $a^0 = 0$ ). Close to the Weyl nodes, the spectrum agrees with that of the simple Lagrangian (5.21), where the axial vector  $\mathbf{a}$  is modified to an effective axial vector  $\mathbf{a}_{\text{eff}}$

$$\mathcal{L}_{WSM,\text{eff},I} = \bar{\psi} (i\not{\partial} - \not{\mathcal{V}} - \not{a}_{\text{eff}}\gamma^5) \psi, \quad (5.24)$$

with  $\vec{a}_{\text{eff}} = \vec{a}\sqrt{\vec{a}^2 - M^2}/|\vec{a}|$  and  $a_{\text{eff}}^0 = 0$ . Away from the Weyl nodes, the mass term leads to significant differences in the effective description (5.24), since the latter exhibits an additional band inversion (figure 5.2) that is avoided for the full Lagrangian (5.23) (figure 5.3).

**Phase II:** For  $\vec{a}^2 < M^2$  we obtain a gapped system (figure 5.3) and an effective description in terms of massive Dirac fermions can be applied, leading to the effective Lagrangian

$$\mathcal{L}_{WSM,\text{eff},II} = \bar{\psi} (i\not{\partial} - \not{\mathcal{V}} + M_{\text{eff}}) \psi, \quad (5.25)$$

where  $M_{\text{eff}} = \sqrt{M^2 - \vec{a}^2}$ .

It is important to note that the Lagrangian (5.23) gives rise to a Lorentz-breaking model because of the preferred direction, which is defined by the constant 4-vector  $\mathbf{a}$ . Similar models have been considered as Lorentz-breaking extensions of QED (cf. reference [114]) and are particularly interesting, because they can be realized effectively in condensed matter physics, which makes tests of theoretical predictions possible. Accordingly, the vector gauge field contribution to the one-loop effective action was examined by [165], implying the following form of the anomalous Hall term of the current 1-point function

$$\langle \vec{j}_V \rangle = \sigma_{\text{AHE}} \vec{a} \times \vec{E} / |\vec{a}|, \quad (5.26)$$

where the conductivity  $\sigma_{\text{AHE}}$  reads

$$\sigma_{\text{AHE}} = |\vec{a}| \begin{cases} C & \text{for } \vec{a}^2 < M^2, \\ C - \frac{1}{2\pi^2} \sqrt{1 - \frac{M^2}{\vec{a}^2}} & \text{for } \vec{a}^2 \geq M^2. \end{cases} \quad (5.27)$$

According to [87], the constant  $C$  should vanish for WSMs, since the trivial phase II is insulating. As a result, the mass term leads to the replacement  $\vec{a} \mapsto \vec{a}_{\text{eff,weak}} = \vec{a}\sqrt{\vec{a}^2 - M^2}/|\vec{a}|$  in the AHE contribution to (5.22) for  $\vec{a}^2 \geq M^2$  and to  $\sigma_{\text{AHE}} = 0$  otherwise, which is in full alignment with our previous discussion of the two phases. We note, that the presence of the anomalous Hall effect can be used as an order parameter of the phase transition from phase II to phase I, since it occurs only in the latter one. Thus, an evident control parameter of the transition is given by  $|\vec{a}|/M$ .

### Quantum phase transition

We remark, that the previous discussion is an example of a so-called quantum phase transition (QPT) [178, 196]. A QPT is induced by quantum fluctuations, in contrast to classical phase transitions, which are driven by thermal fluctuations of the physical system. Consequently, quantum phase transitions occur at zero temperature  $T = 0$  at a precise critical value of an external parameter  $g = g_c$ , i.e. the quantum critical point (QCP). Despite an absolute zero temperature is clearly physically not realizable, the consequences of the QPT extend to a finite temperature region near the critical point, known as quantum critical region (QCR) (see figure 5.4). More in-

terestingly, inside the QCR, the critical nature of the system manifests itself in unconventional but universal physical behaviors such as the linear temperature scaling of the resistivity in strange metals [36]. In recent years QPTs have attracted the interest of many researchers, especially in the condensed matter community, where more and more examples are being discovered: From exotic magnetism, to high- $T_c$  superconductivity and metal-insulator transitions. Quantum phase transitions still represent a big scientific challenge and robust and controllable theoretical models are still under investigation [201].

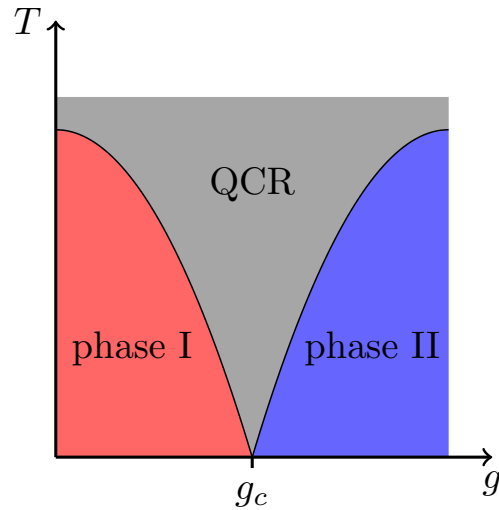


**Figure 5.4:** Sketch of the phase diagram as a function of the temperature  $T$  and an external non-thermal parameter  $g$ . The quantum phase transition between the two phases happens at  $g = g_c$  and  $T = 0$  but it affects the physics of the system on a larger region extending towards the finite temperature regime, i.e. the QCR (gray area).



## 5.2 Holographic model of Weyl semimetals

A holographic model of the quantum field theoretic description of the last section was recently presented in [140, 142]. The present section is devoted to a review of this gauge/gravity dual construction by employing the basics about the AdS/CFT duality that were provided in section 2.3 of chapter 2.

### 5.2.1 The holographic action

The holographic model of the WSM system should be built according to the structure of the QFT Lagrangian (5.23), such that observables on the QFT side can be related to the boundary asymptotics of the classical supergravity model. Therefore, two gauge fields  $V$  and  $A$  are needed for the  $U(1)_V \times U(1)_A$  symmetry. To be precise, the vector gauge field  $V$  is dual to the vector current operator  $j_V^\mu = \bar{\psi}\gamma^\mu\psi$ , while the axial gauge field  $A$  is dual to the axial current operator  $j_V^\mu = \bar{\psi}\gamma^\mu\gamma^5\psi$ . Moreover, a  $U(1)_A$  symmetry breaking mass term, i.e. the operator  $\bar{\psi}\psi$ , is required, which is implemented in terms of a dual massive scalar field  $\phi$  on the gravity side. An additional term similar to the topological counter term (5.18) is necessary for obtaining a non-anomalous vector current, while ensuring the proper Ward identity for the axial current. Consequently, a holographic action obeying these requirements can be obtained, as shown by [117, 140, 142]:

$$S_{AdS} = \frac{1}{2\kappa^2} \int d^5x \sqrt{-g} \left( R + \frac{12}{l_{AdS}^2} \right) + \int d^5x \sqrt{-g} \left( \|D\phi\|^2 - m^2\phi^2 \right) + \frac{1}{2} \int d^5x (F \wedge *F + G \wedge *G) - \frac{2\alpha}{3} \int d^5x A \wedge (3F \wedge F + G \wedge G), \quad (5.28)$$

where  $g$  is the determinant of the metric,  $\kappa = 8\pi G_5$  is the Einstein constant in five dimensions,  $R$  is the Ricci scalar and  $l_{AdS}$  is the AdS radius. Furthermore,  $F = dV$  and  $G = dA$  are the field strengths of the aforementioned gauge fields. The first term is the Einstein-Hilbert action with the corresponding cosmological contribution for  $AdS_5$ . The second term includes a dynamic complex scalar field  $\phi$ , whose boundary value sources the  $U(1)_A$  breaking mass term of the QFT Lagrangian. To accomplish this,  $\phi$  needs to be charged under the axial gauge symmetry with the covariant derivative  $D_\mu = \nabla_\mu - iqA_\mu$  and its mass  $m$  has to be chosen such that the conformal dimension of  $\bar{\psi}\psi$  is  $\Delta_{\bar{\psi}\psi} = 3$ , leading to the condition  $m^2 l_{AdS}^2 = -3$ . The third term is simply the kinetic contribution for the gauge fields  $V$  and  $A$ . The last contribution is a topological Chern-Simons term, which represents the unique choice for removing the anomaly from the vector current  $j_V$  and giving the proper form of the axial anomaly.

The integrals appearing in the action (5.28) are not finite therefore an adequate holographic analysis requires a prior regularization procedure. Appropriate counterterms that are made for canceling the divergences were provided in the references [192, 12]. The regarding contributions are

$$S_{ct} = \frac{1}{\kappa^2} \int_{\rho=\epsilon} d^4x \sqrt{-\gamma} \left( K - \frac{3}{l_{AdS}} \right) + \frac{1}{2} \int_{\rho=\epsilon} d^4x \sqrt{-\gamma} \left( \phi^2 - \frac{1}{2} \log(\rho) \phi \square_\gamma \phi \right) + \frac{1}{4} \int_{\rho=\epsilon} d^4x \sqrt{-\gamma} \log(\rho) \left( F_{ab} F^{ab} + G_{ab} G^{ab} \right), \quad (5.29)$$

where  $\rho$  is the holographic coordinate providing a distance measure from the holographic bound-

ary (cf. section 2.2.1),  $\gamma$  is the induced metric on the hypersurface  $\rho = \varepsilon$ ,  $\square_\gamma$  is the d'Alembert operator with respect to  $\gamma$  and  $K$  is the related intrinsic curvature. The first integral is due to Hawking-Gibbons [81] together with an AdS-specific contribution. The remaining terms are related to the scalar field and the two gauge fields. We recognize that the Chern-Simons term does not contribute to the counter action, since it is subleading compared to the other gauge field terms close to the conformal boundary.

The following gauge field currents can be obtained by varying the on-shell action without taking the Chern-Simons terms into account

$$\langle j_V^\mu \rangle_{cons} = \lim_{\rho \rightarrow 0} \sqrt{-g} \left( F^{4\mu} - 4\alpha \varepsilon^{4\mu\nu\sigma\kappa} A_\nu F_{\sigma\kappa} \right), \quad (5.30)$$

$$\langle j_A^\mu \rangle_{cons} = \lim_{\rho \rightarrow 0} \sqrt{-g} \left( G^{4\mu} - \frac{4\alpha}{3} \varepsilon^{4\mu\nu\sigma\kappa} A_\nu G_{\sigma\kappa} \right), \quad (5.31)$$

where we remind the reader that  $x^4 = \rho$  in our convention. The currents (5.30)-(5.31) are denoted as consistent currents. As expected, the vector current (5.30) is anomalous. The non-anomalous current  $j_V$  is obtained by the subtraction of the Chern-Simons contribution, leading to the following Ward identities for both currents

$$\partial_a \langle j_V^a \rangle = 0, \quad (5.32)$$

$$\partial_a \langle j_A^a \rangle = \lim_{\rho \rightarrow 0} \sqrt{-g} \left[ -\frac{\alpha}{3} \varepsilon^{4\mu\nu\sigma\kappa} (3F_{\mu\nu} F_{\sigma\kappa} + G_{\mu\nu} G_{\sigma\kappa}) - iq \left( \phi \left( D^4 \phi \right)^* - \phi^* D^4 \phi \right) \right]. \quad (5.33)$$

Now the Ward identity of the vector current  $j_V$  comes indeed without anomalous right hand side, while the first term of the axial current  $j_A$  resembles the form of the axial anomaly that was provided in subsection 5.1.2. The scalar field contribution to (5.33) is the holographic version of the fermion mass term  $M\bar{\psi}\gamma^5\psi$  in the Ward identity (5.10) of subsection 5.1.2.

In the following, we use the scale invariance of the AdS space to set  $l_{AdS} = 1$  and work in units  $2\kappa^2 = q = 1$  where not stated otherwise.

## 5.2.2 Equations of motion

The scalar and gauge field equations of motion are obtained by variations of the action (5.28), leading to the component forms

$$\nabla_\nu F^{V\mu} + 2\alpha \varepsilon^{\mu\nu\sigma\kappa\tau} G_{\nu\sigma} F_{\kappa\tau} = 0, \quad (5.34)$$

$$\nabla_\nu G^{V\mu} + \alpha \varepsilon^{\mu\nu\sigma\kappa\tau} (F_{\nu\sigma} F_{\kappa\tau} + G_{\nu\sigma} G_{\kappa\tau}) + iq \left( \phi \left( D^\mu \phi \right)^* - \phi^* D^\mu \phi \right) = 0, \quad (5.35)$$

$$(\square - m^2) \phi = 0, \quad (5.36)$$

with  $\square = D^\mu D_\mu$ .

The topological Chern-Simons term does not contribute to the energy momentum tensor, for which we find

$$\begin{aligned} T_{\mu\nu} = & F_{\mu\sigma} F_\nu^\sigma + G_{\mu\sigma} G_\nu^\sigma - \frac{1}{4} g_{\mu\nu} (F^2 + G^2) + (D_\mu \phi)^* (D_\nu \phi) \\ & + (D_\mu \phi) (D_\nu \phi)^* - g_{\mu\nu} \left( \|D\phi\|^2 + m^2 |\phi|^2 \right), \end{aligned} \quad (5.37)$$

and its trace reads

$$T = -\frac{1}{4} (F^2 + G^2) - 3 \|D\phi\|^2 - 5m^2 |\phi|^2. \quad (5.38)$$

Accordingly, the missing equation of motion for the metric tensor can be obtained by plugging (5.37) and (5.38) into the trace reversed form of the Einstein equations (2.14), that was provided in section 2.1.2.

## 5.3 Surface states in holographic Weyl semimetals

In the previous sections we commented on the importance of so-called Fermi arcs surface states as one of the main characteristics of WSMs. Indeed, the detection of Fermi arcs via angle resolved photoemission spectroscopy (ARPES, reference [215]) was one of the first experimentally confirmed phenomena associated with WSMs, besides the chiral magnetic effect measured by its negative magnetoresistance [112], whereas the measurement of other anomalous transport effects appeared to be more challenging.

Accordingly, within this section we examine whether the holographic model presented so far is able to reproduce the appearance of Fermi arcs at the boundary of different topological phases. Furthermore, we aim for comparing the holographic results corresponding to the strong coupling limit of the WSM system, with the regarding weak coupling results.

We discuss the realization of a WSM phase boundary within an effective weak coupling quantum field model in subsection 5.1.3. In subsection 5.3.2 we provide the related holographic setup and comment on possible generalizations of the weak model. The numerical construction of the holographic model is explained in detail in subsection 5.3.3 followed by the presentation of the results in subsection 5.3.4.

### 5.3.1 Effective quantum field model

We first need to explain, how a phase boundary can be realized within our holographic model. The Hamiltonian of a WSM must interpolate at its surface between the topologically non-trivial gapless phase and the trivial gapped phase which is accompanied by a shrinking of the Weyl node distance  $a = |\vec{a}| \rightarrow 0$  close to the interface. We already noticed, that a mere shrinking of the Weyl node distance results in an annihilation of the antichiral nodes, which leads to a gapless Dirac node. Hence, this would produce a different kind of surface state as desired. Furthermore, we recognized in subsection 5.1.3 that a fermion mass term in the Lagrangian saves us from this scenario, while leading to a gapped Dirac fermion phase. Therefore, we realize a surface in the quantum field model with an axial gauge field  $\mathcal{A}$  rather than a constant node distance  $a$ .  $\mathcal{A}$  should vary only in the vicinity of the surface accompanied with a localized chiral magnetic field  $\vec{B}_5 = \vec{\nabla} \times \vec{\mathcal{A}}$ . The field  $\vec{B}_5$  in turn induces a surface current according to the chiral pseudomagnetic effect (cf. the second contribution to equation (5.22)), which should be reproduced by our holographic model that is presented in the next subsection. We constrain ourselves to a plane surface in an ideal infinitely extended system.

Following the above discussion, the field theory Lagrangian should agree with (5.23) in subsection 5.1.3, namely

$$\mathcal{L}_{WSM} = \bar{\psi} (i\not{\partial} - \not{\mathcal{A}} - M) \psi. \quad (5.39)$$

Obviously, we are free to choose the orientation of the interface and therefore fix it to be perpendicular to the  $x$ -axis of our Cartesian space while the Weyl nodes are separated along the  $z$ -axis. Thus, the axial gauge field has the form  $\mathcal{A} = a(x) dz$ , leading to the chiral magnetic field

$$\vec{B}_5 = -a'(x) \vec{e}_y. \quad (5.40)$$

We use an axial gauge field, that only varies within a finite  $x$ -interval, to model the finite extension of the surface layer with the asymptotics

$$\bar{a}_{L/R} := \lim_{x \rightarrow \pm\infty} \frac{a(x)}{M}. \quad (5.41)$$

This is accomplished by utilizing a spline of adequate  $C^k$  regularity, where the smoothness should be at least  $k = 1$  for having a well-defined magnetic field. Figure 5.5 shows the shape of  $\bar{a}(x) = a(x)/M$  for a 9th order spline.

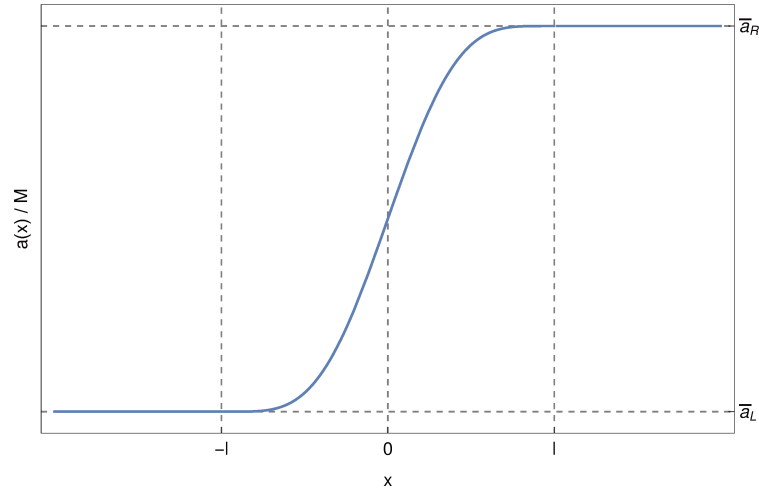


**Figure 5.5:** Profile of the axial gauge field  $\mathcal{A} = a(x)dz$ . We use a 9th order spline interpolation between the left and right side values  $\bar{a}_L$  and  $\bar{a}_R$  continued by constant values.

The arguments presented so far are based on a semi-classical reasoning and we expect a similar adaption of the weak coupling CPME in the presence of a finite fermion mass  $M$  as given in subsection (5.1.3) for the anomalous Hall effect. Accordingly, the magnetic field is replaced by an effective field  $\vec{B}_5 \mapsto \vec{B}_5^{\text{eff}} = -a'_{\text{eff,weak}}(x) \vec{e}_y$  with  $a_{\text{eff,weak}}(x) = \sqrt{a^2(x) - M^2}$  for  $a^2(x) > M^2$  and zero otherwise, leading to the current density

$$j_y = -\frac{\mu}{2\pi^2} a'_{\text{eff,weak}}(x), \quad (5.42)$$

and the total current

$$J_y = \int_{-\infty}^{\infty} j_y dx = \frac{\mu}{2\pi^2} (a_{\text{eff,weak,L}} - a_{\text{eff,weak,R}}). \quad (5.43)$$

The corresponding holographic analogs are provided in the next subsection.

### 5.3.2 Holographic model

The holographic action for a three-dimensional WSM was presented in section 5.2. It remains to provide the concrete form of the fields for implementing the surface of a WSM. In the following, we work in the probe limit, i.e. we assume that the effect of all the matter fields on the spacetime is negligible. This corresponds to the quenched approximation in lattice quantum theory.<sup>4</sup>

To implement a finite temperature parameter (cf. section 2.3), the spacetime background is fixed to pure  $AdS_5$  Schwarzschild, which reads in Poincaré coordinates

$$ds^2 = \frac{1}{\rho^2} \left( -f(\rho) dt^2 + \frac{d\rho^2}{f(\rho)} + dx^2 + dy^2 + dz^2 \right), \quad (5.44)$$

with  $f(\rho) = 1 - \rho^4$ . We recall that fixing the black hole horizon to  $\rho_{\mathcal{H}} = 1$  gives us a trivial Hawking temperature relation  $\pi T = 1$ . This first seems puzzling, but it is a direct consequence of the scale invariance of the holographic model. As shown in [140], we can use the normalized temperature  $\bar{T} = T/M$  as a physical parameter. Subsequently, we refer to  $\bar{T}$  as the temperature and the black hole horizon as the horizon.

The nontrivial components and boundary values of the matter fields  $\phi$ ,  $A$  and  $V$  are crucial for the implementation of the proper quantum field model, since they correspond directly to specific field theoretic quantities via the AdS/CFT dictionary (cf. section 2.3). From the considerations of the previous sections, we already know that the conformal boundary value of the axial field  $A$  can be used for controlling the Weyl node distance. Taking the same orientation for  $A$  as was chosen for  $\mathcal{A}$  in the previous subsection, we have only a nontrivial  $z$ -component  $A = A_z(\rho, x) dz$  accompanied with the boundary condition  $A_z(0, x) = a(x)$ . Recalling that the scalar field  $\phi$  is dual to the fermionic mass operator  $\bar{\psi}\psi$ , which we have to source by  $M$ , we obtain from the dictionary the following boundary asymptotics of  $\phi$  close to  $\rho = 0$

$$\phi(\rho, x) = \rho M + \mathcal{O}(\rho^2). \quad (5.45)$$

The last relation implies the introduction of a rescaled scalar function  $\varphi$  according to  $\phi = \rho\varphi$ . Furthermore, the surface states should be populated in order to induce a surface current. This corresponds to introducing a finite vector chemical potential  $\mu$ , which is according to section 2.3 controlled by the difference of the conformal boundary value and the horizon value of the temporal vector component  $V_t(0, x) - V_t(1, x)$ . All together, this requires a non-trivial  $t$ -component  $V_t$  of the vector gauge field together with a nontrivial  $y$ -component  $V_y$ , as can be seen from the equations of motion. The spatial component  $V_y$  corresponds to the surface current as will be shown shortly. At the conformal boundary, we set  $V_y(0, x) = 0$  for not explicitly sourcing the surface current. In addition, we get rid of an remaining gauge freedom by setting  $V_t(1, x) = 0$  at the horizon.

<sup>4</sup>In lattice theories the quenched approximations is used for fermions and implies that loop contributions of these fermions are neglected.

Putting all together, the matter fields have the structure:

$$A(\rho, x) = A_z(\rho, x) dz, \quad \phi(\rho, x) = \rho \varphi(\rho, x), \quad V(\rho, x) = V_t(\rho, x) dt + V_y(\rho, x) dy \quad (5.46)$$

and the conditions at the conformal boundary are summarized as

$$A_z(0, x) = a(x), \quad \varphi(0, x) = M, \quad V_t(0, x) = \mu, \quad V_y(0, x) = 0. \quad (5.47)$$

The anomalous Hall effect is constrained to the  $x$ - $y$ -plane for the separation of the Weyl nodes along the  $z$ -axis. As shown in [140], the (DC) AHE conductivity is directly related to the horizon value of  $A_z$ :

$$\sigma_{\text{AHE}} = 8\alpha A_z|_{\rho=1}. \quad (5.48)$$

Relation (5.48) implies a non-trivial modification of the weak coupling result (5.27) according to  $a_{\text{eff,weak}} \mapsto a_{\text{eff,hol}} := A_z|_{\rho=1}$ . As a result, also the critical value  $\bar{a}_c = a_c/M$  deviates from the weak coupling result, as shown in [140, 142]. Concretely, the onset of the order parameter starts at  $\bar{a}_c \approx 1.40$  which disagrees from the weak coupling expectation  $\bar{a}_c = 1$ . It is important to note, that the relation (5.48) was derived under the assumption of an homogeneous axial field  $A_z$  (no  $x$ -dependence). Nevertheless, we expect the configuration to settle down to the homogeneous case at some distance of the interface.<sup>5</sup> We are mostly interested in qualitative results and expect that (5.48) provides us with a reliable measure for the order parameter away from the interface region.

At this point we remark, that the holographic direction  $\rho$  can be interpreted as an energy scale for the renormalization group (RG) flow [12]. Then the horizon value of  $A_z$  can be interpreted as the IR value of the UV coupling  $a$ . The same interpretation applies to  $M$  and the horizon value of  $\varphi$  which can be interpreted as effective IR mass.

It remains to derive the explicit expression for the vector current  $j_V$  from the expression (5.30). We find for the only non-trivial component  $j_y$ :

$$\begin{aligned} j_y(x) &= \lim_{\rho \rightarrow 0} \left( f(\rho) \frac{\partial_\rho V_y(\rho, x)}{\rho} - 8\alpha A_z(\rho, x) \partial_x V_t(\rho, x) \right) \\ &= \partial_\rho^2 V_y(0, x), \end{aligned} \quad (5.49)$$

where the limit can only be taken after considering a detailed boundary expansion of the fields. This expansion is provided in the next subsection together with its numerical implications. We remark, that the Chern-Simons contribution to the current  $j_V$  vanishes for the chosen ansatz, hence no further modification is needed for obtaining the non-anomalous vector current.

<sup>5</sup>One can explicitly show that the EOM decouple and become those of the homogeneous case for  $x \rightarrow \pm\infty$ .

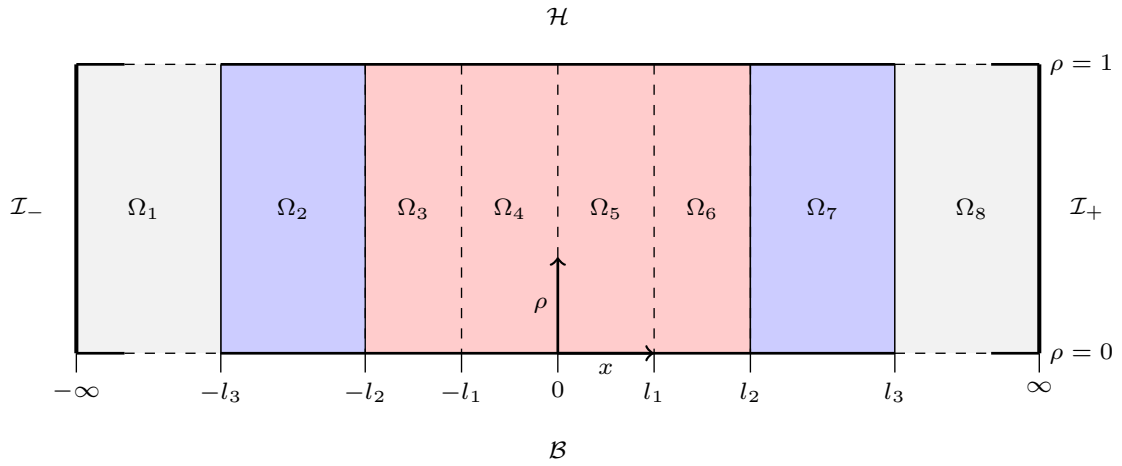


**Figure 5.6:** Sketch of the chosen domain decomposition. The red area represents the part of the integration domain where a non-constant boundary value  $a(x)$  is imposed. The domains  $\Omega_1$  and  $\Omega_8$  are non-compact and extend to  $\pm\infty$  in  $x$  direction.

### 5.3.3 Numerical construction

First we comment on the coordinate system, that was used for the numerical implementation of the holographic WSM model. The problem is effectively two-dimensional in the coordinates  $(\rho, x) \in [0, 1] \times (-\infty, \infty)$ . Again, spectral methods are applied to obtain solutions of the corresponding boundary value problem. We continue with a presentation of the equations of motion together with the boundary conditions.

#### Equations of motion and boundary conditions

Inserting the metric ansatz (5.44) and the fields (5.46) into the equations of motion (5.34)-(5.36) yields a set of four non-trivial partial differential equations that can be found in appendix A.3.1.

The domain of integration, which is shown in figure 5.6, is subject to the following conditions at the different boundaries:

- The conformal boundary  $\mathcal{B}$  ( $\rho = 0$ ):  
The boundary conditions (5.47) were provided in the previous subsection. A  $C^2$  spline with  $C^1$  continuity at the domain boundaries would be sufficient for the profile of  $a(x)$  from the PDE point of view. We tested several splines and also a  $C^\infty$  ansatz and found the same qualitative features of the results.
- The horizon  $\mathcal{H}$  ( $\rho = 1$ ):  
For fixing the remaining gauge freedom of the field equations, we set  $V_t(1, x) = 0$ . The other boundary conditions can be obtained from the partial differential equations (A.24)-(A.27), which are singular at  $\mathcal{H}$ . We obtain

$$\partial_\rho A_z(1, x) = 0, \quad \partial_\rho \varphi(1, x) = 0, \quad V_t(1, x) = 0, \quad \partial_\rho V_y(1, x) = 0. \quad (5.50)$$

- The two asymptotic boundaries  $\mathcal{I}_\pm = \{(\rho, x) : x \rightarrow \pm\infty\}$ :  
Here we do not have any physical constraints or singular points. It suffices to impose the field equations here.

Next we consider a boundary expansion of the fields in the vicinity of the conformal boundary, which is instructive for understanding the convergence behavior of the spectral expansion.

$$V_t(\rho, x) = \mu + V_t^{(1)}(x)\rho^2 + \mathcal{O}(\rho^4) \quad (5.51)$$

$$V_y(\rho, x) = V_y^{(1)}(x)\rho^2 + \mathcal{O}(\rho^4) \quad (5.52)$$

$$A_z(\rho, x) = a(x) + \left( A_z^{(1)}(x) + \frac{1}{2}(2q^2a(x)M^2 - a''(x))\log\rho \right)\rho^2 + \mathcal{O}(\rho^4) \quad (5.53)$$

$$\varphi(\rho, x) = M + \left( \varphi^{(1)}(x) + \frac{1}{2}Mq^2a^2(x)\log\rho \right)\rho^2 + \mathcal{O}(\rho^4) \quad (5.54)$$

We recognize the appearance of logarithmic terms in the expansions of  $A_z(\rho, x)$  and  $\varphi(\rho, x)$  at order  $\rho^2$ . Further logarithmic contributions will emerge at higher orders in  $\rho$  for all fields. As a consequence we have only an algebraic convergence rate of the spectral expansion (cf. the convergence plots in appendix A.3.4) in the  $\rho$ -direction. In addition, we see that the logarithmic contribution in the expansion of  $A_z(\rho, x)$  is coupled to  $a''(x)$ , hence we expect a worse convergence in the region with varying  $a(x)$ . Consequently, we introduce a multi-patch scheme that should prevent a spreading of the worst convergence rate to the entire domain of integration due to the global nature of spectral methods.

### Domain decomposition

The purpose of the domain decomposition is to adapt to the behavior of the solutions in the different regions, while keeping the numerical efforts low. We employ a simple linear domain composition into eight non-overlapping subdomains  $\Omega_i = [0, 1] \times I_i$  (figure 5.6), which are aligned with regions exhibiting different convergence properties. All these domains are mapped to the standard cube  $[-1, 1]^2$  for the approximation in terms of two-dimensional Chebyshev expansions.

The central region is defined by the finite extension of the spline  $a(x)$  within the interval  $x \in [-l, l]$  for some  $l > 0$ . A high number of Chebyshev points within a single region would accumulate at the boundaries of this region and therefore not cover the strong gradients, that are present in the center. Thus we use four subdomains instead of one to increase the number of points significantly, while avoiding the accumulation effect. Buffer domains are introduced next to the interior subdomains to separate the central and the asymptotic regions. The two outer domains extend to  $\pm\infty$  in  $x$ -direction and need to be compactified to  $[-1, 1]$ . As in chapter 4, we use a simple algebraic compactification scheme

$$\begin{aligned} x(s_1) &= \frac{s_1 - 1 - l_1(1 + s_1)}{1 + s_1} & \text{for } x \in I_1 = (-\infty, -l] , \\ x(s_8) &= \frac{s_8 + 1 + l_8(1 - s_8)}{1 - s_8} & \text{for } x \in I_8 = [l, \infty) , \end{aligned}$$

where  $s_{1/8} \in [-1, 1]$  and  $l_{1/8} > 0$  are parameters that can be used to control the map.



In principle the logarithmic contributions in the boundary expansion of the fields imply a further domain decomposition in  $\rho$ -direction, leading to a much improved convergence in the domains that would be connected to  $\rho = 1$ . However, the observed convergence of our data was sufficient, nevertheless we expect this to change when considering the setup with metric backreaction. We use a simple rescaling map to the unit cube  $\rho = \frac{1+s}{2}$ , which leads to a sufficient accuracy of the output.<sup>6</sup>

### Parameters and physical quantities

The nonphysical parameters  $l_1$  and  $l_8$  were set to  $l_1 = l_8 = 15$  after probing their influence on the spectral expansion. Furthermore, we set  $q = 1$  and  $\mu = 1/10$ . We chose a small value for the chemical potential, because high values of  $\mu$  are expected to change the semi-metallic state of the system due to excitations far away from the Weyl nodes. In addition, we found that the total current is proportional to the chemical potential for small values of  $\mu$ , i.e. without loss of generality it suffices to consider  $\mu = 1/10$ . Moreover, the dependence on  $q$  and  $\alpha$  was found to be trivial, as shown in appendix A.3.2.

The horizon value of  $A_z$  is computed in dependence of  $a_L$  and  $a_R$  for the different sides of the interfaces, in order to use the anomalous Hall conductivity  $\sigma_{\text{AHE}}$  as an order parameter between WSM and non-WSM phase as discussed before.

We study the current density  $j_y$  in dependence of the surface width  $l$ , and the asymptotic values  $a_L$  and  $a_R$  of the Weyl node distance for different temperatures  $\bar{T} = 1/(\pi M)$ . The computation of  $j_y$  requires the evaluation of  $\partial_\rho^2 V_y(0, x)$ , which is obtained by direct numerical differentiation. The total current  $J_y$  is obtained by numerical integration, cf. section 3.1.1.

We chose a 9th order spline for producing the data provided in the next subsection. We tested several splines and also a  $C^\infty$  ansatz and found the same qualitative features of the results.

### 5.3.4 Results

We start with an analysis of the anomalous Hall effect in dependence of the provided interface spline  $\bar{a}(x)$ . Subsequently, we consider the obtained profiles for the current densities, followed by a thorough discussion of the integrated currents. The accuracy of the solutions is analyzed in appendix A.3.4.

#### Anomalous Hall effect

Figure 5.7 shows the horizon values of  $A_z$  and  $\varphi$  at high and low temperatures for  $\bar{a}_L < \bar{a}_c$  and  $\bar{a}_R > \bar{a}_c$ , which should correspond to a trivial phase on left side and a WSM phase on the right side. The system becomes homogeneous away from the interface and we can apply relation (5.48) to determine the anomalous Hall conductivity (AHC). For low temperatures,  $a_{\text{eff,hol}} = A_z|_{\rho=1}$  vanishes in the trivial, left phase, as expected implying a zero AHC. Furthermore, the non-vanishing scalar field  $\phi|_{\rho=1}$  can be considered as an effective non-zero mass. Whereas the effective mass vanishes on the non-trivial WSM phase on the right side, where  $\bar{a}(x)$  exceeds the critical value, i.e. we have  $a_{\text{eff,hol}} > 0$  and a non-vanishing AHC. We do not observe

<sup>6</sup>The application of convergence improving maps, such as the maps presented in reference [35], introduces additional problems due to singular Jacobians at the boundaries. For this project, the desired accuracy could simply be obtained by increasing the number of collocation points appropriately. This was not possible for the project presented in section 5.4 and so we employ a convergence improving map there (cf. subsection 5.4.3).

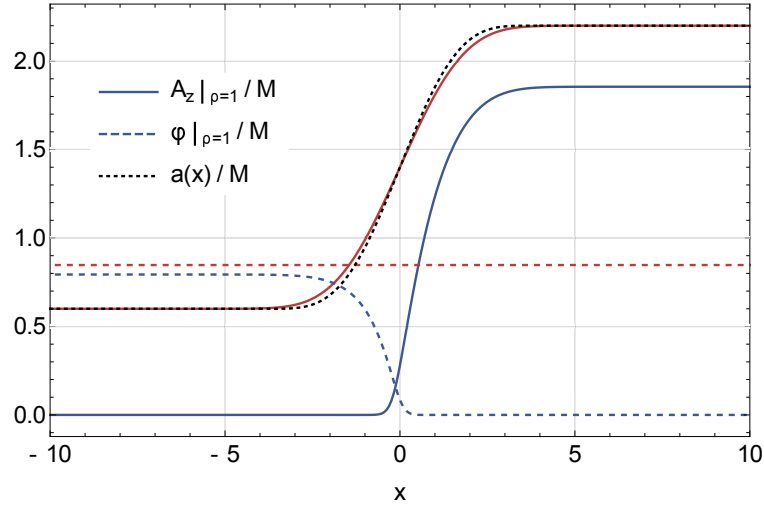


**Figure 5.7:** Horizon values of scalar and axial gauge field (dashed, solid) along the sample for temperatures  $\pi\bar{T} = 100, 1/16$  (red, blue). The black dotted line corresponds to the profile of  $a(x)/M$ .

a sharp transition between the phases, which is a result of the finite extent of the interface and the non-zero temperature.

We recognize a different behavior for high temperatures. Here the scalar field attains a constant value and remains constant over the horizon. Moreover, the axial field does not vanish any more in the trivial phase. We remark, that the concrete profiles depend not only on the temperature, but also on the profile  $\bar{a}(x)$  where the qualitative features remain the same.

### Current profiles

First we note, that there is no scaling symmetry in  $x$ -direction left, since we removed the AdS rescaling symmetry by fixing the location of the horizon to be at  $\rho_H = 1$ <sup>7</sup>. Figure 5.8 shows the electric current  $j_y(x) = \partial_\rho^2 V_y(0, x)$  at low temperature for different choices of the interface width  $l$ . We see, that the current profile becomes more localized around  $x = 0$  as  $l$  decreases, which confirms our interpretation of  $j_y$  as an interface current. Nevertheless, the integral of the current  $J_y$  along the  $x$ -direction remains constant to good accuracy for all configurations under consideration. We further remark that the current  $j_y$  deviates from the weak coupling result (5.42) for  $M > 0$ , even when replacing  $a'_{\text{eff,weak}}$  by  $a'_{\text{eff,hol}}$ .

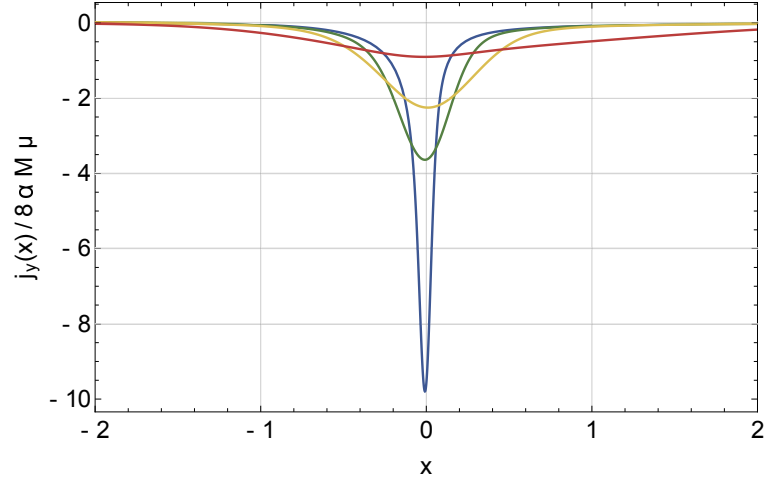
### Integrated current

Figure 5.9 shows the integrated current  $J_y$  for several fixed values of  $\bar{a}_L$  as a function of  $\bar{a}_R$  and for different temperatures  $\bar{T}$ . We recover the weak result (5.43)

$$J_y = \frac{\mu}{2\pi^2} (a_L - a_R) \quad (5.55)$$

for high temperature  $\bar{T}$ , i.e. small mass  $M$ , corresponding to the dashed lines in figure 5.9. This meets our expectation for high temperatures, where the mass becomes negligible the topological phase boundary disappears. Consequently, the integrated current  $J_y$  depends only on the difference of  $a_L$  and  $a_R$  and not on their concrete values.

<sup>7</sup>As a result, all lengths are measured in units of inverse temperature.



**Figure 5.8:** Current profile along the  $x$  direction for different interface widths  $l = 0.1, 0.5, 1, 4$  (blue, green, yellow, red) and low temperature  $\pi\bar{T} = 1/16$ .

On the other hand, the low temperature behavior is different, as shown by the solid lines in figure 5.9. We start with considering the setup with a trivial phase on the l.h.s. (blue line in figure 5.9). No current is generated as long as the r.h.s. remains in the trivial phase, whereas we obtain a finite current for  $\bar{a}_R > \bar{a}_c$  which exhibits a non-trivial dependency on  $\bar{a}_R$ . Concretely, the curve appears to have a kink at  $\bar{a}_R = \bar{a}_c$ , which is in fact smooth due to the finite temperature of the system. According to figure 5.9, this behavior remains as long as  $\bar{a}_L < \bar{a}_c$ . Hence, the integrated current is insensitive to the details of the trivial phase and we see no current at the interface of two trivial phases.

Now we turn on the case of a non-trivial phase on the l.h.s., namely  $\bar{a}_L > \bar{a}_c$ , corresponding to the solid green and red lines in figure 5.9. The main difference to the previous situation is an overall shift of the integrated current depending on  $\bar{a}_L$ . Again we see a plateau for  $\bar{a}_R < \bar{a}_c$  pointing to the insensitivity of the integrated current to the parameter of the trivial phase. Moreover, the current shows the same functional dependence on  $\bar{a}_R$  as before once the r.h.s. undergoes the phase transition and both sides are in the non-trivial phase. We further note that the current vanishes exactly for  $\bar{a}_L = \bar{a}_R$  in agreement with the expected behavior (solid green line in figure 5.9).

The full dependence of the current on  $\bar{a}_L$  and  $\bar{a}_R$  at low temperatures is provided in figure 5.10. We recognize the plateau for  $\bar{a}_{L/R} < \bar{a}_c$  and notice that the current is odd under the left-right exchange  $\bar{a}_L \leftrightarrow \bar{a}_R$  reflecting its chiral nature as a fundamental symmetry of the system.

The previous discussion suggests the following form of the integrated current:

$$J_y = \frac{\mu}{2\pi^2} (\mathcal{F}(a_L) - \mathcal{F}(a_R)), \quad (5.56)$$

where  $\mathcal{F}$  denotes some a-priori unknown map. According to the previous discussion, a possible candidate for  $\mathcal{F}$  is given by  $\mathcal{F}(a) = a_{\text{eff}} = A_z|_{\rho=1}$ , such that we obtain

$$J_y = \frac{\mu}{2\pi^2} (a_{\text{eff},\text{hol},L} - a_{\text{eff},\text{hol},R}) = \mu (\sigma_{\text{AHE},L} - \sigma_{\text{AHE},R}), \quad (5.57)$$

where the last equality follows from (5.48) with the identification  $\alpha = 1/(16\pi^2)$ . This model fits well to our numerical data, with relative deviations of less than 3%.

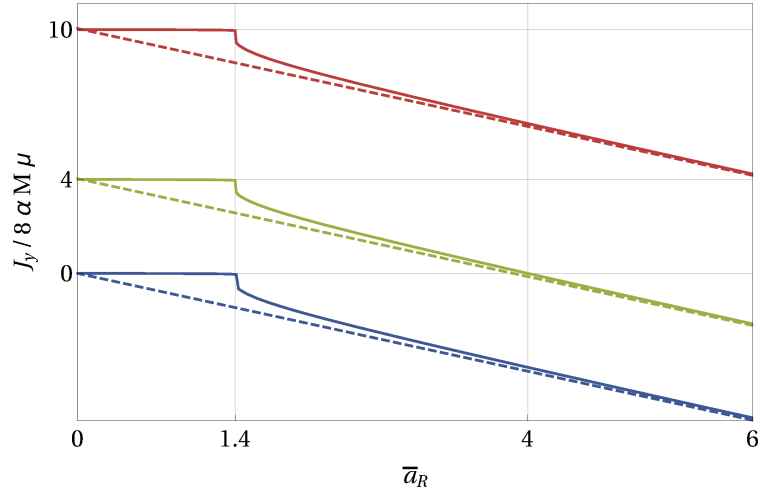


**Figure 5.9:** Integrated current as a function of  $\bar{a}_R$  for  $\bar{a}_L < \bar{a}_c$  (blue) and  $\bar{a}_c < \bar{a}_L \in \{4, 10\}$  (green, red). Solid lines correspond to low temperature  $\pi\bar{T} = 1/16$  and dashed lines to high temperature  $\pi\bar{T} = 1$ .

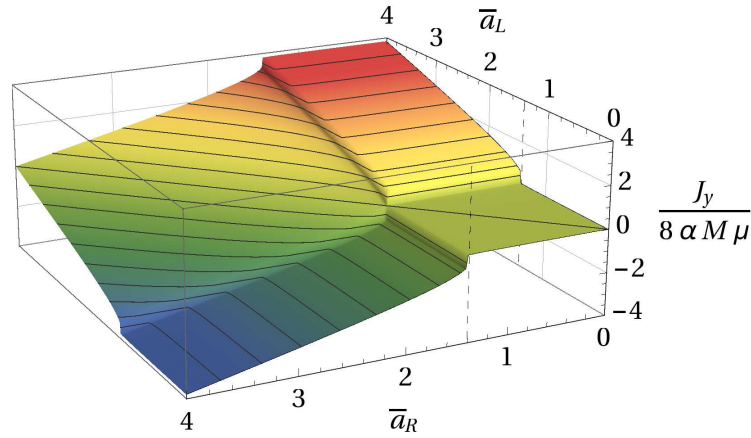


**Figure 5.10:** Integrated current as a function of  $\bar{a}_R$  and  $\bar{a}_L$  at low temperature  $\pi\bar{T} = 1/16$ . Contour lines shown in black.

At this point, we would like to give an interpretation of the presented results. The surface current can be considered as the result of an axial magnetic field  $\vec{B}_A$  that is localized at the boundary layer. First it might appear not as a surprise, that our relation for the integrated current (5.57) can be obtained from the weak result (5.55) in the same way as the corresponding AHE was obtained by replacing  $a_{\text{eff,weak}} \mapsto a_{\text{eff,hol}}$ . Though this is a non-trivial result, because the weak relation (5.55) was supposed to be only valid for homogeneous fields. Hence we conclude, that the high order contributions to the weak coupling induction relation (5.40) are canceled by the integration operation. However, this is not evident, since we do not know about any theoretical restriction on the higher order transport coefficients that would imply such a cancellation.

## 5.4 Finite temperature and disorder effects in holographic Weyl semimetals

The presence of impurities or disorder is unavoidable in realistic situations and it can have a deep impact on the physical features of a system and its behavior across possible phase transitions. The effects of disorder on quantum phase transitions (QPTs) are much stronger than on their classical counterparts and they are subject of intense study in the present days [200, 203].

The goal of this section is to investigate the influence of finite temperature and disorder effects in holographic WSMs and compare the findings with results gained from condensed matter considerations. In subsection 5.4.1 we provide a short overview of disorder effects for quantum phase transitions (QPT). The holographic setup for modeling quenched (i.e. time independent) disorder in WSMs is presented in subsection 5.4.2. The numerical construction of the holographic model is outlined in subsection 5.4.3 followed by the presentation of the results in subsection 5.4.4.

### 5.4.1 Physical background

A common rule to assess whether a phase transition is stable with respect to weak disorder<sup>8</sup> relies on the so-called Harris criterion [97]. According to that criterion, the phase transition will not be affected by the presence of disorder as far as the correlation length critical exponent  $\nu$  satisfies the inequality  $d\nu > 2$ , with  $d$  as the number of spatial dimensions in which disorder is present. If  $d\nu < 2$ , the weak disorder is relevant and its effects increase under coarse graining, i.e. the transition must change.

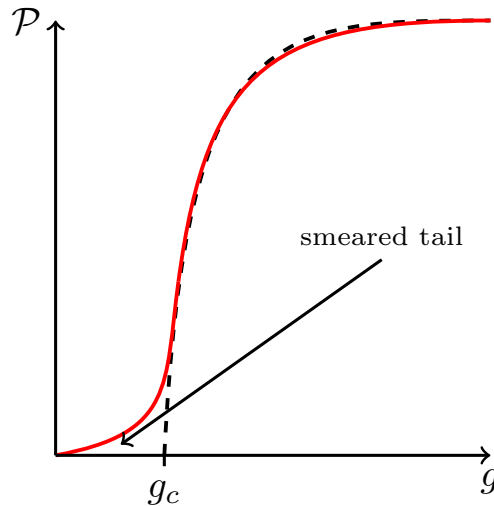


**Figure 5.11:** The evolution of the order parameter  $\mathcal{P}$  across the quantum phase transition at  $T = 0$ . The black dashed line illustrates the clean case where the QPT is sharp while the red line is the smeared disordered QPT.

The Harris criterion relies on classifying the effects of weak disorder under coarse graining. Therefore it refers to the behavior of the system at large length scales and it is not able to capture possible existing features at finite length scale. It thus represents a necessary condition for the

<sup>8</sup>The disorder is considered as weak, if the phases at the (quantum) critical point are not changed qualitatively. Here the notion of “weakness” should not be confused with what is called Harris-irrelevant.

stability of a clean critical point, but not a sufficient one. In other words: Disorder is defined as Harris-irrelevant, if its effects become less and less important at larger scales. Accordingly, it is clear that such a criterion has to be extended and new effects, i.e. rare region effects, are expected to play a fundamental role in disordered QPTs [204, 205]. In particular, the generic consequence of disorder is to smear the sharp quantum phase transition (see figure 5.11) [110, 197].

The smearing or rounding of the sharp QPTs is believed to be a direct manifestation of the so-called rare regions or Griffiths effect [86, 172, 202]. The study of rare large disorder fluctuations can be considered as a complementary approach to the Harris analysis, which concentrates on large scale effects. Indeed, such fluctuations and the corresponding spatial regions play an important role, because the rare regions can be locally in one phase, while the bulk system is in the other. Accordingly Griffiths showed, that this can be the source of non-analyticities (so-called Griffiths singularities) in the free energy of an entire parameters region around the transition [86]. First experimentally observed in quantum magnets [197], these phenomena appear in a variety of systems, ranging from classical Ising magnets with planar defects [198] to nonequilibrium spreading transitions in the contact process [199]. Furthermore, disorder correlations are of special relevance for QPTs; even short-range correlations can qualitatively modify quantum smeared phase transitions. Concretely positive correlations (like in the case of impurity atoms which attract each other) were shown to enhance the smearing of the transition [52, 162, 189]. There have been efforts to relate the different disorder-schemes [204], but the understanding of the physics of disordered QPTs is just at a preliminary stage and a complete classification of the various scenarios is still lacking.

The question whether and how disorder and impurities affect the physics of the WSMs received particular attention recently. The effective field theory for disordered WSMs was built in [9, 10] and several studies regarding the phase diagram and the topological phase transition in presence of randomness were performed [43, 217, 175, 149, 174, 179, 10]. Despite all the effort a robust and definitive verdict is still absent.

In the last years, special attention was paid to the idea of incorporating disorder and its effects in the holographic picture. Throughout our work by disorder we mean quenched disorder. From the (strongly coupled) quantum field theory side this amounts to consider “random couplings” (cf. reference [4]), whose statistical distribution does not depend on the quantum fields. This is implemented in terms of a deformation of the quantum field action

$$S \mapsto S + \int d^d x g_I(x) \mathcal{O}_I(x) , \quad (5.58)$$

where the couplings  $g_I$  are random. Reconsidering the Fefferman-Graham boundary expansion (2.51) of section 2.3, this corresponds to the following source term within the asymptotic boundary expansion for the bulk fields  $\phi_I$

$$\phi_I^{(0)}(x) = j_I(x) + g_I(x) , \quad (5.59)$$

where  $j_I$  denotes the contribution of all non-random sources in  $S$  of the operator  $\mathcal{O}_I$ . Quenched disorder was already considered in various holographic models with particular emphasis on its effects on transport properties [151, 152, 150, 60, 80, 19]. In addition disordered geometries and fixed points were recently studied in [102, 101].

Furthermore, discrete scale invariance (DSI) is believed to be intimately linked to the presence of disorder [188]; it manifests itself in the peculiar log-oscillatory behavior of the thermodynamic and transport observables due to the appearance of a complex critical exponent in the vicinity of a (quantum) phase transition. The signatures of emergent (discrete) scale invariance were observed before in disordered holographic models in [99, 100, 25, 75]<sup>9</sup>.

Finally, the effects of disorder on thermal, but not quantum, phase transitions were already analyzed in holography in [176, 79, 23, 22, 21]. Concretely, in [23] the appearance and effects of rare regions were studied in the context of superconducting phase transitions.

Despite all the recent efforts, the effects of quenched disorder on QPTs has not been investigated so far to the best of our knowledge. In this direction, we aim to provide a first study of a holographic QPT and its quantum critical region in the presence of disorder. In particular, we focus on one dimensional quenched disorder within the holographic Weyl semimetal QPT and examine the following questions:

1. Will the quantum phase transition remain sharp in the presence of quenched disorder?
2. If not, how will its nature get modified?

After discussing how quenched disorder should be implemented by using random couplings, we provide the explicit expressions in terms of boundary values of the holographic fields in the next subsection.

### 5.4.2 Holographic model

The holographic action (5.28) serves once more as the building block for modeling the holographic WSM. Again, we align the Weyl nodes along the  $z$ -axis and hence can recycle the setup that was presented in subsection 5.3.2. This time we set the external vector field  $V$  to zero, since we only want to compute the anomalous Hall conductivity in dependence of the temperature parameter  $\bar{T} = T/M$  and the disorder strength. As for the last project, we choose an inhomogeneous source  $a(x)$  for the  $z$ -component of the axial gauge field  $A_z$  and a homogeneous source  $M$  for the scalar field  $\phi$ . As shown in appendix A.3.3, for inhomogeneous  $A_z$  the averaged AHC can be obtained directly from the averaged axial gauge field component  $A_z$  at the horizon under the assumption of periodic boundary conditions in  $x$ -direction:

$$\langle \sigma_{\text{AHE}} \rangle_\lambda = \frac{8\alpha}{\lambda} \int_0^\lambda dx A_z(x)|_{\rho=1}, \quad (5.60)$$

where  $\lambda$  is the extension of the compact dimension  $x$ .

We further remark that the critical scaling of the Hall conductivity in WSMs in the completely homogeneous setup (no  $x$ -dependency of the Weyl node separation) was already considered for a holographic model [142, 139]. For the latter, the behavior of the order parameter  $\sigma$  close to the QPT was obtained to scale as

$$\sigma_{\text{AHE}} \sim (\bar{a} - \bar{a}_c)^{\Psi_{\text{hom,hol}}}, \quad (5.61)$$

where the critical exponent was estimated to be  $\Psi_{\text{hom,hol}} \approx 0.21$  - in contrast to the mean field result  $\Psi_{\text{hom,weak}} = 1/2$ , cf. equation (5.27). In the following we omit the lower index AHE and write only  $\sigma$  together with the previously introduced averaging subscript if applicable.

<sup>9</sup>Discrete scale invariance has been also studied in holographic systems *without* disorder in [25, 75].

### Implementation of disorder

To implement the effects of one dimensional quenched disorder in terms of a fluctuating Weyl node distance, we introduce 1D Gaussian noise in the source  $a(x)$  of the axial gauge field  $A_z$ . The source  $M$  of the scalar field  $\phi$  is kept constant. Concretely, when assuming a compactified  $x$ -direction, the disorder is implemented in terms of the following spectral representation (cf. reference [183]):

$$a(x) = a_0 + 2\gamma \sum_{j=1}^{N_{\text{dis}}-1} \sqrt{s(k_j)} \sqrt{\Delta k} \cos(k_j x + \delta_j) . \quad (5.62)$$

In expression (5.62),  $k_j = j\Delta k$  denote the equi-distributed momenta with constant separation  $\Delta k = 2\pi/\lambda$ , where  $\lambda$  is the length of the compact direction  $x$ . Furthermore, the  $\delta_j \in [0, 2\pi)$  are  $N_{\text{dis}} - 1$  independent uniformly distributed random phases, which provide the source of the disorder. The parameter  $\gamma$  measures the disorder strength, because it provides the amplitude of the sum of random variables in expression (5.62). Finally, the factor  $s(k_j)$  is the spectral power density of the random signal evaluated at the contributing wave-numbers.

We expect that the excitations of the disordered system within the energy interval corresponding to  $k_1 = 2\pi/\lambda$  and  $k_{N_{\text{dis}}-1} = 2\pi(N_{\text{dis}} - 1)/\lambda$  will lead to the most pronounced effects of disorder in terms of the observables. Hence, the temperature of our thermal state should satisfy

$$k_1 \ll T \ll k_{N_{\text{dis}}-1} , \quad (5.63)$$

to guarantee a thermal population of these states. This can be achieved by choosing  $\lambda$  and  $N_{\text{dis}}$  appropriately.

Choosing the spectral power density  $s$  to be of the form

$$s(\xi) = \xi^{-2\alpha_{\text{cor}}} , \quad (5.64)$$

allows us to control the correlation of the random variable (5.62). In the case  $\alpha_{\text{cor}} = 0$ , i.e.  $s \equiv 1$ , the random variable  $\hat{a}(x) = a(x) - a_0$  describes local, isotropic, Gaussian disorder in the limit  $N_{\text{dis}} \rightarrow \infty$ :

$$\langle \hat{a}(x) \rangle_{\text{dis}} = 0 , \quad \langle \hat{a}(x) \hat{a}(y) \rangle_{\text{dis}} = \gamma^2 \delta(x - y) , \quad (5.65)$$

with all higher momenta vanishing. In particular, positive and large  $\alpha_{\text{cor}}$  corresponds to positive and large correlation (see figure 5.12).

The spectral power  $P$  of the random signal  $\hat{a}(x)$  can be obtained by summing over the spectral power densities of the single contributions weighted by the overall amplitude

$$P = 4\gamma^2 \Delta k \sum_{j=1}^{N_{\text{dis}}-1} k_j^{-2\alpha_{\text{cor}}} = 4\gamma^2 \Delta k^{1-2\alpha_{\text{cor}}} H_{N_{\text{dis}}-1, 2\alpha_{\text{cor}}} , \quad (5.66)$$

where  $H_{N_{\text{dis}}-1, 2\alpha_{\text{cor}}}$  is the  $N_{\text{dis}} - 1$ -th generalized harmonic number of order  $2\alpha_{\text{cor}}$  [118].



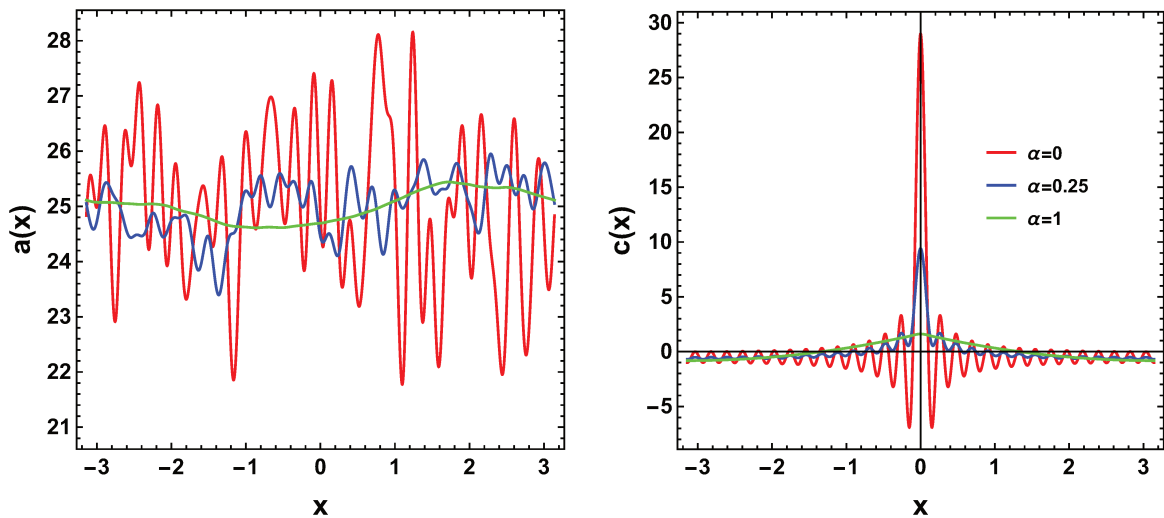


**Figure 5.12:** **Left:** Example of specific disorder realizations (5.62) with  $a_0 = 25$ ,  $N_{\text{dis}} = 30$  and  $\alpha_{\text{cor}} = 0.00, 0.25, 1.00$  (red, blue, green). **Right:** Corresponding correlation functions  $c(x) = \langle \hat{a}(x) \hat{a}(0) \rangle_{\text{dis}}$ .

The goal of this work is to investigate the fate of the WSM quantum phase transition in presence of this type of one-dimensional Gaussian disorder. We note, that the mass-dimension of our disorder is given by  $[\gamma] = [a] - [\sqrt{\Delta k}] = [A_z] - 1/2 = 1/2$ . Hence, the disorder contribution in (5.62) corresponds to a relevant deformation of the quantum field action, which does not satisfy the Harris criterion according to our discussion in the last subsection. Since the relevant dimensionless quantity governing the phase transition is the ratio  $a/M$  we expect similar results to hold for the case of an inhomogeneous source of the scalar field<sup>10</sup>.

### 5.4.3 Numerical construction

The problem is effectively two-dimensional in the coordinates  $(\rho, x) \in [0, 1] \times [0, 2\pi)$ . The problem is discretized by employing a Chebyshev expansion in the  $\rho$ -direction and a Fourier expansion in the  $x$ -direction.

The equations of motion for  $A_z$  and  $\phi$  are obtained from the PDEs (A.24) and (A.27) after setting  $V_t$  and  $V_y$  to zero.

The domain of integration has the same boundary structure with respect to the holographic coordinate  $\rho$  as the interface project (cf. subsection 5.3.3), whereas we do not set any conditions in  $x$ -direction, since the periodicity comes as a behavioral boundary condition of the Fourier expansion (cf. reference [34]).

The boundary expansion of the fields  $A_z$  and  $\phi$  around  $\rho = 0$  agrees with the expansions provided by (5.53) and (5.54). This time we do not need to extract any output at the conformal boundary. Thus we use a quadratic map for mapping  $\rho$  to the standard cube  $\rho(s) = \left(\frac{1+s}{2}\right)^2$ ,  $s \in [-1, 1]$ , which improves the convergence of the spectral expansion by two orders (cf. reference [35] for the application of a similar map of quadratic order in the presence of logarithmic endpoint singularities).

<sup>10</sup>However, let us remark that this second option allows for the study of marginal or irrelevant disorder, by appropriately setting the mass of the associated scalar field in the bulk. Another, numerically more challenging, option to achieve this is to increase the number of dimensions in which the fields are disordered.

### Parameters and physical quantities

The length of the compactified dimension is set to  $\lambda = 20\pi$ . The number of random phases is constrained to  $N_{\text{dis}} = 30$ . We note, that these choices for  $\lambda$  and  $N_{\text{dis}}$  satisfy the criterion (5.63). We use  $\alpha_{\text{cor}} = 0$  where not explicitly stated otherwise, for minimizing the correlation of the disorder.

The mean-value  $\langle f \rangle_{\text{dis}}$  of an observable  $f$  that depends on  $N_{\text{dis}} - 1$  independent random phases is defined as

$$\langle f \rangle_{\text{dis}} = \int \prod_{j=1}^{N_{\text{dis}}-1} \frac{d\delta_j}{2\pi} f. \quad (5.67)$$

We estimate the statistical mean value of the output (i.e. of the integrated Hall conductivity) by taking its average over a sufficient number of random samples.

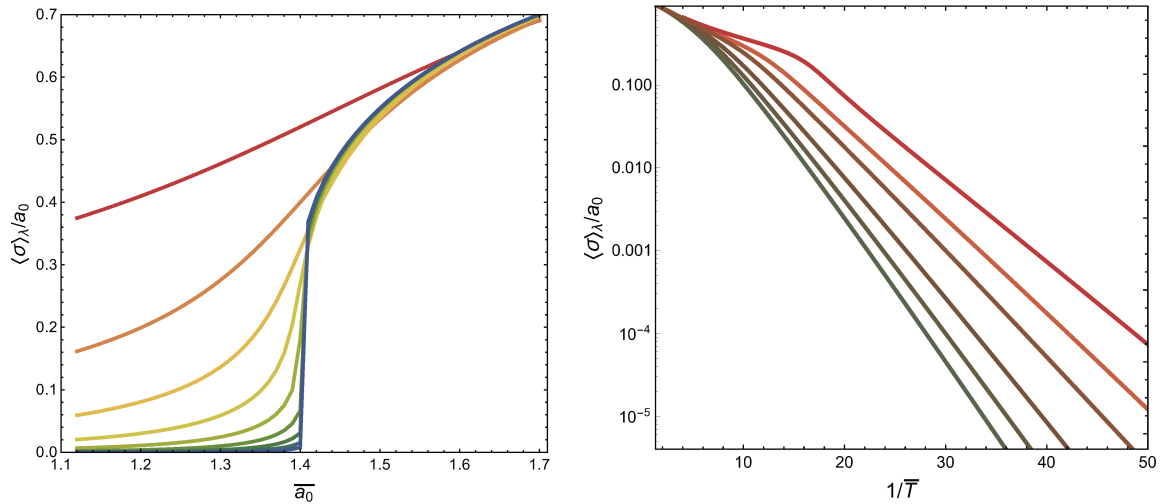


**Figure 5.13:** **Left:** Integrated AHC  $\langle \sigma \rangle_\lambda$  as a function of  $\bar{a}_0$  for zero disorder and at finite temperature  $\pi \bar{T} = 1/k$  with  $k = 2, 3, \dots, 10$  (red-blue). At low enough temperatures (blue) a quantum phase transition occurs. **Right:** Semi-logarithmic plot of the AHC  $\langle \sigma \rangle_\lambda$  vs  $1/\bar{T}$  for fixed  $\bar{a}_0 \in \{1.00, 1.10, 1.20, 1.30, 1.35, 1.39\}$  (green-red). Close to the phase transition, at  $\bar{a}_0 = 1.39$  (red line), a new scaling appears at low  $1/\bar{T}$ . This is an effect of the quantum critical region (see figure 5.14 for a magnified view).

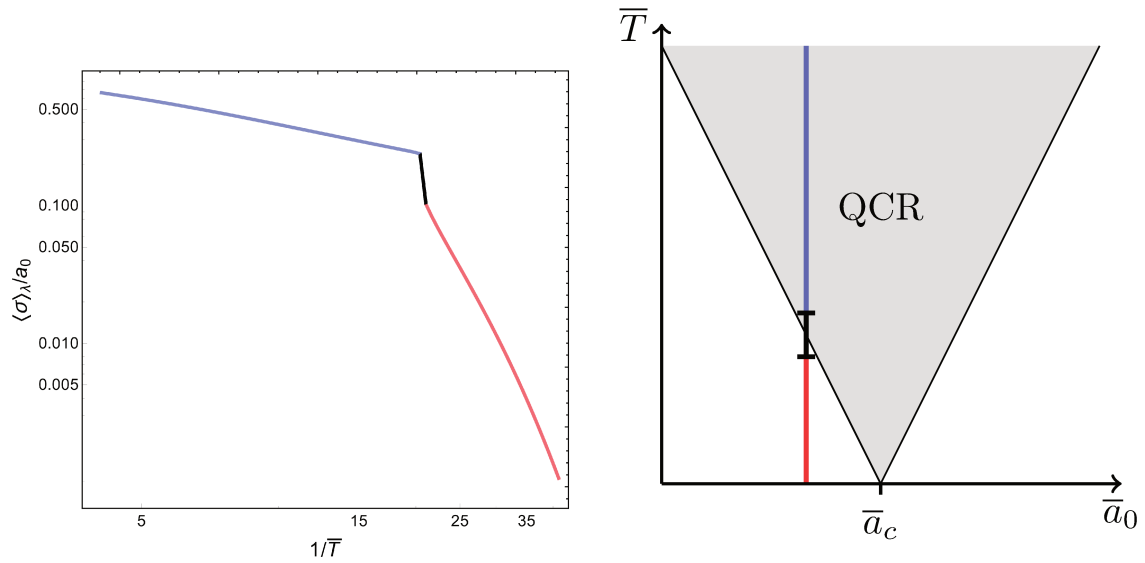


**Figure 5.14:** Log-Log plot of the AHC  $\langle \sigma \rangle_\lambda$  vs  $1/\bar{T}$  very close to the critical point  $\bar{a}_0 \approx 1.40$ . For small enough  $1/\bar{T} \gtrsim 20$  the function fits very well to a power law  $\bar{T}^{-\nu}$  with  $\nu = 0.67$ . At low enough temperature we leave the critical region and the behavior is no longer a power law as depicted in the sketch on the right side.

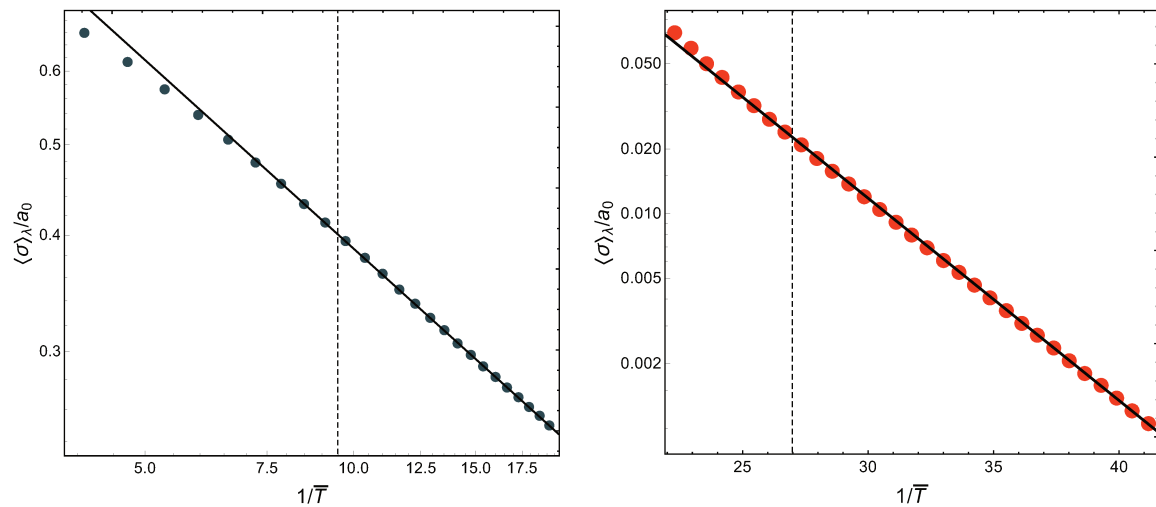


**Figure 5.15:** **Left:** Log-log zoom of the region  $1/\bar{T} \lesssim 20$  shown in figure 5.14 and fit (black line). Only points that are located on the right of the dashed line are used for the fit. **Right:** Log plot zoom for  $1/\bar{T} \gtrsim 20$  (figure 5.14), where an exponential decay is recovered. Again the black line corresponds to the fit where only points that are on the right of the dashed line are taken into account.

#### 5.4.4 Results

We start with analyzing the impact of finite temperature on the QPT in WSMs. Subsequently, we consider the effects of disorder on the smearing of the QPT. Next, we comment on indications for the observation of rare regions, followed by studying the influence of varying the correlation of the disorder signal. The accuracy of the numerical procedure is discussed in appendix A.3.4.

##### Temperature effects

First, we study the effects of a finite temperature on the clean QPT, which were already partially analyzed in [142]. Finite temperature generically smoothens the sharp quantum phase transition into a crossover (see left panel in figure 5.13). Eventually, for high enough temperature, the AHC is non-zero everywhere and the topologically trivial phase becomes inaccessible in the entire  $\bar{a}$ -range. We have analyzed the decay of the anomalous Hall conductivity  $\langle\sigma\rangle_\lambda$  as a function of  $\bar{T} = T/M$  for several values of  $\bar{a}$  moving towards the quantum critical point  $\bar{a}_c$  (right panel of figure 5.13). Outside of the quantum critical region for  $\bar{a} < \bar{a}_c$ , we find an exponential decay of the form (see right panel in figure 5.13):

$$\langle\sigma\rangle_\lambda \sim e^{-c/\bar{T}}, \quad (5.68)$$

where  $c$  is not independent of  $\bar{a}_0$ . The exponential fall-off is consistent with the presence of a mass gap outside the quantum critical region which breaks the scale invariance. Moving close to the quantum critical region, i.e. in the vicinity of  $\bar{a}_c$ , this behavior is modified. As shown in figure 5.14, at high enough  $\bar{T}$  the decay follows a power law:

$$\langle\sigma\rangle_\lambda \sim \bar{T}^{-\nu}, \quad (5.69)$$

where the ‘‘critical exponent’’ is found to be  $\nu = 0.67$  (consider the left half of figure 5.15 for the fit). This is a clear signature of the presence of a scale invariance inside the quantum critical region. Decreasing the  $1/\bar{T}$  parameter further, we get back to an exponential decay. This can be understood from the sketch on the right panel of figure 5.14: When getting close to zero temperature  $\bar{T} = 0$ , the critical region becomes thinner and thinner. At some point the system is again outside the quantum critical region and the exponential behavior due to the mass gap is restored. Following the critical region up to  $\bar{T} = 0$  requires a high numerical accuracy. We leave this for a future investigation including backreaction, which will allow us to directly probe the QCP at zero temperature.

##### Disorder effects

For studying the shape of the quantum phase transition at finite disorder, we computed the integrated anomalous Hall conductivity  $\langle\sigma\rangle_{\lambda,\text{dis}}$  in presence of the Gaussian disorder (5.62) with increasing disorder strength  $\bar{\gamma} \equiv \gamma\Delta k/M$  for a fixed low temperature  $\bar{T} = 1/(10\pi)$  as a function of  $\bar{a}_0$  in the vicinity of the critical region (figure 5.16). The low temperature was chosen for having a pronounced difference between the trivial and the non-trivial phase at zero disorder when sweeping over the critical region. We see that the sharp QPT gets smeared out in the presence of disorder. Close to the critical value  $\bar{a}_c \approx 1.40$  the smearing is well approximated by an exponential tail of the form:

$$\langle\sigma(\bar{a}_0)\rangle_{\lambda,\text{dis}} \sim c_1 e^{c_2(\bar{a}_c - \bar{a}_0)^{c_3}}, \quad (5.70)$$

as depicted in the right panel of figure 5.16. The parameter  $c_3$  was obtained as  $c_3 \approx 1.28$  and was found to be independent of the disorder strength up to the underlying numerical accuracy. On the contrary, the other coefficients  $c_1, c_2$  depend strongly on the disorder strength  $\bar{\gamma}$ . The obtained functional dependence, concretely the invariance of the exponent  $c_3$  with respect to the details of the randomness, is in agreement with the results obtained with optimal fluctuation theory.<sup>11</sup>

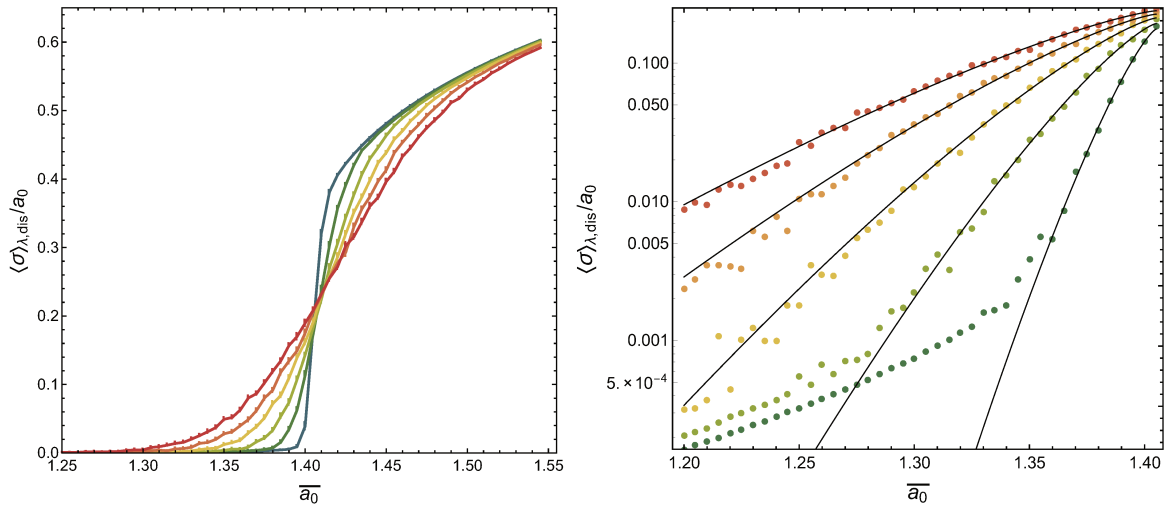


**Figure 5.16:** **Left:** Anomalous Hall conductivity as a function of  $\bar{a}_0$  for  $\bar{\gamma} = (3 + 6k) \cdot 10^{-3}$  with  $k = 0, 1, \dots, 5$  (blue-red). **Right:** Semi-logarithmic plot of the AHC against  $\bar{a}_0$  for  $\bar{\gamma} = (3 + 6k) \cdot 10^{-3}$  with  $k = 1, \dots, 5$  (green-red). At too low disorder the scaling behavior of the clean QPT supersedes the influence of the disorder and the data becomes hard to fit, i.e. we left out the dataset with  $\bar{\gamma} = 3 \cdot 10^{-3}$  here. Black lines correspond to the exponential fit (5.70).

Next we consider the temperature scaling of  $\langle \sigma \rangle_{\lambda, \text{dis}}$  for different but fixed values of the disorder strength  $\bar{\gamma}$  close to the critical configuration  $\bar{a}_0 = \bar{a}_c$ . As a preliminary result, we find evidence for a log-oscillatory behavior in accordance with the predicted existence of a discrete scale invariance at the disordered quantum critical point (cf. subsection 5.4.1). To be precise, we find a behavior that is compatible with the form (see figure 5.17):

$$\langle \sigma(\bar{T}) \rangle_{\lambda, \text{dis}} \sim \frac{a_1}{\bar{T}^{a_2}} (1 + a_3 \sin(a_5 - a_4 \log \bar{T})) , \quad (5.71)$$

though we remark that we do not have enough data points to make a robust statement.

Unfortunately, for extending our computation to very low temperatures and high disorder strengths we must leave the probe limit and take the full backreaction to the spacetime into account, which is out of the scope of this work. Nevertheless, the acquired data provides us with promising indications in favor of a discrete scaling symmetry.

<sup>11</sup>Concretely, we refer to optimal fluctuation theory for composition tuned quantum smeared phase transitions, with  $c_3 = 2 - d/\eta$ , where  $\eta$  is the so-called finite size shift exponent, which depends only on the details of the clean QPT (see for example [111]).

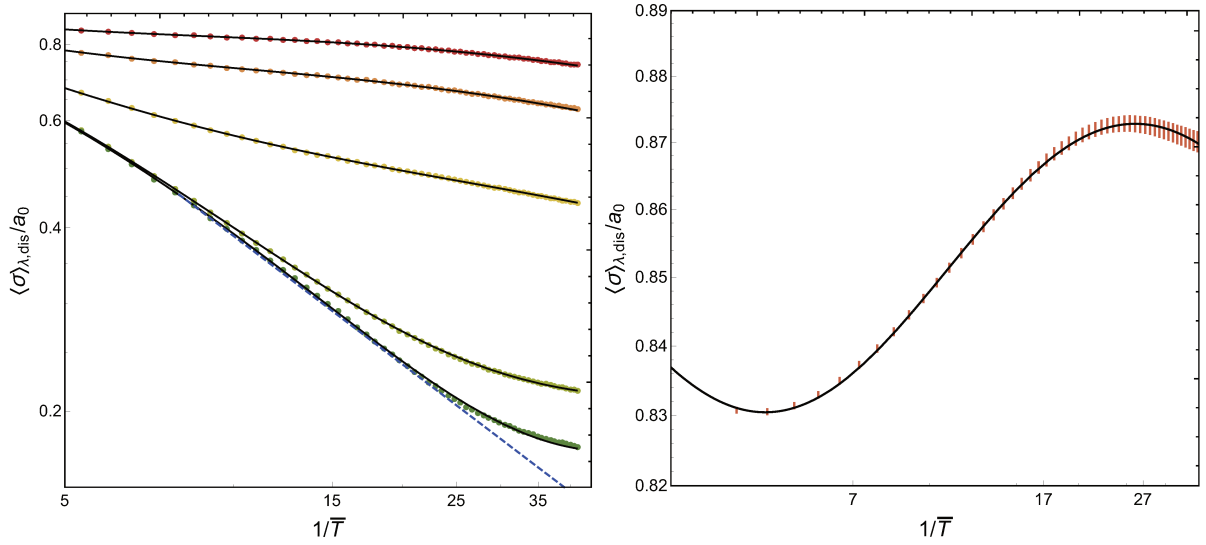


**Figure 5.17:** **Left:** Log-Log plot at the critical point  $\bar{a}_0 = 1.40$  with increasing disorder strength  $\bar{\gamma} \in \{0.03, 0.04, 0.24, 0.44, 0.60\}$  (green-red). At low disorder (green line) the data approximates the power law decay found at zero disorder and shown in blue-dashed line. **Right:** Data at  $\bar{\gamma} = 0.44$  (orange line in the left panel), divided by  $(1/\bar{T})^{0.2}$ , fitted with ansatz (5.71).

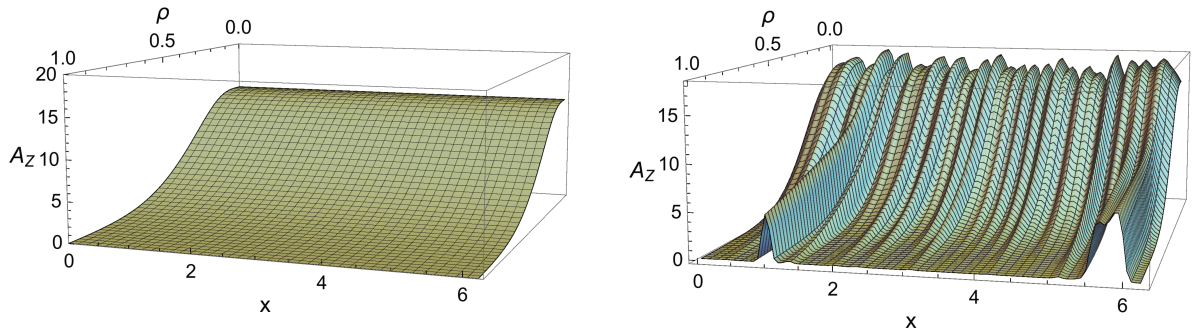


**Figure 5.18:** A concrete configuration of the gauge field along the bulk for  $\pi\bar{T} = 1/10$ ,  $\bar{a}_0 = 1.35$  and  $\bar{\gamma} = 0, 0.002$  (left, right).

### Indications of rare regions

After having described the quantitative effects of disorder on the scaling of the order parameter  $\langle \sigma \rangle_{\lambda}$ , we would like to look at qualitative effects of disorder when considering the bulk field  $A_z$  of our holographic model with special emphasis on its horizon behavior.

Therefore, we consider a concrete but typical realization of the bulk profile of the gauge field component  $A_z$  at low temperature  $\bar{T} = 1/(10\pi)$  for a subcritical value of  $\bar{a}_0 = 1.35$  and compare the results of a homogeneous and a disordered configuration. As expected, we obtain a vanishing gauge field at the horizon, i.e. zero anomalous Hall conductivity, in the absence of disorder (see left panel of figure 5.18).

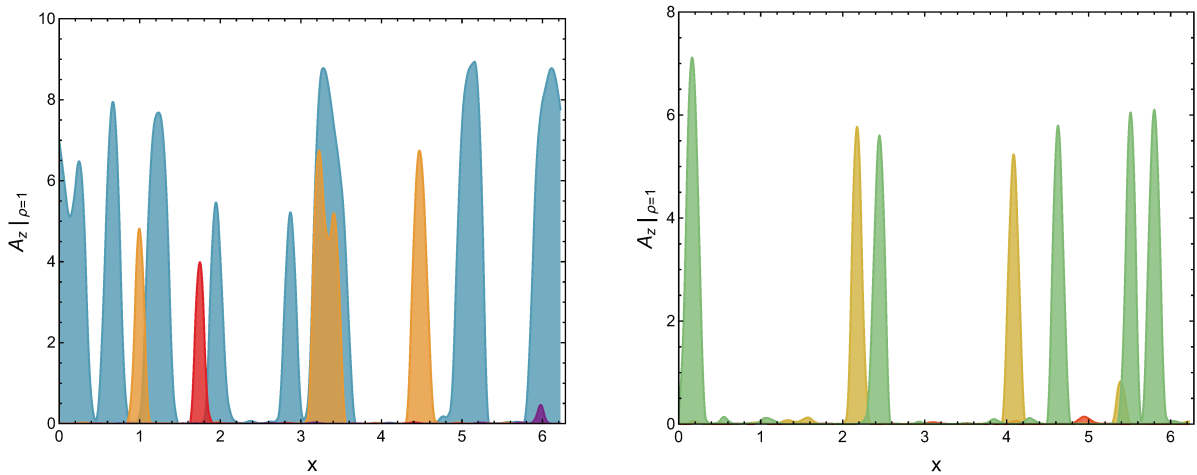


**Figure 5.19:** The profile of the gauge field  $A_z$  at the horizon and the appearance of the rare regions. **Left:** At fixed disorder strength  $\bar{\gamma} = 0.002$  approaching the critical point. We take  $\bar{a}_0 = 1.25, 1.30, 1.35, 1.40$  (purple, red, orange, blue). **Right:** At fixed  $\bar{a}_0 = 1.35$  and increasing strength  $\bar{\gamma} = 0.010, 0.020, 0.025$  (red, yellow, green).

On the other hand, the presence of a disordered source triggers the appearance of localized areas at the horizon where the gauge field  $A_z$  does not vanish (right panel of figure 5.18). As a consequence, the integrated AHC acquires a finite value that was not present in the clean system in accordance with the results of the AHC-disorder scaling analysis, which showed a smearing of the QPT.

Consequently, we extend this qualitative analysis by studying representative properties of the shape of  $A_z|_{\rho=1}$  when varying the order parameter  $\bar{a}_0$  for different disorder strengths  $\bar{\gamma}$ . In the left panel of figure 5.19 we show several realizations of  $A_z|_{\rho=1}$  for fixed disorder strength  $\bar{\gamma}$  and increasing  $\bar{a}_0$ . The appearance of localized areas with non-vanishing AHC is apparent. As the system is tuned closer to the critical value of  $\bar{a}_0$  these rare regions become broader and less rare. A similar behavior is found for fixed  $\bar{a}_0$  and increasing disorder strength  $\bar{\gamma}$ , as shown in the right panel of figure 5.19. We note, that these regions become suddenly large, as soon as the amplitude of  $\bar{a}(x)$  exceeds the critical value  $\bar{a}_c$ , even when its mean  $\bar{a}_0$  is still below  $\bar{a}_c$ . Accordingly, it is tempting to interpret these areas as indications of so-called rare regions, which were discussed in the previous subsection 5.4.1.

Finally we remark, that we considered more than 10 randomly chosen configurations to see whether the observed behavior can be considered as being representative in terms of the underlying statistics. Correspondingly, the qualitative arguments provided in this paragraph should be merely taken as a first step for further research.

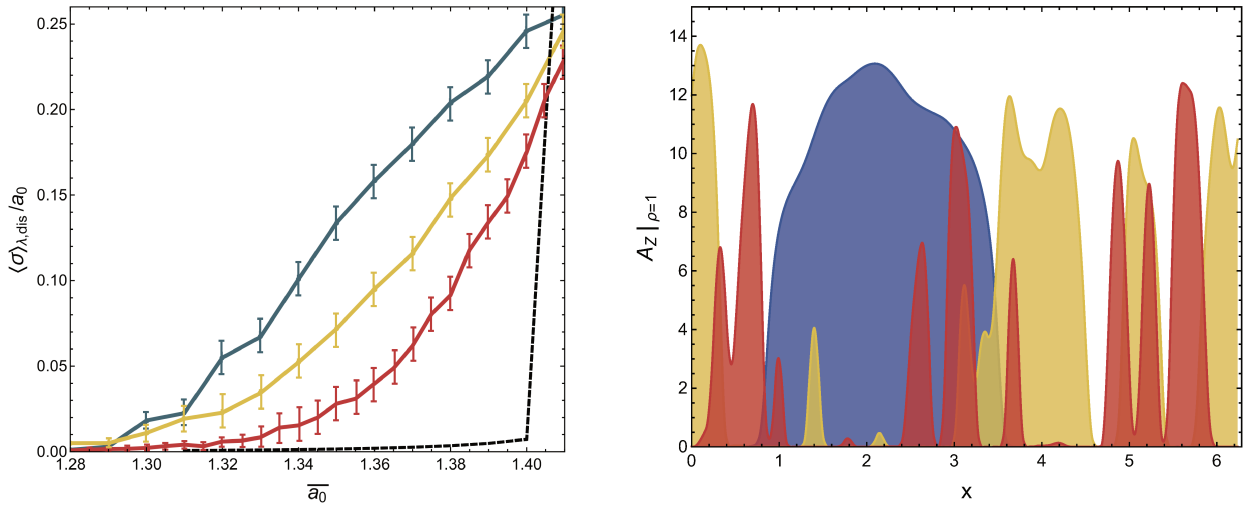


**Figure 5.20:** **Left:** AHC close to the critical  $\bar{a}_0$  for fixed  $P = 0.15$ ,  $\pi \bar{T} = 1/10$  and increasing correlation  $\alpha_{\text{cor}} = 0.0, 0.5, 2.0$  (red, yellow, blue). Black dashed line shows the AHC at zero disorder. **Right:** Evolution of the rare regions with alpha for  $\alpha_{\text{cor}} = 0.0, 0.5, 2.0$  (red, yellow, blue) at fixed  $P = 0.15$ . Localized regions become broader, as expected for increasingly correlated disorder.

### Varying the correlation

Additionally, we studied the role of the disorder correlation on the quantum phase transition and its smearing. Correspondingly, we computed the anomalous Hall conductivity  $\langle \sigma(\bar{a}_0) \rangle_{\lambda, \text{dis}}$  as a function of  $\bar{a}_0$  for three different values of the correlation coefficient  $\alpha_{\text{cor}}$  (cf. relation (5.64)) at fixed spectral power  $P$  (5.66) of the disorder signal and for a constant number of modes  $N_{\text{dis}} = 30$ . Figure 5.20, shows the obtained behavior of the conductivity for  $\alpha_{\text{cor}} = 0.0, 0.5$  and  $2.0$ , where the highest value of  $\alpha_{\text{cor}}$  corresponds to a signal with high correlation. As a result, we see that the disorder correlation indeed plays a role close to the QPT. Concretely, we find that a positive correlation increases the smearing of the order parameter, which is in agreement with the theoretical predictions [52, 162, 189]. On the right panel of figure 5.20 we show a concrete realization of the gauge field  $A_z$  at the horizon for fixed power  $P$  and increasing correlation. We observe how increasing  $\alpha_{\text{cor}}$  gives rise to broader, less rare, regions that have undergone the phase transition. This is in accordance with the theoretical expectation, since a larger correlation length should naturally lead to an increasing length scale of localized structures.



## 5.5 Summary

In the first part of this chapter, we investigated the surface states of a holographic Weyl semimetal. This is a step further in the understanding of topological phases within strongly coupled quantum field theories using holography. At low temperatures, a current is generated in the presence of a chemical potential along the surface of a holographic Weyl semimetal. Crucially, this current vanishes at the interface of two topologically trivial phases. Moreover, the integrated current only depends on the global order parameters, namely the anomalous Hall conductivities of the two phases. This is a strong indication of the topological nature of the surface states. Furthermore, the dependence of the integrated current on the order parameters is completely determined by the anomaly. This is a non-trivial statement since the local current is sensitive to higher order corrections in the effective inhomogeneous axial magnetic field naturally arising in a (realistic) interface. It would be interesting to investigate how our result constrains the form of higher order transport coefficients in the presence of inhomogeneous axial magnetic fields.

In the second part of this chapter, we studied the effects of temperature and quenched disorder on a quantum phase transition in holography. In particular, we focused on the probe limit analysis of the holographic Weyl semimetal quantum phase transition (QPT) in presence of 1-D Gaussian disorder. First we investigated the effects of temperature on the clean QPT appearing at  $\bar{a}_c \approx 1.40$ . Finite temperature enhances the anomalous Hall conductivity (AHC) and tends to destroy the trivial phase, where the AHC vanishes. The decrease of the AHC towards  $\bar{T} \rightarrow 0$  was obtained to be:

- Exponential decay  $\sim e^{-c/\bar{T}}$  for values of the external parameter far from the critical point  $\bar{a} < \bar{a}_c$  outside the quantum critical region. This is consistent with the presence of a finite mass gap.
- Power law decay  $\sim \bar{T}^{-\nu}$  around the critical point  $\bar{a} \approx \bar{a}_c$ , i.e. inside the quantum critical region. This is strong evidence for the presence of scale invariance at criticality.

In addition, we introduced disorder into the system and studied the fate of the QPT. The smearing of the sharp QPT is the main consequence of the presence of disorder. Its shape appears to be consistent with the expectations from condensed matter theory [200] and optimal fluctuations arguments [111]. Moreover, we investigated the temperature fall-off of the integrated AHC  $\langle \sigma(\bar{T}) \rangle_{\lambda, \text{dis}}$  in presence of disorder. We see indications of a log-oscillatory behavior of the AHC as a function of  $\bar{T}$  within the critical region and at sufficiently high disorder strength. This can be interpreted as a first sign for the emergence of a disordered fixed point connected with discrete scale invariance [188].

Subsequently, we showed that modifying the correlation indeed plays a role in the smearing of the quantum phase transition. Concretely, we were able to demonstrate that a positive correlation enhances the smearing of the AHC around the QPT, which is expected from condensed matter theory studies [52, 162, 189].



---

# Conclusions and outlook

---

The main results of this thesis concern two major topics: The numerical construction of localized black holes (LBHs) in five, six and ten spacetime dimensions and numerical studies of interfaces as well as disorder effects in holographic Weyl semimetals (WSMs). We emphasize that a summary regarding the results of the construction of LBHs can be found in subsection 4.4. The results of the investigation of surface states as well as finite temperature and disorder phenomena of WSMs were summarized in subsection 5.5.

In this chapter we would like to draw conclusions from the obtained results, discuss their scientific implications and reflect on significant techniques. Furthermore, we provide an outlook and comment on possible future developments.

## Localized black holes

We presented a robust method for constructing highly accurate numerical approximations of LBH solutions in  $D = 5$ ,  $D = 6$  and  $D = 10$ . We remark, that our method can be easily adapted to different dimensions as well as different compactifications. As a result, we were able to investigate the phase diagram of the corresponding LBH solutions and compare with the regarding non-uniform black string (NBS) results. In particular, in  $D = 5, 6$  our data provides strong evidence in favor of a merger of the LBH and NBS branches, which is accompanied by distorted logarithmic spirals in suitable phase diagrams. Additionally, we were able to show that the critical behavior changes qualitatively when studying the LBH configuration in  $D = 10$ .

Our findings, in particular the concrete values of the critical exponents, are in excellent agreement with the theoretical predictions of [132, 133]. This is a strong evidence in favor of Kol's double cone conjecture. Interestingly, the infinite spiraling behavior in  $D = 5, 6$  is related to a discrete scaling symmetry of the thermodynamic quantities in the critical region (cf. reference [188] for a review of this phenomenon). Moreover, the spirals lead to the formation of an infinite number of small phase space regions describing LBHs with positive specific heat.

We further note, that such a spiraling behavior has been spotted also for other configurations, such as hairy black holes in  $AdS_5 \times S^5$  [31] and when considering the transition of black rings to so-called lumpy black holes [57, 66]. Interestingly, also the study of disorder phenomena in WSMs provided us with first hints in favor of the presence of a discrete scaling symmetry.

Finally we remark, that the presented construction of LBHs would not have been possible without crucial adaptations to the underlying numerical methods. In particular, the decomposition of the integration domains and the utilization of individual coordinate transformations enabled the resolution of the very high gradients at the exposed axis. Furthermore, the special decomposition of the asymptotic region into several linearly connected subdomains guaranteed the rapid fall-off of the spectral coefficients, which would have been otherwise spoiled by non-analytic contributions at the singular boundary corresponding to (compactified) infinity. Finally, to our best knowledge, a non-smooth reference metric within the DeTurck approach has not been used in a similar fashion before. The simple ansatz for the reference metric combined with

uncomplicated coordinate transformations, leads to a notable reduction of the complexity of the resulting field equations and made the numerical scheme much less error prone while improving roundoff-stability together with the computational speed.

After providing highly accurate data for LBHs in five, six and ten dimensions, the investigation of the missing configurations in the interval  $6 < D < 10$  as well as the study of some more high-dimensional setups for  $D > 10$  would be an obvious next step. Especially higher dimensional configurations and the study of different compactification schemes offer the greatest potential for the discovery of new phenomena, since the numerical data is still quite rare here. While the situation for  $6 < D < 10$  should be qualitatively similar to  $D = 5$  and  $D = 6$ , we expect further qualitative changes of the phase diagram of Kaluza-Klein black holes for  $D > 10$  according to references [132, 73]. For  $D > 10$  we expect that the critical behavior is governed by two independent real critical exponents, in contrast to the degenerate case in  $D = 10$ . Furthermore, parts of the NBS branch are expected to become thermodynamically preferred over the UBS solution for  $D > 11$  and the entire NBS branch is supposed to be entropically favored over the UBS branch for  $D > 13$ . Consequently, the development of a simple highly accurate construction scheme for NBS solutions is desirable. References [121, 122] provide an excellent starting point for such a project, raising the question whether the DeTurck method could improve the stability and reduce the complexity of the methods presented there. We remark, that NBS solutions have been constructed before in up to  $D = 15$  dimensions (cf. reference [73]), but a high accuracy analysis of the predicted UBS-NBS merger is still not available for  $D > 11$ .

As another very interesting point, the double cone metric emerged also in the context of other topology changing transitions. A good analytic example is provided by reference [67], investigating the merger of a Kerr black hole horizon in de Sitter spacetime with the related cosmological horizon for  $D > 5$ . In addition, reference [67] provides further examples of possible double-cone related topology changes, such as the aforementioned black ring to lumpy black hole transition for  $D > 5$ . Consequently, the numerical methods provided in this thesis are expected to be applicable in a wide range of fascinating configurations.

As discussed in appendix A.2.4, the  $D = 10$  configuration is conjectured to be dual to certain thermal states of a two-dimensional supersymmetric Yang-Mills (SYM) theory compactified to a circle. Here, the construction of the NBS solution, which corresponds to non-uniform phases of the SYM, was already provided in [59]. Nevertheless, a high accuracy analysis of the corresponding LBH-NBS merger has not been carried out so far and should be one of the next steps to be considered. Needless to say, that this would be a valuable consistency check of the conjectured gauge/gravity duality.

As a final consideration, there is no reason for constraining the study of Kaluza-Klein black hole configurations to asymptotically flat spaces. Correspondingly, asymptotically  $AdS_5 \times S^5$  black holes that are localized on the  $S^5$  were considered in reference [56]. While being thermodynamically preferred at low energies, there is a first order phase transition to  $AdS_5 - \text{Schwarzschild} \times S^5$  at higher energies. According to the AdS/CFT correspondence, this transition is conjectured to be dual to spontaneous symmetry breaking of  $\mathcal{N} = 4$  SYM. We expect, that our method can also be applied for acquiring high accuracy results in this and many similar cases. Specifically the AdS/CFT correspondence provides us with a large diversity of potentially interesting problem setups.

## Holographic WSMs

In the second part of this thesis we studied the effects of inhomogeneities in holographic WSMs. First we developed a model for representing an interface between different topological phases of a WSM. Consequently, we were able to show that this particular model resembles the main characteristics of real world WSM surface states (Fermi arcs), i.e. a finite integrated current localized at the interface (chiral pseudo-magnetic effect). At this point we remark, that an explicit connection of these boundary currents with the surface states of WSMs were established within recent works [88]. As a major result, we were able to relate this integrated current to the difference of the anomalous Hall conductivities of the distinct phases.

The study of finite temperature effects within a homogeneous WSM revealed an algebraic scaling relation of the order parameter (the anomalous Hall conductivity) close to the critical point. This is in agreement with the expected behavior in the vicinity of a quantum critical point and was observed before for other quantum critical systems. For instance, the reader may refer to [76] for an investigation of quantum critical effects in nematic Fermi fluids.

Exposing the holographic WSM model to quenched disorder, that does not satisfy the Harris criterion, led to the predicted smearing of the quantum phase transition. Similar behavior was observed for holographic superconductors, cf. reference [99]. Furthermore, the indications for log-oscillatory behavior in the temperature scaling of the order parameter at finite disorder can be interpreted as the consequence of a discrete scale invariance related to a disordered fixed point, as mentioned before in subsection 5.5. We refer the reader to [75] for a recent work related to discrete scale invariance in holography. These results hint to the question whether the emergence of a discrete scaling symmetry can be considered as a general feature of strongly correlated quantum system at finite disorder. Thus experimental validations of these effects are highly desirable.

As a last point, the formation of rare regions in the disordered phase is not a feature specifically related to our WSM system. We refer the reader to [23] for an investigation of these effects in holographic superconductors. Apart from the holographic approach, these structures were studied before in Ising ferromagnets [86], Ising spin-glasses [172] and metals [202]. Overall, we expect that these results can contribute to the understanding of disorder effects in strongly coupled quantum systems beyond the Harris criterion.

An obvious next step would be the exploration of the full holographic WSM system, including a backreaction to the spacetime metric. While being much more challenging with respect to the required numerics, this corresponds to taking higher order contributions of the fermionic operators on the strongly coupled quantum field side into account. In this realm, we expect the obtained results for the boundary currents within our interface model to remain valid. However, backreaction comes with the possibility for obtaining the “pure”  $T = 0$  configurations. As a result, a high accuracy study of the temperature scaling for the chiral pseudo-magnetic current would be possible in the vicinity of the quantum critical point. Here we expect a scaling behavior that is directly given by the regarding scaling of the anomalous Hall conductivity as suggested by our previous results.

Another interesting task concerns the investigation of the structure of the observed chiral pseudo-magnetic in dependence of the details of the given interface profile. For more complicated shapes of the interface a computation of the longitudinal conductivities could give us new insights. Theoretical expectations predict a negative magnetoresistance in this case, as for the chiral magnetic effect, i.e. a scaling of the conductivity according to  $\sigma \sim B^2$ , cf. reference [159]. In addition, it would be interesting to adapt our model for investigating surface states of topological

insulators within holography.

Also for the disorder analysis the main, numerical demanding, but very valuable direction, would be the study of the same setup with full backreaction. This would allow us to implement several improvements: Full control on the bulk solution up to zero temperature, a complete analysis of the disordered fixed points and the possibility of computing more observables like entropy, heat capacity and longitudinal conductivities as well as viscosities (cf. references [142, 141]) in the presence of disorder. Of course it would be extremely interesting to extend our preliminary results by analyzing the log-oscillatory structures with the required reliability. As another important point, we would like to study disorder effects at different holographic quantum phase transitions, for example [54, 55], and test to which extent our results are universal.

A next step would be the construction of consistent top-down models exhibiting the WSM phase transition between topological trivial and non-trivial phases. These models are expected to come with more complicated interaction terms in the Lagrangian. However, such terms would not change the principal symbol of the underlying differential operator and hence our numerical algorithms could also be applied straightforwardly in these cases.

Of course a study of disorder effects on the properties of an interface configuration would be another attractive project.

As the final words of this thesis we emphasize the significance of studying configurations related to gravity in higher dimensions: As one point higher dimensions provide a possible basis for the unification of the fundamental forces and might also shed some light on the hierarchy problem of physics (cf. reference [171]). Moreover, supergravity configurations in higher-dimensional asymptotically anti-de Sitter spaces can provide us with new insights into strongly coupled quantum systems, that cannot be obtained by other methods that are available today. We expect that the set of numerical routines, which were developed in the course of this thesis, will help to acquire valuable results related to various other problems in higher dimensional gravity.

---

# Supplementary material

---

## A.1 Theoretical basics

### A.1.1 Frame expressions for curvature quantities

As mentioned before, non-coordinate basis formulations can help to remove singular factors from tensor entries.

For illustration, let us consider the following example of a flat space metric in Cartesian coordinates for  $D = 2$  in coordinate basis

$$ds_{2D}^2 = dx^2 + dy^2. \quad (\text{A.1})$$

Compactifying the  $x$ - and  $y$ -directions according to (cf. reference [34])

$$x(\xi) = \frac{\alpha\xi}{\sqrt{1-\xi^2}}, \quad \xi \in [-1, 1], \quad y(\eta) = \frac{\beta\eta}{\sqrt{1-\eta^2}}, \quad \eta \in [-1, 1],$$

with  $\alpha, \beta \in \mathbb{R}_{>0}$ , leads to

$$ds_{2D}^2 = \frac{\alpha^2}{(1-\xi^2)^3} d\xi^2 + \frac{\beta^2}{(1-\eta^2)^3} d\eta^2. \quad (\text{A.2})$$

We note that the metric (A.2) exhibits two independent singular factors  $\alpha^2 / (1-\xi^2)^3$  and  $\beta^2 / (1-\eta^2)^3$  in the coordinate basis frame  $\{d\xi, d\eta\}$ . Introducing the coordinate frame basis according to the following frame coefficients

$$e^\mu_i = \begin{pmatrix} \frac{\alpha}{(1-\xi^2)^{3/2}} & 0 \\ 0 & \frac{\beta}{(1-\eta^2)^{3/2}} \end{pmatrix}, \quad (\text{A.3})$$

we obtain the frame basis metric (in matrix form)

$$\eta_{ij} = \begin{pmatrix} 1 & 0 \\ 0 & 1 \end{pmatrix}, \quad (\text{A.4})$$

which is now free of singular factors. Accordingly, we can avoid singularities in a variety of frame basis quantities. The singular factors are of course not completely erased, but are constrained to the frame coefficients  $e^\mu_i$  and their derivatives.

Starting from the definition of the spin coefficients

$$\omega_\mu^i_j = e_\nu^i e^\lambda_j \Gamma_{\mu\lambda}^\nu - e^\lambda_j \partial_\mu e_\lambda^i, \quad (\text{A.5})$$

we define<sup>1</sup>

$$\omega_{\mu ij} := \eta_{ik} \omega_{\mu j}^k, \quad (\text{A.6})$$

$$\omega_{ijk} := e_i^\mu \eta_{jl} \omega_{\mu k}^l. \quad (\text{A.7})$$

By projecting the indices of the Riemann tensor to the frame basis, we obtain

$$R_{ijkl}^i = \omega_{l j,k}^i - \omega_{k j,l}^i + \omega_{k m}^i \omega_{l j}^m - \omega_{l m}^i \omega_{k j}^m + \omega_{m j}^i \left( \omega_{l k}^m - \omega_{k l}^m \right), \quad (\text{A.8})$$

where

$$\omega_{l j,k}^i = e_k^\mu \partial_\mu \omega_{l j}^i.$$

Correspondingly, the Ricci tensor in the frame basis reads

$$R_{ij} = \omega_{j i,k}^k - \omega_{k i,j}^k + \omega_{k l}^k \omega_{j i}^l - \omega_{j l}^k \omega_{k i}^l + \omega_{l i}^k \left( \omega_{j k}^l - \omega_{k j}^l \right). \quad (\text{A.9})$$

With the help of these tensor relations, a formulation of the Einstein equations, that allows for a nice, explicit control and separation of singularities, can be achieved.<sup>2</sup>

### A.1.2 Conformal transformations

This subsection provides a short summary on conformal transformations. A detailed review on this topic can be found in [32] and [12].

First we provide a rather general definition of a conformal map. We start by considering two semi-Riemannian manifolds  $M$  and  $N$  with metric  $g$  on  $M$  and  $h$  on  $N$ . A smooth map  $\phi : M \rightarrow N$  is called conformal map if the pull-back of  $\phi$  acting on  $h$  satisfies  $\phi^*h = \Omega^2 g$  where  $\Omega \in C^\infty(M)$ . Both manifolds are called conformally equivalent if there exists a diffeomorphic conformal map between them. All conformal diffeomorphisms of a manifold  $M$  onto itself form a group which is called the conformal group  $CO(M, g)$ .

Now let us concentrate on conformal transformations of the Minkowski space  $(M, g) = (\mathbb{R}^{d+1}, \eta^{(d,1)})$  which are of particular interest in the context of quantum field theories. It can be shown that every conformal transformation<sup>3</sup> of Minkowski space can be built as a composition of the following 3 transformations

1. Poincaré transformations, i.e. translations and Lorentz transformations,
2. Dilatations:  $x \mapsto \lambda x$  for  $\lambda \in \mathbb{R}_{>0}$ ,
3. Special conformal transformations (SCFTs):  $x \mapsto \frac{1+x^2 b}{1+2b_\mu x^\mu + b^2 x^2}$  for  $b \in \mathbb{R}^{d+1}$ .

Note the singular nature of the SCFTs for  $x = \frac{b}{b^2}$  which is cured by considering a conformal compactification of Minkowski.

<sup>1</sup>We remark, that the relations (A.6) and (A.7) should be defined explicitly, since the spin connection is no tensor and therefore index operations on it are not clear a priori.

<sup>2</sup>Of course, not all singularities can be separated and removed in this way, cf. true curvature singularities or singularities that develop dynamically.

<sup>3</sup>Actually, we are considering every conformal transformation in the connected component of the identity.



---

The associated conformal algebra  $\mathfrak{co}(d, 1)$  is spanned by the following generators

1.  $P_\mu$  and  $J_{\mu\nu}$ : the generators of translations and Lorentz transformations,
2.  $D$ : the generator of infinitesimal dilatations,
3.  $K_\mu$ : the generator of the SCFTs.

As an interesting fact, one can show that the conformal algebra  $\mathfrak{co}(d, 1)$  is isomorphic to  $\mathfrak{so}(d + 1, 2)$ , which gives a first glimpse on the AdS/CFT correspondence since  $SO(d + 1, 2)$  is the apparent symmetry group of the hyperboloid considered in section 2.2.1 about the anti-de Sitter spacetime.

## A.2 Localized black holes

### A.2.1 Numerical parameters

The values of the grid parameters  $L$ ,  $q_0$ ,  $q_1$ ,  $q_i$ ,  $\varphi_i$ ,  $s_1$  and  $s_2$  for the LBH configuration with almost touching poles can be found in table A.1. The value of  $\lambda$  was adapted for obtaining the desired accuracy. We increased  $\lambda$  up to  $\lambda \approx 10$  for the solutions that are closest to the critical transition.

**Table A.1:** Grid parameters for LBH solutions in the critical regime for  $D = 5, 6$  and  $D = 10$ . The parameters are explained in figures 4.8 and 4.9.

$D$	$L$	$q_0$	$q_1$	$q_i$	$\varphi_i$	$s_1$	$s_2$
5, 6	8	0.5	1.5	1	0.1	0	0.8
10	8	2	3	2.5	0.1	$L$	$5L$

We emphasize that the values in table A.1 are appropriate for the construction of a first solution. As an initial guess for the Newton-Raphson method, we need to use a sufficiently good approximation of a LBH solution. In practice the reference metric (cf. subsection 4.2.2) turned out to be an acceptable first guess for relatively small LBHs, i.e. with  $\kappa \approx 2$  (in units where  $L = 8$ ). Subsequently  $\kappa$  is modified for computing another physically inequivalent solution, where the last obtained solution provides the initial guess. This procedure can be applied until a turning point in  $\kappa$  is reached. Such extreme points are handled with the trick presented in reference [58] section VII.B.

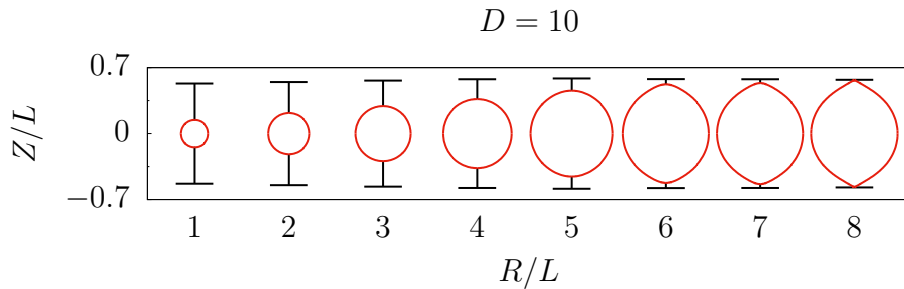


**Figure A.1:** Spatial embeddings of the horizons for different LBH solutions in  $D = 10$ .

### A.2.2 Horizon embeddings for $D = 10$

Figure A.1 displays a number of horizon embeddings for LBH solutions in  $D = 10$ , based on the coordinate embedding relations (4.59) and (4.60). We see that the LBH horizons in  $D = 10$  show less eccentricity than the configurations for  $D = 5, 6$  that were presented in figure 4.14.

### A.2.3 Scaling analysis

#### Scaling of the NBS data in $D = 5, 6$

Table A.2 provides the fit results for the NBS branch in  $D = 5, 6$ , which were taken from reference [122]. As mentioned in subsection 4.3.3, the real critical exponent  $b$  and log-periodicity  $c$  show a good agreement with the predicted values:

- For  $D = 5$ :  $b_{pred,5} = 3/2$  and  $c_{pred,5} = \sqrt{15}/2 \approx 1.9365$ ,
- For  $D = 6$ :  $b_{pred,6} = c_{pred,6} = 2$ .

**Table A.2:** Parameter values of the fit (4.62) for the thermodynamic quantities of the NBS in  $D = 5$  and  $D = 6$ .

	$f$	$f_c$	$a$	$b$	$c$	$d$
$D = 5$	$M/M_{GL}$	1.6771932	0.7161	1.4995	1.9364	3.6215
	$n/n_{GL}$	0.7795282	0.1691	1.5010	1.9375	5.8367
	$T/T_{GL}$	0.6738646	0.2295	1.4998	1.9358	0.6010
	$S/S_{GL}$	2.6718297	2.1232	1.4994	1.9369	3.6237
$D = 6$	$M/M_{GL}$	2.1839096	1.59247	1.99923	1.99932	0.74457
	$n/n_{GL}$	0.5855195	0.30918	1.99487	1.99655	2.76608
	$T/T_{GL}$	0.7419027	0.21640	1.99512	2.00111	4.00513
	$S/S_{GL}$	3.0961720	3.23682	2.00071	1.99891	0.74332

#### Critical scaling of the geometrical quantities in $D = 5, 6$

As stated in subsection 4.3.3, we need an adapted ansatz for examining the critical behavior of the proper horizon length  $L_{\mathcal{H}}$ , due to its continuous growth in the critical regime. We consider the following ansatz, which includes a non-oscillating term

$$L_{\mathcal{H}}(Q) = L_c - a_1 Q^{b_1} + a_2 Q^{b_2} \cos(c_2 \log Q + d_2), \quad (\text{A.10})$$

where  $L_c$ ,  $a_1$ ,  $b_1$ ,  $a_2$ ,  $b_2$ ,  $c_2$  and  $d_2$  are the new fit parameters.  $L_c$  denotes the critical horizon length and we should have  $b_1 < b_2$  for obtaining a leading non-oscillating part. The corresponding fits are depicted in figure A.2, which again show excellent agreement close to the critical point. The computed fit parameters can be found in tables A.3 and A.4. As expected, we notice that the values for  $b_2$  and  $c_2$  are in good agreement to the predicted values. We obtain approximately the same value for  $b_1 \approx 1$  for all configurations and dimensions, i.e. the horizon length is directly proportional to  $Q$  at leading order when approaching the critical point. For  $D = 10$  we were not able to separate the gauge dependent growth contribution from the gauge-invariant part.

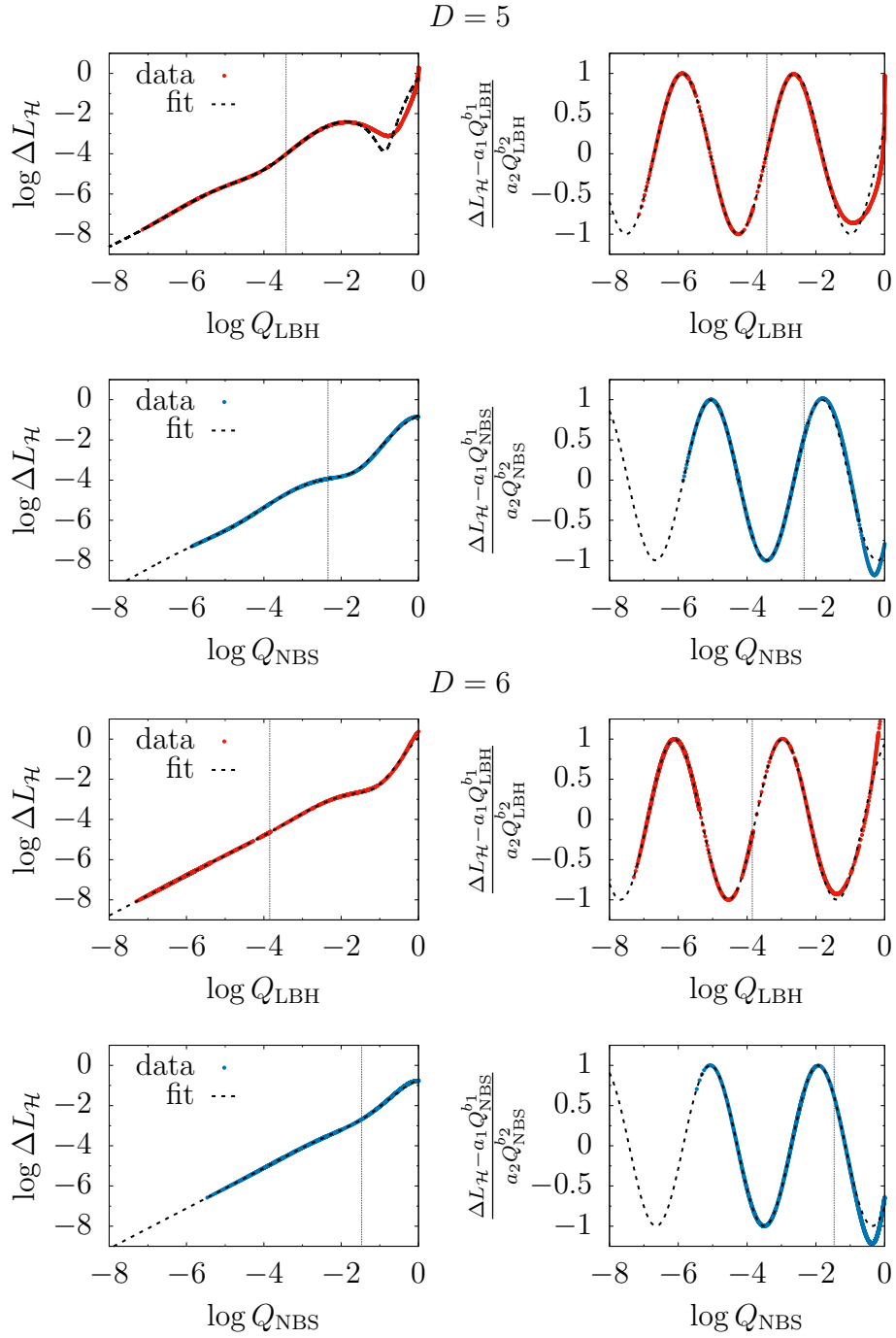


**Figure A.2:** Data points (red dots for LBHs and blue dots for NBSs) and fit (blue solid lines) of the horizon length  $L_{\mathcal{H}}$  as a function of  $Q_{\text{LBH}}$  or  $Q_{\text{NBS}}$ . In the left column the explicit functional dependence is shown, where both axes are log-scaled. To resolve the tiny subleading oscillations of the functions, a rescaled version is shown in the right column, where  $\Delta L_{\text{polar}} = L_{\text{c}} - L_{\mathcal{H}}/L$ . The first two rows correspond to  $D = 5$ , while the last two rows correspond to  $D = 6$ . For each plot, all data points to the left of the dotted vertical line served as input data for the fit.

**Table A.3:** Parameter values for the horizon length  $L_{\mathcal{H}}$  for LBHs and NBSs when fitted with (A.10) in  $D = 5$ .

	$L_c$	$a_1$	$b_1$	$a_2$	$b_2$	$c_2$	$d_2$
LBH	1.428268	0.5548	1.0024	0.7976	1.4976	1.9267	1.9116
NBS	1.428265	0.2441	1.0041	0.2319	1.5046	1.9500	3.5614

**Table A.4:** Parameter values for the horizon length  $L_{\mathcal{H}}$  for LBHs and NBSs when fitted with (A.10) in  $D = 6$ .

	$L_c$	$a_1$	$b_1$	$a_2$	$b_2$	$c_2$	$d_2$
LBH	1.464800	0.4564	0.99999	0.6558	1.9998	2.0001	2.7909
NBS	1.464801	0.3273	0.99960	0.2143	1.9898	1.9985	3.8530

#### A.2.4 Localized black holes and $\mathcal{N} = (8, 8)$ SYM

As mentioned in the main text, KK black holes in  $D = 10$  can be related to certain thermal states of a two-dimensional  $\mathcal{N} = (8, 8)$  supersymmetric Yang-Mills (SYM) theory compactified to a circle  $S^1$  with gauge group  $SU(N)$  in the large  $N$  limit. LBHs correspond to a spatially deconfined phase within the SYM, while UBSs and NBSs are related to spatially confined phases. Note that the aforementioned SYM can be characterized by three dimensionless quantities: The rank of the gauge group  $N$ , the dimensionless 't Hooft coupling constant<sup>4</sup>  $\lambda = Ng_{YM}^2 L^2$  and the dimensionless temperature  $\mathfrak{T}$  given by the product of the ordinary temperature and the length of the circle  $L$ . In the following, we denote the (dimensionless) thermodynamic quantities of the SYM by  $\mathfrak{U}$  for the energy,  $\mathfrak{T}$  for the temperature and  $\mathfrak{S}$  for the entropy.

According to [5, 96, 59], the relation between the SYM and KK black holes in  $D = 10$  can be obtained by applying the following solution generating technique

1. We lift the  $D = 10$  solution up to  $D = 11$  and perform a boost in the new coordinate, followed by a Kaluza-Klein reduction.
2. The result is a solution in type IIA supergravity. Concretely, the LBH solutions in  $D = 10$  with  $\mathbb{R}^{1,8} \times S^1$  asymptotics correspond to localized D0-branes in type IIA supergravity.
3. As a next step a T-duality transformation is applied, which converts the type IIA supergravity solution into an type IIB supergravity solution.
4. As a last step we take the decoupling limit between the string and gravitational length scales on the type IIB gravity side, which corresponds to taking the limit  $N \rightarrow \infty$  with  $\lambda$  fixed on the SYM side, and to consider the large  $\lambda$  limit in a second step. The details of the decoupling limit are rather intricate and we refer the reader to the references [5, 96, 59] for a detailed description of the underlying limits.

<sup>4</sup>Note that the Yang-Mills coupling constant  $g_{YM}$  has the dimension of energy in two-dimensions.

### Thermodynamic quantities

As a result of this procedure, we can interrelate the thermodynamic quantities of the SYM to the thermodynamic properties of the KK black holes. In particular, considering the normalized quantities  $\tilde{\mathcal{U}} = \mathcal{U} \cdot \lambda^2 / N^2$ ,  $\tilde{\mathcal{T}} = \mathcal{T} \cdot \lambda^{1/2}$  and  $\tilde{\mathcal{S}} = \mathcal{S} \cdot \lambda^{3/2} / N^2$ , we obtain (cf. reference [59])

$$\tilde{\mathcal{U}} = 64\pi^2 (2\tilde{M} - \tilde{S}\tilde{T}), \quad \tilde{\mathcal{T}} = 4\sqrt{2}\pi\tilde{S}^{1/2}\tilde{T}^{3/2}, \quad \tilde{\mathcal{S}} = 16\sqrt{2}\pi^3\tilde{S}^{1/2}\tilde{T}^{-1/2}, \quad (\text{A.11})$$

where  $\tilde{M}$ ,  $\tilde{T}$  and  $\tilde{S}$  denote the black hole mass, temperature and entropy normalized according to

$$\tilde{M} = \frac{G_{10}M}{L^7}, \quad \tilde{T} = TL, \quad \tilde{S} = \frac{G_{10}S}{L^8}, \quad (\text{A.12})$$

with the gravitational constant in ten dimensions  $G_{10}$ . In addition, the (dimensionless) free energy  $\mathfrak{F}$  of the canonical SYM ensemble and its normalized version  $\tilde{\mathfrak{F}} = \mathfrak{F} \cdot \lambda^2 / N^2$  are given by  $\mathfrak{F} = \mathcal{U} - \mathcal{S}\mathcal{T}$  and  $\tilde{\mathfrak{F}} = \tilde{\mathcal{U}} - \tilde{\mathcal{S}}\tilde{\mathcal{T}}$ .

### Results

Figure A.3 shows the phase diagrams of the microcanonical (left) and canonical (right) ensemble of the uniform (blue) and localized (red) phases of the  $\mathcal{N} = (8, 8)$  SYM. For the microcanonical ensemble, we see that the localized phase is thermodynamically preferred over the uniform phase up to some threshold value of the normalized internal energy  $\tilde{\mathcal{U}}_{PT}$ , where the uniform phase starts to dominate. There is a first order phase transition, where the entropy of the uniform phase exceeds the entropy of the localized branch. We have a similar picture when considering the canonical phase diagram. Here, lower values of the free energy  $\tilde{\mathfrak{F}}$  correspond to the thermodynamically preferred phase. Accordingly, we see that the localized phase is dominating for small values of the normalized temperature  $\tilde{\mathcal{T}}$ . As before, the uniform phase becomes thermodynamically preferred at some threshold value  $\tilde{\mathcal{T}}_{PT}$ . We remark that including the inhomogeneous SYM phase (corresponding to NBSs) would not alter this picture of thermodynamic stability, since the related branch is thermodynamically inferior for all configurations, as can be seen from the data presented in reference [59].

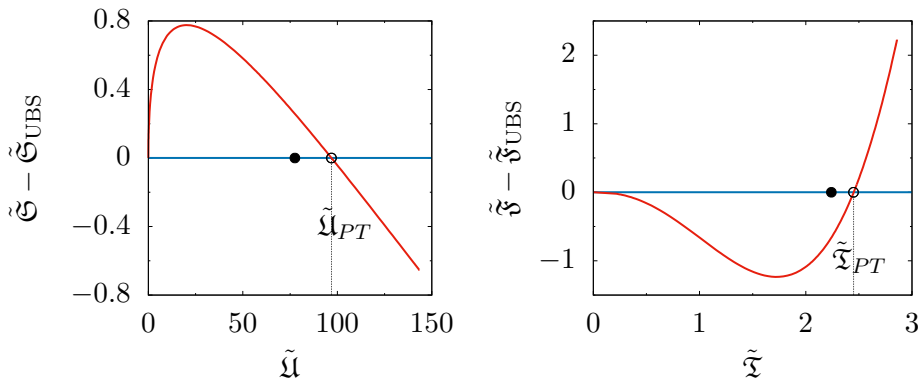


**Figure A.3:** Phase diagram of  $\mathcal{N} = (8, 8)$  SYM on a circle with length  $L$  in the microcanonical (left) and canonical (right) ensemble. We plot the difference of entropy and free energy, respectively, to the corresponding values of the uniform branch, which is represented as the blue zero line in these diagrams with the black circle indicating the solution where the Gregory-Laflamme instability arises. The localized branch, represented by the red line, is thermodynamically favored over the uniform branch for small masses or small temperatures.

With the procedure described at the end of the current section, we determine the first order phase transition between the localized and the uniform phase in the microcanonical ensemble to be at

$$\tilde{\mathcal{U}}_{PT} = 96.9053906163(1). \quad (\text{A.13})$$

For the canonical ensemble we find

$$\tilde{\mathcal{T}}_{PT} = 2.451118333749(1). \quad (\text{A.14})$$

Moreover, the (dimensionless) latent heat associated with the first order phase transition is given by

$$\Delta\tilde{\mathcal{Q}} = \tilde{\mathcal{T}}_{PT} \cdot (\tilde{\mathcal{S}}_{UBS}(\tilde{\mathcal{T}}_{PT}) - \tilde{\mathcal{S}}_{LBH}(\tilde{\mathcal{T}}_{PT})), \quad (\text{A.15})$$

where  $\tilde{\mathcal{S}}_{UBS}(\tilde{\mathcal{T}}_{PT})$  and  $\tilde{\mathcal{S}}_{LBH}(\tilde{\mathcal{T}}_{PT})$  are the normalized entropies associated with the uniform phase (UBS) and the localized phase (LBH). Note that we can obtain the latent heat also by differentiating the normalized free energy with respect to  $\tilde{\mathcal{T}}$ , i.e.:

$$\Delta\tilde{\mathcal{Q}} = \tilde{\mathcal{T}}_{PT} \left. \frac{\partial (\tilde{\mathcal{S}}_{LBH} - \tilde{\mathcal{S}}_{UBS})}{\partial \tilde{\mathcal{T}}} \right|_{\tilde{\mathcal{T}}=\tilde{\mathcal{T}}_{PT}}. \quad (\text{A.16})$$

By means of our numerics we determine the latent heat to be

$$\Delta\tilde{\mathcal{Q}} = 9.47738683316(1). \quad (\text{A.17})$$

We used both formulas (A.15) and (A.16) and compared the results for obtaining the value (A.17). The comparison showed a slightly better convergence of the specific heat obtained from (A.15) (by two digits), which is not surprising, since formula (A.16) involves the evaluation of a numerical derivative.

## Summary

We obtained the phase diagrams of the localized and uniform phases of the two-dimensional  $\mathcal{N} = (8, 8)$  supersymmetric SYM theory compactified to a circle  $S^1$  with gauge group  $SU(N)$  in the large  $N$  limit from the corresponding LBH and UBS data. The localized branch was found to be predominating for small energies or temperatures, whereas the uniform phase becomes thermodynamically favored at some threshold values of the energy  $\tilde{\mathcal{U}}_{PT}$  or temperature  $\tilde{\mathcal{T}}_{PT}$ . We obtained the threshold values with unprecedented accuracy and additionally computed the latent heat  $\Delta\tilde{\mathcal{Q}}$  of the related first order phase transition.

Especially the values  $\tilde{\mathcal{U}}_{PT}$ ,  $\tilde{\mathcal{T}}_{PT}$  and  $\Delta\tilde{\mathcal{Q}}$  are the basis for a comparison of our results with regarding data from quantum lattice calculations. We refer the reader to the references [42, 41, 116] for lattice results that show indications of a first-order phase transition.

## Determining the phase transition

In order to obtain a highly-accurate value for the position of the first order phase transition, we have to find the intersection point of the localized and the uniform branch in the phase diagrams, cf. figure A.3. For this purpose, we compute a series of localized black hole solutions with values of the control parameter  $\kappa$  that are distributed on a Lobatto grid around the intersection, i.e. for

$$\kappa_j = \frac{\kappa_{\text{end}} + \kappa_{\text{start}}}{2} - \frac{\kappa_{\text{end}} - \kappa_{\text{start}}}{2} \cos\left(\frac{\pi j}{N_\kappa}\right), \quad j = 0, \dots, N_\kappa. \quad (\text{A.18})$$

An interval  $\kappa \in [\kappa_{\text{start}}, \kappa_{\text{end}}]$  in which the corresponding phase transition is located can be easily identified once the data for producing the phase diagrams in figure A.3 is at hand. We took  $\kappa_{\text{start}} = 0.98$  and  $\kappa_{\text{end}} = 1.02$  (recall that we set  $L = 8$  in our computations). At each of the Lobatto points we calculate the relevant physical quantities (mass and entropy). By using standard pseudo-spectral techniques we are able to express these quantities in the given interval as a truncated Chebyshev series depending on  $\kappa$  with expansion order  $N_\kappa$ . Finally, we identify the phase transition point by determining the root of the difference of these functions and the analytically known uniform branch.

Moreover, this procedure even gives a straightforward way to calculate derivatives of the thermodynamic quantities in the corresponding interval  $[\kappa_{\text{start}}, \kappa_{\text{end}}]$  by using standard spectral algorithms, which can be employed for obtaining the latent heat, cf. equation (A.15). Besides that, we are able to check the first law of thermodynamics  $d\tilde{U} = \tilde{\chi}d\tilde{\mathcal{S}}$  in this interval as an additional consistency check of the numerical results. Indeed, the deviation from this law rapidly drops down as the resolution is increased and saturates at values of  $10^{-12}$ . The spectral convergence of this interpolation procedure is discussed in the next subsection.

### A.2.5 Accuracy

The numerical quality of the obtained LBH solutions was estimated by comparing a high-resolution reference solution  $u_{\text{ref}}$  to solutions  $u_N$  of lower resolution  $N$ . To carry out the comparison we interpolate the reference  $u_{\text{ref}}$  and the  $u_N$ 's to a high resolution grid  $\Sigma$  and take the maximum of their point-wise difference as an error norm

$$\mathcal{R}_N = \sup_{x \in \Sigma} |u_{\text{ref}}(x) - u_N(x)|. \quad (\text{A.19})$$

We observe a rapid decay of the residue  $\mathcal{R}_N$  as a function of  $N$  (l.h.s. of figure A.4) until saturation is reached at  $10^{-9}$  (for  $D = 5$  and  $D = 10$ ) and  $10^{-10}$  (for  $D = 6$ ) as a consequence of having a finite machine precision<sup>5</sup> combined with rounding errors. Note that we display  $\mathcal{R}_N$  in figure A.4 (left) for a configuration close to the critical transition, which serves as a kind of lower bound for the accuracy, since solutions away from the critical region are converging much faster.

In addition, we investigated the numerical violation of the Smarr relation  $\Delta_{\text{Smarr}}$  (r.h.s. of figure A.4) as a consistency check for the obtained solutions. The r.h.s. of figure A.4 shows a rapid decrease of  $\Delta_{\text{Smarr}}$  with increasing resolution until some saturation levels are approached. We notice that  $\Delta_{\text{Smarr}}$  saturates for  $D = 6$  at a level, that differs about two orders in magnitude from the corresponding level for  $D = 5$  and  $D = 10$ . The reason is that we performed two derivatives in order to extract the asymptotic coefficient  $c_t$  in  $D = 6$ , while only one derivative was used in  $D = 5$  and  $D = 10$ .

<sup>5</sup>For obtaining the results we used 80-bit extended double precision.



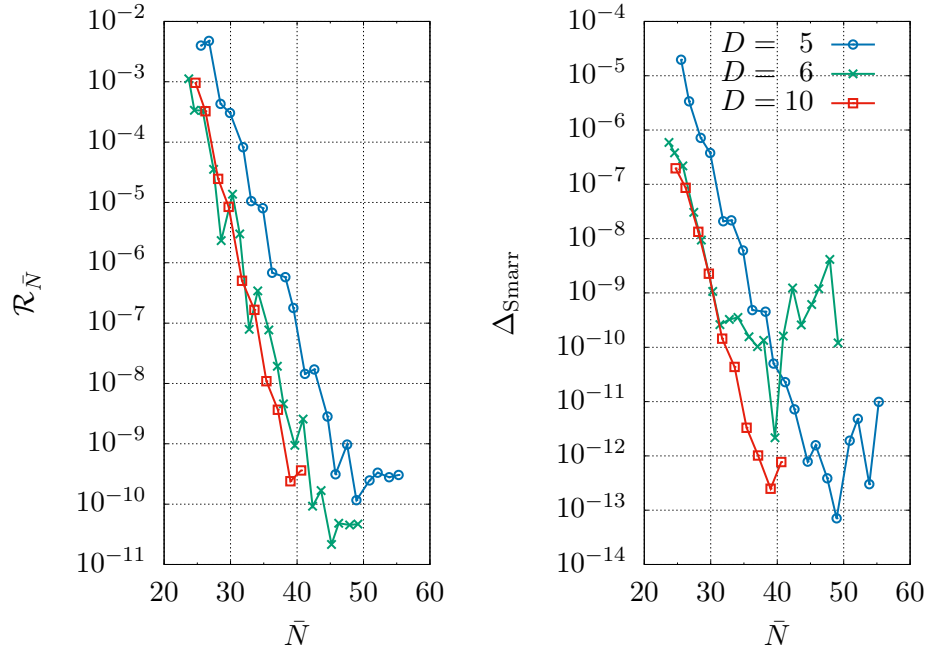


**Figure A.4:** Convergence of the residue  $\mathcal{R}_{\bar{N}}$  and the deviation from Smarr's relation  $\Delta_{\text{Smarr}}$  for the LBH solutions as a function of the mean resolution  $\bar{N}$ . The respective numerical solutions correspond to LBHs with proper separation of the poles of  $L_{\mathcal{A}}/L \approx 0.0029$  for  $D = 5$ ,  $L_{\mathcal{A}}/L \approx 0.00083$  for  $D = 6$  and  $L_{\mathcal{A}}/L \approx 0.007$  for  $D = 10$ .

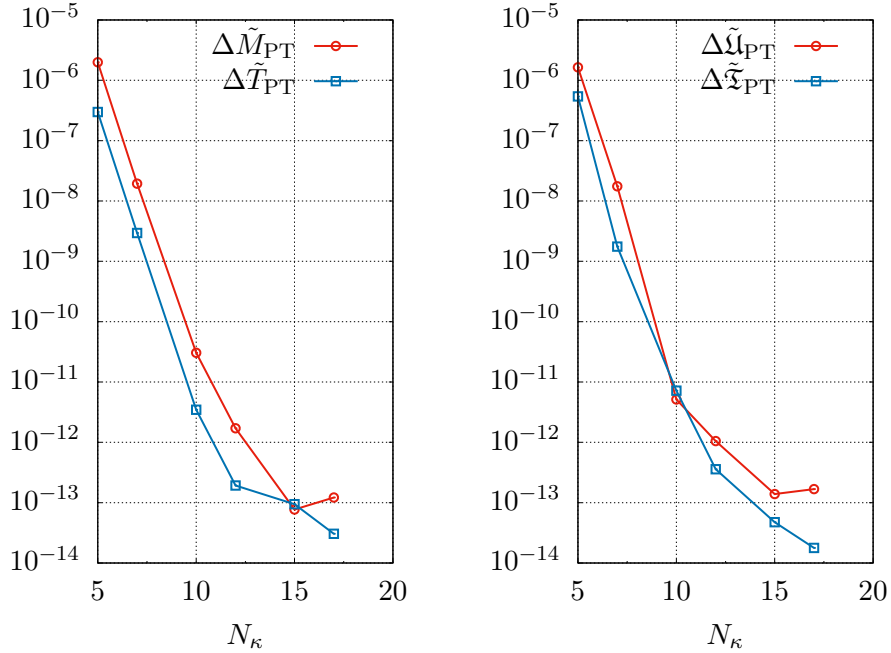


**Figure A.5:** Convergence of the numerical positions of the first order phase transition between the localized and the uniform phase. We show the phase transition points for the bare LBH data (A.12) (left) and for the transformed data (A.11) (right).

As the last point we monitored the non-trivial components of the DeTurck vector field  $\tilde{\zeta}^\mu$  (cf. subsection 2.1.2) to be always smaller than  $10^{-10}$  in magnitude on each point of the grid for all considered configurations. As we stated earlier, it is important that  $\sup_{x \in \Sigma} |\tilde{\zeta}^\mu(x)|$  remains small compared to the magnitudes of all the metric functions.

### Accuracy of the phase transition quantities for LBHs in $D = 10$ related to $\mathcal{N} = (8, 8)$ SYM

Due to the high accuracy of our localized black hole solutions, the spectral interpolation procedure for obtaining  $\tilde{\mathcal{U}}_{PT}$ ,  $\tilde{\mathcal{Z}}_{PT}$  and  $\Delta\tilde{\mathcal{Q}}$  (cf. subsection A.2.4) will give highly accurate values for the intersection points as well, at least if the resolution  $N_\kappa$  is high enough. Since we chose a rather small interval  $[\kappa_{\text{start}}, \kappa_{\text{end}}]$ , comparably small values of  $N_\kappa$  suffice. Moreover, this approach provides a natural estimation of accuracy for the phase transition values, simply by comparing the values obtained for different resolutions, similarly to the procedure described above. The result of this convergence analysis is shown in figure A.5. Note, that we obtained the phase transition points for the bare LBH data (A.12) (left) and for the transformed data (A.11) (right).

## A.3 Holographic Weyl semimetals

### A.3.1 Equations of motion

As described in chapter 5, the static AdS Schwarzschild metric and the following ansatz for the fields was used for the numeric construction

$$ds^2 = \frac{1}{\rho^2} \left( -f(\rho) dt^2 + \frac{d\rho^2}{f(\rho)} + dx^2 + dy^2 + dz^2 \right), \quad (\text{A.20})$$

$$A = A_z(x, \rho) dz, \quad (\text{A.21})$$

$$V = V_t(x, \rho) dt + V_y(x, \rho) dy, \quad (\text{A.22})$$

$$\phi = \phi(x, \rho). \quad (\text{A.23})$$

Here,  $f(\rho) = 1 - \rho^4$  is the blackness function. Plugging these fields in into the equations of motion (5.34)-(5.36), yields four elliptic PDEs for the non-trivial field components:

$$\begin{aligned} -\phi (q^2 \rho^2 A_z^2 + m^2) + (\rho^2 f' - 3\rho f) \partial_x \phi \\ + \rho^2 (\partial_\rho^2 \phi + f \partial_x^2 \phi) = 0, \end{aligned} \quad (\text{A.24})$$

$$\begin{aligned} 8\alpha \rho^2 f (\partial_x A_z \partial_\rho V_y - \partial_\rho A_z \partial_x V_y) + f \partial_x V_t \\ - \rho (\partial_\rho^2 V_t + f \partial_x^2 V_t) = 0, \end{aligned} \quad (\text{A.25})$$

$$\begin{aligned} (f - \rho f') \partial_x V_y + 8\alpha \rho^2 (\partial_x A_z \partial_\rho V_t - \partial_\rho A_z \partial_x V_t) \\ - \rho (\partial_\rho^2 V_y + f \partial_x^2 V_y) = 0, \end{aligned} \quad (\text{A.26})$$

$$\begin{aligned} -2q^2 \phi^2 A_z + \rho (\rho f' - f) \partial_x A_z + 8\alpha \rho^3 (\partial_\rho V_t \partial_x V_y - \partial_x V_t \partial_\rho V_y) \\ + \rho^2 (\partial_\rho^2 A_z + f \partial_x^2 A_z) = 0. \end{aligned} \quad (\text{A.27})$$

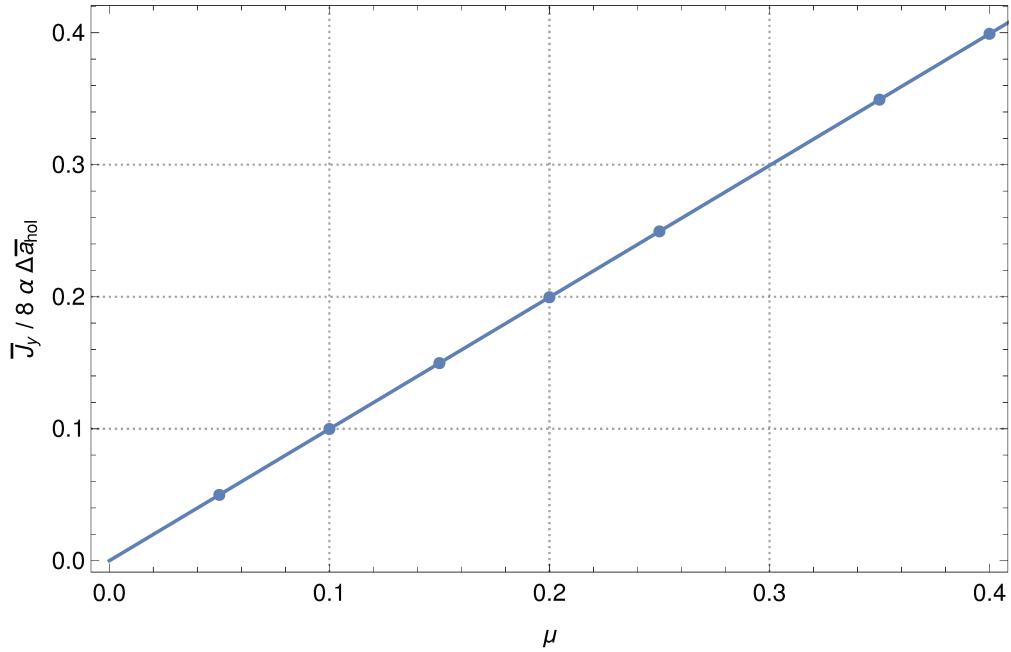


**Figure A.6:** Total current  $\bar{J}_y = J_y/M$  divided by  $8\alpha\Delta\bar{a}_{hol} = 8\alpha(a_L - a_R)/M$  as a function of the chemical potential  $\mu$  for fixed parameters  $\bar{a}_L = 0.4$ ,  $\bar{a}_R = 3$  and  $\pi\bar{T} = 1/16$ . We refer the reader to the weak result (5.55) for understanding the origin of the employed normalization.

### A.3.2 Parameter studies

The following studies were carried out to analyze the behavior of the holographic WSM system on all related parameters.

#### Chemical potential

The chiral pseudo-magnetic effect,  $\vec{j} = \mu\vec{B}_5$ , suggests a direct proportionality of the current density and the chemical potential. We remark, that we were not able to construct any solutions for values higher than  $\mu = 0.4$  with reasonable effort. This could be caused by an insufficient first guess or might be related to a breakdown of the probe-limit, since strong enough magnetic fields make the consideration of higher Fermion loop contributions necessary. The total current as a function of  $\mu$  is provided in figure A.6 for  $\alpha = 1$ ,  $\bar{a}_L = 0.4$ ,  $\bar{a}_R = 3$  and  $\pi\bar{M} = 1/16$ . Fitting the normalized total current  $\bar{J}_y = J_y/M$  as a linear function of  $\mu$ , gives a slope of 0.998 and an offset of  $10^{-8}$ , in agreement with our assumption.

#### Interface width

When studying the influence of the interface width  $l$ , we see that the obtained solutions depend strongly on  $l$  (cf. figure 5.8 in subsection 5.3.4), which is not surprising, since all scale invariance was removed from the EOM, when the location of the black hole horizon was fixed to be at  $\rho = 1$ . However, we note that the integrated current is independent of  $l$  to a good accuracy (cf. figure A.7). Fitting the points in figure A.7, yields a slope of 0.998 and an offset of  $-2 \times 10^{-5}$ . We remark that this result fits well to our interpretation of the current as a topological quantity.

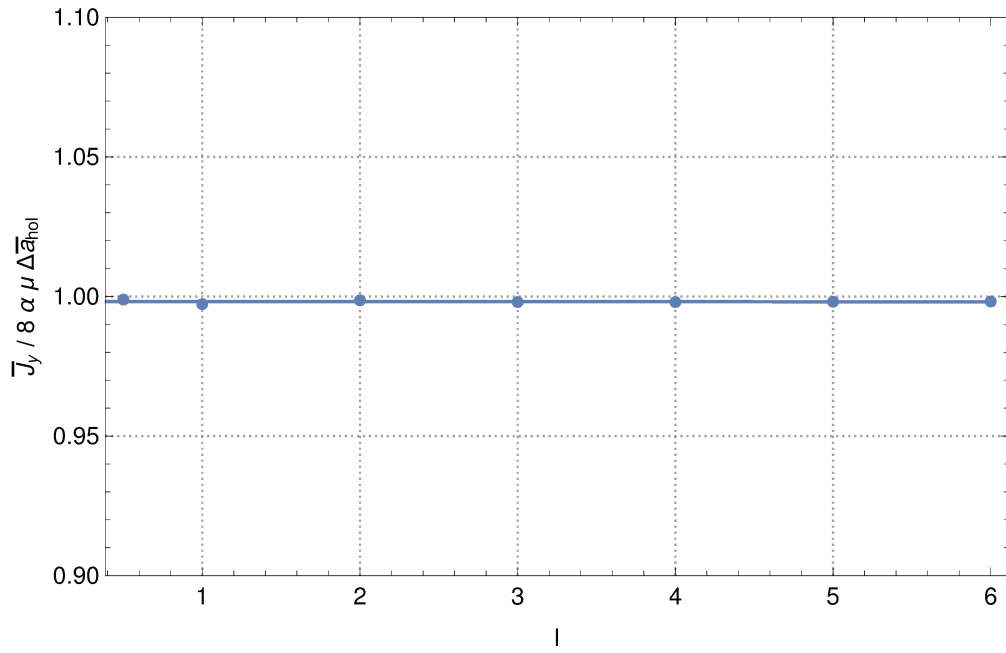


**Figure A.7:** Total current  $\bar{J}_y = J_y/M$  divided by  $8\alpha\mu\Delta\bar{a}_{hol} = 8\alpha\mu(a_L - a_R)/M$  as a function of the transition width  $l$  for fixed parameters  $\mu = 0.1$ ,  $\bar{a}_L = 0.4$ ,  $\bar{a}_R = 3$  and  $\pi\bar{T} = 1/16$ .

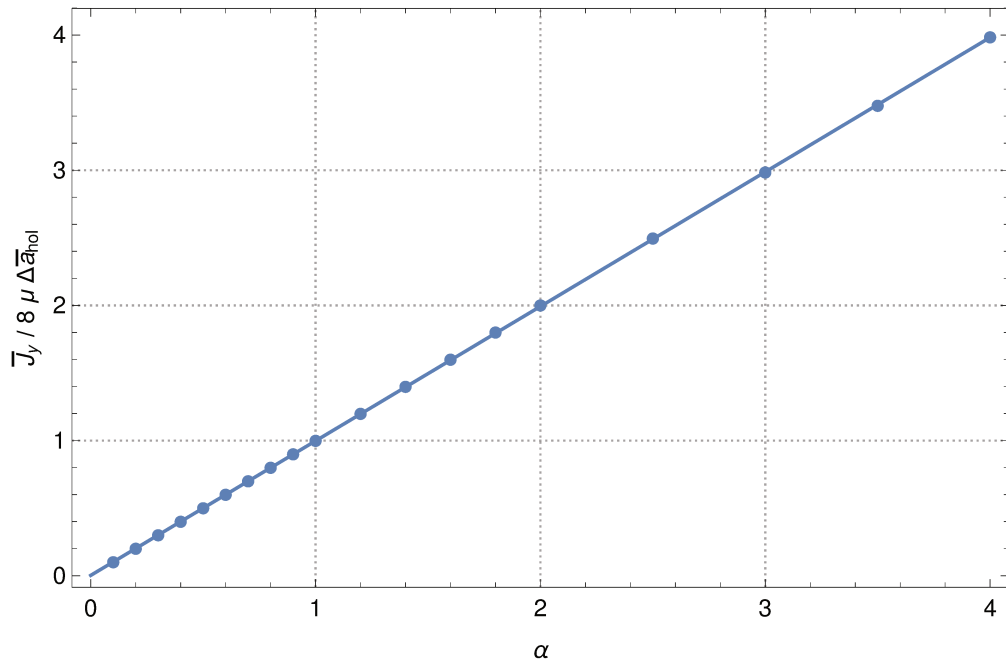


**Figure A.8:** Total current  $\bar{J}_y = J_y/M$  divided by  $8\mu\Delta\bar{a}_{hol} = 8\mu(a_L - a_R)/M$  as a function of the Chern-Simons coupling  $\alpha$  for fixed parameters  $\mu = 0.1$ ,  $\bar{a}_L = 0.4$ ,  $\bar{a}_R = 3$  and  $\pi\bar{T} = 1/16$ .

### Chern-Simons coupling

Studying the dependence of the integrated current as a function of the Chern-Simons coupling  $\alpha$ , we find a linear relation within the interval  $0 < \alpha < 4$  (see figure A.8). Fitting the points with a linear ansatz yields the result  $\bar{J}_y / (8\mu\Delta\bar{a}_{\text{hol}}) = 0.995\alpha + 0.003$ . Accordingly, we consider the current dependence on  $\alpha$  to be trivial in the corresponding interval and we can use an arbitrary value of  $0 < \alpha < 4$  for producing our results.

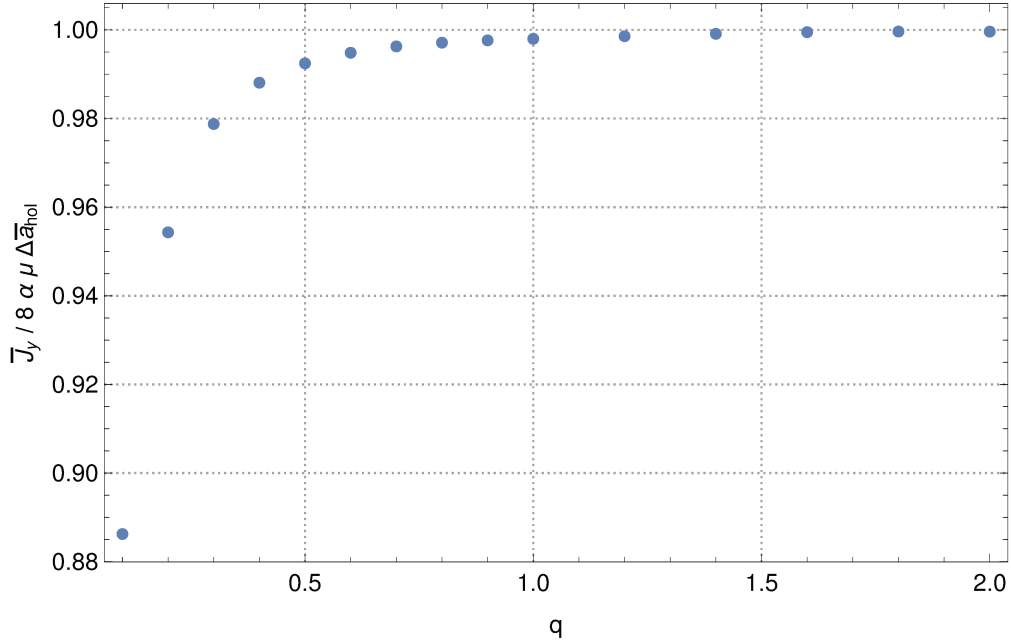


**Figure A.9:** Total current  $\bar{J}_y = J_y / M$  divided by  $8\alpha\mu\Delta\bar{a}_{\text{hol}} = 8\alpha\mu(a_L - a_R) / M$  as a function of the charge  $q$  for fixed parameters  $\mu = 0.1$ ,  $\bar{a}_L = 0.4$ ,  $\bar{a}_R = 3$  and  $\pi\bar{T} = 1/16$ .

### Axial charge of the scalar field

The integrated current depends in a non-trivial way on the charge  $q$  of the scalar field under the axial gauge field, which enters the formula for the axial anomaly (5.33), and hence contributes to the magnitude of the axial anomaly. Plotting the dependence of integrated current on  $q$  (cf. figure A.9), we notice that  $J_y$  first strongly increases for small  $q$  followed a plateau of saturation. This plateau is reached for  $q \approx 1$  where the deviation from 1 is less than 1%. This means, that our results do not depend on the concrete value of  $q$  for  $q \geq 1$ .

### A.3.3 Anomalous Hall conductivity

In this appendix we provide details about the computation of the anomalous Hall conductivity (AHC)  $\sigma_{\text{AHE}} := \sigma_{\text{AHE},yx}$ <sup>6</sup> in the inhomogeneous (but periodic) holographic Weyl semimetal. The computation is split in two parts: First we compute the so-called covariant part of  $\sigma_{\text{AHE},yx}$ . In a second step we calculate the contribution of the Chern-Simons term.

The full AHC is obtained by the Kubo formula (cf. reference [12])

$$\sigma_{\text{AHE},yx} = \lim_{\omega \rightarrow 0} \frac{1}{i\omega} \langle j_V^y j_V^x \rangle_{\text{cons}}, \quad (\text{A.28})$$

where  $\langle j_V^y j_V^x \rangle_{\text{cons}}$  denotes the consistent current 2-point function. The consistent current is given by (5.30):

$$\langle j_V^\mu \rangle_{\text{cons}} = \lim_{\rho \rightarrow 0} \sqrt{-g} \left( F^{4\mu} - 4\alpha \epsilon^{4\mu\tau\sigma\kappa} A_\tau F_{\sigma\kappa} \right), \quad (\text{A.29})$$

where we remind the reader that  $x^4 = \rho$  in our convention.

Accordingly, the consistent two-point function is given by

$$\begin{aligned} \langle j_V^\nu j_V^\mu \rangle_{\text{cons}} &= \delta \langle j_V^\mu \rangle_{\text{cons}} / \delta V_\nu \\ &= \lim_{\rho \rightarrow 0} \sqrt{-g} \left\{ \frac{\delta F^{4\mu}}{\delta V_\nu} - 4\alpha \epsilon^{4\mu\tau\sigma\kappa} \left( \frac{\delta A_\tau}{\delta V_\nu} F_{\sigma\kappa} + A_\tau \frac{\delta F_{\sigma\kappa}}{\delta V_\nu} \right) \right\}. \end{aligned} \quad (\text{A.30})$$

The covariant part of the two-point function is given by

$$\langle j_V^\nu j_V^\mu \rangle_{\text{cov}} = \lim_{\rho \rightarrow 0} \left( \sqrt{-g} \frac{\delta F^{4\mu}}{\delta V_\nu} \right). \quad (\text{A.31})$$

We obtain the Chern-Simons contribution as the remaining part of  $\langle j_V^\nu j_V^\mu \rangle_{\text{cons}}$ :

$$\langle j_V^\nu j_V^\mu \rangle_{\text{cons}} - \langle j_V^\nu j_V^\mu \rangle_{\text{cov}} = -4\alpha \epsilon^{4\mu\tau\sigma\kappa} \lim_{\rho \rightarrow 0} \sqrt{-g} \left( \frac{\delta A_\tau}{\delta V_\nu} F_{\sigma\kappa} + A_\tau \frac{\delta F_{\sigma\kappa}}{\delta V_\nu} \right). \quad (\text{A.32})$$

#### Covariant contribution

We consider an electric field in the  $x$ -direction and define the Hall conductivity as the response in the transverse  $y$ -direction while omitting the AHE lower index on  $\sigma_{\text{AHE},yx}$ :

$$\langle j_y \rangle = \sigma_{yx} E_x. \quad (\text{A.33})$$

In order to determine  $\sigma_{yx}$  we consider the following fluctuations of the vector gauge field  $V$  (for a vanishing background  $V_{BG} = 0$ )

$$\delta V = \left( \tilde{v}_t(\rho, x) e^{-i\omega t}, \tilde{v}_x(\rho, x) e^{-i\omega t}, \tilde{v}_y(\rho, x) e^{-i\omega t}, 0, 0 \right). \quad (\text{A.34})$$

<sup>6</sup>Recall that the AHE is constrained to the  $x$ - $y$ -plane for the separation of the Weyl nodes along the  $z$ -axis.

We impose in-going boundary conditions at the horizon as follows (cf. reference [12]):

$$\tilde{v}_t(\rho, x) = v_t(\rho, x) (1 - \rho)^{1-i\omega/4}, \quad (\text{A.35})$$

$$\tilde{v}_x(\rho, x) = v_x(\rho, x) (1 - \rho)^{-i\omega/4}, \quad (\text{A.36})$$

$$\tilde{v}_y(\rho, x) = v_y(\rho, x) (1 - \rho)^{-i\omega/4}, \quad (\text{A.37})$$

where  $v_\mu(\rho, x)$  are regular functions at the horizon. The covariant part of  $\sigma_{yx}$  is obtained from (A.31):

$$\sigma_{yx} = \lim_{\omega \rightarrow 0} \left[ \partial_\rho^2 v_y(0, x) / (i\omega) \right]. \quad (\text{A.38})$$

We are interested in the DC Hall conductivity. Hence we have to solve the equations of motion for the fluctuations only to first order in  $\omega$ . Moreover, we also perform an expansion in the Chern-Simons coupling  $\alpha$  and neglect terms of order  $\alpha^2$ :

$$v_t(\rho, x) = v_t^{(0,0)}(\rho, x) + v_t^{(1,0)}(\rho, x) \omega + v_t^{(0,1)}(\rho, x) \alpha + v_t^{(1,1)}(\rho, x) \omega \alpha + \dots, \quad (\text{A.39})$$

$$v_x(\rho, x) = v_x^{(0,0)}(\rho, x) + v_x^{(1,0)}(\rho, x) \omega + v_x^{(0,1)}(\rho, x) \alpha + v_x^{(1,1)}(\rho, x) \omega \alpha + \dots, \quad (\text{A.40})$$

$$v_y(\rho, x) = v_y^{(0,0)}(\rho, x) + v_y^{(1,0)}(\rho, x) \omega + v_y^{(0,1)}(\rho, x) \alpha + v_y^{(1,1)}(\rho, x) \omega \alpha + \dots, \quad (\text{A.41})$$

where the neglected terms (indicated by dots) are of order  $\mathcal{O}(\alpha^2, \omega^2, \dots)$ . In the following we discuss now the differential equations for  $v_t^{(m,n)}$ ,  $v_x^{(m,n)}$  and  $v_y^{(m,n)}$ .

Let us first consider the order  $\alpha^0 \omega^0$ . We obtain the following equations of motion for  $v_t^{(0,0)}$ ,  $v_x^{(0,0)}$  and  $v_y^{(0,0)}$  by plugging the expansions (A.39)-(A.41) into the full set of EOM (5.34) and expanding to lowest order in  $\omega$  and  $\alpha$

$$(1 + \rho + \rho^2 + \rho^3) v_t^{(0,0)} - (1 + \rho)^2 (1 + \rho^2) \partial_\rho v_t^{(0,0)} + \rho (1 - \rho^4) \partial_\rho^2 v_t^{(0,0)} + \rho \partial_x^2 v_t^{(0,0)} = 0, \quad (\text{A.42})$$

$$(1 + 3\rho^4) \partial_\rho v_x^{(0,0)} - \rho (1 - \rho^4) \partial_\rho^2 v_x^{(0,0)} = 0, \quad (\text{A.43})$$

$$(1 + 3\rho^4) \partial_\rho v_y^{(0,0)} - \rho (1 - \rho^4) \partial_\rho^2 v_y^{(0,0)} - \rho \partial_x^2 v_y^{(0,0)} = 0, \quad (\text{A.44})$$

while the constraint (equation (5.35)) evaluated at the horizon  $\rho = 1$  reduces to:

$$v_t^{(0,0)}(1, x) - \partial_x v_x^{(0,0)}(1, x) = 0. \quad (\text{A.45})$$

Switching on an electric field with a single component in  $x$ -direction, leads us to impose the following boundary conditions at the AdS boundary  $\rho = 0$ ,

$$v_t^{(0,0)}(0, x) = 0, \quad v_x^{(0,0)}(0, x) = 1, \quad v_y^{(0,0)}(0, x) = 0. \quad (\text{A.46})$$

The solution of (A.42)-(A.45) respecting these boundary conditions reads:

$$v_t^{(0,0)}(\rho, x) = 0, \quad v_x^{(0,0)}(\rho, x) = 1, \quad v_y^{(0,0)}(\rho, x) = 0. \quad (\text{A.47})$$



Next, we proceed with order  $\omega^1 \alpha^0$ . Repeating the same procedure as for the lowest order, we obtain for  $v_t^{(1,0)}$  and  $v_y^{(1,0)}$  the trivial solutions:

$$v_t^{(1,0)}(\rho, x) = 0, \quad v_y^{(1,0)}(\rho, x) = 0, \quad (\text{A.48})$$

while the solution for  $v_x^{(1,0)}(\rho, x)$  reads

$$v_x^{(1,0)}(\rho, x) = -\frac{i}{4} (\log(1 + \rho) - \log(1 + \rho^2)), \quad (\text{A.49})$$

where we imposed that  $v_x^{(1,0)}(0, x) = 0$  as well as regularity of  $v_x^{(1,0)}$  at the horizon. The order  $\omega^0 \alpha^1$  is trivial and we obtain

$$v_t^{(0,1)}(\rho, x) = 0, \quad v_x^{(0,1)}(\rho, x) = 0, \quad v_y^{(0,1)}(\rho, x) = 0. \quad (\text{A.50})$$

At order  $\omega^1 \alpha^1$  we are only interested in  $v_y^{(1,1)}(\rho, x)$ <sup>7</sup>, cf. equation (A.38). The relevant differential equation (A.26) yields

$$(1 + 3\rho^4) \partial_\rho v_y^{(1,1)} - \rho (1 - \rho^4) \partial_\rho^2 v_y^{(1,1)} - \rho \partial_x^2 v_y^{(1,1)} + 8i \rho^2 \partial_\rho A_z = 0. \quad (\text{A.51})$$

The solution to this differential equation is not  $x$ -independent and hence not simple to tackle with analytic methods.

Using the previous results, we can modify our expression for  $\sigma_{yx}$  as follows:

$$\sigma_{yx} = -i\alpha \partial_\rho^2 v_y^{(1,1)}(0, x). \quad (\text{A.52})$$

The last relation is obtained by taking the  $\omega \rightarrow 0$  limit. We define the averaged (or integrated) anomalous Hall conductivity  $\langle \sigma_{yx} \rangle_\lambda$  to be

$$\langle \sigma_{yx} \rangle_\lambda = -\frac{i\alpha}{\lambda} \int_0^\lambda dx \left[ \partial_\rho^2 v_y^{(1,1)}(0, x) \right]. \quad (\text{A.53})$$

In order to determine  $\langle \sigma_{yx} \rangle_\lambda$  we have to solve the partial differential equation (A.51). Let us first solve the homogeneous equation, i.e.

$$(1 + 3\rho^4) \partial_\rho v_y^{(1,1)} - \rho (1 - \rho^4) \partial_\rho^2 v_y^{(1,1)} - \rho \partial_x^2 v_y^{(1,1)} = 0. \quad (\text{A.54})$$

It is convenient to use a separation of variables ansatz of the form

$$v_y^{(1,1)}(\rho, x) = \sum_n v_{y(n)}^{(1,1)}(\rho) f_n(x). \quad (\text{A.55})$$

As a result of the assumed periodicity in  $x$ -direction, we can use a Fourier basis in this direction:

$$f_n(x) = \exp\left(i \frac{2\pi n}{\lambda} x\right), \quad (\text{A.56})$$

---

<sup>7</sup>For the electric field in  $x$ -direction, the solution for  $v_t^{(1,1)}$  and  $v_x^{(1,1)}$  is still trivial, i.e. it vanishes. As a result, the constraint is also satisfied.

and hence the homogeneous differential equation (A.54) for  $v_{y(n)}^{(1,1)}(\rho)$  becomes

$$(1 + 3\rho^4) \partial_\rho v_{y(n)}^{(1,1)} - \rho (1 - \rho^4) \partial_\rho^2 v_{y(n)}^{(1,1)} + \rho \left( \frac{2\pi n}{\lambda} \right)^2 v_{y(n)}^{(1,1)} = 0. \quad (\text{A.57})$$

Note that this is now an ordinary differential equation.

As a result of the averaging procedure, we obtain for  $\langle \sigma_{yx} \rangle_\lambda$ :

$$\langle \sigma_{yx} \rangle_\lambda = -i\alpha \partial_\rho^2 v_{y(0)}^{(1,1)}(0).$$

Note that all  $v_{y(n)}^{(1,1)}$  with  $n > 0$  drop out, since their integral over  $x$  vanishes. Hence it suffices to consider the case  $n = 0$  in the differential equation.

Integrating the homogeneous differential equation (A.57) for  $n = 0$  is straightforward. First of all, we can introduce  $\tilde{v}_{y(0)}^{(1,1)} = \partial_\rho v_{y(0)}^{(1,1)}$  and integrate the (now first order ordinary) differential equation, yielding

$$\tilde{v}_{y(0)}^{(1,1)} = \frac{\tilde{C} \rho}{1 - \rho^4}. \quad (\text{A.58})$$

Imposing the boundary condition  $v_{y(0)}^{(1,1)}(0) = 0$  at the conformal boundary, we obtain the following solution for  $v_{y(0)}^{(1,1)}(\rho)$  by quadrature

$$v_{y(0)}^{(1,1)}(\rho) = \frac{\tilde{C}}{4} (\log(1 + \rho^2) - \log(1 - \rho^2)). \quad (\text{A.59})$$

Note that this solution is not regular at the horizon.

Let us now proceed with the inhomogeneous differential equation. Also using the separation ansatz (A.55) we end up with

$$(1 + 3\rho^4) \partial_\rho v_{y(n)}^{(1,1)} - \rho (1 - \rho^4) \partial_\rho^2 v_{y(n)}^{(1,1)} + \rho \left( \frac{2\pi n}{\lambda} \right)^2 v_{y(n)}^{(1,1)} + 8i\rho^2 \partial_\rho A_{z(n)} = 0. \quad (\text{A.60})$$

Again, we only have to solve the differential equation for  $n = 0$  and we may view it as a first order differential equation for  $\tilde{v}_{y(0)}^{(1,1)}$ .

$$(1 + 3\rho^4) \tilde{v}_{y(0)}^{(1,1)} - \rho (1 - \rho^4) \partial_\rho \tilde{v}_{y(0)}^{(1,1)} + 8i\rho^2 \partial_\rho A_{z(0)} = 0. \quad (\text{A.61})$$

We use the *variation of constants* method and promote the parameter  $\tilde{C}$  to a function of  $\rho$ , denoted by  $\tilde{C}(\rho)$ . We can derive a differential equation for  $\tilde{C}(\rho)$  by substituting the ansatz for  $\tilde{v}_{y(0)}^{(1,1)}$

$$\tilde{v}_{y(0)}^{(1,1)}(\rho) = \tilde{C}(\rho) \frac{\rho}{1 - \rho^4} \quad (\text{A.62})$$

into (A.61). In particular we obtain

$$\tilde{C}'(\rho) = 8i \partial_\rho A_{z(0)}(\rho), \quad (\text{A.63})$$

which gives rise to the solution

$$\tilde{C}(\rho) = 8i \left( A_{z(0)}(\rho) - A_{z(0)}(1) \right). \quad (\text{A.64})$$

In particular we fixed the constant such that the total solution

$$\tilde{v}_{y(0)}^{(1,1)}(\rho) = 8i \left( A_{z(0)}(\rho) - A_{z(0)}(1) \right) \frac{\rho}{1-\rho^4} \quad (\text{A.65})$$

is regular at  $\rho = 1$ . As a result, the covariant part of the average AHC is given by

$$\langle \sigma_{yx} \rangle_\lambda = -i\alpha \partial_\rho^2 v_{y(0)}^{(1,1)}(0) = -i\alpha \partial_\rho \tilde{v}_{y(0)}^{(1,1)}(0) = 8\alpha \left( A_{z(0)}(0) - A_{z(0)}(1) \right). \quad (\text{A.66})$$

### The Chern-Simons term and the consistent current

We consider the case of a vanishing background, i.e.  $F_{\sigma\kappa} = 0$ , and the only non trivial background axial gauge field component is  $A_z$ . Consequently, starting from (A.67) we obtain for the desired part of the two-point function in the  $x$ - $y$ -plane

$$\begin{aligned} \langle j_V^y j_V^x \rangle_{cons} - \langle j_V^y j_V^x \rangle_{cov} &= -4\alpha \epsilon^{4xz\sigma\kappa} \lim_{\rho \rightarrow 0} \sqrt{-g} \left( A_z \frac{(\nabla_\sigma \delta V_\kappa - \nabla_\kappa \delta V_\sigma)}{\delta V_y} \right) \\ &= -8\alpha \epsilon^{4xz\sigma\kappa} \lim_{\rho \rightarrow 0} \sqrt{-g} \left( A_z \frac{\nabla_\sigma \delta V_\kappa}{\delta V_y} \right) \\ &= i\omega 8\alpha \epsilon^{4xzt y} A_z(0, x), \end{aligned} \quad (\text{A.67})$$

where the harmonic time dependency (A.34) of  $\delta V_y$  was used. We remark, that our coordinate tuple is arranged as  $(t, x, y, z, \rho) = (x^0, x^1, x^2, x^3, x^4)$  and therefore  $\epsilon^{4xzt y} = \epsilon^{41302} = -1$ .

Combining the Kubo formula (A.28) with the results (A.66) and (A.67) yields the total averaged AHC, that also includes the Chern-Simons contribution:

$$\langle \sigma_{yx} \rangle_\lambda = -8\alpha A_{z(0)}(1) = -\frac{8\alpha}{\lambda} \int_0^\lambda dx A_z(1, x) \quad (\text{A.68})$$

Note that the sign of expression (A.68) differs from the sign of (5.48) and (5.60). This change of sign comes from considering  $\sigma_{xy}$  in (5.48) and (5.60) instead of  $\sigma_{yx}$  and can be understood by considering the Onsager relations. These relations guarantee the symmetry of the DC conductivity tensor under time reversal or by multiplying the external fields with a factor of  $-1$  respectively, where the latter explains the origin of the sign change.

### A.3.4 Accuracy

#### Surface states in holographic Weyl semimetals

The estimation of the numerical quality of the solutions follows the procedure outlined in subsection A.2.5. Figure A.10 shows the residual  $\mathcal{R}_N$  in dependence of the grid sizes in  $\rho$ - and  $x$ -direction. The three-dimensional plot allows us to recognize the different convergence behavior in the two directions. We clearly see a poor algebraic convergence rate in  $\rho$ -direction as expected due to the logarithmic contributions at order  $\rho^2$  of the series expansions of  $A_z$  and  $\varphi$  around  $\rho = 0$  (cf. equations (5.53)-(5.54)). Whereas the convergence in the  $x$ -direction is much better and can be considered as spectral convergence due to its linear slope in the logarithmic plot. We note that the same convergence analysis for the field derivatives yields a loss of one to two orders in convergence for each derivative that was taken, which is important for assessing the accuracy of the numerical approximation to  $\partial_\rho^2 V_y$ . As a compromise in terms of accuracy, speed, memory consumption and size of the output we used a resolution of  $(N_\rho, N_x) = (55, 45)$  for the production of the plots in section 5.3. This relates to a point-wise accuracy bound for the fields of  $10^{-6}$  and  $10^{-2}$  for the second derivatives.

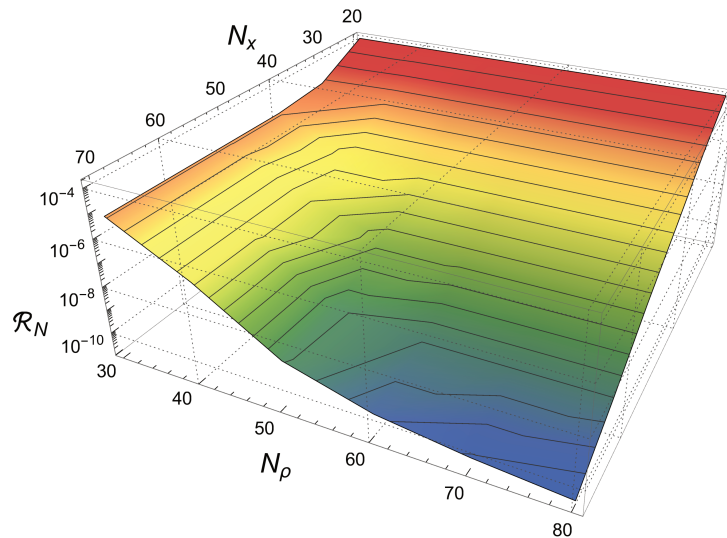


**Figure A.10:** Residual of the field  $V_y$  as a function of the average grid resolutions for all domains in  $x$  and  $\rho$  direction, obtained for  $\pi\bar{T} = 1/16$ ,  $l = 1$ ,  $\bar{a}_L = 0.6$  and  $\bar{a}_R = 2.2$ .

#### Finite temperature and disorder effects in holographic Weyl semimetals

The discussion of the numerical quality of the results of section 5.4 relies on estimating the two major sources of errors, namely the numerical error related to our numerical approximation scheme and the statistical error, which is a necessary consequence of estimating statistical quantities by looking only at a finite number of randomly chosen samples.

In particular, at least 50 random samples were computed for each data point and the corresponding variance was taken as an estimate of the statistical error. The magnitude of the statistical error was indicated by error-bars in the plots of section 5.4, whenever necessary (i.e. whenever being large enough). Accordingly, the plots of the results section are based on more than 10.000 single solutions of the corresponding boundary value problem.

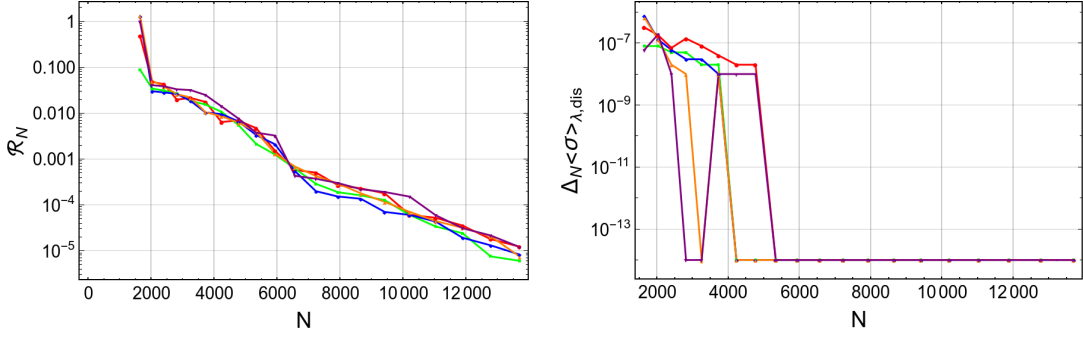


**Figure A.11:** **Left:** Convergence plot for five randomly chosen samples: residual  $\mathcal{R}_N$  as a function of the total number of grid points  $N$ . **Right:** Convergence plot for the integrated Hall conductivity for five random samples: residual  $\Delta_N \langle \sigma \rangle_{\lambda, \text{dis}}$  as a function of the total number of grid points  $N$ .

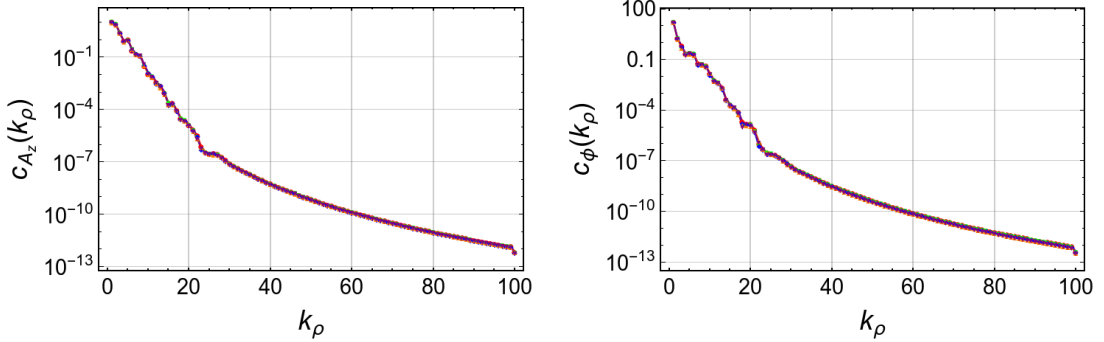


**Figure A.12:** Example coefficient convergence plot for the gauge field  $A_z$  (left) and scalar field  $\phi$  (right) for five randomly chosen samples at  $\pi T = 1/10$ ,  $\bar{\gamma} = 0.45$ ,  $\bar{a}_0 = 1.4$ ,  $\alpha = 0$ : maximum Chebyshev absolute coefficient as a function wave number  $k_\rho$ , where the maximum is taken over the remaining  $x$ -direction.

Due to the large number of solutions, that were computed in order to improve the statistical estimates, it is not possible to save or inspect the numerical convergence for every sample, apart ensuring convergence in the Newton-Raphson scheme. To check the numerical quality of the obtained solutions, we studied at least five samples with different generic random boundary data for each tuple of parameters according to the procedure outlined in section 4.3 of chapter 4. Figure A.11, shows the convergence of the residual  $\mathcal{R}_N$  with increasing resolution for five generic random samples at low temperature and high disorder strength. We see that the convergence is comparatively slow due to the high number of random Fourier modes at the conformal boundary, which couple directly to the logarithmic contributions (cf. the boundary expansion of the fields as specified in (5.53)-(5.54)). Nevertheless, the convergence plot for the corresponding values of  $\langle \sigma \rangle_\lambda$  (see right panel of figure A.11) shows a much faster convergence, since calculating the related integrals corresponds to extracting the lowest order Fourier coefficient of  $A_z$  at the horizon  $\rho = 1$ . Overall, we see that the numerical error is much smaller than the statistical error for all considered samples.

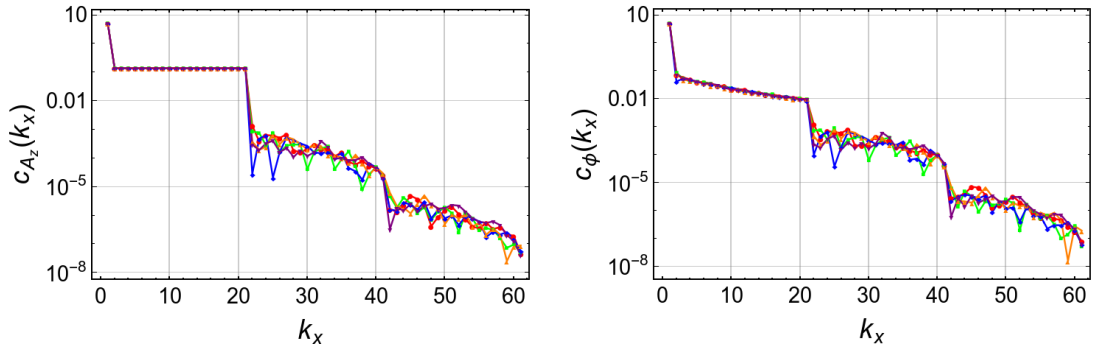


**Figure A.13:** Coefficient convergence plot for the gauge field  $A_z$  (left) and scalar field  $\phi$  (right) for five randomly chosen samples at  $\pi T = 1/10$ ,  $\bar{\gamma} = 0.45$ ,  $\bar{a}_0 = 1.4$ ,  $\alpha = 0$ : maximum absolute normalized Fourier coefficient  $c_k = \frac{1}{2} \sqrt{\alpha_k^2 + \beta_k^2}$  (where  $\alpha_k$  and  $\beta_k$  are the coefficients of the sine/cosine representation) as a function wave number  $k_x$ , where the maximum is taken over the remaining  $\rho$ -direction.

Furthermore, it is instructive to study the convergence rate of the spectral coefficients for non-vanishing disorder. As a result, we clearly see the lag of convergence in the  $\rho$ -direction which is caused by the logarithmic contributions (cf. A.12). Furthermore, we notice the plateau of Fourier coefficients for the convergence plot related to the  $x$ -direction, which originates from the random coefficients of the boundary data (figure A.13).

Finally, we would like to comment on the influence of the number of random phases  $N_{\text{dis}}$  in the spectral representation of the disorder signal (5.62). Despite we checked the qualitative independence of the results when varying  $N_{\text{dis}}$  over a finite range, a large  $N_{\text{dis}}$  scaling analysis would be necessary to make further and robust statements about the concrete quantitative results, like the critical exponent values. Unfortunately this is out of the scope of this thesis.

## A.4 Details of the numerical implementation

In this section we provide additional technical details about the numerical routines. We remark that the projects realized within this thesis were implemented in terms of a self-written C code named APDES<sup>8</sup>, that was later updated and transferred into a C++ header library, called APDES++. Concretely, the LBH and WSM interface projects were implemented with the older APDES C-style version of the code, while the WSM disorder project was realized on the basis of the C++ header library. Figure A.14 shows a summarizing flow chart of the overall solution process, including the numerical core routines.

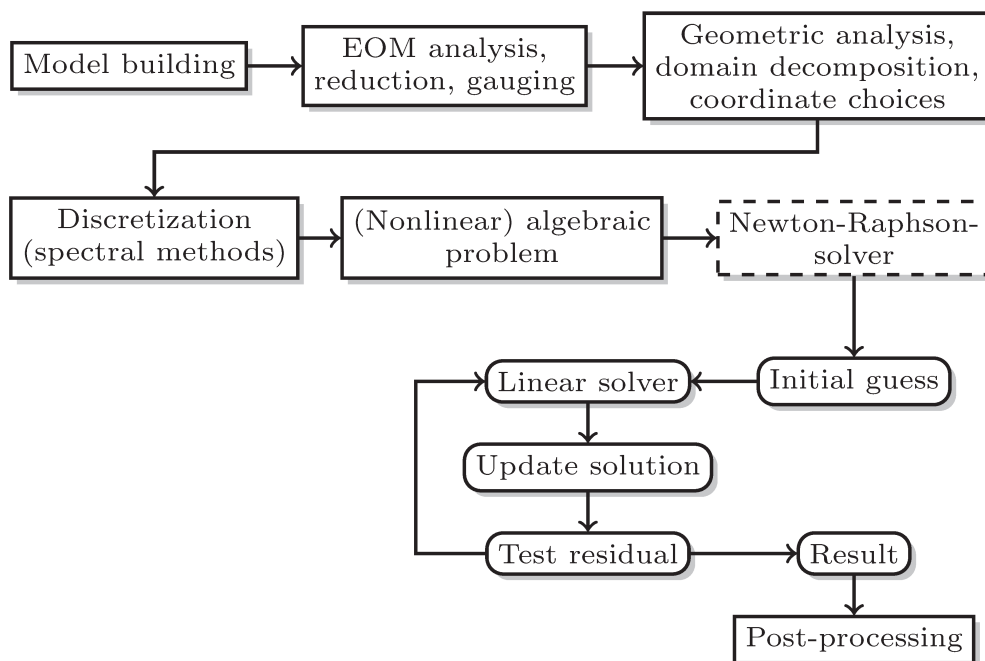


**Figure A.14:** Flow chart of the overall solution process: From the modeling stage, over the numerical core routines to the post-processing.

The concrete implementation of the spectral routines is covered in subsection A.4.1 together with additional information about the implementation of the multi-domain algorithm. Subsection A.4.2 contains additional information about the implementation of the Newton-Raphson method, including the underlying linear solver routines. Finally, supplementary routines and programs that were employed in the scope of the solution process are summarized in subsection A.4.3.

### A.4.1 Spectral discretization

As outlined in section 3.1, the Fourier and Chebyshev methods can be implemented in terms of the fast Fourier algorithm (FFT). Accordingly, we utilized the highly optimized FFTW library [77] for transforming between the collocation and coefficient representation of the spectral expansions.

Within the pseudo-spectral collocation method, we solve directly for the collocation values. Thus, we only employ the spectral-transformation for computing the derivatives in the coefficient

<sup>8</sup>APDES is the acronym for Automatic PDE Solver.

space by employing the relations (3.3) (Fourier method) and (3.6) (Chebyshev method) and for interpolating from the given collocation grid to arbitrary points in the domain of integration. As covered with great detail in [106], the recursive relation (3.6) for obtaining the spectral coefficients of the derived function is prone to round-off errors, leading to the loss of around 2 significant digits per derivative operation. We were able to reduce this loss by redefining every single summation in terms of a Kahan summation [119]. We remark, that the Kahan approach prevents a parallelization of the recursive summation (3.6). Furthermore, also the FFT algorithm is a potential source of round-off errors, though the FFTW library provides us with a high-quality low round-off implementation<sup>9</sup>.

The interpolation to arbitrary points within the domain of the collocation grid is implemented in terms of the Clenshaw algorithm [46], which provides an improved summation technique for computing the sum

$$f(x) \approx \sum_{k=0}^N c_k \Phi_k(x), \quad (\text{A.69})$$

with the spectral coefficients  $c_k$  and the spectral basis functions  $\Phi_k$ .

We mention that differentiation-matrices provide another efficient way for implementing the differentiation operation for pseudo-spectral methods. Though having a complexity of  $\mathcal{O}(N^2)$ , this approach can be more efficient than the FFT method for small to average numbers of collocation points  $N$ . However, we decided to use the FFT algorithm for making the method also efficient for larger collocation grids.

As mentioned before the convergence of spectral methods can be significantly enhanced by employing maps to rearrange the collocation points. A review on the analytic mesh refinement technique that was employed in the scope of the LBH project can be found in the appendix of [120]. As another example [35] provides some information on the convergence improvement in the presence of logarithmic endpoint singularities by utilizing quadratic maps. More convergence improving coordinate transformation can be found in reference [34].

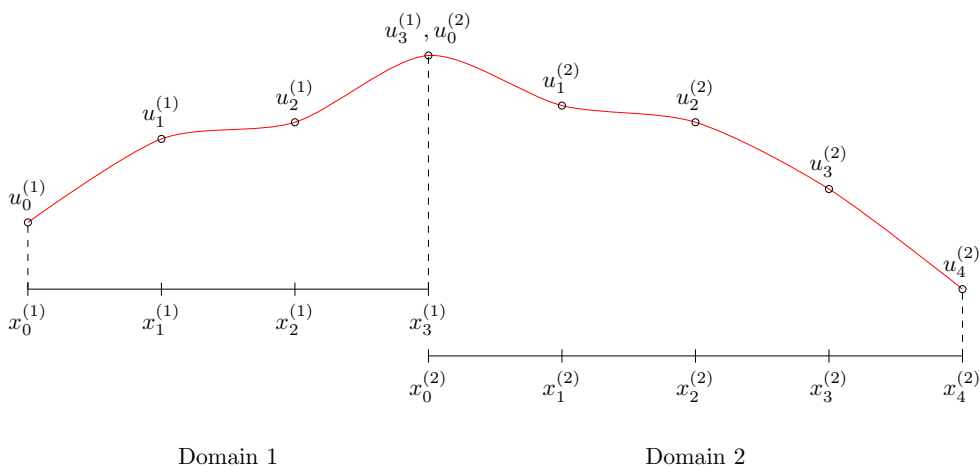


**Figure A.15:** Illustration of the non-overlapping domain matching with two subdomains in one dimension.  $x_i^{(k)}$  denotes the coordinate of the  $i$ -th collocation point of the  $k$ -th subdomain, and  $u_i^{(k)}$  is the function value at the corresponding grid point.

<sup>9</sup>We remark that the FFTW library also supports 80bit extended and 128bit precision out of box.



## Multiple domains

For the implementation of the non-overlapping multi-patch method for elliptic boundary value problems, we followed the approach presented in [168], i.e. we enforce the corresponding Dirichlet and Neumann conditions directly at the patch boundaries.

Figure A.15 provides a sketch of a one-dimensional configuration of two non-overlapping domains. For this illustrative setting, the implemented collocation method works as follows:

- We collocate the underlying differential equation on all internal points:  $\{x_1^{(1)}, x_2^{(1)}, x_1^{(2)}, x_2^{(2)}, x_3^{(2)}\}$ ,
- The boundary conditions are enforced directly at the outer boundaries  $x_0^{(1)}$  and  $x_4^{(2)}$ ,
- The matching point  $x_3^{(1)} = x_0^{(2)}$  is present in the grid of both domains. Therefore we must implement two conditions here: one for  $u_3^{(1)}$  in domain 1 and the other for  $u_0^{(2)}$  in domain 2. As mentioned before, the Dirichlet and Neumann couplings provide us with the two desired conditions at the inter-domain boundary, i.e.

$$u_3^{(1)} = u_0^{(2)} \quad \text{together with} \quad \frac{\partial u_3^{(1)}}{\partial x} = \frac{\partial u_0^{(2)}}{\partial x}, \quad (\text{A.70})$$

for our example.

When coupling domains in more than one-dimension, we interpolate the boundary data of adjacent domains on the neighbor-grid. This interpolation is carried out by means of the spectral interpolation technique, that was mentioned above. This approach allows us to couple grids of different resolutions, which is the basis of an economic distribution of the collocation points according to the convergence properties of the expansions on the different domains.

As an important point, care must be taken when considering more complicated domain setups: A domain with no external boundaries shall not be coupled to its neighbors only by Neumann conditions, since the regarding boundary value problem is potentially ill-posed<sup>10</sup>. We addressed this issue by writing a Mathematica based domain connecting routine.

### A.4.2 Newton-Raphson

As mentioned in section 3.2, we utilized a standard Newton-Raphson scheme for solving the nonlinear algebraic problem arising from the spectral discretization. Newton's method can be derived by expanding the residual  $\vec{F}(\vec{X})$  in a Taylor series and neglecting terms of order  $\Delta\vec{X}^2$  and higher

$$\vec{F}(\vec{X}_m + \Delta\vec{X}) = \vec{F}(\vec{X}_m) + \left. \frac{\partial \vec{F}}{\partial \vec{X}} \right|_{\vec{X}=\vec{X}_m} \Delta\vec{X} + \mathcal{O}(\Delta\vec{X}^2). \quad (\text{A.71})$$

<sup>10</sup>This can be seen easily by considering the Laplace equation with Neumann conditions on all boundaries: The corresponding solution is obviously not unique.

Setting  $\vec{F}(\vec{X}_m + \Delta\vec{X}) = 0$  yields an iteration scheme for obtaining the correction  $\Delta\vec{X}$  of a given  $\vec{X}_m$ , that lies more closely to the true solution  $\vec{X}_{sol}$ :

$$\Delta\vec{X} \approx - \left( \frac{\partial\vec{F}}{\partial\vec{X}} \Big|_{\vec{X}=\vec{X}_m} \right)^{-1} \vec{F}(\vec{X}_m). \quad (\text{A.72})$$

As a common approach, the Jacobian  $J_{ij} = \partial F_i / \partial X_j$  can be approximated by a finite difference scheme:

$$J_{ij}(\vec{X}_m) \approx \frac{F_i(\vec{X}_m + \varepsilon\vec{e}_j) - F_i(\vec{X}_m - \varepsilon\vec{e}_j)}{2\varepsilon} \quad (\text{A.73})$$

and subsequently be inverted by a standard LU solver for obtaining the correction  $\Delta\vec{X}$  from (A.72).

However, this approach leads to large memory requirements and exceedingly high computation times, since the Jacobian related to a spectral collocation method is usually dense and the corresponding LU algorithm scales as  $\mathcal{O}(N_{total}^3)$ , where  $N_{total}$  is the total number of unknowns. As a consequence, we decided to utilize a matrix-free approach<sup>11</sup>, which is based on the combination of the Fréchet derivative functional for generating the Jacobian together with an iterative linear solver.

### Matrixfree Jacobian

The Fréchet derivative of a set of differential equations  $\vec{F}(\vec{X}, \vec{X}', \vec{X}'')$  is obtained by considering its total differential (cf. reference [34])

$$\begin{aligned} d\vec{F}(\vec{X}, \vec{X}', \vec{X}'') &= \frac{\partial\vec{F}(\vec{X}, \vec{X}', \vec{X}'')}{\partial\vec{X}} d\vec{X} + \frac{\partial\vec{F}(\vec{X}, \vec{X}', \vec{X}'')}{\partial\vec{X}'} d\vec{X}' + \frac{\partial\vec{F}(\vec{X}, \vec{X}', \vec{X}'')}{\partial\vec{X}''} d\vec{X}'' \\ &= \left[ \frac{\partial\vec{F}(\vec{X}, \vec{X}', \vec{X}'')}{\partial\vec{X}} + \frac{\partial\vec{F}(\vec{X}, \vec{X}', \vec{X}'')}{\partial\vec{X}'} \mathcal{D} + \frac{\partial\vec{F}(\vec{X}, \vec{X}', \vec{X}'')}{\partial\vec{X}''} \mathcal{D}^2 \right] d\vec{X}, \end{aligned} \quad (\text{A.74})$$

where the operator  $\mathcal{D}$  yields the coordinate-derivatives of the vector of unknowns according to  $\mathcal{D}\vec{X} = \vec{X}'$ .

Expression (A.74) provides a nice analytic form for the matrix-vector product  $\frac{\partial\vec{F}}{\partial\vec{X}} \Big|_{\vec{X}=\vec{X}_m} \Delta\vec{X}$ , when the linear relationship of the spectrally discretized versions of  $\vec{X}'$  and  $\vec{X}''$  to  $\vec{X}$  is recalled. Furthermore this allows us to define the matrix-vector product of an arbitrary vector  $\vec{V}$  with the Jacobian  $J(\vec{X})$  at a given  $\vec{X}$  according to

$$J(\vec{X}) \vec{V} = \left[ \frac{\partial\vec{F}(\vec{X}, \vec{X}', \vec{X}'')}{\partial\vec{X}} + \frac{\partial\vec{F}(\vec{X}, \vec{X}', \vec{X}'')}{\partial\vec{X}'} \mathcal{D} + \frac{\partial\vec{F}(\vec{X}, \vec{X}', \vec{X}'')}{\partial\vec{X}''} \mathcal{D}^2 \right] \vec{V}, \quad (\text{A.75})$$

where  $\mathcal{D}\vec{V}$  now denotes the spectral derivative operation on the given vector  $\vec{V}$ , while the expressions  $\partial\vec{F}(\vec{X}, \vec{X}', \vec{X}'') / \partial\vec{X}$ ,  $\partial\vec{F}(\vec{X}, \vec{X}', \vec{X}'') / \partial\vec{X}'$  and  $\partial\vec{F}(\vec{X}, \vec{X}', \vec{X}'') / \partial\vec{X}''$  can be predefined analytically.

<sup>11</sup> Actually, we still have to compute the inverse of a sparse preconditioning matrix.

ically. This approach allows us to build the matrix-vector product with  $\mathcal{O}(N_{total})$  effort, if  $\vec{V}$  and its spectral derivatives  $\vec{V}'$  and  $\vec{V}''$  are available at no extra cost<sup>12</sup>, while the full matrix  $J(\vec{X})$  is generated at no point of the procedure, saving us the corresponding memory.

### Preconditioned iterative linear solver

The big advantage of this second matrix-free Jacobian-vector-product formulation comes when combining it with the power of an iterative matrix solver. Since the employed iterative Krylov subspace solvers rely only on the computation of matrix-vector products of the form  $J(\vec{X})\vec{V}$ , our approximate matrix solver has theoretically  $\mathcal{O}(N_{total})$  effort. However, the convergence of these methods relies on a low condition number of the corresponding matrix. Apart from trivial special cases, low condition numbers require a preconditioning of the regarding linear system

$$J(\vec{X}_m)\Delta\vec{X} = -\vec{F}(\vec{X}_m), \quad (\text{A.76})$$

which is obtained by multiplying both sides of the system with an approximation  $J_{pre}^{-1}(\vec{X}_m)$  of  $J^{-1}(\vec{X}_m)$ :

$$J_{pre}^{-1}(\vec{X}_m)J(\vec{X}_m)\Delta\vec{X} = -J_{pre}^{-1}(\vec{X}_m)\vec{F}(\vec{X}_m). \quad (\text{A.77})$$

While a constant approximation of  $J^{-1}(\vec{X}_m)$  by a diagonally dominant matrix often suffices for constant coefficient equations on equidistant grids, we have to put considerable effort in the generation of a good preconditioner due to the complicated non-constant coefficient equations under consideration combined with non-equidistant meshes (at least for the Chebyshev method). We use a second order finite difference approximation of the Jacobian as a preconditioner. This approximate Jacobian can be obtained by employing relation (A.75):

- By setting  $\vec{V} = \vec{e}_i$  for  $i = 0, \dots, N_{total} - 1$  we obtain subsequently all rows of the full Jacobian,
- The approximation is done, when the derivatives  $\mathcal{D}\vec{e}_i$  and  $\mathcal{D}^2\vec{e}_i$  are computed - here we use second order finite differences instead of the spectral derivative, that is used for the true Jacobian. The result is a sparse approximation of  $J(\vec{X}_m)$ .

The centered second order finite difference stencil on an equidistant grid  $\{\zeta_k\}_{k=0}^N$  with grid spacing  $h$  reads as follows

$$\frac{\partial f_k}{\partial \zeta} \approx \frac{f_{k+1} - f_{k-1}}{2h}, \quad \frac{\partial^2 f_k}{\partial \zeta^2} \approx \frac{f_{k+1} - 2f_k + f_{k-1}}{h^2}. \quad (\text{A.78})$$

While the Fourier method provides us with an equidistant grid, we need to transform the non-equidistant Chebyshev grids  $\{x_k\}_{k=0}^N$  on  $[-1, 1]$  to an equidistant one as follows:

$$x(\zeta) = -\cos(\zeta), \quad (\text{A.79})$$

<sup>12</sup>Otherwise the effort would be dominated by the spectral derivative operation, yielding  $\mathcal{O}(N_{total} \log N_{total})$  for the FFT implementation.

where  $\xi \in [0, \pi]$  and  $\xi_k = \pi k/N$  (for the Lobatto grid).

Furthermore, we need to built the stencils that touch the grid boundaries with additional care. For Fourier methods, we need to take care of the periodic boundary conditions, when implementing the finite difference stencil on the Fourier grid. For the Chebyshev methods, we need to take the singular boundaries into account, when transforming the derivatives from the equidistant grid back onto the Chebyshev nodes. In particular we have

$$\frac{\partial f}{\partial \xi} = \frac{\partial x}{\partial \xi} \frac{\partial f}{\partial x} = \sin(\xi) \frac{\partial f}{\partial x} \quad (\text{A.80})$$

$$\frac{\partial^2 f}{\partial \xi^2} = \frac{\partial^2 x}{\partial \xi^2} \frac{\partial f}{\partial x} + \left( \frac{\partial x}{\partial \xi} \right)^2 \frac{\partial^2 f}{\partial x^2} = \cos(\xi) \frac{\partial f}{\partial x} + \sin^2(\xi) \frac{\partial^2 f}{\partial x^2} \quad (\text{A.81})$$

$$\begin{aligned} \frac{\partial^3 f}{\partial \xi^3} &= \frac{\partial^3 x}{\partial \xi^3} \frac{\partial f}{\partial x} + 3 \frac{\partial^2 x}{\partial \xi^2} \frac{\partial x}{\partial \xi} \frac{\partial^2 f}{\partial x^2} + \left( \frac{\partial x}{\partial \xi} \right)^3 \frac{\partial^3 f}{\partial x^3} \\ &= -\sin(\xi) \frac{\partial f}{\partial x} + 3 \cos(\xi) \sin(\xi) \frac{\partial^2 f}{\partial x^2} + \sin^3(\xi) \frac{\partial^3 f}{\partial x^3} \end{aligned} \quad (\text{A.82})$$

$$\begin{aligned} \frac{\partial^4 f}{\partial \xi^4} &= \frac{\partial^4 x}{\partial \xi^4} \frac{\partial f}{\partial x} + 3 \left( \frac{\partial^2 x}{\partial \xi^2} \right)^2 \frac{\partial^2 f}{\partial x^2} + 4 \frac{\partial^3 x}{\partial \xi^3} \frac{\partial x}{\partial \xi} \frac{\partial^2 f}{\partial x^2} + 6 \frac{\partial^2 x}{\partial \xi^2} \left( \frac{\partial x}{\partial \xi} \right)^2 \frac{\partial^3 f}{\partial x^3} + \left( \frac{\partial x}{\partial \xi} \right)^4 \frac{\partial^4 f}{\partial x^4} \\ &= -\cos(\xi) \frac{\partial f}{\partial x} + 3 \cos^2(\xi) \frac{\partial^2 f}{\partial x^2} - 4 \sin^2(\xi) \frac{\partial^2 f}{\partial x^2} + 6 \cos(\xi) \sin^2(\xi) \frac{\partial^3 f}{\partial x^3} + \sin^4(\xi) \frac{\partial^4 f}{\partial x^4} \end{aligned} \quad (\text{A.83})$$

Considering the left end point of the interval, i.e.  $\xi = 0$ , we see that relation (A.80) becomes degenerate and we need to use (A.81) to obtain  $\partial f/\partial x$  from  $\partial^2 f/\partial \xi^2$ . The same happens for  $\partial^2 f/\partial x^2$  when considering (A.81). Accordingly, at  $\xi = 0$  we need to obtain the fourth order derivative  $\partial^4 f/\partial \xi^4$  on the  $\xi$ -grid to obtain a non-singular expression for  $\partial^2 f/\partial x^2$  from (A.83). Consequently, we also need the second order finite difference approximation of the  $\partial^4 f/\partial \xi^4$  derivative

$$\frac{\partial^4 f_k}{\partial \xi^4} \approx \frac{f_{k+2} - 4f_{k+1} + 6f_k - 4f_{k-1} + f_{k-2}}{h^4}, \quad (\text{A.84})$$

for obtaining the proper approximations of  $\partial f/\partial x$  and  $\partial^2 f/\partial x^2$  on the non-equidistant grid. This makes preconditioning for the Chebyshev method substantially harder than for the Fourier method.

Nevertheless, the additional efforts pay out, since the resulting approximation of the Jacobian is only a sparse matrix<sup>13</sup>. This matrix does not only need considerably less memory space<sup>14</sup>, but can be inverted much faster, than the full Jacobian. So overall the real runtime of our matrix-solver is bounded by the effort of a sparse matrix LU, which depends on the concrete block-size and the distribution of its off-diagonal entries. In practice we used the high-performance sparse matrix solvers provided by the SLU library [146] and the Intel MKL Pardiso implementation [167, 166].

Finally, we implemented the GMRES [177] and BiCGSTAB [194] Krylov subspace solvers for the iterative solving process. As mentioned before, these solvers rely only on products of the preconditioned matrix with vectors. Importantly the GMRES and BiCGSTAB methods are appli-

<sup>13</sup>More specifically, we obtain a doubly bordered block-diagonal matrix, when considering multiple domains. The off-diagonal borders are a result of the direct domain-couplings via the aforementioned Dirichlet/Neumann conditions.

<sup>14</sup>The sparse preconditioning matrix that was used throughout the high-accuracy multi-domain LBH project had only about 1% non-trivial entries.

---

cable to non-symmetric matrices. A good review on Krylov subspace methods and specifically on the GMRES and BiCGSTAB solvers can be found in reference [155].

### A.4.3 Miscellaneous

Additional tools for the realization of the projects within this thesis were:

- Wolfram Mathematica for the preparation of the EOM, analysis of the coordinates, preparation of the meshes, data visualization and data fitting,
- GNU parallel [190] for the parallel data production related to the study of disorder effects in WSMs,
- gnuplot [209] for data visualization.

As a last point we restrained from using arbitrary precision numerics, as provided by the BOOST C++ libraries [33], since they cannot be combined with the high-performance FFTW and sparse-matrix routines of SLU or Intel MKL. Nevertheless, since the entire APDES++ library uses C++ templates for the data-type specification, an arbitrary precision data container would be commensurable with the design of APDES++, if the regarding FFT and sparse-matrix routines are provided.



---

# References

---

1. B. P. e. a. Abbott. GW170817: Observation of Gravitational Waves from a Binary Neutron Star Inspiral. *Phys. Rev. Lett.*, 119:161101, Oct 2017. 3
2. S. L. Adler. Axial-Vector Vertex in Spinor Electrodynamics. *Physical Review*, 177(5):2426–2438, Jan. 1969. 61, 62, 65
3. O. Aharony, S. S. Gubser, J. Maldacena, H. Ooguri, and Y. Oz. Large N field theories, string theory and gravity. *Physics Reports*, 323(3-4):183–386, Jan. 2000. 4, 20
4. O. Aharony, Z. Komargodski, and S. Yankielowicz. Disorder in Large-N Theories. *JHEP*, 04:013, 2016. 84
5. O. Aharony, J. Marsano, S. Minwalla, and T. Wiseman. Black hole-black string phase transitions in thermal 1+1 dimensional supersymmetric Yang-Mills theory on a circle. *Class. Quant. Grav.*, 21:5169–5192, 2004. 107
6. L. Alberte, M. Ammon, M. Baggioli, A. Jiménez, and O. Pujolàs. Black hole elasticity and gapped transverse phonons in holography. *Journal of High Energy Physics*, 2018(1):129, Jan 2018. 5
7. L. Alberte, M. Ammon, M. Baggioli, A. Jiménez-Alba, and O. Pujolàs. Holographic Phonons. *ArXiv e-prints*, Nov. 2017. 5
8. G. Altarelli. The Higgs and the Excessive Success of the Standard Model. *Frascati Phys. Ser.*, 58:102, 2014. 4
9. A. Altland and D. Bagrets. Effective Field Theory of the Disordered Weyl Semimetal. *Phys. Rev. Lett.*, 114:257201, Jun 2015. 84
10. A. Altland and D. Bagrets. Theory of the strongly disordered Weyl semimetal. *Phys. Rev. B*, 93:075113, Feb 2016. 84
11. M. Ammon, M. Baggioli, A. Jiménez-Alba, and S. Moeckel. A smeared quantum phase transition in disordered holography. *Journal of High Energy Physics*, 2018(4):68, Apr 2018. 7, 61
12. M. Ammon and J. Erdmenger. *Gauge/gravity duality*. Cambridge Univ. Pr., Cambridge, UK, 2015. 21, 22, 24, 67, 71, 76, 102, 117, 118
13. M. Ammon, J. Erdmenger, V. Grass, P. Kerner, and A. O’Bannon. On holographic p-wave superfluids with back-reaction. *Physics Letters B*, 686(2):192 – 198, 2010. 5
14. M. Ammon, J. Erdmenger, M. Kaminski, and P. Kerner. Superconductivity from gauge/-gravity duality with flavor. *Physics Letters B*, 680(5):516 – 520, 2009. 5
15. M. Ammon, J. Erdmenger, M. Kaminski, and A. O’Bannon. Fermionic operator mixing in holographic p-wave superfluids. *Journal of High Energy Physics*, 2010(5):53, May 2010. 5

- 
16. M. Ammon, J. Erdmenger, P. Kerner, and M. Kaminski. Flavor superconductivity from gauge/gravity duality. *Journal of High Energy Physics*, 2009(10):067, 2009. 5
  17. M. Ammon and M. Gutperle. Supersymmetric holographic dual of a fractional topological insulator. *Phys. Rev. D*, 86:025018, Jul 2012. 5
  18. M. Ammon, M. Heinrich, A. Jiménez-Alba, and S. Moeckel. Surface States in Holographic Weyl Semimetals. *Phys. Rev. Lett.*, 118(20):201601, 2017. 7, 61
  19. T. Andrade, A. M. García-García, and B. Loureiro. Coherence effects in disordered geometries with a field-theory dual. 2017. 84
  20. T. Appelquist, A. Chodos, and P. G. O. Freund, editors. *Modern Kaluza-Klein Theories*. 1987. 3
  21. D. Arean, A. Farahi, L. A. Pando Zayas, I. S. Landea, and A. Scardicchio. Holographic superconductor with disorder. *Phys. Rev.*, D89(10):106003, 2014. 85
  22. D. Arean, A. Farahi, L. A. Pando Zayas, I. S. Landea, and A. Scardicchio. Holographic p-wave Superconductor with Disorder. *JHEP*, 07:046, 2015. 85
  23. D. Arean, L. A. Pando Zayas, I. S. Landea, and A. Scardicchio. Holographic disorder driven superconductor-metal transition. *Phys. Rev.*, D94(10):106003, 2016. 85, 99
  24. V. Asnin, B. Kol, and M. Smolkin. Analytic evidence for continuous self similarity of the critical merger solution. *Class. Quant. Grav.*, 23:6805–6827, 2006. 6, 40
  25. K. Balasubramanian. Gravity duals of cyclic RG flows, with strings attached. 2013. 85
  26. J. M. Bardeen, B. Carter, and S. W. Hawking. The Four laws of black hole mechanics. *Commun. Math. Phys.*, 31:161–170, 1973. 17
  27. W. A. Bardeen. Anomalous Ward Identities in Spinor Field Theories. *Phys. Rev.*, 184:1848–1859, Aug 1969. 66
  28. T. Baumgarte and S. Shapiro. *Numerical Relativity: Solving Einstein's Equations on the Computer*. Cambridge University Press, 2010. 11
  29. J. S. Bell and R. Jackiw. A PCAC puzzle:  $\pi^0 \rightarrow \gamma\gamma$  in the  $\sigma$ -model. *Il Nuovo Cimento A (1965-1970)*, 60(1):47–61, Jan. 1969. 61, 62, 65
  30. R. A. Bertlmann. *Anomalies in Quantum Field Theory*. Clarendon Press, Nov. 2000. 65, 66
  31. S. Bhattacharyya, S. Minwalla, and K. Papadodimas. Small Hairy Black Holes in  $AdS_5 \times S^5$ . *JHEP*, 11:035, 2011. 97
  32. R. Blumenhagen and E. Plauschinn. *Introduction to Conformal Field Theory*, volume 779 of *Lecture Notes in Physics*. Springer-Verlag Berlin Heidelberg, 2009. 21, 102
  33. Boost. Boost C++ Libraries. <http://www.boost.org/>, 2015. Last accessed 2015-06-30. 131
  34. J. Boyd. *Chebyshev and Fourier Spectral Methods: Second Revised Edition*. Dover Books on Mathematics. Dover Publications, 2001. 27, 28, 87, 101, 126, 128



- 
35. J. P. Boyd. The asymptotic Chebyshev coefficients for functions with logarithmic endpoint singularities: mappings and singular basis functions. *Applied Mathematics and Computation*, 29(1):49–67, Jan. 1989. 79, 87, 126
  36. J. A. N. Bruin, H. Sakai, R. S. Perry, and A. P. Mackenzie. Similarity of Scattering Rates in Metals Showing T-Linear Resistivity. *Science*, 339(6121):804–807, 2013. 70
  37. A. A. Burkov and L. Balents. Weyl Semimetal in a Topological Insulator Multilayer. *Physical Review Letters*, 107(12):127205, Sept. 2011. 61
  38. A. A. Burkov, M. D. Hook, and L. Balents. Topological nodal semimetals. *Physical Review B*, 84(23):235126, Dec. 2011. 61
  39. C. Canuto, M. Hussaini, A. Quarteroni, and J. Thomas A. *Spectral Methods in Fluid Dynamics*. Scientific Computation. Springer Berlin Heidelberg, 2012. 27
  40. C. Canuto, M. Hussaini, A. Quarteroni, and T. Zang. *Spectral Methods: Fundamentals in Single Domains*. Scientific Computation. Springer Berlin Heidelberg, 2007. 27
  41. S. Catterall, R. G. Jha, D. Schaich, and T. Wiseman. Testing holography using lattice super-Yang-Mills theory on a 2-torus. *Phys. Rev. D*, 97:086020, Apr 2018. 109
  42. S. Catterall, A. Joseph, and T. Wiseman. Thermal phases of D1-branes on a circle from lattice super Yang-Mills. *Journal of High Energy Physics*, 2010(12):22, Dec 2010. 109
  43. C.-Z. Chen, J. Song, H. Jiang, Q.-f. Sun, Z. Wang, and X. C. Xie. Disorder and Metal-Insulator Transitions in Weyl Semimetals. *Physical Review Letters*, 115(24):246603, Dec. 2015. 84
  44. M. N. Chernodub, A. Cortijo, A. G. Grushin, K. Landsteiner, and M. A. H. Vozmediano. Condensed matter realization of the axial magnetic effect. *Phys. Rev.*, B89(8):081407, 2014. 62
  45. M. W. Choptuik, L. Lehner, I. Olabarrieta, R. Petryk, F. Pretorius, and H. Villegas. Towards the final fate of an unstable black string. *Phys. Rev.*, D68:044001, 2003. 38
  46. C. W. Clenshaw. A note on summation of Chebyshev series. *Math. Comp.*, 9:118–120, 1955. 126
  47. J. W. Cooley and J. W. Tukey. An algorithm for the machine calculation of complex Fourier series. *Mathematics of Computation*, 19:297–301, 1965. URL: <http://cr.yp.to/bib/entries.html#1965/cooley>. 28
  48. A. Cortijo, Y. Ferreira, K. Landsteiner, and M. A. H. Vozmediano. Elastic Gauge Fields in Weyl Semimetals. *Phys. Rev. Lett.*, 115(17):177202, 2015. 62, 67
  49. A. Cortijo, Y. Ferreira, K. Landsteiner, and M. A. H. Vozmediano. Hall viscosity from elastic gauge fields in Dirac crystals. *2D Materials*, 1(3):011002, 2016. 62
  50. J. L. Davis, P. Kraus, and A. Shah. Gravity dual of a quantum Hall plateau transition. *Journal of High Energy Physics*, 2008(11):020, 2008. 5
  51. P. Delplace, J. Li, and D. Carpentier. Topological Weyl semi-metal from a lattice model. *EPL (Europhysics Letters)*, 97(6):67004, 2012. 61

- 
52. L. Demkó, S. Bordács, T. Vojta, D. Nozadze, F. Hrahsheh, C. Svoboda, B. Dóra, H. Yamada, M. Kawasaki, Y. Tokura, and I. Kézsmárki. Disorder Promotes Ferromagnetism: Rounding of the Quantum Phase Transition in  $\text{Sr}_{1-x}\text{Ca}_x\text{RuO}_3$ . *Phys. Rev. Lett.*, 108:185701, May 2012. 84, 94, 95
  53. E. D'Hoker and D. Z. Freedman. Supersymmetric Gauge Theories and the AdS/CFT Correspondence. *ArXiv High Energy Physics - Theory e-prints*, Jan. 2002. 22
  54. E. D'Hoker and P. Kraus. Magnetic Field Induced Quantum Criticality via new Asymptotically  $\text{AdS}_5$  Solutions. *Class. Quant. Grav.*, 27:215022, 2010. 100
  55. E. D'Hoker and P. Kraus. Quantum Criticality via Magnetic Branes. *Lect. Notes Phys.*, 871:469–502, 2013. 100
  56. O. J. Dias, J. E. Santos, and B. Way. Localised  $\text{AdS}_5 \times \text{S}^5$  Black Holes. *Phys. Rev. Lett.*, 117(15):151101, 2016. 98
  57. O. J. C. Dias, J. E. Santos, and B. Way. Rings, Ripples, and Rotation: Connecting Black Holes to Black Rings. *JHEP*, 07:045, 2014. 97
  58. O. J. C. Dias, J. E. Santos, and B. Way. Numerical Methods for Finding Stationary Gravitational Solutions. *Class. Quant. Grav.*, 33(13):133001, 2016. 45, 104
  59. O. J. C. Dias, J. E. Santos, and B. Way. Localised and nonuniform thermal states of super-Yang-Mills on a circle. *JHEP*, 06:029, 2017. 6, 33, 36, 39, 52, 53, 98, 107, 108
  60. A. Donos and J. P. Gauntlett. The thermoelectric properties of inhomogeneous holographic lattices. *JHEP*, 01:035, 2015. 84
  61. J. Droste. The field of a single centre in Einstein's theory of gravitation, and the motion of a particle in that field. *Koninklijke Nederlandse Akademie van Wetenschappen Proceedings Series B Physical Sciences*, 19:197–215, 1917. 16
  62. F. W. Dyson, A. S. Eddington, and C. Davidson. A determination of the deflection of light by the sun's gravitational field, from observations made at the total eclipse of may 29, 1919. *Philosophical Transactions of the Royal Society of London A: Mathematical, Physical and Engineering Sciences*, 220(571-581):291–333, 1920. 3
  63. A. Einstein. Über einen die Erzeugung und Verwandlung des Lichtes betreffenden heuristischen Gesichtspunkt. *Annalen der Physik*, 322(6):132–148, 1905. 3
  64. A. Einstein. Die Feldgleichungen der Gravitation. *Sitz. Preuß. Akad. Wiss.*, pages 844–847, 1915. 3, 16
  65. A. Einstein. Die Grundlage der allgemeinen Relativitätstheorie. *Annalen der Physik*, 354:769–822, 1916. 3
  66. R. Emparan, P. Figueras, and M. Martinez. Bumpy black holes. *JHEP*, 12:072, 2014. 97
  67. R. Emparan and N. Haddad. Self-similar critical geometries at horizon intersections and mergers. *JHEP*, 10:064, 2011. 98
  68. R. Emparan, R. Luna, M. Martinez, R. Suzuki, and K. Tanabe. Phases and Stability of Non-Uniform Black Strings. 2018. 54

- 
69. R. Emparan, R. Suzuki, and K. Tanabe. Evolution and End Point of the Black String Instability: Large D Solution. *Phys. Rev. Lett.*, 115(9):091102, 2015. 38
  70. L. Evans and A. M. Society. *Partial Differential Equations*. Graduate studies in mathematics. American Mathematical Society, 1998. 11
  71. C. Fefferman and C. Graham. *The Ambient Metric (AM-178)*. Annals of Mathematics Studies. Princeton University Press, 2011. 23
  72. P. Figueras, J. Lucietti, and T. Wiseman. Ricci solitons, Ricci flow, and strongly coupled CFT in the Schwarzschild Unruh or Boulware vacua. *Class. Quant. Grav.*, 28:215018, 2011. 12
  73. P. Figueras, K. Murata, and H. S. Reall. Stable non-uniform black strings below the critical dimension. *JHEP*, 11:071, 2012. 33, 36, 40, 54, 98
  74. B. Finlayson and L. Scriven. The method of weighted residuals - A review. 19:735–748, 01 1966. 27
  75. M. Flory. Discrete scale invariance in holography revisited. 2017. 85, 99
  76. E. Fradkin, S. A. Kivelson, M. J. Lawler, J. P. Eisenstein, and A. P. Mackenzie. Nematic Fermi Fluids in Condensed Matter Physics. *Annual Review of Condensed Matter Physics*, 1(1):153–178, 2010. 99
  77. M. Frigo and S. G. Johnson. The fastest Fourier transform in the west. Technical Report MIT-LCS-TR-728, Massachusetts Institute of Technology, September 1997. 125
  78. K. Fujikawa and H. Suzuki. *Path Integrals and Quantum Anomalies*. Clarendon Press, Apr. 2004. 65
  79. M. Fujita, Y. Hikida, S. Ryu, and T. Takayanagi. Disordered Systems and the Replica Method in AdS/CFT. *JHEP*, 12:065, 2008. 85
  80. A. M. García-García and B. Loureiro. Marginal and Irrelevant Disorder in Einstein-Maxwell backgrounds. *Phys. Rev.*, D93(6):065025, 2016. 84
  81. G. W. Gibbons and S. W. Hawking. Action integrals and partition functions in quantum gravity. *Phys. Rev. D*, 15:2752–2756, May 1977. 72
  82. D. Gorbonos and B. Kol. A Dialogue of multipoles: Matched asymptotic expansion for caged black holes. *JHEP*, 06:053, 2004. 33
  83. D. Gorbonos and B. Kol. Matched asymptotic expansion for caged black holes: Regularization of the post-Newtonian order. *Class. Quant. Grav.*, 22:3935–3960, 2005. 33
  84. R. Gregory and R. Laflamme. Black strings and p-branes are unstable. *Phys. Rev. Lett.*, 70:2837–2840, 1993. 6, 33, 38
  85. R. Gregory and R. Laflamme. The Instability of charged black strings and p-branes. *Nucl. Phys.*, B428:399–434, 1994. 6, 33, 38
  86. R. B. Griffiths. Nonanalytic Behavior Above the Critical Point in a Random Ising Ferromagnet. *Phys. Rev. Lett.*, 23:17–19, Jul 1969. 84, 99

- 
87. A. G. Grushin. Consequences of a condensed matter realization of Lorentz-violating QED in Weyl semi-metals. *Physical Review D*, 86(4):045001, Aug. 2012. 68, 69
  88. A. G. Grushin, J. W. F. Venderbos, A. Vishwanath, and R. Ilan. Inhomogeneous Weyl and Dirac semimetals: Transport in axial magnetic fields and Fermi arc surface states from pseudo Landau levels. *arXiv:1607.04268 [cond-mat]*, July 2016. arXiv: 1607.04268. 68, 99
  89. S. S. Gubser. On nonuniform black branes. *Class. Quant. Grav.*, 19:4825–4844, 2002. 6, 33
  90. S. S. Gubser, I. R. Klebanov, and A. M. Polyakov. Gauge theory correlators from non-critical string theory. *Physics Letters B*, 428(1-2):105–114, May 1998. 4, 20
  91. S. S. Gubser and S. S. Pufu. The gravity dual of a p -wave superconductor. *Journal of High Energy Physics*, 2008(11):033, 2008. 5
  92. F. Guinea, M. I. Katsnelson, and A. K. Geim. Energy gaps and a zero-field quantum Hall effect in graphene by strain engineering. *Nature Physics*, 6(1):30–33, Jan. 2010. 67
  93. T. Harmark. Small black holes on cylinders. *Phys. Rev.*, D69:104015, 2004. 6, 33
  94. T. Harmark, V. Niarchos, and N. A. Obers. Instabilities of black strings and branes. *Class. Quant. Grav.*, 24:R1–R90, 2007. 38
  95. T. Harmark and N. A. Obers. New phase diagram for black holes and strings on cylinders. *Class. Quant. Grav.*, 21:1709, 2004. 34, 35
  96. T. Harmark and N. A. Obers. New phases of near-extremal branes on a circle. *JHEP*, 09:022, 2004. 107
  97. A. B. Harris. Effect of random defects on the critical behaviour of Ising models. *Journal of Physics C: Solid State Physics*, 7(9):1671, 1974. 83
  98. S. A. Hartnoll, C. P. Herzog, and G. T. Horowitz. Building a Holographic Superconductor. *Physical Review Letters*, 101(3):031601, July 2008. 5
  99. S. A. Hartnoll, D. M. Ramirez, and J. E. Santos. Emergent scale invariance of disordered horizons. *JHEP*, 09:160, 2015. 85, 99
  100. S. A. Hartnoll, D. M. Ramirez, and J. E. Santos. Thermal conductivity at a disordered quantum critical point. *JHEP*, 04:022, 2016. 85
  101. S. A. Hartnoll and J. E. Santos. Cold planar horizons are floppy. *Phys. Rev.*, D89(12):126002, 2014. 84
  102. S. A. Hartnoll and J. E. Santos. Disordered horizons: Holography of randomly disordered fixed points. *Phys. Rev. Lett.*, 112:231601, 2014. 84
  103. S. W. Hawking. Black hole explosions. *Nature*, 248:30–31, 1974. 17
  104. M. Headrick, S. Kitchen, and T. Wiseman. A New approach to static numerical relativity, and its application to Kaluza-Klein black holes. *Class. Quant. Grav.*, 27:035002, 2010. 33, 36, 43, 59
  105. C. Herring. Accidental Degeneracy in the Energy Bands of Crystals. *Physical Review*, 52:365–373, Aug. 1937. 61

- 
106. J. Hesthaven, S. Gottlieb, and D. Gottlieb. *Spectral Methods for Time-Dependent Problems*. Cambridge Monographs on Applied and Computational Mathematics. Cambridge University Press, 2007. 27, 28, 29, 126
  107. G. T. Horowitz, editor. *Black holes in higher dimensions*. Cambridge Univ. Pr., Cambridge, UK, 2012. 6
  108. P. Hosur, S. A. Parameswaran, and A. Vishwanath. Charge Transport in Weyl Semimetals. *Physical Review Letters*, 108(4):046602, Jan. 2012. 61
  109. C. Hoyos, K. Jensen, and A. Karch. Holographic fractional topological insulators. *Phys. Rev. D*, 82:086001, Oct 2010. 5
  110. J. A. Hoyos and T. Vojta. Theory of Smeared Quantum Phase Transitions. *Physical Review Letters*, 100(24):240601, June 2008. 84
  111. F. Hrahsheh, D. Nozadze, and T. Vojta. Composition-tuned smeared phase transitions. *Phys. Review B*, 83(22):224402, June 2011. 91, 95
  112. X. Huang, L. Zhao, Y. Long, P. Wang, D. Chen, Z. Yang, H. Liang, M. Xue, H. Weng, Z. Fang, X. Dai, and G. Chen. Observation of the Chiral-Anomaly-Induced Negative Magnetoresistance in 3d Weyl Semimetal TaAs. *Physical Review X*, 5(3):031023, Aug. 2015. 7, 61, 73
  113. N. Itzhaki, J. M. Maldacena, J. Sonnenschein, and S. Yankielowicz. Supergravity and the large N limit of theories with sixteen supercharges. *Phys. Rev.*, D58:046004, 1998. 6
  114. R. Jackiw. When radiative corrections are finite, but undetermined. *International Journal of Modern Physics B*, 14(19n20):2011–2021, Aug. 2000. 69
  115. J. H. Jeans. The Stability of a Spherical Nebula. *Phil. Trans. R. Soc. A*, 199:1–53, 1902. 38
  116. Jha, Raghav G., Catterall, Simon, Schaich, David, and Wiseman, Toby. Testing the holographic principle using lattice simulations. *EPJ Web Conf.*, 175:08004, 2018. 109
  117. A. Jimenez-Alba, K. Landsteiner, Y. Liu, and Y.-W. Sun. Anomalous magnetoconductivity and relaxation times in holography. *Journal of High Energy Physics*, 2015(7):117, July 2015. 71
  118. H. C. John and R. K. Guy. *The Book of Numbers*, volume 2. 1995. 86
  119. W. Kahan. Pracniques: Further Remarks on Reducing Truncation Errors. *Commun. ACM*, 8(1):40–, Jan. 1965. 126
  120. M. Kalisch. *Numerical construction and critical behavior of Kaluza-Klein black holes*. PhD thesis, Jena, Jan 2018. Dissertation, Friedrich-Schiller-Universität Jena, 2018. 7, 29, 34, 47, 49, 126
  121. M. Kalisch and M. Ansorg. Highly Deformed Non-uniform Black Strings in Six Dimensions. In *14th Marcel Grossmann Meeting on Recent Developments in Theoretical and Experimental General Relativity, Astrophysics, and Relativistic Field Theories (MG14) Rome, Italy, July 12-18, 2015*, 2015. 6, 33, 98
  122. M. Kalisch and M. Ansorg. Pseudo-spectral construction of non-uniform black string solutions in five and six spacetime dimensions. *Class. Quant. Grav.*, 33(21):215005, 2016. 6, 11, 33, 34, 36, 40, 41, 52, 53, 55, 56, 57, 60, 98, 105

- 
123. M. Kalisch, S. Moeckel, and M. Ammon. Critical behavior of the black hole / black string transition. *JHEP*, 08:049, 2017. 6, 7, 34, 39, 40, 41
124. T. Kaluza. Zum Unitätsproblem der Physik. *Sitz. Preuß. Akad. Wiss.*, pages 966–972, 1921. 3
125. A. Karch, J. Maciejko, and T. Takayanagi. Holographic fractional topological insulators in  $2 + 1$  and  $1 + 1$  dimensions. *Phys. Rev. D*, 82:126003, Dec 2010. 5
126. R. P. Kerr. Gravitational field of a spinning mass as an example of algebraically special metrics. *Phys. Rev. Lett.*, 11:237–238, 1963. 16
127. H.-J. Kim, K.-S. Kim, J.-F. Wang, M. Sasaki, N. Satoh, A. Ohnishi, M. Kitaura, M. Yang, and L. Li. Dirac versus Weyl Fermions in Topological Insulators: Adler-Bell-Jackiw Anomaly in Transport Phenomena. *Physical Review Letters*, 111(24):246603, Dec. 2013. 61
128. B. Kleihaus, J. Kunz, and E. Radu. New nonuniform black string solutions. *JHEP*, 06:016, 2006. 33, 36, 40
129. O. Klein. Quantentheorie und fünfdimensionale Relativitätstheorie. *Z. Phys.*, 37(12):895–906, 1926. 3
130. O. Klein. The Atomicity of Electricity as a Quantum Theory Law. *Nature*, 118:516, 1926. 3
131. B. Kol. Explosive black hole fission and fusion in large extra dimensions. 2002. 6
132. B. Kol. Topology change in general relativity, and the black hole black string transition. *JHEP*, 10:049, 2005. 6, 33, 34, 40, 60, 97, 98
133. B. Kol. Choptuik scaling and the merger transition. *JHEP*, 10:017, 2006. 6, 34, 41, 53, 97
134. B. Kol. The Phase transition between caged black holes and black strings: A Review. *Phys. Rept.*, 422:119–165, 2006. 40
135. B. Kol, E. Sorkin, and T. Piran. Caged black holes: Black holes in compactified space-times. 1. Theory. *Phys. Rev.*, D69:064031, 2004. 34, 35
136. B. Kol and T. Wiseman. Evidence that highly nonuniform black strings have a conical waist. *Class. Quant. Grav.*, 20:3493–3504, 2003. 33, 41
137. H. Kudoh and T. Wiseman. Properties of Kaluza-Klein black holes. *Prog. Theor. Phys.*, 111:475–507, 2004. 33, 36, 43
138. H. Kudoh and T. Wiseman. Connecting black holes and black strings. *Phys. Rev. Lett.*, 94:161102, 2005. 33, 36
139. K. Landsteiner. Notes on Anomaly Induced Transport. *Acta Phys. Polon.*, B47:2617, 2016. 85
140. K. Landsteiner and Y. Liu. The holographic Weyl semi-metal. *Phys. Lett.*, B753:453–457, 2016. 7, 71, 75, 76
141. K. Landsteiner, Y. Liu, and Y.-W. Sun. Odd viscosity in the quantum critical region of a holographic Weyl semimetal. *Phys. Rev. Lett.*, 117(8):081604, 2016. 100

- 
142. K. Landsteiner, Y. Liu, and Y.-W. Sun. Quantum phase transition between a topological and a trivial semimetal from holography. *Phys. Rev. Lett.*, 116(8):081602, 2016. 7, 71, 76, 85, 90, 100
  143. K. Landsteiner, E. Megías, and F. Peña Benitez. *Anomalous Transport from Kubo Formulae*. Strongly interacting matter in magnetic fields. Springer Berlin, 2013. 68
  144. L. Lehner and F. Pretorius. Black Strings, Low Viscosity Fluids, and Violation of Cosmic Censorship. *Phys. Rev. Lett.*, 105:101102, 2010. 38
  145. L. Lehner and F. Pretorius. Final State of Gregory-Laflamme Instability. In G. T. Horowitz, editor, *Black holes in higher dimensions*. Cambridge University Press, Cambridge, UK, 2012. 38
  146. X. S. Li. An overview of superlu: Algorithms, implementation, and user interface. *ACM Trans. Math. Softw.*, 31(3):302–325, Sept. 2005. 130
  147. H. Liu, J. McGreevy, and D. Vegh. Non-Fermi liquids from holography. *Phys. Rev. D*, 83:065029, Mar 2011. 5
  148. Z. K. Liu, L. X. Yang, Y. Sun, T. Zhang, H. Peng, H. F. Yang, C. Chen, Y. Zhang, Y. F. Guo, D. Prabhakaran, M. Schmidt, Z. Hussain, S.-K. Mo, C. Felser, B. Yan, and Y. L. Chen. Evolution of the Fermi surface of Weyl semimetals in the transition metal pnictide family. *Nature Materials*, 15(1):27–31, Jan. 2016. 61
  149. T. Louvet, D. Carpentier, and A. A. Fedorenko. New quantum transition in Weyl semimetals with correlated disorder. *Phys. Review B*, 95(1):014204, Jan. 2017. 84
  150. A. Lucas. Hydrodynamic transport in strongly coupled disordered quantum field theories. *New J. Phys.*, 17(11):113007, 2015. 84
  151. A. Lucas and S. Sachdev. Conductivity of weakly disordered strange metals: from conformal to hyperscaling-violating regimes. *Nucl. Phys.*, B892:239–268, 2015. 84
  152. A. Lucas, S. Sachdev, and K. Schalm. Scale-invariant hyperscaling-violating holographic theories and the resistivity of strange metals with random-field disorder. *Phys. Rev.*, D89(6):066018, 2014. 84
  153. J. Maldacena. The Large-N Limit of Superconformal Field Theories and Supergravity. *International Journal of Theoretical Physics*, 38(4):1113–1133, 1999. 4, 20
  154. T. Mathew. *Domain Decomposition Methods for the Numerical Solution of Partial Differential Equations*. Lecture Notes in Computational Science and Engineering. Springer Berlin Heidelberg, 2008. 32
  155. A. Meister and C. Vömel. *Numerik linearer Gleichungssysteme*. Vieweg+Teubner Verlag, 2011. 32, 131
  156. R. C. Myers. Higher Dimensional Black Holes in Compactified Space-times. *Phys. Rev.*, D35:455, 1987. 6, 33
  157. M. Nakahara. *Geometry, Topology and Physics*. Institute of Physics Publishing, London, 2 edition, 2003. 62

- 
158. E. T. Newman and A. I. Janis. Note on the Kerr Spinning-Particle Metric. *J. Math. Phys.*, 6:915–917, June 1965. 16
159. H. B. Nielsen and M. Ninomiya. The Adler-Bell-Jackiw anomaly and Weyl fermions in a crystal. *Physics Letters B*, 130(6):389–396, Nov. 1983. 61, 64, 99
160. G. Nordström. Über die Möglichkeit, das elektromagnetische Feld und das Gravitationsfeld zu vereinigen. *Physik. Z.*, 15:504–506, 1914. 3
161. G. Nordström. On the Energy of the Gravitation field in Einstein's Theory. *Koninkl. Ned. Akad. Wetenschap.*, 20:1238–1245, 1918. 16
162. D. Nozadze, C. Svoboda, F. Hrahsheh, and T. Vojta. Modification of smeared phase transitions by spatial disorder correlations. In A. Avella and F. Mancini, editors, *American Institute of Physics Conference Series*, volume 1550 of *American Institute of Physics Conference Series*, pages 263–267, Aug. 2013. 84, 94, 95
163. S. A. Orszag. Comparison of Pseudospectral and Spectral Approximation. *Studies in Applied Mathematics*, 51(3):253–259. 27
164. S. Parker. *McGraw-Hill Dictionary of Scientific and Technical Terms*. Dictionary of Scientific and Technical Terms. McGraw-Hill Education, 2003. 30
165. M. Pérez-Victoria. Exact Calculation of the Radiatively Induced Lorentz and CPT Violation in QED. *Physical Review Letters*, 83(13):2518–2521, Sept. 1999. 69
166. C. G. Petra, O. Schenk, and M. Anitescu. Real-time stochastic optimization of complex energy systems on high-performance computers. *IEEE Computing in Science & Engineering*, 16(5):32–42, 2014. 130
167. C. G. Petra, O. Schenk, M. Lubin, and K. Gärtner. An augmented incomplete factorization approach for computing the Schur complement in stochastic optimization. *SIAM Journal on Scientific Computing*, 36(2):C139–C162, 2014. 130
168. H. P. Pfeiffer, L. E. Kidder, M. A. Scheel, and S. A. Teukolsky. A multidomain spectral method for solving elliptic equations. *Computer Physics Communications*, 152(3):253 – 273, 2003. 127
169. D. I. Pikulin, A. Chen, and M. Franz. Chiral anomaly from strain-induced gauge fields in Dirac and Weyl semimetals. *arXiv:1607.01810 [cond-mat]*, July 2016. arXiv: 1607.01810. 67
170. R. V. Pound and G. A. Rebka. Gravitational red-shift in nuclear resonance. *Phys. Rev. Lett.*, 3:439–441, 1959. 3
171. L. Randall and R. Sundrum. Large Mass Hierarchy from a Small Extra Dimension. *Physical Review Letters*, 83:3370–3373, Oct. 1999. 100
172. M. Randeria, J. P. Sethna, and R. G. Palmer. Low-Frequency Relaxation in Ising Spin-Glasses. *Phys. Rev. Lett.*, 54:1321–1324, Mar 1985. 84, 99
173. H. Reissner. Über die Eigengravitation des elektrischen Feldes nach der Einsteinschen Theorie. *Ann. Phys. (Berlin)*, 355(9):106–120, 1916. 16



- 
174. B. Roy and S. Das Sarma. Quantum phases of interacting electrons in three-dimensional dirty Dirac semimetals. *Phys. Rev. B*, 94:115137, Sep 2016. 84
  175. B. Roy, R.-J. Slager, and V. Juricic. Global Phase Diagram of a Dirty Weyl liquid and Emergent Superuniversality. 2016. 84
  176. S. Ryu, T. Takayanagi, and T. Ugajin. Holographic Conductivity in Disordered Systems. *JHEP*, 04:115, 2011. 85
  177. Y. Saad and M. H. Schultz. GMRES: A Generalized Minimal Residual Algorithm for Solving Nonsymmetric Linear Systems. *SIAM Journal on Scientific and Statistical Computing*, 7(3):856–869, 1986. 130
  178. S. Sachdev. *Quantum phase transitions*. Cambridge University Press, Cambridge, second ed. edition, 2011. 69
  179. B. Sbierski, G. Pohl, E. J. Bergholtz, and P. W. Brouwer. Quantum Transport of Disordered Weyl Semimetals at the Nodal Point. *Physical Review Letters*, 113(2):026602, July 2014. 84
  180. M. Schechter. Solution of the Dirichlet problem for systems not necessarily strongly elliptic. *Communications on Pure and Applied Mathematics*, 12(2):241–247. 11
  181. F. Schwabl. *Quantenmechanik für Fortgeschrittene (QM II)*. Springer-Lehrbuch. Springer Berlin Heidelberg, 2008. 62
  182. K. Schwarzschild. Über das Gravitationsfeld eines Massenpunktes nach der Einsteinschen Theorie. *Sitz. Preuß. Akad. Wiss.*, pages 189–196, 1916. 16
  183. M. Shinozuka and G. Deodatis. Simulation of Stochastic Processes by Spectral Representation. *Applied Mechanics Reviews*, 44(4):191–204, Apr 1991. 86
  184. T. Shiromizu, D. Ida, and S. Tomizawa. Kinematical bound in asymptotically translationally invariant space-times. *Phys. Rev.*, D69:027503, 2004. 35
  185. E. Sorkin. A Critical dimension in the black string phase transition. *Phys. Rev. Lett.*, 93:031601, 2004. 33, 36, 54
  186. E. Sorkin. Non-uniform black strings in various dimensions. *Phys. Rev.*, D74:104027, 2006. 33, 36, 41
  187. E. Sorkin, B. Kol, and T. Piran. Caged black holes: Black holes in compactified space-times. 2. 5-d numerical implementation. *Phys. Rev.*, D69:064032, 2004. 33, 36, 43
  188. D. Sornette. Discrete-scale invariance and complex dimensions. *Physics Reports*, 297(5):239–270, 1998. 85, 95, 97
  189. C. Svoboda, D. Nozadze, F. Hrahsheh, and T. Vojta. Disorder correlations at smeared phase transitions. *EPL (Europhysics Letters)*, 97(2):20007, 2012. 84, 94, 95
  190. O. Tange. GNU Parallel - The Command-Line Power Tool. *login: The USENIX Magazine*, 36(1):42–47, Feb. 2011. 131
  191. F. R. Tangherlini. Schwarzschild field in n dimensions and the dimensionality of space problem. *Nuovo Cimento*, 27(3):636–651, 1963. 18

- 
192. M. Taylor-Robinson. More on counterterms in the gravitational action and anomalies. *arXiv:hep-th/0002125*, Feb. 2000. arXiv: hep-th/0002125. 71
193. J. H. Traschen. A Positivity theorem for gravitational tension in brane space-times. *Class. Quant. Grav.*, 21:1343–1350, 2004. 35
194. H. A. van der Vorst. BI-CGSTAB: A Fast and Smoothly Converging Variant of BI-CG for the Solution of Nonsymmetric Linear Systems. *SIAM J. Sci. Stat. Comput.*, 13(2):631–644, Mar. 1992. 130
195. A. Vilenkin. Equilibrium parity-violating current in a magnetic field. *Phys. Rev. D*, 22:3080–3084, Dec 1980. 68
196. M. Vojta. Quantum phase transitions. *Reports on Progress in Physics*, 66:2069–2110, Dec. 2003. 69
197. T. Vojta. Disorder-Induced Rounding of Certain Quantum Phase Transitions. *Phys. Rev. Lett.*, 90:107202, Mar 2003. 84
198. T. Vojta. Smearing of the phase transition in Ising systems with planar defects. *Journal of Physics A: Mathematical and General*, 36(43):10921, 2003. 84
199. T. Vojta. Broadening of a nonequilibrium phase transition by extended structural defects. *Phys. Rev. E*, 70:026108, Aug 2004. 84
200. T. Vojta. Rare region effects at classical, quantum and nonequilibrium phase transitions. *Journal of Physics A Mathematical General*, 39:R143–R205, June 2006. 83, 95
201. T. Vojta. Computing quantum phase transitions. *ArXiv e-prints*, Sept. 2007. 70
202. T. Vojta. Quantum Griffiths Effects and Smeared Phase Transitions in Metals: Theory and Experiment. *Journal of Low Temperature Physics*, 161:299–323, Oct. 2010. 84, 99
203. T. Vojta. Phases and phase transitions in disordered quantum systems. In A. Avella and F. Mancini, editors, *American Institute of Physics Conference Series*, volume 1550 of *American Institute of Physics Conference Series*, pages 188–247, Aug. 2013. 83
204. T. Vojta and J. A. Hoyos. Criticality and quenched disorder: rare regions vs. Harris criterion. *ArXiv e-prints*, Sept. 2013. 84
205. T. Vojta and R. Sknepnek. Critical points and quenched disorder: From Harris criterion to rare regions and smearing. *Physica Status Solidi B Basic Research*, 241:2118–2127, July 2004. 84
206. R. Wald. *General Relativity*. University of Chicago Press, 1984. 16
207. X. Wan, A. M. Turner, A. Vishwanath, and S. Y. Savrasov. Topological semimetal and Fermi-arc surface states in the electronic structure of pyrochlore iridates. *Physical Review B*, 83(20):205101, May 2011. 61, 62
208. H. Weyl. Elektron und Gravitation. I. *Zeitschrift für Physik*, 56(5):330–352, May 1929. 61
209. T. Williams, C. Kelley, and many others. Gnuplot 4.6: an interactive plotting program. <http://gnuplot.sourceforge.net/>, April 2013. 131

- 
210. T. Wiseman. From black strings to black holes. *Class. Quant. Grav.*, 20:1177–1186, 2003. 33, 36
211. T. Wiseman. Static axisymmetric vacuum solutions and nonuniform black strings. *Class. Quant. Grav.*, 20:1137–1176, 2003. 33, 36
212. T. Wiseman. Numerical construction of static and stationary black holes. In G. T. Horowitz, editor, *Black holes in higher dimensions*. Cambridge University Press, Cambridge, UK, 2012. 11, 12
213. E. Witten. Anti De Sitter Space And Holography. *Adv. Theor. Math. Phys.*, 2:253–291, Feb. 1998. 4, 20
214. J. Woithe, G. J. Wiener, and F. F. Van der Veken. Lets have a coffee with the Standard Model of particle physics! *Physics Education*, 52(3):034001, May 2017. 4
215. S.-Y. Xu, I. Belopolski, N. Alidoust, M. Neupane, G. Bian, C. Zhang, R. Sankar, G. Chang, Z. Yuan, C.-C. Lee, S.-M. Huang, H. Zheng, J. Ma, D. S. Sanchez, B. Wang, A. Bansil, F. Chou, P. P. Shibayev, H. Lin, S. Jia, and M. Z. Hasan. Discovery of a Weyl fermion semimetal and topological Fermi arcs. *Science*, 349(6248):613–617, Aug. 2015. 7, 61, 73
216. K.-Y. Yang, Y.-M. Lu, and Y. Ran. Quantum Hall effects in a Weyl semimetal: Possible application in pyrochlore iridates. *Physical Review B*, 84(7):075129, Aug. 2011. 61
217. Y. X. Zhao and Z. D. Wang. Disordered Weyl Semimetals and Their Topological Family. *Physical Review Letters*, 114(20):206602, May 2015. 84
218. B. Zwiebach. *A first course in string theory*. Cambridge University Press, 2006. 4
219. A. A. Zyuzin, S. Wu, and A. A. Burkov. Weyl semimetal with broken time reversal and inversion symmetries. *Physical Review B*, 85(16):165110, Apr. 2012. 61



---

# Abbreviations and notation

---

We use Greek letters for  $D = d + 1$ -dimensional indices running from 0 to  $d$  and Latin letters starting from  $\{a, b, c, \dots\}$  for  $d$ -dimensional indices running from 0 to  $d - 1$ , where not indicated otherwise. Latin letters starting from  $\{i, j, k, \dots\}$  are used for generic indices and non-coordinate tensor expressions.

The following abbreviations are used throughout the thesis:

aAdS	asymptotically anti-de Sitter
AdS	anti-de Sitter
AHC	anomalous Hall conductivity
AHE	anomalous Hall effect
ARPES	angle resolved photoemmission spectroscopy
BB	black brane
BC	boundary condition
BVP	boundary value problem
CFT	conformal field theory
CME	chiral magnetic effect
CPME	chiral pseudo-magnetic effect
DSI	discrete scale invariance
FFT	fast Fourier transform
FG	Fefferman-Graham
GR	general relativity
GL	Gregory-Laflamme
KK	Kaluza-Klein
LBH	localized black hole
NBS	non-uniform black string
ODE	ordinary differential equation
PDE	partial differential equation
QCP	quantum critical point

QCR	quantum critical region
QPT	quantum phase transition
SM	standard model
SYM	supersymmetric Yang-Mills
UBS	uniform black string
VEV	vacuum expectation value
MWR	method of weighted residuals
WSM	Weyl semimetal

---

# Acknowledgements

---

I want to thank my supervisor, Martin Ammon, who showed support for all the questions that arose in the course of writing this thesis.

Furthermore, I am grateful to Michael Kalisch, without him the work about localized black holes would have never been accomplished. I would like to thank Markus Heinrich and Amadeo Jiménez-Alba for the beneficial collaboration regarding the holographic Weyl semimetal project. Furthermore I would like to thank David Hilditch and Marcus Bugner for the (still unfinished) collaboration about a full 3+1 time evolution of scalar field on  $AdS_{3+1}$  and especially David for the nice stay in Lisbon.

In addition, I would like to express my gratitude to the IT team, in particular Alexander Blinne and Andre Sternbeck, for offering support for all my special software matters.

Many thanks at this point to Martin Ammon, Marcel Dresbur, Markus Heinrich, Amadeo Jiménez-Alba, Michael Kalisch and my brother Thomas Möckel for proof reading and their valuable comments.

Finally, I acknowledge financial support by the Deutsche Forschungsgemeinschaft (DFG) graduate school GRK 1523/2 and by the University of Jena.





---

# Ehrenwörtliche Erklärung

---

Ich erkläre hiermit ehrenwörtlich, dass ich die vorliegende Arbeit selbstständig, ohne unzulässige Hilfe Dritter und ohne Benutzung anderer als der angegebenen Hilfsmittel und Literatur angefertigt habe. Die aus anderen Quellen direkt oder indirekt übernommenen Daten und Konzepte sind unter Angabe der Quelle gekennzeichnet.

Bei der Auswahl und Auswertung des Materials haben mir die nachstehend aufgeführten Personen unentgeltlich geholfen:

1. Jun.-Prof. Dr. Martin Ammon
2. Dr. Amadeo Jiménez-Alba
3. Dr. Michael Kalisch
4. Markus Heinrich

Weitere Personen waren an der inhaltlich-materiellen Erstellung der vorliegenden Arbeit nicht beteiligt. Insbesondere habe ich hierfür nicht die entgeltliche Hilfe von Vermittlungs- bzw. Beratungsdiensten (Promotionsberater oder andere Personen) in Anspruch genommen. Niemand hat von mir unmittelbar oder mittelbar geldwerte Leistungen für Arbeiten erhalten, die im Zusammenhang mit dem Inhalt der vorgelegten Dissertation stehen.

Die Arbeit wurde bisher weder im In- noch im Ausland in gleicher oder ähnlicher Form einer anderen Prüfungsbehörde vorgelegt.

Die geltende Promotionsordnung der Physikalisch-Astronomischen Fakultät ist mir bekannt.

Ich versichere ehrenwörtlich, dass ich nach bestem Wissen die reine Wahrheit gesagt und nichts verschwiegen habe.

Jena, den 29. Mai 2018

Sebastian Möckel